



**LIGHT SCATTERING BY SMOKE AND  
NUISANCE AEROSOLS**

DARRYL WAYNE WEINERT

A research dissertation submitted in fulfilment of requirements for  
the degree of

**Doctor of Philosophy**

undertaken at the

Centre for Environmental Safety and Risk Engineering

Faculty of Science, Engineering and Technology

Victoria University of Technology

AUSTRALIA.

**2003**

WER THESIS  
628.9225 WEI  
30001008559389  
Weinert, Darryl Wayne  
Light scattering by smoke  
and nuisance aerosols

## ACKNOWLEDGMENTS

I would like to thank first and foremost my supervisors, Dr. George Mulholland, Dr. Paula Beever and Prof. Ian Thomas. I would also like to include Dr. Martin Cole for initiating and encouraging this research. To you my supervisors, I extend my heart-felt thanks.

Dr. Mulholland is my smoke guru, besides that he has also taught me to steer a canoe and how to go hiking in the rain. It has been an absolute pleasure and honour to be both his guest researcher and pupil. My thanks also to Nancy Mulholland for her work and support during draft editing and reading. Dr. Beever has been with me since the initiation of this research project including all the rough funding times. I have harassed Dr. Beever at many different stages for editorial comments, but usually to ask for some handy words of wisdom and motivation, or to discuss over a beer the strange things Fire Safety Engineers do. Prof. Thomas inherited me with a change of administration and has facilitated the completion of this thesis since then, while at the same time emphasising the realities of the field surrounding this research. I would also like to thank Dr. Martin Cole for initiating this line of research some years ago, encouraging me throughout and for proof reading the final draft.

My thanks to Vision Systems, VESDA Division, for their support in recent years as partners in the Australian Postgraduate Award (Industry).

The bulk of this dissertation is reliant on work conducted at the Building and Fire Research Laboratory, National Institute of Standards and Technology, in the United States where I was a guest researcher. To everyone at NIST that made my stay productive and so much fun, thank you very much. Specifically I would like to draw attention to Thomas Cleary for his help with smoke and nuisance aerosol generation. Paula Garret, Michel Donnelly, Marco Fernandez and Mike Selepak for helping with all the daily details -- particularly when I broke something.

I have to thank my Mum and Dad. I know my mum is going to make me go to the graduation just so she can take photographs of me in silly clothes. Love you both.

Finally I would like to express my deepest appreciation to Zuzana for her steadfast support, even when various oceans and two or three continental landmasses got in our way. Simply meeting Zuzi has been the greatest outcome of this thesis. Words just fail me.....

## ABSTRACT

This study was aimed at discriminating between three classes of aerosols, namely those generated by flaming and non-flaming (smouldering & forced pyrolysis) fires as well as nuisance aerosols. This was undertaken using a scattering cross section based on the mass concentration of aerosols as opposed to the traditional arbitrary units. A key feature was to develop a calibration method for measurement of the differential (angular distribution) mass scattering cross section [ $\text{m}^2 \cdot \text{g}^{-1} \cdot \text{sr}^{-1}$ ] of the smoke and nuisance aerosols. These measurements were made for two linear polarizations and the scattering angle,  $\theta$ , in the range of  $5^\circ$  to  $135^\circ$  at a wavelength of  $\lambda = 632.8 \text{ nm}$ .

The calibration method used polystyrene latex spheres as calibration particles for their well-characterised sizes and refractive index. A least mean squared method was then used to determine a calibration constant linking the experimental and ideal theoretical (Mie) results for the polystyrene spheres. A gravimetric measurement of the time average mass concentration of aerosols in the scattering volume yields the scattering cross section in terms of mass. The aerosol mass concentrations varied from about 1 to  $10 \text{ mg} \cdot \text{m}^{-3}$ .

Aerosol size distributions were also measured, revealing that smouldering cotton lamp wick smoke particles fell into the range typical of flaming fire smoke particles. Analysis of light scattering results has distinguished small diameter particles from large particles using a forward scattering ratio. The method has exceptions when discriminating soot created in flaming fires from both non-flaming fire generated smoke and nuisance aerosols. Discrimination of soot from the other aerosols is demonstrated by the asymmetry ratio of forward ( $45^\circ$ ) to backward scattering ( $135^\circ$ ) and the polarization ratio of horizontal to vertical polarisation. These methods were not successful at discriminating between the non-flaming smoke and nuisance aerosols.

A novel method of soot discrimination based on the scattering parameter,  $q = 4\pi\lambda^{-1} \sin(\theta/2)$ , has been demonstrated. Again discrimination between non-flaming smoke and nuisance aerosols was not possible. The scattering parameter method has shown that the power law behaviour of non-flaming fire generated smoke and nuisance aerosols have an index (the “q-slope”) that ranges from -2.8 to -4.2, compared with a range of -1.6 to

-2.0 for flame generated smoke aerosols. The scattering by a non-flaming fire generated smoke or nuisance aerosol is of the form  $\sigma_{VV}(q) \propto \langle q^{-3} \rangle_R$  for larger particles, having an index around -3. Here the angled brackets represent the ensemble average over the size distribution for the case of vertical polarisation. The result for the large non-flaming smoke and nuisance aerosols was found to differ from that proposed recently (Sorensen and Fischbach, 2000). Agreement was observed between this study and that predicted by Sorensen and Fischbach (2000) for smaller mean sized particles, which have an index of about -4 as described by Porod's law. The results for soot are typical of their fractal morphology, which typically ranges from -1.7 to -1.85.

# TABLE OF CONTENTS

## **Chapter 1: Introduction**

1.1 Introduction.....	1
1.2 Smoke Detection and Motivation .....	2
1.3 Overview of this study.....	5

## **Chapter 2: Overview of the theory of light scattering by small particles**

2.1 Introduction.....	12
2.2 Lognormal size distributions .....	13
2.2.1 Distribution equations.....	13
2.3 Light scattering by spheres.....	17
2.3.1 Mie Theory .....	17
2.3.2 Amplitude scattering matrix and the far field.....	19
2.4 Differential mass scattering cross section .....	22
2.4.1 Introducing a mass formalism .....	22
2.4.2 Scattering cross section of a single arbitrary particle .....	23
2.4.3 Scattering cross section of a cloud of polydisperse particles .....	25
2.4.4 Detector signal and scattering cross sections.....	29
2.4.5 Ratios for scattering data analysis.....	30
2.5 Light scattering by agglomerates.....	31
2.5.1 Fractal soot agglomerates .....	31
2.5.2 Scattering parameter and the structure factor.....	34
2.5.2.1 Structure factor for $qR_g < 1$ .....	36
2.5.2.2 Structure factor in the transition region .....	36
2.5.2.3 Structure factor for $qR_g > 1$ .....	37
2.6 Scaling Approach to Scattering by spheres.....	37
2.7 Summary.....	40

## **Chapter 3: Light Scattering Apparatus**

3.1 Introduction.....	42
3.1.1 Historical overview .....	42
3.1.2 An overview of other light scattering apparatus .....	44
3.1.3 Angular light scattering applied to smoke aerosols .....	46
3.2 General features .....	51
3.3 Optical System.....	53
3.3.1 The optical components .....	53
3.3.2 Signal detection.....	57
3.3.3 Stray and background light.....	58
3.3.4 Scattering volume correction .....	59
3.4 Aerosol transport.....	60
3.4.1 Summary of aerosol generation methods.....	62
3.4.1.1 Fuels used to generate smoke and nuisance aerosols .....	63
3.4.1.2 Fire Emulator/Detector Evacuator and aerosol sampling.....	64

**Chapter 4: Calibration**

4.1 Introduction .....	68
4.1.1 Historical overview of calibration methods .....	68
4.1.2 Calibration Overview .....	70
4.2 Calibration theory .....	72
4.3 Calibration method.....	75
4.3.1 Properties of the calibration particles.....	75
4.3.1.1 Calibration aerosol generation.....	78
4.3.1.2 Mass concentration measurement.....	84
4.4 Light scattering calibration measurement .....	85
4.4.1 Method.....	85
4.5 Calibration verification .....	86
4.5.1 Method.....	86
4.5.2 Results .....	88
4.6 Uncertainty analysis.....	93
4.6.1 Type A and Type B uncertainties.....	93
4.6.2 Uncertainty in the calibration verification .....	94
4.6.2.1 Type A uncertainty .....	94
4.6.2.2 Type B: Polystyrene sphere uncertainty .....	96
4.6.2.3 Type B: Refractive index uncertainty .....	99
4.6.2.4 Calibration verification: combined and expanded uncertainty.....	100
4.6.3 Component uncertainty analysis: Type A.....	102
4.6.3.1 Uncertainty in repeat experiments.....	102
4.6.3.2 Detector signal uncertainty .....	103
4.6.3.3 Mass concentration time dependence .....	106
4.6.4 Component uncertainty analysis: Type B .....	108
4.6.4.1 Scattering angle deviations .....	108
4.6.4.2 Uncertainty in polariser setting.....	109
4.6.4.3 Multiple scattering.....	112
4.6.4.4 Polystyrene sphere doublets .....	113
4.6.5 Combined Component uncertainty .....	114
4.7 Discussion .....	115

**Chapter 5: Smoke aerosols form non-flaming fires**

5.1 Introduction .....	117
5.1.1 Overview.....	117
5.1.2 Smoke aerosols form non-flaming fires.....	117
5.2 Methods.....	123
5.2.1 Non-flaming fuels and smoke aerosols.....	123
5.2.2 Smoke aerosol sampling and transport.....	130
5.2.2.1 Sampling for size distribution.....	130
5.2.2.1.1 Mass distribution .....	131
5.2.2.1.2 Number distribution .....	133
5.2.2.2 Sampling for number and mass concentration in the FE/DE.....	136
5.2.2.3 Sampling for light scattering .....	137
5.2.3 Theoretical light scattering methods.....	139
5.3 Results.....	140
5.3.1 Size distribution .....	141
5.3.1.1 Mass and number distribution.....	141

5.3.1.2 Mass and number concentration.....	147
5.3.2 Mass extinction cross section.....	150
5.3.3 Angular light scattering .....	151
5.3.3.1 Uncertainty analysis of drum dilution.....	151
5.3.3.2 Smoke aerosol from beech wood .....	157
5.3.3.3 Smoke aerosol from smouldering cotton lamp wick.....	160
5.3.3.4 Smoke aerosol from polyurethane foam .....	162
5.3.4 Analysis of angular scattering.....	163
5.3.4.1 Forward scattering and asymmetry ratios .....	163
5.3.4.2 Polarisation ratio .....	165
5.3.5 Truncated and total light scattering .....	167
5.3.6 Scattering parameter .....	168
5.3.6.1 q-slope.....	168
5.3.6.2 Envelope approach to the q-slope.....	171
5.4 Discussion .....	173

**Chapter 6: Smoke aerosols from Flaming fires**

6.1 Introduction.....	175
6.2 Method.....	178
6.2.1 Soot generation and transport .....	178
6.2.2 Light scattering methods .....	182
6.3 Light scattering Results.....	182
6.3.1 Angular scattering .....	182
6.3.1.1 Forward scattering and asymmetry ratio .....	186
6.3.1.2 Polarisation ratio .....	188
6.3.1.3 Truncated scattering cross section.....	188
6.3.2 Scattering parameter .....	188
6.4 Scattering measurements of the radius of gyration .....	190
6.4.1 Method.....	190
6.4.1.1 Acetylene and ethylene at different fuel flow rates.....	192
6.4.1.2 Agglomerate post-flame growth of acetylene and ethylene.....	192
6.4.2 Results .....	194
6.4.2.1 Radius of gyration at different fuel flow rates .....	194
6.4.2.2 Post-flame agglomerate growth of acetylene and ethylene.....	197
6.5 Discussion .....	201

**Chapter 7: Nuisance aerosols**

7.1 Introduction.....	203
7.2 Method.....	204
7.2.1 Nuisance aerosol generation, sampling and transport .....	204
7.2.2 Mass size distribution, mass and number concentration.....	207
7.2.3 Light scattering measurements .....	208
7.2.3.1 Theoretical light scattering methods .....	208
7.3 Results.....	209
7.3.1 Size distribution, mass and number concentrations in the FE/DE.....	209
7.3.2 Extinction mass cross section.....	213
7.3.3 Angular light scattering of nuisance aerosols.....	213
7.3.3.1 Forward scattering and asymmetry ratios .....	214
7.3.3.2 Polarisation ratio .....	217
7.3.3.3 Truncated and total light scattering.....	217
7.3.4 Scattering parameter .....	219

7.3.4.1 q-slope.....	219
7.3.4.2 Envelope approach to q-slope .....	221
7.4 Discussion .....	222

**Chapter 8: Discussion**

8.1 Introduction.....	225
8.2 Differential mass scattering cross section .....	226
8.2.1 Calibration and measurement .....	226
8.3 Light scattering characterisation.....	230
8.3.1 Overview.....	230
8.3.2 Aerosol particle size .....	232
8.3.2.1 Size distribution of smoke and nuisance aerosols .....	233
8.3.2.2 Forward scattering ratio.....	236
8.3.2.3 Soot agglomerate size and post-flame growth .....	238
8.3.3 Asymmetry Ratio.....	239
8.3.4 Polarisation Ratio .....	241
8.3.5 Truncated scattering and extinction .....	243
8.3.6 Comparison of experimental and Mie theory results .....	245
8.4 Light scattering as a function of scattering parameter.....	246
8.4.1 Scattering parameter .....	246
8.4.2 Scaling approach.....	247
8.4.2.1 Comparison of q-slope results .....	248
8.4.2.2 Scaling method and ensemble averaging .....	254
8.5 Discrimination and application to smoke detection .....	255
8.5.1 Light scattering ratios .....	255
8.5.2 q-slope .....	256
8.6 Final Comments.....	257

**Chapter 9: Conclusions**

9.1 Conclusions.....	259
9.2 Future Work .....	262

**Appendix I**

I. Introduction.....	264
II. Calibration .....	264
Polystyrene sphere preparation .....	264
Calibration light scattering measurements.....	265
III. Mass measurement.....	265
Mass flow rate.....	265
Weighing filters.....	265
IV. Light scattering measurements .....	266
Differential scattering measurements.....	266

**Appendix II**

The Papers .....	268
Full peer reviewed publication .....	269
NIST internal Technical Paper .....	281

<b>References.....</b>	<b>290</b>
------------------------	------------

TABLE OF FIGURES AND TABLES

Figures

Figure 1.1: Image of a soot agglomerate and incense smoke particles.....7

Figure 2.1: Calculated differential mass scattering cross sections of a 702 nm polystyrene sphere and a polydisperse distribution of spheres with MMD of 702 nm ..... 28

Figure 3.1: The angular scattering system of the LAOF ..... 54

Figure 3.2: A Schematic of the aerosol transport circuit ..... 61

Figure 3.3: Fire Emulator/Detector Evaluator ..... 65

Figure 3.4: FE/DE test section and aerosol transport system..... 67

Figure 4.1: Differential mass scattering cross section for calibration particles..... 77

Figure 4.2: Schematic of the polystyrene sphere aerosol generator..... 80

Figure 4.3: Schematic of the aerosol nebuliser ..... 82

Figure 4.4: Comparison of experimental and calculated scattering results for 499 nm diameter polystyrene spheres, using different calibration constants ..... 87

Figure 4.5: Standard deviation (95 % confidence limits) about the theoretical result for 802 nm diameter polystyrene spheres..... 91

Figure 4.6: Comparison of a calibration verification experiment using 802 nm diameter polystyrene spheres with the Mie theory results. .... 92

Figure 4.7: Plot of the relative standard deviation,  $s(\theta)/\sigma_{th}(\theta)$  ..... 95

Figure 4.8: The results of Mie calculation for single ( $d_p = 802$  nm) and monodisperse ( $d_p = 796$  nm and 808 nm,  $s = 9.6$  nm) polystyrene spheres..... 98

Figure 4.9: Data from Figure 4.6 with error bars showing the expanded uncertainty..... 101

Figure 4.10: This plot shows the average of the verification experiments relative to the theoretical result and the relative standard uncertainty of repeat experiments..... 104

Figure 4.11: Results demonstrating mass fluctuations in the calibration aerosol generator and the detector signal uncertainty..... 107

Figure 4.12: The polarisation ratio normalised (at  $\theta = 5^\circ$ ) and non-normalised along with the Mie result. .... 111

Figure 5.1: Image of smoke aerosol from smouldering wood and incense smoke particles .  
..... 120

Figure 5.2: Image of a Teflon smoke particle, the particle source was overheating Teflon wire insulation in micro-gravity ..... 122

Figure 5.3: The arrangement of wood blocks on the hot plate and the staged-wick-ignition device used to produce the cotton lamp wick smoke aerosol..... 125

Figure 5.4: a) Transmission measured by the upper laser of the FE/DE while pyrolysing the beech wood blocks. b) The number concentration as measured by the CPC. ....	127
Figure 5.5: A plot of the typical transmission measured by the upper laser of the FE/DE for non-flaming fuels. ....	129
Figure 5.6: Schematic of the diluter used in the aerosol measurement experiments.....	135
Figure 5.7: Histogram of the mass-size distribution of the non-flaming fuel smoke particles. ....	143
Figure 5.8: Log-probability plot of the mass-size distribution of the non-flaming fuel smoke particles. ....	144
Figure 5.9: a) Number distribution of beech wood and cotton lamp wick smoke aerosol. b) Comparison of mass and volume distribution data for the same fuels. ....	146
Figure 5.10: The continuous mass concentration of the smoke aerosol from non-flaming fires measured in the FE/DE. ....	148
Figure 5.11: The continuous mass and number concentration of smoke aerosol from cotton lamp wick and polyurethane generated.....	149
Figure 5.12: Light scattering results aimed at quantifying the uncertainty in the mass concentration when using the drum as a means of aerosol transport .....	153
Figure 5.13: This plot shows the results of successive angular scans of polystyrene aerosol flowing from the drum into the LAOF.....	155
Figure 5.14: This figure shows a correction estimate for dilution of the first run from the drum .....	156
Figure 5.15: Differential mass scattering cross section of smoke aerosol generated by pyrolysing beech wood blocks along with the results of Mie calculation.....	158
Figure 5.16: A plot of the average differential mass scattering cross section measurement for repeat experiments using beech wood .....	159
Figure 5.17: A plot of the differential mass scattering cross section of smoke aerosol from a) smouldering cotton lamp wicks and b) smouldering polyurethane. ....	161
Figure 5.18: The polarisation ratio of smoke aerosol generated by beech wood blocks, cotton lamp wick and polyurethane foam.....	166
Figure 5.19: Differential mass scattering cross section of smoke aerosols from non-flaming fires as a function of the scattering parameter for polarisation settin.....	170
Figure 6.1: Image of a small soot particle from flaming polyurethane foam and soot from turbulent acetylene and ethylene flame burners.....	177
Figure 6.2: Light transmission of the upper laser in the FE/DE for propylene and heptane soot generation.. ....	181
Figure 6.3: Differential mass scattering cross section [ $\text{m}^2 \cdot \text{g}^{-1} \cdot \text{sr}^{-1}$ ] for propylene and heptane generated in the FE/DE and transported by drum. ....	183
Figure 6.4: Differential mass scattering cross section [ $\text{m}^2 \cdot \text{g}^{-1} \cdot \text{sr}^{-1}$ ] for acetylene and ethylene generated in the co-flow laminar burner attached to the LAOF.....	184
Figure 6.5: Comparison of differential mass scattering cross section [ $\text{m}^2 \cdot \text{g}^{-1} \cdot \text{sr}^{-1}$ ] for all of the soots.....	185

Figure 6.6: The normalised polarisation ratio for propylene, heptane, acetylene and ethylene. .....	187
Figure 6.7: Shows the scattering of propylene, heptane, acetylene and ethylene re-plotted against the scattering parameter. ....	189
Figure 6.8: Schematic of condensation particle counter connection to the LAOF.....	193
Figure 6.9: The results of light scattering measurements in the forward direction for acetylene and ethylene generated soot. ....	195
Figure 6.10: Results of radius of gyration analysis for acetylene and ethylene using.....	196
Figure 6.11: The light scattering results for acetylene soot growing by coagulation (aging) in an isolated volume .....	198
Figure 6.12: The light scattering results for ethylene soot growing by coagulation (aging) in an isolated volume .....	199
Figure 7.1: Light transmission through the nuisance aerosols generated by burning toast, over-heating cooking oil, and dust.....	206
Figure 7.2: The size-mass distribution as a histogram of nuisance aerosols from <b>a)</b> burning toast as well as cooking oil and in <b>b)</b> ISO fine dust measured in the FE/DE. ...	210
Figure 7.3: Log-probability graph of the size-mass distribution of all the nuisance aerosols measured in the FE/DE.....	211
Figure 7.4: Results of the continuous number and mass concentration monitoring of toast and cooking oil aerosols in the FE/DE. ....	212
Figure 7.5: Differential mass scattering cross section results for burning (pyrolysing) toast and overheating (pyrolysing) cooking oil.....	215
Figure 7.6: Differential mass scattering cross section results for ISO Fine Dust. ....	216
Figure 7.7: The normalised (at 5°) polarisation ratio of the nuisance aerosols. ....	218
Figure 7.8: Differential mass scattering cross-section as a function of scattering parameter for nuisance aerosols.....	220
Figure 8.1: The total scattering cross section per mass as a function of mass median diameter of a polydisperse ensemble of particles with refractive index of $m= 1.5$ .....	229
Figure 8.2: Log-probability plot of the size distribution of the non-flaming smoke and nuisance aerosols.....	234
Figure 8.3: Differential mass scattering cross section as a function of scattering parameter, $q$ , for a selection of non-flaming fire generated smoke and nuisance aerosols. ....	237
Figure 8.4: The normalised polarisation ratio and normalised degree of linear polarisation of the aerosols.....	242
Figure 8.5: Plot of experimental and Mie theory results of nuisance aerosol generated by burning toast. ....	252

**Tables**

Table 4.1: Physical properties of polystyrene spheres..... 76

Table 4.2: The angular average of the relative standard deviation,  $\langle s(\theta)/\sigma_{rh}(\theta) \rangle$ , calculated for the different calibration constant methods..... 90

Table 4.3: Relative standard uncertainty results for size, distribution, and refractive index calculation with respect to Mie theory from verification data sets ..... 99

Table 4.4: A summary of the component Type A and Type B uncertainty analysis..... 115

Table 5.1: List of MOUDI impact cascader stage aerodynamic (cut) diameters. .... 132

Table 5.2: Tabulated results of the mass median aerodynamic diameter and geometric standard deviations from the histogram and log-probability analysis methods... 144

Table 5.3: Results of extinction coefficient estimates. .... 151

Table 5.4: Average mass concentrations for the Beech wood experiments used in the repeatability experiments. .... 160

Table 5.5: Forward scattering and asymmetry ratio for smoke aerosols generated in non-flaming fires..... 164

Table 5.6: Polarisation ratio at  $\theta = 90^\circ$  for the non-flaming fire generated smoke aerosols normalised to 1 at  $\theta = 5^\circ$ . .... 166

Table 5.7: Experimental and Theoretically calculated total and truncated mass scattering cross section for the smoke aerosols from the non-flaming fuels..... 168

Table 5.8: Results of q-slope regression analysis for experimental and theoretical scattering results at both polarisation settings, VV and HH..... 171

Table 5.9: Results of q-slope envelope analysis using linear regression for experimental and theoretical scattering results at polarisation setting, VV ..... 172

Table 6.1: Results of analysis of differential mass scattering cross section. .... 187

Table 6.2: Soot fractal dimension and q-slope measured from lights scattering measurements of soot ..... 189

Table 6.3: The radius of gyration for different fuel flow rates of acetylene and ethylene used to generate soot. .... 196

Table 6.4: Tabulated results of the radius of gyration for different fuel flow rates of acetylene and ethylene used to generate soot..... 201

Table 6.5: Acetylene and Ethylene soot number concentrations for steady state, and ratio of initial to final number concentration after one hour of isolation. .... 201

Table 7.1: Size distribution parameters determined from the MOUDI..... 211

Table 7.2: Results of extinction coefficient estimates. .... 213

Table 7.3: Forward scattering ratio and asymmetry ratio for nuisance aerosols. .... 216

Table 7.4: Polarisation ratio at  $90^\circ$  for the nuisance aerosols ..... 218

Table 7.5: Truncated and total mass scattering cross sections for nuisance aerosols ..... 219

Table 7.6: Results of q-slope regression analysis for experimental and theoretical scattering results..... 221

Table 7.7: Results of q-slope envelope regression analysis for experimental and theoretical scattering results .....	222
Table 8.1: The size distribution parameters of both the non-flaming fire generated smoke and nuisance aerosols measured with the MOUDI cascade impactor. ....	233
Table 8.2: Forward scattering ratio of the aerosol particles examined in this study.....	237
Table 8.3: Asymmetry ratio of the aerosol particles examined in this study.....	240
Table 8.4: The truncated mass scattering cross section and extinction mass cross sections of the aerosol particles examined.....	244
Table 8.5: q-slope non-flaming smoke and nuisance aerosols examined in this study....	249
Table 8.6: The fixed range q-slope and fractal dimensions for post-flame soot agglomerates .....	249
Table 8.7: The phase shift parameters based on number mean and mass median diameters for the non-flaming smoke aerosols and nuisance aerosols. ....	250
Table 8.8: The q-slope envelope of the scattering data for non-flaming smoke aerosols and nuisance aerosols.....	252

## LIST OF SYMBOLS

$a$	radius of a sphere.
$a_n$ and $b_n$	scattering coefficients, Equ. 2.14.
$C_{abs}$	absorption cross section.
$C_{ext}$	extinction cross section, Equ. 2.21.
$C_{sca}$	total scattering cross section, Equ. 2.20
$C_{Tsca}$	truncated scattering cross section, Equ. 5.1
$D_f$	fractal dimension of an agglomerate
$D_e$	spatial dimension in which an agglomerate is embedded, $D_e = 3$
$d_p$	particle diameter variable
$d_n$	mean number diameter, Equ. 2.2
$d_i$	median diameter of the $i^{\text{th}}$ diameter bin.
$d_m$	mass median diameter, Equ. 2.5
$E_s$	scattered electric field
$E_{s\parallel}$ and $E_{s\perp}$	electromagnetic field components parallel and perpendicular to the scattered plane, respectively. Subscripts of $s$ and $i$ indicate scattered and incident fields.
$E_{s\theta}$ and $E_{s\phi}$	angular components of the scattered fields, Equ. 2.16
$g(r)$	pair correlation or autocorrelation function, Equ. 2.37
$\gamma$	phase shift parameter of a sphere, $\gamma = 2kR m - 1 $ .
$H_s$	scattered magnetic field
$h(r/R_g)$	cut-off function, Equ. 2.37

$i$	as a superscript or normal notation is the complex constant, $i = \sqrt{-1}$ ; as a subscript $i$ is a counting index.
$i(q)$	scattered irradiance as a function of $q$
$i_0$	incident irradiance
$i_{\parallel}$ and $i_{\perp}$	parallel and perpendicular irradiances
$K_l$	calibration constant for polarisation $l$
$k_a$	constant of proportionality or pre-factor, Equ. 2.36
$k$	wave propagation number in air, $k = 2\pi/\lambda$
$l$	polarisation notation $l = VV$ or $HH$ for perpendicular or parallel polarisation respectively. Often dropped to reduce clutter.
$\lambda$	incident radiation wavelength
$M$	mass concentration Equ. 2.4
$M_0$	total mass of particles
$m_i$	mass of particles in the $i^{\text{th}}$ diameter bin
$m_p$	mass of a particle
$m$	relative complex refractive index, $m = m_p/m_0$
$m_0$	complex refractive index of the medium about the particle, $m_0 = 1$ .
$m_1$	particle complex refractive index.
$\mu$	magnetic permeability
$n(\ln d_p)$	lognormal number distribution function, Equ. 2.1
$N_0$	number concentration
$N_c$	convergence term for the scattering coefficient series expansion, Equ. 2.17.
$N$	number of primary particles in an agglomerate particle, Equ. 2.36.
$\omega$	angular frequency of an em wave

*List of Symbols*

$\rho$	particle material bulk density
$\rho(\theta)$	polarisation ratio, Equ. 2.33
$P(\theta)$	degree of linear polarisation, Equ. 2.34
$\phi$	azimuthal scattering angle, perpendicular to the scattering plane
$\pi_n$ and $\tau_n$	angular scattering functions, Equ. 2.13
$q$	scattering parameter, Equ. 2.40
$r$	radial coordinate
$R_g$	radius of gyration, Equ. 2.38
$R$	characteristic radius of a scatterer.
$r_0$	radius of the primary particles making up an agglomerate
$S(\theta, \phi)$	amplitude scattering matrix
$S_j, j = 1 \dots 4$	elements of the amplitude scattering matrix
$S(q)$	scattering structure factor, Equ. 2.39
$\sigma_g$	geometric standard deviation of the particle size distribution, Equ. 2.3
$\sigma_{sca}(\theta)$	differential scattering cross section of a particle as a function of scattering angle.
$\sigma_{msca}(\theta)$ and $\sigma_{th}$	Mie theory result for the differential mass scattering cross section, Equ.2.26.
$\sigma_l(\theta)$	measured differential mass scattering cross section at polarisation $l$
$\sigma_R(q)$	Rayleigh scattering cross section of the primary particles in an agglomerate.
$t$	time of aerosol sample collection
$\theta$	scattering angle, parallel to the scattering plane
$U(\theta)$	detected signal with background subtracted
$u_l(\theta)$	corrected scattering signal at polarisation $l$ , $u_l(\theta) = U(\theta)\sin(\theta)$

*List of Symbols*

$\dot{V}$	volume flow rate
$\Delta w$	aerosol weight collected on a sample filter
$x$	size parameter, $x = 2\pi a/\lambda$
CPC	Condensation particle counter
FE/DE	Fire emulator/ Detector evacuator
LAOF	Large agglomerate optical facility
MOUDI	Micro orifice uniform deposit impactor
TEOM	Tapered element oscillating microbalance

## INTRODUCTION

### 1.1 INTRODUCTION

Unwanted fires cost lives, cause injury and damage or destroy property. Awareness of the occurrence of a fire at an early stage of its growth is extremely important. Early awareness means that the damaging effects of the fire can be minimised by appropriate responses, such as suppression or evacuation. Awareness of a fire is as a result of perception of fire cues, which are changes in the environment caused by a fire, such as increases in heat, olfactory or ocular observation of smoke, or visible flames or alarms. Fire detectors are instruments aimed at detecting cues in unoccupied areas or when occupant awareness is reduced, in some instances this includes detection of cues at extremely low levels above the ambient environment. Fire detectors are designed to then give an alarm to which people can respond or to activate automated systems for fire suppression. An alarm warns people who are not intimately involved with a fire's ignition. Early and reliable smoke detector performance under these conditions is of great importance and is the principle motivation behind this thesis.

The objective of this study was to measure and study light scattering by a selection of smoke and nuisance aerosols. The principal objective was to measure the angular distribution of scattered light, which is measured in terms of the differential scattering cross section per unit mass per steradian [ $\text{m}^2 \cdot \text{g}^{-1} \cdot \text{sr}^{-1}$ ]. The subsequent objective was to then examine this data for differences and similarities between smoke and nuisance aerosols. Measurements and analysis were made possible by developing a novel calibration method that is based on a gravimetric approach to light scattering by a cloud of polystyrene spheres. This means that this study was analogous to a survey of the light scattering characteristics of smoke and nuisance aerosols, with the subsequent analysis focusing on discrimination of the aerosols

based on the surveyed data. The result was the most complete examination of light scattering measurements of smoke aerosols generated by non-flaming fires and nuisance aerosols to date.

The differential light scattering measurements are made using the scattering angle,  $\theta$ , and the scattering parameter dependence,  $q = 4\pi\lambda^{-1} \sin(\theta/2)$ . Analysis in terms of the scattering angle is traditional for light scattering by small particles, using the scattering parameter is not. This study presents results that test a recently developed scattering parameter description of light scattering by spheres (Sorensen and Fischbach, 2000).

The details of the theory used in this study are presented along with an overview of the historical development of the light scattering theory in **Chapter 2**. The apparatus developed for the light scattering measurements is presented in **Chapter 3**, while the calibration method to make the differential mass scattering cross section measurements is detailed in **Chapter 4**.

Three smoke aerosol classes are examined in this study: those generated by non-flaming fires (**Chapter 5**), soot generated in flaming fires (**Chapter 6**) and finally nuisance aerosols (**Chapter 7**). The method of aerosol generation is different for each class. To keep the description of methods continuous with the results presented, the methods used are detailed in the first part of each aerosol chapter. An overview of the literature pursuant to an aerosol class is included at the start of each of these chapters.

Discussions and comparison of results between the different aerosols and previous reported studies is presented in **Chapter 8**.

## **1.2 SMOKE DETECTION AND MOTIVATION**

Smoke is made up of airborne solid and liquid particulate and gases evolved when a material undergoes pyrolysis or combustion, included in smoke is the air that is entrained or mixed

into the mass (National Fire Protection Association, 1993). The particle component of smoke is the smoke aerosol, since an aerosol is defined as solid or liquid particles transported by a gas (Hinds 1982). The scattering of light by smoke aerosols is the focus of this study and has relevance to the design of smoke detectors based on light scattering. The majority of smoke detectors are currently based on one of two principles of operation. Firstly there are those based on the principle of scattering or extinction of light caused when an incident light beam interacts with the mass of an aerosol particle. Smoke detectors based on light scattering have photodetectors placed at an angle to the direction of travel of the incident light beam. Thus when an aerosol passes through the incident light beam, light is scattered in all directions and the photodetector receives the light scattered onto its active element. This scattered signal then results in alarm activation. Light scattering based detectors are growing in use and availability due to lower component cost and improving technology associated with the optoelectronic components. If a fire did not generate the aerosol that triggered the alarm then the alarm would be considered to be a “nuisance alarm”. It must be noted that the term nuisance alarm is not synonymous with a “false alarm”. A false alarm has come to mean an alarm given by a faulty smoke detector or an event that is not a fire; for example, due to an internal electrical fault, electrical interference or a nuisance aerosol such as a dust. A false alarm does not necessarily require the presence of an aerosol. This distinction between nuisance and false alarms is mainly in manufacturer and detector community usage. The general public typically refers to nuisance alarms as false alarms. In this thesis the nuisance alarm usage is continued.

The other smoke detection method is the ionisation detector. In these detectors a small amount of radioactive isotope ionizes some air molecules in a gap causing an ion current to flow between two electrodes. An aerosol present in the air gap removes ions because they attach to the aerosol particles, reducing the ion current. The drop in current causes an alarm

to be given. Ideally the aerosol would be a smoke aerosol but any aerosol could penetrate into the air-gap and cause an alarm. In that case an aerosol not generated by a fire would result in a nuisance alarm. Ionisation based detectors are the most common residential detectors due to their low cost.

In one and two-family residential buildings, the benefit of smoke detectors is believed to be a reduction in the risk to life safety of about 52 % compared with homes without detectors installed (Aherns, 1998). On the other hand the risk to life in multi-occupancy buildings (apartments, townhouses etc.) is only reduced by about 14 % by the presence of smoke detectors (Aherns, 1998). It is not known exactly what is causing the difference in the risk measures quoted above. It is well recognised that the effectiveness of smoke detectors in the home is reduced by a high frequency of nuisance alarms (Smith et al., 1997; Aherns, 1998). A high rate of nuisance alarms simply frustrates the occupants, to the extent that in some cases they disconnect the power source or otherwise render the detector useless. The reduction of nuisance alarms in residential occupancies is a means by which the risk to life safety can be decreased further. The potential for increased efficiency of detectors in multi-occupancies is substantial. Anecdotally this frustration with nuisance alarms also occurs in industrial and commercial buildings, sometimes resulting in no or slow response to fires.

In unoccupied or rarely visited areas detection systems are necessary to reduce the risk of death and injurious events, damage to property or mitigation of reduced operations. Such installations are usually aimed at a reduction in the risk to an enterprise (industrial or commercial). These risks are substantially reduced through combined measures such as detectors, sprinklers, fire drills and training, as well as fire safety awareness during design and operation of a facility.

In some instances an enterprise may find that their facility or operations are of extreme importance. In such cases very sensitive smoke detection is a solution. A result of high sensitivity can be an increase in nuisance alarm rates. In some instances a single nuisance alarm could have substantial influence on the operation of an enterprise. For example, aircraft that register an in-flight fire alarm must land immediately and begin emergency evacuation from the aircraft. While the actual incidence of these events varies over different aircraft fleets, the cost is acknowledged as substantial to flight operations (Beall et al., 2001).

The discussion above highlights application of smoke detection and some of the problems associated with their use. One promising approach to dealing with nuisance alarms is the monitoring of multiple cues from a fire; for example, the combination of CO<sub>2</sub> and smoke detection. Multi-parameter detection gathers more information about an event allowing more confident identification of a fire event, at the possible expense of a delayed response. Another development with smoke detection is the growing use of light scattering detector as mentioned above, analysis of light scattering signals has been examined in the past as a means of discriminating smoke aerosols from nuisance aerosols (Aggarwal and Motevalli, 1997; Loepfe et al., 1997).

### **1.3 OVERVIEW OF THIS STUDY**

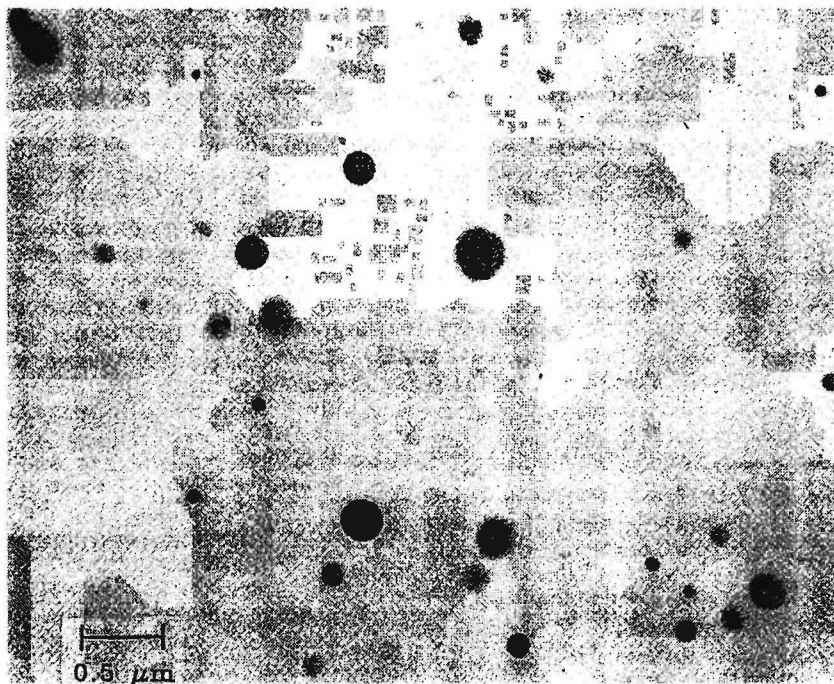
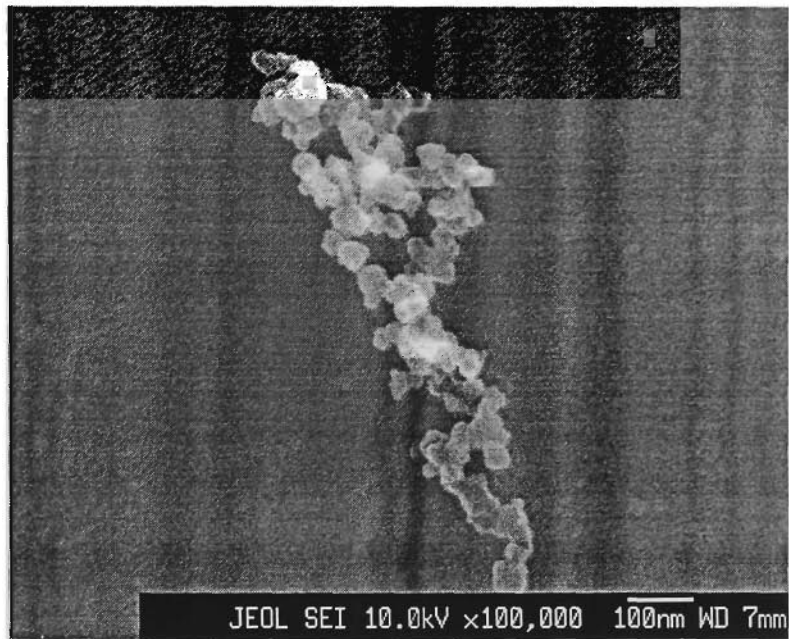
This study refers to a fire as a time series of chemical reactions, usually combustion but includes forced pyrolysis particularly at the incipient or pre-heating stage. That is to say a fire is the series of chemical reactions that usually but not necessarily lead to flaming combustion. Fire science is different to combustion science in the sense that combustion science aims at understanding and optimising the combustion reaction. Fire in its most common form is an incomplete combustion reaction. Fire science and engineering is associated with understanding uncontrolled fire and its many form with the aim of increasing life safety.

The development of a fire is dependent on three main factors: oxygen supply, thermal environment, and fuel characteristics. In some circumstances a fire might progress from an incipient stage to a non-flaming form of combustion such as smouldering. Whether the fire progresses to a flaming stage is dependent on the fuel characteristics, thermal environment and oxygen supply. Smoke detection in the earliest incipient stage of a fire is relevant to very sensitive detection discussed above.

Smoke aerosols generated by flaming and non-flaming fires are the two classes of smoke aerosols of interest to this study. “Non-flaming fire” as used in this study includes the incipient stage of a fire. For example, this would include smouldering and forced pyrolysis events. Smouldering is a true self-sustaining combustion event (Moussa et al. 1979; Ohlemiller, 1995). A cigarette is an example of smouldering combustion even though it is not necessarily a hazard in the sense of a fire. Smouldering mattresses and landfills are also examples of this type of combustion. Forced pyrolysis events represent ignition or early incipient stages of potential fires, such as the overheating of an electrical wire. Forced pyrolysis is not a combustion reaction nor self-sustaining as it requires an external heat source (Ohlemiller, 1995). At a later stage of their existence non-flaming fires can undergo a transition to a flaming fire. Non-flaming fires have slow to very slow growth rates in comparison to flaming fires.

Smoke aerosols from non-flaming fires generally comprise of droplet-like spherical particles, while smoke aerosols from well-ventilated flaming fires are agglomerate particles, as seen in **Figure 1.1**. The differences between the two types of smoke aerosols are striking. The pattern of the light scattering by these particles will reflect the differences in the morphology of the particles. Non-flaming smoke aerosols form as a result of condensation of high boiling point hydrocarbon products from non-flaming fires; the term “non-flaming smoke” refers to the source of the smoke aerosol. Smoke aerosol particles generated by a flaming fire

**Figure 1.1:** a) A scanning electron microscope image of a soot agglomerate from flaming polyurethane. b) A transmission electron microscope image of incense smoke particles (Cheng et al. 1995).



are simply referred to as soot and sometimes as soot agglomerates to emphasize their morphology. Soot is an agglomerate particle that is formed from the aggregation of very small primary particles (10-80 nm in diameter). These primary particles (also called monomer particles) aggregate into clusters in the flame environment. The resulting clusters usually grow larger by aggregation with other clusters (called agglomeration) or primary particles (Meakin, 1984; Mountain and Mulholland, 1988). Post-flame growth of the clusters also occurs through agglomeration of soot particles.

Smoke aerosols from non-flaming fires have attracted far less interest in terms of light scattering characterisation compared with smoke aerosols generated by flaming fires, but they have been studied extensively in terms of their size distributions (Lee and Mulholland, 1977; Bankston et al. 1981; Mulholland and Ohlemiller, 1982; Cheng et al. 1995). Unfortunately the few studies of light scattering by these particles have not also measured the size distributions of the particles they were examining (Meacham and Motevalli, 1992; Aggarwal and Motevalli, 1997; Loepfe et al. 1997). This study presents for the first time the light scattering and size distribution characteristics of smoke aerosols from non-flaming fires. Size distribution information is important to this study to allow comparison of experimental and computed results. The computations make use of Mie theory adapted to lognormally distributed particles in terms of the mass scattering cross section, this treatment is presented in **Chapter 2**. The comparison has made use of previously published refractive index data from various sources.

Two smoke aerosols generated and characterized in this study are similar to those used in standard smoke detector tests (EN54, 1982; UL 217, 1993). These smoke aerosol sources are beech wood blocks and cotton lamp wick. A third fuel source used is polyurethane foam commonly used in couches. The methods and results of measurements made on these smoke aerosols are presented in **Chapter 5**.

Light scattering studies into soot formation and morphology in a flame have been conducted over the last four or five decades and developed to a high degree of understanding (Haynes and Wagner, 1981; Glassman, 1988; Charalampopoulos, 1992; Sorensen, 2001). This study limits its scope to angular light scattering studies of post-flame soot and makes use of findings from work characterising the morphology of soot agglomerates using angular light scattering. In the case of the latter attention has been drawn to some in-flame soot studies, particularly those examining the fractal nature of the soot agglomerates. The influence of the agglomerate morphology on the light scattering by soot particles is outlined in **Chapter 2**. Four flaming fires are used to generate the soot examined in this study: propylene, acetylene and ethylene are gaseous fuels for which burners are used; the final flaming fuel was a small pool of heptane. The methods and results of measurements made on soots from various flaming fires are detailed in **Chapter 6**.

The most common source of nuisance alarms in the house is cooking and the kitchen is also the source of the majority of real accidental fires (Watanabe et al. 1985). Two of the three nuisance aerosols examined in this study are cooking generated aerosols: overheating cooking oil and burning toast. Both of these nuisance aerosols could be classed as non-flaming fires since they are forced pyrolysis events that can make a transition to a flaming fire. This is particularly the case for the cooking oil, which is the cause of about 30 % of house fires (Wijayasinghe and Makey, 1997). Nevertheless, these nuisance sources represent high frequency events that do lead to disabling smoke detectors as discussed above. The third nuisance aerosol used in this study is a standardised dust, ISO Fine Dust. As an aerosol it represents a nuisance event that is not as well defined as those above. It comes closest to an aerosol that might be expected in an industrial situation, is irregular (non-spherical) in shape and has the advantage of being standardised in its original powder form. The methods and

results of experiments conducted in this study on nuisance aerosols are detailed in **Chapter 7**.

Analysis methods applied to the angular scattering data collected in this study are compared with past work. The motivation of this analysis, such as polarisation analysis, is the desire to discriminate nuisance aerosols from aerosols generated by fires. Discrimination has proven successful in the past when differentiating flaming and non-flaming fire generated aerosols (Loepfe et al. 1997). This study demonstrates the same result but explains more clearly the reasons for the result, which are essentially due to the differences in morphology between soot agglomerates and near spherical particles from non-flaming fires.

Discrimination of soot from the other aerosols is also approached in terms of the scattering parameter. The differences are examined in terms of the power law relationship of the scattering results to the scattering parameter. The agglomerate nature of the soot particles dominates their scattering parameter dependence, showing the effects of the agglomerate fractal structure. The fractal dimension of the soot agglomerates is determined from the light scattering results. The results of the non-flaming smoke and nuisance aerosols are also examined in an analogous manner. This results in a novel approach to discrimination of soot from the non-flaming smoke and nuisance aerosols examined.

A description of light scattering by spherical particles has recently been presented by Sorensen and Fischbach (2000). The model describes the light scattering in terms of the length scales of the scattering event, characterized by the scattering parameter and the length scales of the scattering particles; subsequently it will be referred to as the scaling method. Analyses of the light scattering results measured in this study are used to test the findings of Sorensen and Fischbach (2000) for a range of polydisperse aerosols, namely the non-flaming smoke and nuisance aerosols. Polydisperse aerosols are made up of particles with a wide

distribution of sizes, “monodisperse” aerosols have very narrow size distributions approximated by delta functions and are sometimes referred to as having a single size. The test of the scaling approach and a comparison of differential mass scattering cross sections in terms of angular and scattering parameter dependence is presented and discussed in **Chapter 8**. The conclusions of this study follow in **Chapter 9**.

Two appendices are attached to this dissertation. The first, Appendix 1, presents the experimental steps for operation of the Large Agglomerate Optical Facility (LAOF) developed for the differential light scattering measurements made in this study. The LAOF is located at the National Institute of Standards and Technology (NIST) in Gaithersburg, MD, U.S.A. The experimental process is the same for each of the aerosols examined in this study; only the method of aerosol generation and transport to the LAOF is different. Appendix 2, presents papers generated by this study: principally a paper entitled “Light scattering characterization and size distributions of smoke and nuisance aerosols” (Weinert et al. 2002) fully reviewed and presented at the premier fire science conference; the 7<sup>th</sup> International Fire Safety Science Symposium 2002, Boston, USA. A paper reviewed internally at NIST and currently submitted as a technical note, entitled “Moment method for obtaining particle size measures of test smokes” (Cleary et al. *To be published*), has been included for reference. This latter paper demonstrates application of the size distribution results to inverting ionisation detector signals to determine mean particle sizes.

## OVERVIEW OF THE THEORY OF LIGHT SCATTERING BY SMALL PARTICLES

### 2.1 INTRODUCTION

The principle motivation behind this thesis is to obtain quantitative light scattering data from smoke and nuisance aerosols. This light scattering data can then be analysed to observe the effects of particle morphology on the scattered light; that is the effects of size and shape. The morphology of a particle is the way in which its mass is distributed in space to define its size and shape. Differences in morphology can then be used to examine discrimination of smoke aerosols generated by different fire modes (non-flaming and flaming) or from nuisance aerosols. Comparing soot agglomerates from flaming fires with smoke droplet particles generated by non-flaming fires, the morphological differences are striking, see **Figure 1.1**. The differences in mass distribution affect the way in which light is scattered by the particles a process that is a result of interaction between light and the mass of a particle. Since the distribution of mass (matter) in the agglomerates is very different from that in the spherical smoke droplets, the scattering of light incident on the particles will be influenced by the difference in the mass distribution in the particles. This in turn will affect the scattered light signal, which can be measured and examined for characteristics that might be used to discriminate between the two types of smoke aerosol. The next step will be to examine nuisance aerosols, such as those caused in burning toast or by dust, to see if similar methods can differentiate them from fire generated aerosols.

To accomplish discrimination, this study has measured the scattered light in terms of the differential (angular distribution) scattering cross section per unit mass [  $\text{m}^2 \cdot \text{g}^{-1} \cdot \text{sr}^{-1}$  ]. This is the first time that differential mass scattering cross sections have been measured for fire-generated aerosols. This has been achieved by developing a light scattering calibration

method using a gravimetric method for polystyrene spheres of a known size. This chapter introduces the theoretical basis of the differential mass scattering cross section so that it can be computed for use in calibration and for comparison of experimental results. Comparison of experimental and calculated results will be conducted for light scattering by monodisperse and polydisperse ensembles of spheres. In the case of the polydisperse spheres the size distribution is characterised by a lognormal distribution. The key features of the lognormal distribution needed to compute the differential scattering per mass are presented. Following this is an overview of the agglomerate nature of soot and how this nature influences the light scattering by these particles as described by the scattering parameter,  $q$ . This is followed by a scattering parameter dependent description of light scattering by spheres, an important consideration in correlating light scattering from soot agglomerates and polydisperse spheres.

## 2.2 LOGNORMAL SIZE DISTRIBUTIONS

### 2.2.1 DISTRIBUTION EQUATIONS

Particles in a natural aerosol are usually dispersed over a range of sizes or diameters characterised by a size distribution. The lognormal size distribution is often found to be a close approximation to the real size distribution. Another aspect of the lognormal distribution is the ease of mathematical manipulation between moments and moment averages of the distribution. Lognormal distributions are characterised principally by the geometric mean and geometric standard deviation. The distribution is normalised so that the area under the distribution gives the total quantity of the distribution, such as the total number or mass of particles in the distribution. This section presents the lognormal distribution in a manner consistent with the experimental measurements made in this study.

The lognormal number distribution function is given by,

$$n(\ln d_p) = \frac{N_0}{\ln \sigma_g \sqrt{2\pi}} \exp\left[-\frac{(\ln d_p - \ln d_n)^2}{2 \ln^2 \sigma_g}\right], \quad (2.1)$$

where  $n(\ln d_p)$  is the number of particles with diameters whose logarithm lies in the interval of  $\ln d_p$  to  $\ln d_p + d(\ln d_p)$ . Here  $d_p$  is the particle size,  $d_n$  is the geometric mean number diameter,  $\sigma_g$  is the geometric standard deviation (GSD) of the distribution characterising the width and  $N_0$  is the number concentration of particles. In a lognormal number distribution the logarithm of the diameter of a particle,  $\ln d_p$ , is normally distributed about  $\ln d_n$ . The geometric mean diameter or number mean diameter,  $d_n$ , is given by the relation,

$$\ln d_n = \int_0^{\infty} \ln d_p n(\ln d_p) d \ln d_p. \quad (2.2)$$

The geometric standard deviation is the square root of the variance of the logarithm of the diameters,

$$\ln^2 \sigma_g = \int_0^{\infty} (\ln d_p - \ln d_n)^2 n(\ln d_p) d \ln d_p. \quad (2.3)$$

The light scattering calibration method developed in this study relies on a gravimetric determination of the mass concentration,  $M$ , of the scattering particles. The mass concentration is proportional to the third moment of the number-size distribution. That is,

$$M = \frac{\rho\pi}{6} \int_0^{\infty} d_p^3 n(\ln d_p) d \ln d_p, \quad (2.4)$$

where  $\rho$  is the material bulk density of the particle.

Measurements are also made of the smoke and nuisance aerosol mass-size distribution at their source, both for completeness of the characterisation and for calculations using Mie theory for a cloud of particles. This mass based measurement is made in terms of the mass median diameter,  $d_m$  or MMD, not the geometric mean number diameter. The 50th percentile of the distribution gives the median diameter while the geometric standard deviation is given by either the ratio of the 50<sup>th</sup> to the 16<sup>th</sup> percentile size or the ratio of the 84<sup>th</sup> to the 50<sup>th</sup> percentile size. This is the basis of analysis of the mass-size distribution using a log-probability graph. Analysis of the mass-size distribution by means of a histogram is accomplished by determining the mass median diameter (MMD) from a discrete form analogous to **Equ. 2.2**,

$$\ln d_m = \frac{\sum_{i=0}^{\infty} m_i \ln d_i}{M_0}, \quad (2.5)$$

where  $m_i$  is the mass of particles, and  $i$  denotes the  $i^{\text{th}}$  bin with the logarithm of the diameter,  $d_i$ , and  $M_0$  is the total mass collected. Similarly the geometric standard deviation is given by,

$$\ln^2 \sigma_g = \frac{\sum_{i=0}^{\infty} m_i (\ln d_i - \ln d_m)^2}{M_0}. \quad (2.6)$$

For this study light scattering measurements of the differential scattering cross section are made in terms of the unit mass of aerosols in the scattering volume. To compute the light scattering per mass it is important to express the mass concentration given by **Equ. 2.4** in terms of the number concentration, the mass median diameter,  $d_m$ , and the geometric standard deviation,  $\sigma_g$ . An important characteristic of the lognormal distribution is that any

moment of the distribution can be expressed as a function of these parameters. The first step in rewriting the mass concentration involves substituting **Equ. 2.1** into **Equ. 2.4** and moving the cubed particle diameter into the exponential of the number distribution function. By then expanding the squared term the results is,

$$M = Q \int_0^{\infty} \exp \left[ \frac{-(\ln^2 d_p - 2 \ln d_p \ln d_n + \ln^2 d_n - 6 \ln d_p \ln^2 \sigma_g)}{2 \ln^2 \sigma_g} \right] d \ln d_p, \quad (2.7a)$$

where

$$Q = \frac{N_0 \rho \pi}{\ln \sigma_g \sqrt{2\pi}} \frac{\rho \pi}{6}. \quad (2.7b)$$

Applying the relation,  $z^2 + bz + c = \left( z + \frac{1}{2}b \right)^2 - \frac{1}{4}b^2 + c$  with  $z = \ln d_p$ , to the numerator in the exponential of **Equ. 2.7a** and then using the Hatch-Choate equations (Hinds, 1982),

$$\ln d_m = \ln d_n + 3 \ln^2 \sigma_g, \quad (2.8)$$

leads to the final form of the mass concentration that is applied to the scattering problem. This form is,

$$M = Q \exp \left( 3 \ln d_m - \frac{9}{2} \ln^2 \sigma_g \right) \int_0^{\infty} \exp \left[ \frac{-(\ln d_p - \ln d_m)^2}{2 \ln^2 \sigma_g} \right] d \ln d_p. \quad (2.9)$$

The integral reduces to one and the mass concentration is given by,

$$M = \frac{N_0 \rho \pi}{6} \exp \left( 3 \ln d_m - \frac{9}{2} \ln^2 \sigma_g \right) = \frac{N_0 \rho \pi}{6} d_m^3 \exp \left( -\frac{9}{2} \ln^2 \sigma_g \right). \quad (2.10)$$

How well the lognormal distribution approximates the observed distribution is a limiting factor of the Mie calculations that are discussed in the next section. Any deviation from a lognormal distribution or uncertainty in the measured mass median diameter will contribute to uncertainty in the calculated result.

## 2.3 LIGHT SCATTERING BY SPHERES

### 2.3.1 MIE THEORY

Calculating the light scattering by spheres has become a commonplace undertaking using modern computers and well developed numerical algorithms. The analytical solution was first developed over the end of the nineteenth and beginning of the twentieth century. The history of contributions from various researchers to the problem are dealt with by Kerker (1969). One name most commonly associated with the analytical solution of plane wave scattering by a sphere is that of Gustav Mie (1868 – 1957) (Lilionfeld, 1991), who formulated the solution of plane wave scattering from conducting spheres after observation of glories in colloidal gold (Mie, 1908). Throughout this study the name “Mie theory” is used for this solution of light scattering by spheres. Many texts cover the solution to this scattering problem (van de Hulst, 1981; Kerker, 1969; Born and Wolf, 1999; Bohren and Huffman, 1998) and what follows is a summary pertinent to this study.

The Mie theory solution is developed from Maxwell’s equations and expands the incident field in terms of spherical harmonics. The boundary conditions across the scattering surface are then used to determine the internal and scattered fields from the incident field solution. The scattered electronic,  $\mathbf{E}_s$ , and magnetic field,  $\mathbf{H}_s$ , components are found to be (Bohren and Huffman, 1998),

$$\mathbf{E}_s = \sum E_n \left( i a_n \mathbf{N}_{e1n}^{(3)} - b_n \mathbf{M}_{o1n}^{(3)} \right), \quad (2.11a)$$

$$\mathbf{H}_s = \frac{k}{\omega\mu} \sum H_n (ia_n \mathbf{N}_{oln}^{(3)} + b_n \mathbf{M}_{eln}^{(3)}), \quad (2.11 \text{ b})$$

for the far field condition  $kr \gg 1$ , where  $r$  is the distance to the detector/observer, and

$$E_n = E_0 i^n \frac{2n+1}{n(n+1)}, \quad i^n = \sqrt[n]{-1} \quad \text{for } n = 1, 2, 3 \dots \infty, \quad (2.12)$$

where  $E_0$  is the incident field magnitude. The spherical harmonic vector functions  $\mathbf{N}_{oln}^{(3)}$ ,  $\mathbf{M}_{eln}^{(3)}$  and their orthogonal counter parts are solutions to the wave equation; the superscript (3) means that they have a spherical Hankel function (spherical Bessel function of the third kind) radial component. The subscripts o and e represent orthogonal sinusoidal functions for the azimuthal angular component (from the spherical polar coordinate system); and finally the scattering angle component is a first order associated Legendre polynomial of degree  $n$ , in this case  $P_n^1(\cos\theta)$  denoted by the subscript 1 and  $n$ . The scattering angle dependent behaviour of the vector functions can be encapsulated in two angular functions,

$$\pi_n = \frac{P_n^1(\cos\theta)}{\sin\theta} \quad \text{and} \quad \tau_n = \frac{dP_n^1(\cos\theta)}{d\theta} \quad (2.13)$$

The expansion coefficients of the scattered field, simply called scattering coefficients (or Mie scattering coefficients), determined from the boundary conditions are,

$$a_n = \frac{m\psi_n(mx)\psi_n'(x) - \psi_n(x)\psi_n'(mx)}{m\psi_n(mx)\xi_n'(x) - \xi_n(x)\psi_n'(mx)}, \quad (2.14a)$$

$$b_n = \frac{\psi_n(mx)\psi_n'(x) - m\psi_n(x)\psi_n'(mx)}{\psi_n(mx)\xi_n'(x) - m\xi_n(x)\psi_n'(mx)}, \quad (2.14b)$$

given that the electromagnetic permeability of the particle and surroundings are equal. In **Equ. 2.14**, the Riccati-Bessel functions have been used,  $\psi_n(\gamma) = \gamma j_n(\gamma)$  and  $\xi_n(\gamma) = \gamma h_n^{(1)}(\gamma)$ , such that,  $j_n(kr)$ , is a Bessel functions are of the first kind and,  $h_n^{(1)}(kr)$ , is a Bessel function of the third kind and first order, i.e. a Hankel function. The primed functions in **Equ. 2.14** indicate the derivative with respect to the function argument. One can appreciate the apparent complexity of light scattering by single spheres by simply contemplating the behaviour of the angular functions, **Equ. 2.13**, and the scattering coefficients, **Equ. 2.14**. They are a collection of Legendre polynomials and Bessel functions of various breeds all put together in a linear combination. Until the advent of the modern computer these functions were not trivial to calculate. The modern computer and easy access to code has made the solution of scattering by spheres a simple undertaking in comparison.

Importantly the scattering coefficients are dependent on  $m$ , the complex relative refractive index. The relative refractive index is the ratio between the refractive index of the particle and surrounding medium. The scattering coefficients are also dependent on the size parameter of the particle,  $x = 2\pi a/\lambda$ , a ratio of particle radius,  $a$ , to the wavelength,  $\lambda$ , of the incident radiation. When the ratio is such that  $a/\lambda < 0.1$  then Rayleigh scattering theory applies and if  $a/\lambda > 10$  then geometrical optics theories are applicable. Between these two limits Mie theory is often applied to any particle even though it is a theory for spheres of arbitrary size.

### 2.3.2 AMPLITUDE SCATTERING MATRIX AND THE FAR FIELD

For dealing with the angular scattering of light in the far field it will be beneficial to define the scattering problem in an initially arbitrary form and relate this back to the Mie solution above. This has the benefit of explicitly bringing polarisation into the formalism and thus relates the

Mie result to the experimental situation in this study. The matrix form of the scattering amplitude,  $\mathbf{S}(\theta, \phi)$ , which maps the incident field to the scattered far field for an arbitrary particle is then given by (Bohren and Huffman, 1998),

$$\begin{pmatrix} E_{\parallel s} \\ E_{\perp s} \end{pmatrix} = \frac{e^{ik(r-z)}}{-ikr} \begin{pmatrix} S_2 & S_3 \\ S_4 & S_1 \end{pmatrix} \begin{pmatrix} E_{\parallel i} \\ E_{\perp i} \end{pmatrix}. \quad (2.15)$$

The angular notation has been ignored for the sake of minimising clutter. The basis set used is in terms of the linear polarisations parallel (vertical) and perpendicular (horizontal) to the scattering plane, overlaying the Cartesian coordinate system with the incident field propagating in the  $z$  direction (Bohren and Huffman, 1998). The elements of the amplitude scattering matrix,  $S_j$ , are complex functions containing amplitude and phase information. For spherical particles the transverse  $(\theta, \phi)$  field components for the scattered far field are, from **Equ. 2.11** (Bohren and Huffman, 1998),

$$\mathbf{E}_{s\theta} \sim \mathbf{E}_0 \frac{e^{ikr}}{-ikr} \cos \phi S_2(\cos \theta), \quad (2.16a)$$

$$\mathbf{E}_{s\phi} \sim -\mathbf{E}_0 \frac{e^{ikr}}{-ikr} \sin \phi S_1(\cos \theta). \quad (2.16b)$$

The angular functions and scattering coefficients have been collected into the matrix elements,

$$S_1 = \sum_n^{N_c} \frac{2n+1}{n(n+1)} (a_n \pi_n(\cos \theta) + b_n \tau_n(\cos \theta)), \quad (2.17a)$$

$$S_2 = \sum_n^{N_c} \frac{2n+1}{n(n+1)} (a_n \tau_n(\cos \theta) + b_n \pi_n(\cos \theta)). \quad (2.17b)$$

The series expansion in **Equ. 2.17** is complete after  $N_c$  terms, corresponding to convergence of the series and satisfies the relation  $kr \gg N_c^2$  which allows asymptotic simplification in deriving **Equ. 2.17**. The number  $N_c$  is a very important creature as convergence of the series is of great importance in the numerical computation of the series (Wiscombe, 1980).

From **Equ. 2.16a** and **2.16b** it follows that the scattering by a spherical particle is,

$$\begin{pmatrix} E_{\parallel s} \\ E_{\perp s} \end{pmatrix} = \frac{e^{ik(r-z)}}{-ikr} \begin{pmatrix} S_2 & 0 \\ 0 & S_1 \end{pmatrix} \begin{pmatrix} E_{\parallel i} \\ E_{\perp i} \end{pmatrix}. \quad (2.18)$$

**Equation 2.18** leads directly to the irradiance of the scattered far field for the two polarisation settings that are used in this study, i.e. VV (vertical: perpendicular incident and perpendicular scattered) and HH (horizontal: parallel incident and parallel scattered), when the irradiance of the field is determined from the square of the modulus of the fields the result is,

$$i_{HH} = i_{\parallel} = \frac{|S_2|^2}{(kr)^2} \quad \text{and} \quad i_{VV} = i_{\perp} = \frac{|S_1|^2}{(kr)^2} \quad (2.19)$$

The first,  $i_{\parallel}$ , is the scattered irradiance of parallel polarisation per unit incident irradiance for incident light polarised parallel to the scattering plane, that is  $\phi = 0$  in **Equ. 2.16**. The second,  $i_{\perp}$ , is the scattered irradiance of perpendicular polarisation per unit incident irradiance for incident light polarised perpendicular to the scattered plane, that is  $\phi = \pi/2$  in **Equ. 2.16**. These irradiances are not measured directly instead the detector signals,  $u_{VV}$  and  $u_{HH}$ , are measured and by calibration related to the differential mass scattering cross

sections. The following section introduces the mass scattering cross section and relate experimental signal measurements and theoretical calculations to it.

## 2.4 DIFFERENTIAL MASS SCATTERING CROSS SECTION

### 2.4.1 INTRODUCING A MASS FORMALISM

A mass formalism of the scattering cross sections is useful because it is an experimental measure that is readily compared to theoretical values. It also has the advantage of returning an understanding of the amount of scattered light that can be expected from particles of a given mass concentration. Smoke mass concentration is a quantity of interest to fire scientists and engineers as it is related to smoke detector activation, human sight and exposure, as well as defining smoke yield from a fire. Measurement of mass scattering cross sections is more useful to characterise per mass concentration than per number concentration because at high number concentration, there is rapid coagulation with a resulting decrease in number concentration. On the other hand, the mass concentration is conserved during the coagulation process. Another advantage is that for spherical particles in the size range of about  $0.5 \mu\text{m}$  to  $1 \mu\text{m}$ , the scattering cross section per mass is relatively insensitive to the particle (number) diameter.

The measurement of the differential mass scattering cross section provides an angular map of the light scattering strength of particles in terms of their mass. This characteristic map can be used to plan detector designs, such as where to place detectors, and understand alarm activation based on a given mass concentration of smoke. The metrology of the differential mass scattering cross section is the science in this study while the application is the engineering.

### 2.4.2 SCATTERING CROSS SECTION OF A SINGLE ARBITRARY PARTICLE

But what exactly is the concept behind a scattering cross section? Consider a sphere surrounding a single arbitrary particle such that a beam or cone from the source to the particle intersects an area,  $C_{sca}$ , of the spheres surface. The average rate of energy scattered out of the sphere in all directions is equal to the average rate of incident energy falling on the area,  $C_{sca}$ . This area is called the total scattering cross section as it describes the average rate at which energy is scattered in all directions per unit incident energy (Jones, 1955; Born and Wolf, 1999; Bohren and Huffman, 1998). The differential scattering cross section,  $\sigma_{sca}(\Omega)$ , is the angular functional form of  $C_{sca}$  and defines the average rate of energy scattered into a solid angle element,  $\Omega(\theta, \phi)$ , per average rate of incident field energy falling on  $C_{sca}$ . The angle  $\theta$  is the scattering angle and  $\phi$  is the azimuthal angle, which is ignored in the case of a spherical scatterer due to symmetry.

The relation between total and differential scattering cross sections is given by,

$$C_{sca} = \int_{4\pi} \sigma_{sca}(\Omega) d\Omega. \quad (2.20)$$

The energy balance argument above can be used to define the absorption cross section,  $C_{abs}$  as equal to the average rate of incident energy absorbed by the particle, transforming it into other forms of energy. Also the rate of energy loss from the incident field can be defined in terms of the extinction cross section,  $C_{ext}$ , from which it follows by the law of conservation of energy,

$$C_{ext} = C_{sca} + C_{abs}. \quad (2.21)$$

A particle absorbs light when its refractive index has a non-zero imaginary part, i.e.  $k > 0$  in the refractive index  $m_1 = n + ik$ . If a particle is non-absorbing then the conservation of energy implies,  $C_{ext} = C_{scat}$ . When the cross sections are measured in terms of the mass concentration then they are referred to as mass specific cross sections; for example, the mass scattering cross section that will be defined in the following section.

The optical theorem is a formulation of the extinction loss of energy from an incident field, in the forward direction,  $\theta = 0$ , and results in a general form of the extinction cross section (Bohren and Huffman, 1998; van de Hulst, 1949),

$$C_{ext} = \frac{4\pi}{k^2} \text{Re}\{(\mathbf{S} \cdot \hat{\mathbf{e}}_X)_{\theta=0}\}, \quad (2.22)$$

here  $\mathbf{S}$  is the vector scattering amplitude from **Equ. 2.15** and  $X$  denotes the incident polarisation. Similarly the explicit form of the total scattering cross section for an arbitrary particle is,

$$C_{scat} = \int_0^{2\pi} \int_0^\pi \frac{|\mathbf{S}_X(\theta, \phi)|^2}{k^2} \sin \theta \, d\theta \, d\phi = \int_{4\pi} \frac{|\mathbf{S}_X(\theta, \phi)|^2}{k^2} \, d\Omega. \quad (2.23)$$

The component inside the integral of **Equ. 2.23**,  $|\mathbf{S}_X(\theta, \phi)|^2/k^2$ , is known as the differential scattering cross section. This use of the word differential is a reference to the traditional notation style  $dC_{scat}/d\Omega$ , which is used as an aid to memory for the angular dependence of the quantity. In this study the notation above is dropped in favour of  $\sigma_{scat, X}(\theta, \phi)$  for a particular polarisation.

Bohren and Huffman (1998) refers to  $C_{mscat}$  as the mass scattering coefficient, as do Holland and Gagne (1970). Mulholland and Choi (1998) used terms mass specific or simply specific

cross sections. Holland and Draper (1967) made the first measurements of what they and this study called the differential mass scattering cross section as far as this study is aware. The method used by Holland and Draper varies significantly from that developed in this study as will be shown in **Chapter 4**.

### 2.4.3 SCATTERING CROSS SECTION OF A CLOUD OF POLYDISPERSE PARTICLES

The scattering experiments conducted in this study are concerned not with single particles but with clouds of particles. This means that the number of particles in the scattering volume amplifies the scattering. When the particles are also distributed over a range of sizes then the number of particles must be replaced by the number distribution function. It is then necessary to integrate over the sizes of the particles in the ensemble of particles. The differential scattering cross section for an arbitrary particle at a polarisation X is then given by,

$$\sigma_{sca,X}(\theta, \phi) = \int_0^{\infty} \frac{|\mathbf{S}_X|^2}{k^2} n(\ln d_p) d \ln d_p . \quad (2.24)$$

This gives the scattering in terms of the number concentration, i.e. per unit volume, but as mentioned earlier in this chapter the mass concentration is measured in this study. By introducing the mass concentration the differential scattering cross section per mass concentration can be determined as,

$$\sigma_{msca,X}(\theta, \phi) = \frac{\int_0^{\infty} \frac{|\mathbf{S}_X|^2}{k^2} n(\ln d_p) d \ln d_p}{M} , \quad (2.25)$$

where  $M$  is the mass concentration. Substituting the number distribution, **Equ. 2.1**, and the mass concentration, **Equ. 2.10**, into **Equ. 2.25** the differential mass scattering cross section is given by,

$$\sigma_j(\theta) = W \int_0^{\infty} |S_j(d_p, \lambda, m, \theta)|^2 \exp\left[\frac{-(\ln d_p - \ln d_n)^2}{2 \ln^2 \sigma_g}\right] d \ln d_p, \quad (2.26a)$$

$$W = \frac{N_0}{k^2 M \ln \sigma_g \sqrt{2\pi}} = \frac{6}{k^2 \pi \rho d_m^3 \exp\left(-\frac{9}{2} \ln^2 \sigma_g\right) \ln \sigma_g \sqrt{2\pi}}. \quad (2.26b)$$

The units of the constant term,  $W$ , are  $\text{m}^2 \cdot \text{g}^{-1}$ . The subscript  $j$  denotes the amplitude scattering matrix element and thus the polarisation under consideration such that  $j=1$  corresponds to VV and  $j=2$  to HH polarisation settings.

In the case of very narrow distributions the approximation that the number distribution is the product of a delta function and the number concentration suffices. When the particles in an ensemble are the same size, then the mass concentration is given by  $M = N_0 m_p$  where  $m_p$  is the mass of a particle, see **Equ. 2.4**. For spherical particles with monodisperse (very narrow) size distributions the differential mass scattering cross section is,

$$\sigma_j(\theta) = \frac{|S_j(d_p, \lambda, m, \theta)|^2}{m_p k^2}. \quad (2.27)$$

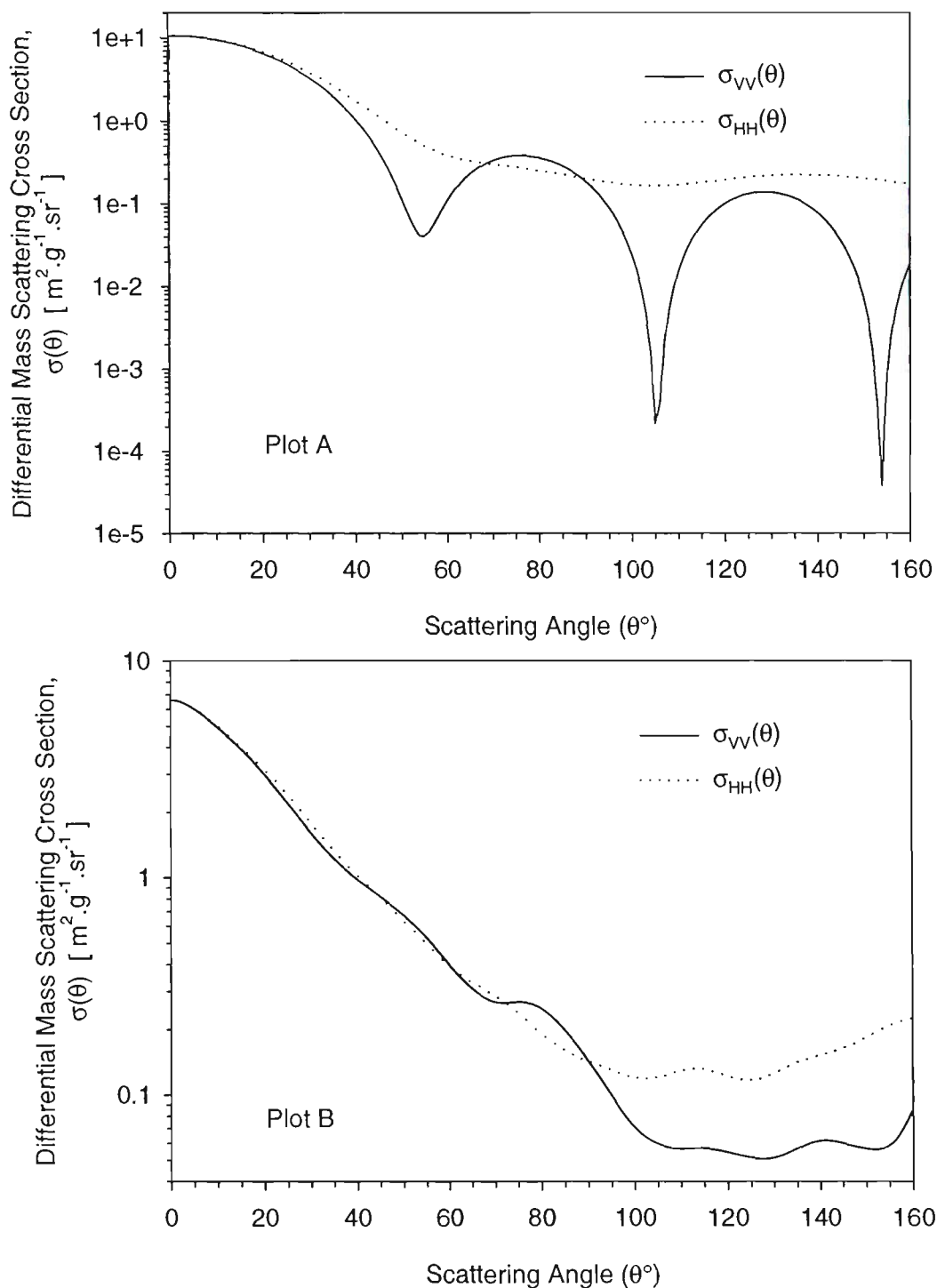
Thanks to modern computers the Mie scattering coefficients and angular functions can be computed in a fast and convenient manner. The Mie calculation for monodisperse spheres has used a routine known as BHMIE (Bohren and Huffman, 1998). To calculate the differential mass scattering cross section for a collection of polydisperse particles, **Equ. 2.26**, the numerical solution breaks into two sections. One part is solving the scattering problem thus determining  $|S_j(d_p, \lambda, m, \theta)|^2$  and the other part is integration over the size distribution. A Gauss-Hermite integration is used to calculate numerically **Equ. 2.26a** (Press et al., 1995; Abramowitz and Stegun, 1968), its general form being ,

$$\int_{-\infty}^{\infty} \exp(-v^2) f(v) dv = \sum_{i=1}^N w_i f(v), \quad (2.28)$$

using a substitution,  $v^2 = (\ln d - \ln d_n)^2 / 2 \ln^2 \sigma_g$ . The number diameter,  $d_n$ , is determined by the mass median diameter,  $d_m$ , and geometric standard deviation,  $\sigma_g$ , from an adjusted form of the Hatch-Cholate equation, **Equ. 2.8**. In **Equ. 2.28** the  $w_i$ 's contain the size distribution information as a Gaussian distribution and the function,  $f(v)$ , is equivalent to the  $S_j$ 's. The polydisperse calculations have used elements of the C++ objects from the SCATMECH library (Germer, 2001) for light scattering by spherical particle in free space. SCATMECH is derived from BHMIE, both make use of the algorithm study by Wiscombe (Wiscombe, 1980).

The results shown in **Figure 2.1** have been calculated using **Equ. 2.26** and the SCATMECH object library. In **Figure 2.1a** the differential mass scattering cross section is given for a single particle of 702 nm diameter and a refractive index of  $m_1 = 1.59 + i0$ . The deep minima in the calculated result are due to surface resonances in the near field of the particle causing interference features in the far field. This is typical of interference features seen in single particles size scattering. The scattering signal from polydisperse clouds has “averaged out” the minima seen in the scattering signal of a single particle or monodisperse cloud of particles. Presented in **Figure 2.1b** is the calculated result of a lognormal distribution (polydisperse cloud) of particles with mass median diameter of 702 nm, GSD = 2 and  $m_1 = 1.59 + i0$ . The effect of the polydisperse cloud is that the overall form of the scattering function is somewhat simplified. The Legendre and Bessel functions of different order and kind are still there; they are simply averaged or smoothed out. Mie scattering by a polydispersion of spherical particles does however have a form that can be described in a physically intuitive manner. This description (Sorensen and Fischbach, 2000) of scattering

**Figure 2.1:** The calculated differential mass scattering cross sections of **a)** a particle of size 702 nm,  $m = 1.59 + i0$  and **b)** particles distributed over a size range with mass median diameter 702 nm, GSD = 2 and  $m = 1.59 + i0$ .



for Mie particles is apparently only a recent development given the long period of analysis of light scattering by spheres. In a later section this new description is discussed.

#### 2.4.4 DETECTOR SIGNAL AND SCATTERING CROSS SECTIONS

The measurable scattering quantities are directly proportional to each other, i.e.  $u_l \propto i_l \propto \sigma_l$ , due principally to their dependence on the amplitude scattering matrix. The subscript denotes the polarisation either VV (vertical in, vertical out) or HH (horizontal, horizontal). The detected scattering signal measured in this study,  $u_l(\theta)$ , is a volume scattering measurement since the detector sees a volume in which light and a cloud of particles are interacting. This means that the connection between the detector signal and the differential mass scattering cross section must contain the number, or in this case the mass, concentration of particles in the scattering volume. Proportionality of the scattering quantities means that the scaling constant that relates the detector signal to the scattering cross section can be determined if both are known for the same ensemble of particles. These polarisation dependent calibration constants,  $K_{VV}$  and  $K_{HH}$ , are determined by a least means square fitting of the detector signal to the theoretical value of  $\sigma_l(\theta)$  from Mie theory. This is discussed in detail in **Chapter 3** on the calibration. When the calibration constant has been determined, an experiment with an unknown aerosol is performed and the differential mass scattering cross section is determined from the detector signal by the relation,

$$\sigma_l(\theta) = \frac{u_l(\theta)}{MK_l} \quad (2.29)$$

The total scattering cross section for incident unpolarised light with two components parallel and perpendicular to the scattering plane is then given by,

$$C_{scat} = 2\pi \int_0^\pi \frac{(\sigma_{VV} + \sigma_{HH})}{2} \sin \theta d\theta. \quad (2.30)$$

#### 2.4.5 RATIOS FOR SCATTERING DATA ANALYSIS

Throughout this study the angular scattering measured as  $\sigma_i(\theta)$  is examined to extract information about the particles. The light scattering smoke detector background of this thesis means that these methods of examination must be readily accessible to a minimum number of detectors at fixed angular positions. There are some common ratios defined to examine size dependence effects in Mie scattering that will be used in this study.

The first set angle ratio is the forward scattering ratio defined as,

$$\sigma_{VV}(5^\circ)/\sigma_{VV}(20^\circ), \quad (2.31)$$

that is of use when comparing the size of the aerosols under examination since the forward scattered light is sensitive to size (Hodkinson, 1962; van de Hulst, 1981; Kerker, 1969).

Another measure that is used to examine the symmetry in angular scattering measurements is the asymmetry ratio given by (Dobbins et al., 1984),

$$\sigma_{VV}(45^\circ)/\sigma_{VV}(135^\circ). \quad (2.32)$$

The angles on which the asymmetry ratio is dependent are chosen to avoid forward scattering and emphasise the differences at 45° above and below 90°. Finally the polarisation ratio is defined as (Kerker, 1969; Hsu et al., 1991),

$$\rho(\theta) = \sigma_{HH}(\theta)/\sigma_{VV}(\theta), \quad (2.33)$$

which is related to the degree of linear polarisation,

$$P(\theta) = \frac{\sigma_{VV}(\theta) - \sigma_{HH}(\theta)}{\sigma_{VV}(\theta) + \sigma_{HH}(\theta)} = \frac{1 - \rho(\theta)}{1 + \rho(\theta)}, \quad (2.34)$$

and has been used in past studies of smoke aerosol light scattering to demonstrate the discrimination of soot agglomerates from non-flaming smoke aerosols (Loepfe et al., 1997).

## 2.5 LIGHT SCATTERING BY AGGLOMERATES

### 2.5.1 FRACTAL SOOT AGGLOMERATES

Agglomerate and droplet particles have radically different morphologies. Their mass is distributed in very different ways defining the particle morphology (shape and size), see **Figure 1.1**. Thus light scattering can be used to differentiate smoke aerosols of spherical nature from soot agglomerates. As outlined above the scattering by spherical particles is well understood from the exact formal solution, Mie theory. This section introduces the light scattering by fractal soot agglomerates.

The dissemination of fractal geometry (Mandelbrot, 1983) initiated studies that have uncovered many characteristics of aggregate particles. When Forest and Witten (1979) identified that aggregate structures were fractal in nature (Mandelbrot, 1983) an intense field of study was initiated. A fractal has been described as the cluster property (ie. perimeter, area or volume) having a Hausdorff-Besicovitch dimension, which is not an integer and is greater than or equal to the topographical dimension (Mandelbrot, 1983). The Hausdorff-Besicovitch dimension,  $D_f$ , is defined such that

$$n \propto (d)^{D_f}, \quad (2.35)$$

where  $n$  is the number of spheres of diameter  $d$ , necessary to completely contain all points of the cluster.

The formation of primary particles into aggregates is a kinetic stochastic process, in which primary particles randomly collide and stick to each other forming clusters. The use of statistical techniques, Diffusion Limited Aggregation (DLA) (Witten and Sander, 1981), modern computers, and the realisation that aggregates were fractal structures opened a new way of investigating the process. The simulation of particle aggregation which followed this has increased greatly the understanding of the formation processes behind these aggregates (Jullien and Botet, 1987; Meakin, 1998).

Diffusion limited cluster aggregation (DLCA, also called cluster-cluster aggregation) is the growth mechanism by which clusters themselves diffuse until they collide and stick to each other or collect small primary particles (or monomers) as they go (Kolb et al., 1983; Meakin, 1984). The term agglomerate has come into use as a description of a particle that grows through cluster-cluster aggregation (Mountain and Mulholland, 1988a). Aggregation processes are not limited to soot growth but find application in other processes such as electrodeposition, yeast flocculation (beer!), and dielectric breakdown to name but a few.

In the case of soot agglomerates the Hausdorff-Besicovitch dimension,  $D_f$ , generally called the fractal dimension, is related to the distribution of mass or number of primary spheres (of unit mass) by (Wu and Friedlander, 1993; Cleary et al., 1990; Mandelbrot, 1983)

$$N = k_a \left( \frac{R_g}{r_o} \right)^{D_f}, \quad (2.36)$$

where  $N$  is the number of primary spheres in an agglomerate cluster. **Equ. 2.36** is asymptotic and holds only for agglomerates for which  $N$  is large, or  $R_g \gg r_o$ . Where  $R_g$  is the radius of gyration and  $r_o$  is the radius of the primary particle. It is implicit in **Equ. 2.36** that the primary particle radius is uniform for all  $N$  primary spheres. For soot agglomerates

the primary particles typically have a narrow distribution with the standard deviation divided by the mean equal to about 18 % for laminar diffusion flames (Koylu and Faeth, 1994b). The term  $k_u$  is known as the “pre-factor” and is representative of the packaging of the primary particles. Both  $D_f$  and  $k_u$  are necessary to fully describe the structure of the agglomerate. This morphological characteristic of soot agglomerates has a strong influence on the light scattering by the agglomerate.

Soot particles are not ideal fractal structures, which means they are not self-similar on all length scales and thus have a limiting upper and lower length unit. The lower bound is the radius,  $r_p$ , of the primary particle making up the agglomerate. Also the upper bound of the soot agglomerate particle is its characteristic length. In soot agglomerate studies this is the radius of gyration,  $R_g$ . When examining the scaling behaviour of the fractal description of soot structures, Sorensen and Feke (1996) measured the mean size of their soot agglomerate particles to be  $0.3 \mu\text{m}$ , with the largest observed agglomerate being  $400 \mu\text{m}$ . **Equation 2.36** has been found to apply over five orders of magnitude in the radius of gyration (Sorensen and Feke, 1996).

The main agglomerate characteristic of interest to this study is the fractal dimension that characterises the distribution of mass in soot agglomerates (Witten and Sander, 1981; Schaefer et al., 1984; Kolb et al., 1983; Meakin, 1984). The light scattering by agglomerates has attracted a great deal of attention over the past four decades or so. Of particular relevance to this study are the angular light scattering studies (Dobbins and Megaridis, 1991; Gangopadhyay et al., 1991; Mountain and Mulholland, 1988b); specifically post flame soot is of interest (Koylu and Faeth, 1994a; Sorensen and Feke, 1996).

### 2.5.2 SCATTERING PARAMETER AND THE STRUCTURE FACTOR

The fundamental quantity in characterising the fractal structure of an agglomerate is the pair correlation (density autocorrelation) function of the primary particles. This is the function that contains the information about the mass distribution in the soot agglomerate. For a mass fractal structure the pair correlation function is (Sorensen and Wang, 1999),

$$g(r) \sim r^{D_f - D_e} h(r/R_g), \quad (2.37)$$

here  $r$  is the pair separation scalar distance,  $D_e$  is the dimension of the space in which the agglomerate is embedded, and  $h(r/R_g)$  is the cut-off function. In **Equ. 2.36** and **2.37** the radius of gyration of the agglomerate,  $R_g$ , is defined by the pair correlation function as,

$$R_g^2 = \frac{1}{2N} \sum_i^N \sum_j^N (r_i - r_j)^2 = \frac{1}{2} \int_0^\infty r^2 g(r) d^3r. \quad (2.38)$$

The cut-off function,  $h(r/R_g)$ , describes the finite scaling of the agglomerate. It is independent of the fractal dimension of the agglomerate and has behaviour that goes to zero faster than a power law for large values of  $r/R_g$ . A widely used cut-off function is  $e^{-(r/R_g)^\beta}$ , where  $\beta$  has a value of about 2. When the cut-off function is determined, the form of the structure factor follows (Mountain and Mulholland, 1988a).

The Fourier transform of the pair correlation function for the primary particles,  $g(r)$ , leads to the structure factor,  $S(q)$ , which describes the scattering by agglomerate particles (Berry and Percival, 1986; Martin and Hurd, 1987; Jullien and Botet, 1987). The structure factor and the pair correlation function are Fourier transform pairs. The structure factor describes the

scattering contribution of the spatially distributed mass (the primary particles) and is defined by,

$$S(q) = i(q)/i_0 = N^{-2} \sum_j^N \sum_l^N \exp(i\mathbf{q} \cdot (\mathbf{r}_j - \mathbf{r}_l)), \quad (2.39)$$

here,  $q$ , is the scattering parameter defined as the magnitude of the scattering elastic wave vector,  $\mathbf{q}$ ;  $i(q)$  and  $i_0$  are the scattered and incident irradiances. The scattering parameter is simply the magnitude of the vector difference between the incident,  $\mathbf{k}_i$ , and scattered,  $\mathbf{k}_s$ , wave vectors, each pointing in the direction of propagation of their respective waves. The elastic condition implies that there is no change in wavelength of the incident to scattered wave,  $|\mathbf{k}_i| = |\mathbf{k}_s| = k = 2\pi/\lambda$ . The scattering parameter,  $q$ , is then given by,

$$q = \frac{4\pi}{\lambda} \sin(\theta/2). \quad (2.40)$$

A form factor,  $\sigma_R(q)$ , is a function that describes the scattering by a primary particle. This form factor corresponds to the Rayleigh component of the scattering by the primary particles. The structure factor,  $S(q)$ , is multiplied by the scattering of the primary particle,  $\sigma_R(q)$ , to obtain the differential scattering cross section as a function of the scattering parameter (Mountain and Mulholland, 1988a),

$$\sigma_{scat}(q) = S(q)\sigma_R(q). \quad (2.41)$$

For a Rayleigh scatterer in the vertical-vertical polarisation  $\sigma_{R,VV}(q)$  is a constant and thus the behaviour of  $S_{VV}(q)$  dominates the angular scattering. For this reason most measurements with light scattering uses only the VV polarisation when considering the scattering by soot agglomerates. The structure factor is not very sensitive to the polarisation

and thus a ratio of scattered signals at different polarisations, **Equ. 2.33** and **2.34**, will reveal the Rayleigh scattering nature of the primary particles. Another consequence of **Equ. 2.41** or **2.39** is that the differential mass scattering cross section as a function of the scattering parameter is proportional to the structure factor,  $\sigma(q) \propto S(q)$ .

### 2.5.2.1 Structure factor for $qR_g < 1$

For a system of randomly orientated agglomerates the structure factor is given by (Jullien and Botet, 1987),

$$S(q) = \int_0^{\infty} g(r) \frac{\sin(qr)}{qr} r^2 dr. \quad (2.42)$$

The series expansion of the sine function and its denominator leads to the following form of **Equ. 2.42**, using the radius of gyration defined above,

$$S(q) \approx 1 - \frac{1}{3} q^2 R_g^2 + \dots \quad (2.43)$$

Which can also be determined from the angular average of **Equ. 2.39** for small  $q$ . **Equation 2.43** is the Guinier regime (Guinier et al., 1955), valid for what is commonly called “small  $q$ ”, that is  $qR_g < 1$ . In this study the scattering at small angles is measured for some soot agglomerates and **Equ. 2.43** is then used to determine the radius of gyration of those agglomerates (**Sec. 6.4**).

### 2.5.2.2 Structure factor in the transition region

When  $qR_g$  is of order one, then the cut-off function,  $h(r/R_g)$ , strongly affects the structure factor. In this study on post-flame soot agglomerates interest is focused on the  $qR_g > 1$  region.

### 2.5.2.3 Structure factor for $qR_g > 1$

This is what is referred to as the “large q-regime” where  $qR_g > 1$ . In this regime the fractal nature of the agglomerate controls the scattering. The Fourier transform of the pair correlation function gives the structure factor,

$$S(q) = \int e^{i\mathbf{q}\cdot\mathbf{r}} g(\mathbf{r}) d\mathbf{r}, \quad (2.44)$$

which is equivalent to **Equ. 2.39**. Using the appropriate pair correlation function, **Equ. 2.37** (Sorensen and Wang, 1999), and computing the Fourier transform, **Equ. 2.44**, then the following important relation exists,

$$S(q) \propto q^{-D_f}. \quad (2.45)$$

This relation is the behaviour of interest to this study since it tells us that at “large q” a plot of the logarithm of the structure factor, or differential scattering cross section as per **Equ. 2.41**, versus the logarithm of the scattering parameter will give the fractal dimension of the soot agglomerate as the slope of this plot.

## 2.6 SCALING APPROACH TO SCATTERING BY SPHERES

As discussed above, the theory determined by Mie (Mie, 1908) (and others) provides essentially an exact description of scattering by spheres whether as a function of angle or when parameterised as a function of q. However, the qualitative features for a particular scattering regime are not always evident from the general mathematical formulation. For the case of q-dependent scattering Sorensen et al. (Oh and Sorensen, 1999; Sorensen and Fischbach, 2000) have developed a scaling approach to light scattering that applies to both agglomerates and spheres. The approach developed by Sorensen et al. describes the envelope of the scattering parameter dependence in terms of the length scales of the scattering event. Thus the approach is referred to as the scaling method. This simply

executed and physically intuitive scaling description is of importance to this study because it has been extended to describe scattering by spheres and has particular importance to polydisperse ensembles.

Recently Sorensen and Fischbach (2000) have supplied a physically intuitive model for the functional behaviour of scattering by a sphere in terms of  $q$  that is particularly useful for polydispersions. There has been relatively little study regarding the  $q$ -dependence of scattering by spheres until recent work by Sorensen and Fischbach (2000). This is surprising given the extensive research into scattering by spheres. The exact solution offered by Mie theory (Mie, 1908) might be the reason for this apparent lack of interest.

The scaling method (Sorensen, 1997; Oh and Sorensen, 1999; Sorensen and Fischbach, 2000) compares the length scale of the scattering,  $q^{-1}$ , to the length scale of the scatterers of the system. Importantly this is the spatial distribution of the mass and thus leads to the structure factor. The length scales in a scattering system determine how phases of the scattered waves combine, either constructive or randomly, in the far field depending on these length scales.

The usefulness of a scaling approach to this study is that it describes the overall functional behaviour of light scattering, what Sorensen and Fischbach (2000) refer to as the “envelope” of the scattering as a function of the scattering parameter. Sorensen and Fischbach (2000) identified three main power law regimes by ignoring the interference features (the minima) and plotting a straight line along the peaks of the ripples, see **Figure 2.1**. Importantly they also found that the phase shift parameter,  $\gamma = 2kR|m - 1|$ , dictated the transition between these regimes. That is to say the underlying scattering character became clear in terms of the  $q$  dependence of the structure factor. For small values of  $\gamma$  the scaling method used for agglomerates above was used in a straightforward manner to derive,

$$S(q) \propto \begin{cases} 1 & \text{for } qR < 1 \\ (qR)^{-4} & \text{for } qR > 1 \end{cases} \quad \text{and small } \gamma \quad (2.46)$$

For larger values of  $\gamma$  the internal field is less homogeneous and tends to localise near the surface of the sphere. Sorensen and Fischbach (2000) approximated this by defining a layer of width,  $l$ , in which point like scatterers are located. The structure factor they derived by applying the scaling method is,

$$S(q) \propto \begin{cases} 1 & \text{for } q < l^{-1} \\ (qR)^{-2} & \text{for } l^{-1} > q > R^{-1} \text{ and large } \gamma . \\ R^2 (qR)^{-4} & \text{for } q > l^{-1} \end{cases} \quad (2.47)$$

For small phase shift parameter, **Equ. 2.46**, particles there is no -2 region and the scattering as a function of  $q$  has a slope of -4 at intermediate and large  $q$ . The two regimes of interest for polydispersions of large phase shift parameter, **Equ. 2.47**, are the ones corresponding to  $q$  dependent slopes of -2 and -4. For very large values of  $\gamma$  the -2 region is expected to dominate the scattering over a wide range of  $q$  and the -4 region will be forced to higher values of  $q$ . For ease of reference the  $q$ -slope will refer to the slope of the scattering over a given range of  $q$  values.

The theory outlined above is based on a monodisperse aerosol. Still, it is tantalising to apply this approach to the polydisperse aerosols in our study since this will be one of the first tests of the utility of this scaling approach to an important class of particles. Sorensen and Fischbach (2000) demonstrated **Equ. 2.47** when they observed the light scattered by a polydispersion of water droplets, this is discussed further in **Chapter 8** after the different aerosol results are presented.

## 2.7 SUMMARY

This study is focused on obtaining quantitative light scattering data and determining whether the scattering data together with theory allow discrimination between aerosol products of flaming combustion and non-flaming fire events. An extension to this is that similar techniques might be able to discriminate fire aerosols from non-fire or nuisance aerosols. Nuisance aerosols are those aerosols that cause a high frequency of alarms but are not unwanted fires. The observation that has inspired this study is that the morphology of flame-generated soot is so different from that of particles generated by a non-flaming fire. This is accomplished by analysing the measured scattering data using various ratios, such as the forward scattering and asymmetry ratios defined above. The polarisation ratio is also used and the reason why this has been successfully utilised in the past has been described above. These ratios are also useful means of comparing findings with other studies.

A major contribution of this study is the application of the scaling method to the light scattering measurements of this study and the comparison of these results with those of Sorensen and Fischbach (2000). While the soot has been studied extensively in the past both in-flame and post-flame and much is known about light scattering behaviour as a function of scattering parameter, the same cannot be said of smoke aerosol from non-flaming fires. Nuisance aerosols will also be examined using both Mie theory and the scaling method. The recent findings of Sorensen and Fischbach (2000) are timely as the results measured in this study can be compared with their model (Sec. 8.4.2).

As has been shown above, the scattering of light by spherical and agglomerate particles has very different forms or envelopes. In particular, the slope calculated from a log-log plot of differential mass scattering cross sections against the scattering parameter might be a viable means to discriminate between the particles. It is well known the soot agglomerate particles will yield fractal dimensions from light scattering measurements of about -1.7 to -1.8

(Sorensen and Feke, 1996; Koylu and Faeth, 1994a). Smoke particle generated in non-flaming fires (smouldering or pyrolysis) should yield slopes of about -2 or -4, based on **Equ. 2.46** and **2.47**, depending on the particles phase shift parameter or an average if ensemble averaging is occurring.

The theory for soot agglomerates above is not well known to the fire detector manufacturing community, similarly there are no data on angular light scattering by common smoke and nuisance aerosols. Demonstration of the theory and availability of differential mass scattering cross sections can more clearly benefit detector manufacturers when they consider different designs. As well these address some needs of fire scientists and engineers when considering scattering by smoke aerosols.

## LIGHT SCATTERING APPARATUS

### 3.1 INTRODUCTION

#### 3.1.1 HISTORICAL OVERVIEW

Experimentally this study aims to measure the angular distribution of light scattered by selected smoke and nuisance aerosols. The apparatus used for these measurements is described in this chapter after presenting an overview of light scattering apparatus from other studies. The similarities of our apparatus and those of other studies are strongest in the optical system of the apparatus. The main differences lie in the fundamental areas of calibration, and the dependence on gravimetric mass concentration measurement, as well as the transport of aerosols to the light scattering apparatus. The major focus of our approach was to obtain the quantitative differential scattering cross section per mass of the aerosols examined. This chapter presents the details of the angular scattering system of the apparatus, including the aerosol transport, optical components, and signal detection.

The Large Agglomerate Optical Facility (LAOF) was constructed at the National Institute of Standards and Technology (NIST), Gaithersburg, USA, in the early 1990's (Mulholland and Bryner, 1994). The LAOF was designed for a study commissioned by the National Aeronautic and Space Agency (NASA), aimed at investigating the growth of agglomerate aerosols into larger high mass carbon particles. Early work with the LAOF made use of its Transmission Cell Reciprocal Nephelometer (TCRN) design to measure extinction and total scattering by flame generated soot (Mulholland and Bryner, 1994). Later studies followed using the same TCRN configuration of the apparatus to determine the mass extinction and total mass scattering cross section of ethylene and acetylene generated soots (Mulholland and Choi, 1998). Although the LAOF was first designed with both extinction measurements as well as integrating (total) and angular (differential) scattering measurements in mind,

circumstances led to its main use for extinction and total scattering measurements. This study has completed the commissioning of the angular scattering capabilities of the LAOF, which completed work that had been attempted at different stages over the years since its construction. The Transmission Cell Reciprocal Nephelometer (TCRN) aspect of the LAOF has not been used in this study as all interest was aimed at investigating angular scattering characteristics of smoke aerosols. Details about the TCRN design have been published elsewhere (Mulholland and Bryner, 1994).

The name nephelometer derives from the Greek word *nephele* meaning cloud; thus, its literal meaning is cloud meter, which finds its roots in the work of atmospheric scientists interested in visibility and cloud aerosols. The nephelometer was developed on both sides of the Atlantic during World War II to quantify visibility through clouds for aviation. For example, Beuttell and Brewer (Beuttell and Brewer, 1949) describe many nephelometer designs. There are two general types of nephelometer: integrating and polar. An integrating nephelometer measures total scattered light by collecting all the scattered light over a large range of angles, say  $\theta = 5^\circ \dots 175^\circ$  (Crosby and Koerber, 1963; Charlson et al., 1967). This allows the total scattering of the aerosol under investigation to be determined as in **Equ 2.29**. Polar nephelometers (Prichard and Elliot, 1960) are designed to measure the angular scattering function. The angular range for the polar nephelometers is usually slightly truncated compared with that of the integrating nephelometers. Integrating nephelometers have come to be labelled by the name nephelometer, while the distinction of polar nephelometer is not used as often except in the atmospheric aerosol fields. Integrating nephelometers have fixed components; polar nephelometers generally require moving components to make angular scans. Moving parts and the polar nephelometer's requirement for high gains over a large dynamic range, has lead principally to the integrating nephelometers development as an aerosol light scattering instrument for fieldwork. This has occurred mainly in atmospheric

and environmental science. Technological development of solid-state electro-optical components has led to widespread application of angular light scattering techniques for a variety of applications including the photoelectric smoke detector. Nevertheless, the integrating nephelometer did make a transition from atmospheric and environmental aerosols research to applied smoke detection in Australia (Packham et al., 1975). This type of detector is no longer being manufactured because angular scattering based on solid-state technology has replaced the design, a result of low maintenance, low power requirements and low cost of solid-state components.

### **3.1.2 AN OVERVIEW OF OTHER LIGHT SCATTERING APPARATUS**

Light scattering by an ensemble of particles, a cloud, results in an increase of the scattering signal proportional to the number of particles in the scattering volume; which is the volume of the incident beam visible to the detector. Another angular scattering technique is to measure the light scattered by a single particle. This is made possible by electrostatic levitation of a single particle in the scattering volume using an adapted Millikan oil drop apparatus. The development of an angular scanning apparatus for single particle scattering was started with the work of Guker and Egan (1961) and later developed further with the work of Wyatt and Phillips (Wyatt and Phillips, 1972). Application of this single particle scattering technique has been made by various researchers for either or both size and refractive index studies (Pluchino et al., 1980; Wyatt, 1980; Mulholland et al., 1985a; Marx and Mulholland, 1983). The application to refractive index measurement in particular is of great importance to scattering studies but the technique suffers due to signal noise associated with single particle scattering. Also electrostatic levitation is not conducive to affordable and simply operated field devices. These factors and the polydisperse nature of natural aerosols make field operation somewhat impractical and costly as opposed to a simpler particle cloud

scattering method. The LAOF makes use of the particle cloud scattering method in both the TCRN and angular scanning modes.

The LAOF also makes use of the linear polarisation of light for differential (angular) scattering. The incident and scattered beams can have their polarisations set and measured, respectively, in any linear polarisation. In this study, polarisation orientations horizontal (parallel) and vertical (perpendicular) to the scattering plane have been examined. One of the original motivations for this study was to examine the intensity scattering matrix of the smoke aerosols (van de Hulst, 1981; Bohren and Huffman, 1998), but this was not pursued due to the sophisticated optical apparatus required. The approach taken in this study does examine the linear polarisation components of the intensity scattering matrix. Measurement of the elements of the scattering matrix has been developed since Prichard and Elliot's (Prichard and Elliot, 1960) study of atmospheric aerosols, which measured the various combinations of scattering matrix elements incorporating parallel, perpendicular, 45° degree and circular polarisation orientations. Research work that followed, aimed at investigation of particle characteristics of size and shape using the intensity scattering matrix, which carries information about both, and comparing results with Mie theory. The earlier studies of this type used manually operated polarisers (Holland and Gagne, 1970; Holland and Draper, 1967), but development of piezo-optic modulators (Kemp, 1969) led to an automated scattering matrix measurement method (Perry et al., 1978; Hunt and Huffman, 1973). This approach was developed to a high degree by Thompson et al. (Thompson et al., 1980) resulting in fast (120 second) measurement of all sixteen elements of the scattering matrix. Contemporary opto-electronics would not use piezo-optic technology but instead use liquid crystal modulators, removing the need for high voltage power systems. The angular scattering system developed for the LAOF and used in this study uses manually operated polarisers.

As mentioned above, atmospheric and environmental aerosol scientists have made use of nephelometers for many years; for example, Eccleston et al. (1974) used an integrating nephelometer and mass sampling from a small aircraft downwind of a bushfire. Studies of smoke aerosols in the atmosphere are generally rare, although a great deal of interest was generated during the 1970's and 80's about nuclear winter scenarios and later the role that light-absorbing aerosols play in global warming (Johnson D. W. et al., 1991). Smoke aerosol concentrations are commonly measured in terms of the light extinction described by the Beers-Lambert Law for light transmission/attenuation (Mulholland, 1995). In the field of fire science this measure is usually called the "obscuration", and is made by a relatively straightforward measurement of the attenuation of a light beam passing through smoke (Mulholland, 1982). As the smoke mass concentration increases the attenuation of light and thus the obscuration also increases. Smoke obscuration measurement has been undertaken for many reasons including human exposure, visibility, quantifying smoke production, and investigating smoke detector activation (Jin, 1978; Seader and Einhorn, 1976; Rasbash and Phillips, 1978; Mulholland, 1995). Atmospheric scientists have made similar investigations into mass concentration correlations with total scattered light using nephelometers (Charlson et al., 1967; Waggoner et al., 1981), although this fundamentally requires some knowledge about the imaginary part of the refractive index for absorbing particles. One interesting early study of the light attenuation caused by smoke aerosols was driven by the need to measure smoke as a food additive (colouring, flavouring and preservation) (Foster, 1959).

### 3.1.3 ANGULAR LIGHT SCATTERING APPLIED TO SMOKE AEROSOLS

The angular scattering studies of smoke aerosols have in general been limited to two main areas. The first is that of soot formation in flames and the second is smoke detector performance and design. Soot formation (Wagner, 1979; Haynes and Wagner, 1981; Glassman, 1988) in a flame has been an area of interest for many years and will continue to

be so, particularly as requirements for cleaner-burning diesel and gas turbine engines increase. Light scattering methods have been used in developing an understanding of formation mechanisms and morphology of flame generated smoke aerosols (i.e. soot); see the review by Charalampopoulos (1992). In the case of soot, this study limits its scope to that of differential light scattering measurements of post-flame soot and soot morphology. In the case of the latter, reference is made to some inflame differential scattering studies on morphology, where angular scattering methods to examine soot morphology were developed.

Light scattering systems used in soot morphology studies have generally been angular scanning systems (Gangopadhyay et al., 1991; Koylu and Faeth, 1994). Angular information is necessary for morphological aspects of soot to be examined using light scattering data (Sec. 2.5). The dominant factor for use of light scattering in the study of soot morphology is that their fractal nature is visible in angular scattering data (Martin and Hurd, 1987; Dobbins et al., 1998). Angular scattering information of this type is available using the differential scattering system of the LAOF.

Light scattering systems aimed at examining soot morphology (Gangopadhyay et al., 1991; Koylu and Faeth, 1994) have the same basic layout as the differential scattering system shown in **Figure 3.1**. The work of Koylu and Faeth (1994) examined post-flame soot flowing out of a sampling duct above a burner. Gangopadhyay et al. (1991) varied the height of the scattering volume to measure scattering of soot in a flame at different heights. The angular range of the apparatus developed by Koylu and Faeth (1994) was  $\theta = 5^\circ$  to  $160^\circ$ , while Gangopadhyay et al. (1991) used an angular span of about  $\theta = 10^\circ$  to  $115^\circ$ . The source for scattering measurements used in both studies was an argon-ion type laser,  $\lambda = 514.5$  nm with a beam power of slightly less than 2 W. This high power is useful for resolution of the scattering signal from small incipient in-flame soot (Gangopadhyay et al., 1991). Also a small detector aperture is used to resolve small scattering volume (Koylu and Faeth, 1994). Later

work introduced polarisation measurement to examine the depolarisation effects of scattering by soot aggregates (Lu and Sorensen, 1994). Koylu and Faeth (1994) and made differential measurements at both linear polarisations, as has been done in this study. All of these studies have made use of frequency filtering, i.e. beam chopping and lock-in amplification, to improve signal discrimination from the flame or remove background effects. In all of the studies mentioned, the detectors were photomultipliers so that high signal gain was available. The detectors were also mounted on rotation stages with a burner or burner exhaust flow at the centre of revolution. This basic design is also used in this study.

A very useful light scattering study (Mulholland et al., 1985b) measured the refractive index and evaporation rates of individual smoke particles from  $\alpha$ -cellulose in a non-flaming mode. The work made use of the electrostatic balance light scattering device developed by Wyatt and Phillips (1972) to capture a single smoke particle and then measure the scattered light from that particle. The work by Mulholland et al. (1985b) measured the scattering signal of a single particle of known size. They isolated particles of a narrow size distribution, and then used the electrostatic balance to trap one of these particles. After measuring the scattering signal they applied the method developed by Marx and Mulholland (1983) by which the refractive index was determined by a best-fit algorithm. The refractive index results are of particular importance in a later chapter for numerical calculation of the light scattering by smoke aerosols generated by non-flaming fires.

Mulholland et al. (1985b) also measured the evaporation rate of captured particles, showing that they undergo an initial rapid evaporation because of the water content of the particles. This affects the size of the particles and is expected to have already occurred before the particles are introduced to the LAOF in this study.

Meacham and Motevalli (Meacham and Motevalli, 1992) developed a Scattered Light Detection Instrument (SLDI) for the assessment of light scattering by various smoke aerosols. The first use of this instrument was aimed at examining light scattering characteristics of smoke aerosol from non-flaming fires. The SLDI used fixed detectors at nominal angles of  $20^\circ$ ,  $40^\circ$  and  $60^\circ$  on both sides of a forward direction detector. The whole assembly was mounted perpendicular to the ceiling so that the smoke jet from test fires in the test room passed through the scattering volume. Meacham and Motevalli tested a large number of smoke aerosols generated by many different fuels, but were limited to use of the detector at  $20^\circ$  because of what they considered the effects of multiple scattering at larger angles. With the detector positioned at  $20^\circ$ , they observed that the signal changed as the position of the source fuel in the test room was changed and thus demonstrated the underlying dependence of the particle characteristics on the transport history of the aerosol. A later study was conducted by Aggarwal and Motevalli (1997) using the SLDI and a measuring ionisation chamber (MIC) to examine the response of the scattered light and ionisation instruments to smokes generated by various fuels. Aggarwal and Motevalli observed that for the range of fuels examined the MIC response signal was generally strongest with fuels for which the SLDI response was weakest, and the MIC response weakest for the fuels giving the strongest SLDI response. These measurements were made at the same light transmission levels, which equates to the same mass concentration. Aggarwal and Motevalli did not have aerosol-sizing instruments and could not isolate this as a cause of the differences between the scattered and ionisation signal. Also, as with the majority of scattering experiments, they did not have any information on refractive index of the smoke particles. Neither of these studies (Meacham and Motevalli, 1992; Aggarwal and Motevalli, 1997) utilised polarisation information.

Loepfe et al. (1997) developed a similar apparatus to the SLDI. It was a horizontally mounted ceiling system in a fire test room similar to that used in EN54 smoke detector standard test fires (EN54-Part 9, 1982). The fuels used to generate the smoke aerosols were in fact those required by EN54, and some nuisance aerosols such as a water mist, oil vapour, candle wax vapour and burning toast. The light scattering apparatus had 14 fixed position detectors, each with its own photodetector diode and gain circuit. Each gain circuit was set to an appropriate amplification to give the required signal range over the angular span. The scattering volume correction for each detector position was also determined using Monte-Carlo and ray tracing methods. Two co-linear incident beams were generated with polarisation horizontal (parallel) and vertical (perpendicular) to the scattered plane. Using the polarisation information they reported the degree of linear polarisation (Equ. 2.34) of the light scattered by various smoke and nuisance aerosols. Using this polarisation measure they were able to distinguish flame generated smoke aerosols from those generated by the non-flaming fires (\*\*INSERT GRAPH). They also found that the nuisance aerosols could be distinguished from flaming fire-generated aerosols, in the sense that nuisance aerosols had results similar to smoke generated by non-flaming fuels. They also observed a peak in the degree of polarisation at  $\theta = 155^\circ$  that could be used for discrimination of steam, a nuisance aerosol, from the other aerosols. Similar to earlier studies Loepfe et al. (1997) did not have aerosol-sizing instruments available and could not isolate size characteristics as a contributing factor. The work reported by Loepfe et al. (1997) did not recognise the role that agglomerate scattering of light had on their results. They described the soot scattering as Rayleigh-like (particle size much less than the incident light's wavelength): this is not the case as discussed in Sec. 2.5.1 and Sec. 8.3.4. Discrimination using polarised light is examined in more detail in this study.

This study makes use of the differential (angular) scattering system of the LAOF, to make measurements of the differential light scattering properties of smoke and nuisance aerosols. In this thesis the emphasis is placed on an examination of the angular distribution of polarised light scattered by smoke aerosols that are introduced into the LAOF. These differential scattering experiments are conducted to address the lack of angular light scattering data available in practical units of measurement. The angular information will be analysed to determine characteristics that distinguish between different smoke and nuisance aerosols. Different generation and transport methods particular to the aerosol source are used to introduce the smoke into the LAOF. The means of aerosol generation are different for different fuels. This is discussed in detail in the separate result chapters relevant to the particular smoke aerosol. They are summarised in the following section of this chapter, where the aerosol transport sub-system to the LAOF is also described. Thus the LAOF has two essentially different sub-systems. One is the aerosol system, which generates and transports the aerosol under investigation through the scattering volume. The other component is the optical system that generates the required incident light and detects the light after it is scattered by the aerosols.

### **3.2 GENERAL FEATURES**

As mentioned above, the LAOF was originally designed to examine large agglomerate growth. The design goal was to isolate soot agglomerates in the vertical glass column section of the LAOF. The light extinction and scattering properties of the particles were then to be observed with time. This meant that the facility had to be mounted vertically on an optical bench, so that the mean agglomerate velocity was in the direction of the gravity field. This gave the agglomerates a long period of free fall in the column and minimised their chance of being lost to the walls, as the mean aerosol flow is downward.

The glass sections of the LAOF are in three parts: the upper, main or scattering cell, and lower sections. The changes to the LAOF from the original design have been mainly concerned with commissioning the angular scattering system. The original upper glass column has been changed to facilitate aerosol mixing and changing between different aerosols under investigation. This new design is shown in **Figure 3.1** as the inlet tubes and upper section. The optical components of **Figure 3.1** will be dealt with in detail in the next section, but the basic principles of a detector moving to different angles about a centrally located scattering volume is shown.

Returning to the glass sections, they are basically cylindrical in shape and about 110 mm external diameter. Each section joins its neighbour by means of ground glass flanges, which are sealed with vacuum silicon grease and a flange bracket. The upper section is capped with a removable lid and has two opposed inlets where the aerosol transport lines are connected. The middle section, where the aerosol particles scatter the incident laser beam, has appropriate holes for attachment of an entrance window and Rayleigh horn light trap. Both the window and the light trap are held in place and sealed by Teflon tape as used in plumbing. The side of the main section opposite the detector is coated in carbon black paint to minimize reflection. The lower glass section continues down about 150 mm then tapers into a small 25 mm tube that connects to the top of an isolation valve and filter manifold. Settling of particles to walls occurs over a number of experiments, after which time it is prudent to clean the scattering (middle) glass sections to remove this soot. The silicone grease used to seal the glass sections must also be handled with care as it has a habit of finding its way onto almost all surfaces touched. Cleaning the scattering cell requires some delicate treatment as well since the black anti-reflection coating opposite the detector consists of a base layer of matt black paint with a carbon paint upper layer. The carbon paint layer is

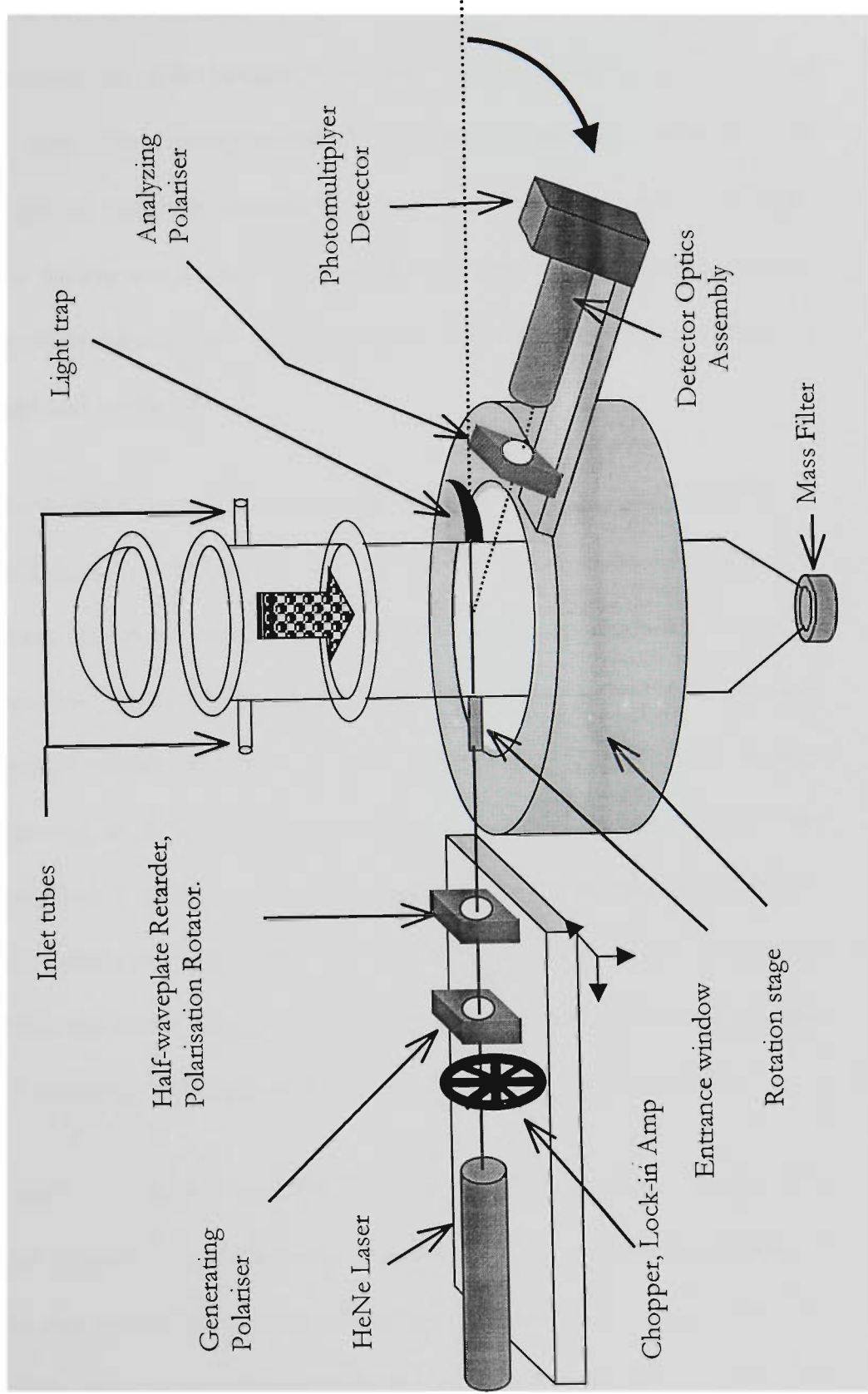
very easily removed by cleaning and it may be necessary to frequently reapply the carbon paint.

### 3.3 OPTICAL SYSTEM

#### 3.3.1 THE OPTICAL COMPONENTS

The light scattering cell is located in the midsection of the LAOF and is fabricated from 100 mm interior diameter glass tubing ending in ground glass flanges. The flanges allow connection to the upper and lower neighbours, which are also fabricated from glass. The scattering cell has an entrance window for the incident light beam and a light trap directly opposite. The plane in which the incident and scattered beams lie defines the scattering plane; in the case of this study the horizontal plane is used. The scattering angle,  $\theta$ , is given by the angle measured from the direction of propagation, so that  $\theta = 0^\circ$  is the forward direction of the incident beam. The incident beam originates from a HeNe laser (wavelength  $\lambda = 632.8$  nm) in continuous wave mode, which has a 500:1 (orthogonal) linear polarisation ratio. The main polarisation axis is aligned horizontal to the scattering plane. The beam is immediately passed through a rotating chopper ( $f = 80$  Hz) to reduce background noise when measuring low signals. The incident beam then passes through an optical train of polarizing elements that prepare the optical properties of the beam. This optical train consists of a linear Glan-Taylor type generating polariser orientated with its optical axis at an angle  $\phi_p = 0^\circ$ , where  $\phi_p$  is the angle of the optical axis of the polariser from the scattering plane. A subscript H then is used to denote this polarisation as the horizontal polarisation. This generated polarisation essentially eliminates the residual perpendicular or vertical (subscript V) polarisation of the laser. The next optical element is a quartz zero-order half-waveplate retarder. This is the key element in the incident optical train as a  $45^\circ$  rotation of its fast axis from the scattering plane induces a rotation of the beam from horizontal to vertically polarised light.

Figure 3.1: The angular scattering system of the LAOF



In this way an incident polarisation of either horizontal or vertical orientation can be chosen. The next optical element before the scattering volume is the entrance window, which is set at a slight angle to avoid multiple reflection of the incident beam. This angle does have an effect of reducing the intensity of the incident beam, as do all the other elements within the incident light optical train. After passing through the window, the laser beam passes through a 100 mm path length of uniformly distributed smoke or calibration aerosol. The light scattering is visible to the eye as a red line of light with a few bright spots arising from large agglomerate particles in the case of soot. A Rayleigh horn is used as a light trap to collect the forward scattered light and incident beam.

The light scattered to the detector first passes through the wall of the LAOF's scattering cell with a slight loss of light due to reflection. The opposite side of the scattering cell to the detectors view has been coated in a base layer of matte black paint and then a layer of carbon paint was added onto this. This black absorbent background reduced reflection of scattered light entering the detector field of view. This is particularly important near the entrance window and the light trap, as reflections and stray light are appreciable in these areas. The entrance window itself had to be kept to a small diameter, so that plasma light from the laser and scattering by the optical elements would not illuminate an area bigger than the entrance of the light trap, which was 5 mm. This stray light at the entrance window and near the light trap entrance would otherwise add significantly to the scattered light signal at  $\theta = 5^\circ$ .

To align the polariser's optical axes correctly, the first generating polariser was set in a precision mount and referenced to a polarizing beam splitter. The generated polarisation is horizontal when the two split beams are horizontal. Checking the height of the beams also gives an estimate of the standard uncertainty of the generated polarisation as  $\pm 0.1^\circ$  about the scattering plane. This uncertainty is small in comparison with that caused by correct manual setting of the other polarising elements discussed below. A null or crossed polariser

approach is then applied to the generated incident beam to determine the required positions for the half-waveplate and the analyser. These positions corresponded to horizontal incident and horizontal scattered polarised light (HH) and vertical-vertical polarisation (VV). The analyser is a linear polariser used to measure the vertical or horizontal scattered light incident on the detector. The generating polariser was set at either  $\phi_p = 90^\circ$  or  $\phi_p = 0^\circ$  to cross the analyser during alignment, but was not changed from the  $\phi_p = 0^\circ$  position during an experiment. Once the polariser and analyser were aligned, the half-waveplate retarder was placed in the optical train and aligned. The analyser,  $\phi_A$ , and retarder,  $\phi_R$ , angles are changed manually as required when conducting an experiment.

The scattered light was detected by a series of optical elements mounted on a rotation stage with stepper motor drive and encoder feedback. PC control of the rotation stage was accomplished by a computer program and interfaced through an indexer-board in the PC. This program also monitored the detector signal via an analogue-to-digital converter board. The rotation stage would move the detector and its optical elements in  $\Delta\theta = 5^\circ$  steps in the scattering plane from  $5^\circ$  to  $135^\circ$  to measure the scattered light. Essentially any angle in the range could be chosen for a measurement. For example, an extra measurement is usually made at  $\theta = 8^\circ$  to validate forward scattering, which was sensitive to misalignment. Alignment of the detector zero position was also automated but required the placement of neutral density filters in the incident beam and removal of the light trap. The rotation stage was then positioned manually until the point where the detector indicated peak intensity. The computer program then made the rotation stage scan a range of  $\pm 2.5^\circ$  about this peak position in  $0.25^\circ$  steps. The peak signal detected was then redefined as zero and another fine step scan was conducted from  $\pm 1^\circ$  of this position in  $0.1^\circ$  steps; again the peak position was redefined if necessary and this became the  $\theta = 0^\circ$  position. The detector would then move out of the beam to the  $4^\circ$  resting position to await the beginning of an experimental scan.

The assumption that the beam intensity profile is Gaussian in form is used in this zeroing procedure.

The first optical element carried by the detector rotation stage was the analysing polariser, a Glan-Taylor prism, which was aligned to analyse either the horizontal,  $\phi_A = 0^\circ$ , or vertical polarisation,  $\phi_A = 90^\circ$  component of the scattered light for a given scan. Following the analyser was a 5 mm entrance aperture of the detector housing. The detector housing is a sealed tube containing (in order), an achromatic lens, a 1 mm diameter aperture stop, a diffuser and finally the vertically mounted photomultiplier tube. The achromatic lens with the aperture at the focal point of the lens is positioned to limit the scattered light to  $\pm 0.3^\circ$  of the scattering angle. This small acceptance angle is important for minimizing the forward scattering bias at small angles. A large area diffuser is positioned between the aperture stop and PMT to spread the initially focused beam over the active area of the PMT and reduce the effects of PMT polarisation dependence.

### 3.3.2 SIGNAL DETECTION

The signal from the photomultiplier passed through a variable (resistor) voltage divider that pre-scaled the photomultiplier output before the signal went into the lock-in amplifier. This pre-amplifier circuit converted the current output of the photomultiplier to a voltage that was within the limits of the lock-in amplifier input range. The lock-in amplifier used a chopper to provide the lock-in frequency, 80 Hz, that was never changed. The sensitivity of the amplifier was changed manually as the detector was moved to a new position. Changing the sensitivity range of the lock-in amplifier was the main means by which the two to three orders of magnitude in signal variation across the angular scan were resolved. In a series of calibration and smoke experiments the sensitivity of the lock-in amplifier was usually the only parameter in the detection circuit that was changed.

The output signal from the lock-in amplifier was then passed through a simple voltage divider to the analogue-to-digital converter (ADC) in the controlling computer. The voltage divider was required because the lock-in amplifier output range (1-10 V) was not compatible to that of the ADC (1-25 mV).

### 3.3.3 STRAY LIGHT AND BACKGROUND

Stray light adds to the scattering signal in unwanted ways so the best solution was to avoid it when ever possible. Generally, the largest amounts of stray light are easily identified when they cause large peaks in the scattered signal that are not in agreement with expected results. Other causes of stray light include obstructions and marks on the glass walls of the LAOF scattering section. These are easily identified as minima in the scattering signal where none are expected or have jagged angular behaviour as opposed to smoother transitions observed in scattering by the particle clouds. The use of the circular cross section of the scattering section helps to reduce the refractive effects. One effect of refraction is negligible loss of light refracted out of the detector's view or conversely some collection of light; these processes are ignored in this study. Polarisation dependence of refraction and reflection are most noticeable for small scattering angles, resulting from light scattering by the entrance window and the tube that held it to the LAOF central section. The small acceptance angle of the detector acts to reduce the amount of off axis light making its way to the detector and contributing to the scattered signal. The main problem with stray light in the LAOF is in the forward angles,  $\theta < 10^\circ$ , where two effects contributed substantially to the stray light. The first is light generated by the laser plasma, which is seen as specular reflection of a blueish halo about the actual laser beam. This was reduced by painting an entrance aperture on the entrance window about 5 mm x 5 mm. The second and harder effect to reduce was the effect of laser beam and residual plasma light scattering off the entrance window and then the walls of the tube holding the window. These contributions to the stray light in the

forward direction meant that detector operation was not possible at  $\theta \leq 4^\circ$ . Measuring the background and subtracting it from the scattering signal caused by aerosol particles reduced this entrance window effect. A scan of the background light was made before a set of experiments, at both polarisations for all angles. Background light levels were noted to be greatest near the entrance window at angles of  $\theta = 5 - 15^\circ$ . The detected scattering signal before data reduction is denoted as  $U_s(\theta)$ . This background signal,  $U_b(\theta)$ , can then be subtracted from the detected scattering signal to give,  $U(\theta) = U_s(\theta) - U_b(\theta)$ .

### 3.3.4 SCATTERING VOLUME CORRECTION

As the detector scans through the scattering angles, the scattering volume changes in proportion to  $1/\sin(\theta)$ , which is due to the beams defined by the detector view and the incident beam. This angular dependence is contained in the detected signal and results in more than a factor of 10 change in the detector's view of the scattering volume as the scattering angle increases from  $5^\circ$  to  $90^\circ$ . To correct for this angular dependence in the background-corrected detector signal,  $U(\theta)$ , the volume corrected detector signal is determined by multiplying by a factor of  $\sin(\theta)$ . The volume corrected detector signal is denoted by  $u(\theta) = \sin(\theta)U(\theta)$ .

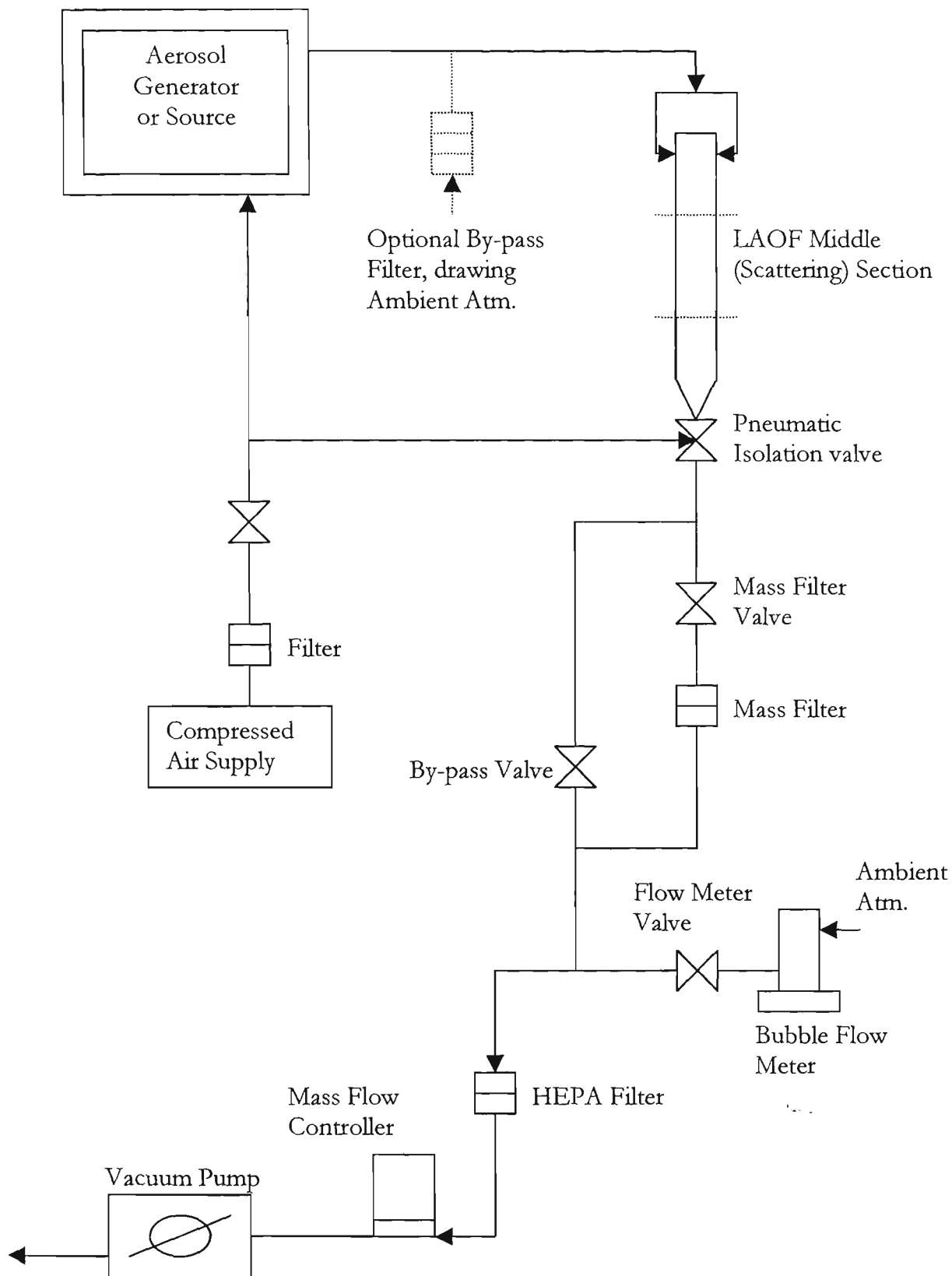
The corrected detector signal then has to be scaled to the differential mass scattering cross section by means of a calibration. This calibration is the subject of the next chapter, where the uncertainties in the scattering results are also examined. The procedure used to measure the scattering signal of an aerosol is detailed in the **Appendix A1**, since this procedure was the same for all aerosols. The following section is a description of the aerosol transport and generation, this aspect of the apparatus changes with the aerosol under investigation.

### 3.4 AEROSOL TRANSPORT

A system of pressurized air and controlled flow vacuum are the driving mechanisms for the aerosol transport through the LAOF. A vacuum pump is attached to the bottom of the LAOF and draws the aerosol and dilution (or make-up) air into the system. More importantly, the flow-controlled transport allows the time averaged mass concentration of the aerosol to be determined. This is a key point in this study that will be presented in detail in the following calibration chapter.

**Figure 3.2** is a schematic of the aerosol transport circuit of the LAOF. The flow rate of the vacuum is controlled by a mass flow controller, which is set to a flow rate of about  $1.67 \times 10^{-4} \text{ m}^3 \cdot \text{s}^{-1}$  ( $10 \text{ L} \cdot \text{min}^{-1}$ ). The laboratory compressed air line is cleaned with a high efficiency particle filter (HEPA) and tapped at a manifold with multiple outlets. The air is used to drive pneumatic valves, supply air to aerosol generators such as nebulisers, and to supply dilution air at metered rates before the aerosol enters the LAOF. The different means of generating the aerosols used in this study are summarised below and discussed in more detail in the chapters presenting results on particular aerosols. In general a transport line of diluted aerosol is connected to the LAOF at the top of the glass section. This flow enters the upper glass section at two directly opposing sides of the glass cylinder to aid even distribution of the aerosol in the LAOF, see **Figure 3.1**. The aerosol under consideration then flows down through the LAOF glass column. The lowest section of the LAOF has various valves that allow the LAOF to be isolated, or to divert the flow through or around a filter, see **Figure 3.2**. This filter is used to collect mass samples of aerosol. The mass of the filter together with the flow rate through the system is used to determine the mass concentration in the LAOF. This is then used to determine the mass scattering cross section, see **Equ. 2.29**. The HEPA filters used for this purpose are 47 mm polyfluorocarbon filters with a capture efficiency of at least 99.99 %. The bypass and filter valves allow the flow to either

Figure 3.2: A Schematic of the aerosol transport circuit.



pass through or around the filter. Bypassing the filter is used when drawing aerosol into the LAOF or for removal of aerosol if the generator is shut off. When the aerosol source or generator is shut off clean make-up air is drawn through the LAOF. Either the laboratory air supplies the make-up air or an optional HEPA filter is used to clean ambient air that is drawn into the LAOF. The optional ambient filter also helps to avoid accidental positive or negative pressures in the LAOF. Another valve combination (isolation valve closed and flow meter valve open) isolates the LAOF and allows the vacuum to draw in ambient air bypassing the filter: this line is used to check the vacuum flow rate of the path with a bubble flow meter (Gilibrator-2 Primary Flow Calibrator, Gilian Instruments Inc.). In this manner the mass flow controller can be checked and adjusted as required before an experiment is commenced. At the end of an experiment the mass flow rate is recorded along with the mass collection time, for determination of the mass concentration of the aerosol in the LAOF. The gravimetric methods of mass concentration measurement are dealt with in the following chapter.

These general operational aspects of the LAOF are simple to deal with and form the basic housekeeping of the operation of the facility. The following section summarises the methods of generating the aerosol under investigation in this study. More specific detail is given in the results chapters pertinent to a particular smoke or nuisance aerosol.

### **3.4.1 SUMMARY OF AEROSOL GENERATION METHODS**

Four types of aerosol particles were examined in this study: polystyrene spheres, smoke particles produced by non-flaming fuels, smoke particles (soot) produced by flaming fuels and nuisance aerosols. For each type of aerosol there was a different generation system and transport system.

In the case of the polystyrene spheres an aerosol generator was constructed and connected directly to the LAOF. This aerosol generator was mainly used for calibration to compare the measured scattering results with Mie theory calculations for the monodisperse polystyrene spheres. When this calibration aerosol generator was used, an optional make-up air filter was used (**Figure 3.2**) and pressurised air was supplied to the generator to operate a nebuliser. A full discussion of the polystyrene aerosol generator is given in the following calibration chapter. The rest of the aerosol transport system was the same as that shown in **Figure 3.2** above.

#### **3.4.1.1 Fuels used to generate smoke and nuisance aerosols**

The smoke aerosols from non-flaming fuels (beech wood, cotton lamp wick and polyurethane), nuisance aerosols (cooking oil, burning toast and ISO fine dust) and soot from two flaming fuels (propylene and heptane) examined in this study were generated in the Fire Emulator/Detector Evaluator (FE/DE) (Cleary et al., 2001; Grosshandler, 1997) shown in **Figure 3.3**. Two other soots from the fuels ethylene and acetylene were generated using a co-flow laminar burner attached directly to the LAOF. This was the same burner used in previous studies (Samson et al., 1987; Mulholland and Choi, 1998).

The non-flaming fire generated smoke aerosols include a forced pyrolysis of beech wood and self-sustained smouldering of cotton lamp wicks. Both of these fuels are test fire fuels used in standards EN54 and UL217 (EN54, 1982; UL 217, 1993). The polyurethane is cut from a seat cushion of a normal living room armchair and is fire retarded. Its mode of non-flaming fire is assumed to be smouldering and a hot wire inserted into the foam is the ignition source. These fuels and the conditions under which they were ignited to generate smoke aerosols are discussed in **Chapter 5**. Three gaseous fuels (propylene, acetylene and ethylene) were used to generate soot using a co-flow laminar burner. In the case of the propylene the burner was attached to the FE/DE while the other two fuels used a different burner attached to the

LAOF. For liquid heptane a small pool fire was ignited in a petri dish in the FE/DE. The details about these flaming fuels and their smoke generation will be discussed further in **Chapter 6**.

Two of the nuisance aerosols result from forced pyrolysis, namely the burning toast and the overheated cooking oil. Both are aerosols that cause frequent alarming of smoke detectors in or near kitchens. The third nuisance aerosol is ISO Fine dust, also called Arizona Road Dust, which is predominantly  $\text{SiO}_2$  (75 % to 90 %), but has main trace elements of  $\text{AlO}_2$  (10 % to 5 %) and  $\text{FeO}_2$  (>5 %) as well as smaller amounts of other metal oxides. This is the only irregularly shaped nuisance aerosol examined in this study. The nuisance aerosols will be discussed in more detail in **Chapter 7**.

#### *3.4.1.2 Fire Emulator/Detector Evaluator and aerosol sampling*

The Fire Emulator/Detector Evaluator (FE/DE) is a facility designed to emulate the smoke of a fire for fire detector assessment (Grosshandler, 1997). The operating principle of the FE/DE is that of a single pass wind tunnel, into which a smoke or nuisance aerosol is released. A test sensor section contains smoke detectors and instruments to measure various parameters including the light transmission through the generated aerosol, the air velocity (typically  $0.2 \text{ m}\cdot\text{s}^{-1}$ ), temperature, and response of a measuring ionisation chamber (MIC). A sampling line was inserted into this section to sample smoke and nuisance aerosol for transport to the light scattering apparatus. The sampling was done at a flow velocity of about  $8.7 \text{ m}\cdot\text{s}^{-1}$  for samples used in light scattering experiments. The sampling was carried out at a height of 50 mm below the top of the sensor section duct, which had a height of 300 mm. Transport of the aerosol relied on drawing an aerosol sample into a  $0.2 \text{ m}^3$  drum, see **Figure 3.4**. In this study about  $0.12 \text{ m}^3$  of smoke was drawn at a rate of  $3.3 \times 10^{-4} \text{ m}^3\cdot\text{s}^{-1}$  ( $20 \text{ L}\cdot\text{min}^{-1}$ ) into the drum. The drum transport of the aerosols was necessary since the LAOF and the FE/DE were in different laboratories on different floors of the building. Once the

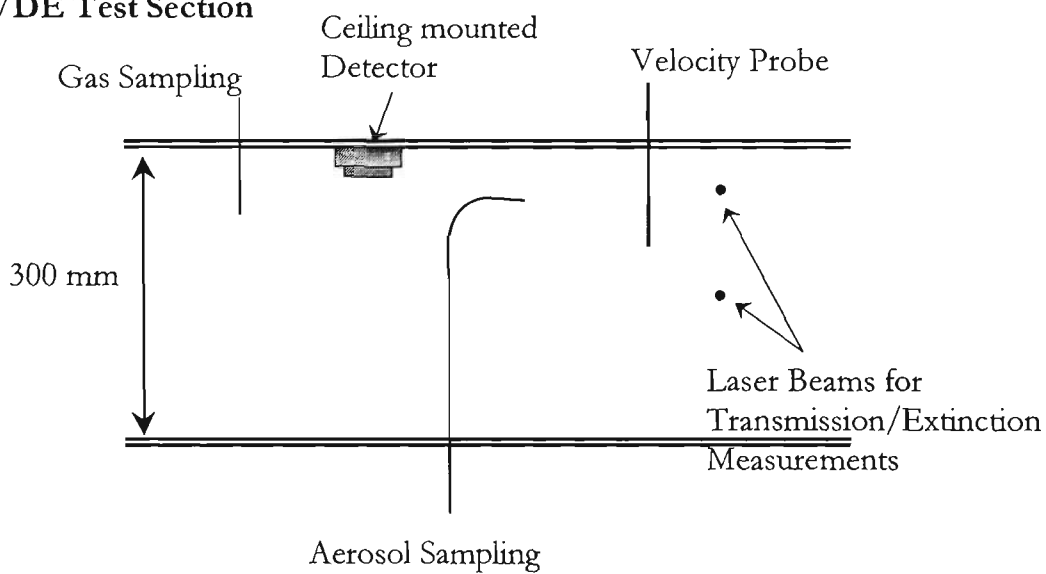


drum was filled with its sample of aerosol it was transported to the laboratory in which the LAOF was situated. The drum was then connected to the LAOF via its outlet valve and the inlet valve had a filter attached through which clean make-up air would enter the drum. The drum collection method results in some settling of larger particles and wall losses in the drum. Settling of particles mainly affects those bigger than about 3  $\mu\text{m}$  and some coagulation growth or aging of the particles in the drum also occur. Affects on the volume or mass of the smoke particles, to which light scattering is sensitive, is small in comparison with the aging effects on number concentration (Lee and Mulholland, 1977). Another side effect of using the drum for aerosol transport was that drawing the aerosol into the LAOF would slowly deplete the mass concentration. The effect of this on the scattering signal and mass concentration measurement is dealt with in more detail in later chapters.

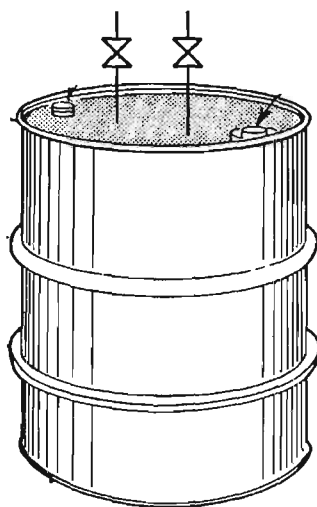
In the case of two flame-generated soots from acetylene and ethylene the FE/DE was not used. These soots were generated using a laminar co-flow burner of the type described by Samson et al. (1987) and later changed by Mulholland and Choi (1998). The laminar burner produces a steady thread of soot at its centre that is mixed with air at a tripper plate. A small amount of the soot is passed into a diluter, where a mass controlled amount of make-up air is added to the soot flow. This flow is then drawn into the LAOF for the light scattering measurements.

Figure 3.4: FE/DE test section and aerosol transport system.

FE/DE Test Section



FE/DE generated smoke and nuisance aerosol transportation system (The Drum)



## CALIBRATION

### 4.1 INTRODUCTION

#### 4.1.1 HISTORICAL OVERVIEW OF CALIBRATION METHODS

A crucial element of this study is the calibration of the light scattering apparatus. A relatively simple method has been developed that provides perhaps the most useful form of light scattering measurements: the differential light scattering cross section per mass concentration of the aerosol. The two main features of the calibration technique are light scattering by particles of known size and a gravimetric measurement. The former are polystyrene spheres whose scattering characteristics can be determined exactly from Mie theory. The latter enables optical scattering properties to be determined per unit mass. This is of particular interest to those who are working on problems of light scattering by a given aerosol concentration, such as smoke detector designers and those trying to estimate the visibility through smoke. The characteristic light scattering property measured in this study is the differential mass scattering cross section,  $\sigma(\theta)$  [ $\text{m}^2 \cdot \text{g}^{-1} \cdot \text{sr}^{-1}$ ] (Sec. 2.4).

An early study by Prichard and Elliot (1960) developed a method that used an accurately characterised device to reflect a known amount of light from the incident beam, as it was moved through the scattering volume. The calibration constant is then given by the ratio of the theoretical and measured reflection result. Thus their calibration is in terms of the absolute irradiance (intensity). They reported their findings in terms of the differential volume scattering coefficient (common to atmospheric aerosol studies) and dimensionless scattering matrix components. The use of polystyrene spheres in light scattering experiments did not become commonplace until the late 1960's or early '70s. Their use has usually been limited to testing systems by comparison with Mie theory, not explicitly as calibration particles. Studies examining the Mueller or intensity scattering matrix (Hunt and Huffman,

1973; Perry et al., 1978; Thompson et al., 1980) have used polystyrene spheres but focused on the angular distribution of the normalised scattered signal and not absolute intensity calibration. Their approach was motivated by intensity scattering matrix measurements for which normalised (dimensionless) intensity is sufficient. These studies have used polystyrene spheres to confirm the operation of their instrument and the primary calibration is based on an optical element of known Mueller matrix e.g. a reflector or retarder. For example, Thompson et al. (1980) used a suspension of polystyrene spheres in a liquid as well as a single sphere electrostatically suspended to compare their fast Mueller matrix measuring instrument response to Mie theory. The actual calibration was aimed at polarisation measurements and based on different optical devices such as a rotating polariser or quarter wave-plate retarder. Other light scattering studies (Pinnick et al., 1976) have made use of polystyrene spheres but not absolute intensity calibration. One study of note from a smoke characterisation point of view is that by Loepfe et al. (1997) who have used polystyrene spheres to test their light scattering apparatus and inverted the data to determine the polystyrene spheres size distribution. Meacham and Motevalli (1992) made use of atomised propylene glycol to evaluate their instruments performance but not to obtain absolute results as they reported only scattering detector signal (volts) for their smoke characterisation.

Another method of calibration makes use of the Rayleigh scattering properties of gases (Sivathanu and Faeth, 1990; Charalampopoulos, 1992; Sorensen et al., 1992). Usually the laser power is high, about 2 watts, or the refractive index of gas is large such as Freon (Sachweh et al., 1995). Laser diagnostics of soot in flames have either used nitrogen, oxygen or the fuel gas as the calibration gas. Sorensen et al. (1992) have used calculated Rayleigh ratios for three fuel gases and compared this with the measured scattering signal at  $\theta = 20^\circ$ . A plot of these quantities is expected to be linear and give the calibration constant as the slope of the line, which is the scaling ratio between experiment and theory. Koylu and Faeth

(1994a; 1994b) make comparisons between experimental results for Rayleigh scattering by nitrogen and the exact theoretical results, using published optical properties of nitrogen. They found a difference of about 10 % between experimental and theoretical results, and determined that the experimental (expanded) uncertainty due to the optical system was about 20 %. The Rayleigh scattering based method gives absolute cross sections [ $\text{m}^2$ ], from which the scattering cross section in terms of the mass of scattering aerosol can be determined given a mass measurement of the aerosol under consideration.

A series of studies by Holland et al. (Holland and Draper, 1967; Holland and Gagne, 1970; Holland, 1980) determined the scattering from irregular particles in terms of the differential mass scattering cross section. Their work aimed at investigating the correlation between Mie scattering and that of irregularly shaped randomly orientated particles. Holland et al. made use of Pritchard and Elliot's (1960) method for absolute intensity calibration and determining the mass concentration of the jet of particles passing through their scattering volume. The first study (Holland and Draper, 1967) determined the mass of the scattering particles by determining the mass expended during an experiment. This was facilitated by the fact that their aerosols were an easily weighed talc powder. They accounted for fluctuations in this mass flow by monitoring variations using another scattering channel. A later study (Holland and Gagne, 1970) used a more advanced and complex means of measuring mass distribution in the jet. They accomplished this by mapping the jet velocity field then determining the mean aerosol mass concentration in the scattering volume in terms of the axial jet velocity in that volume and the mass flow rate of the jet. The scattering measurements of Holland et al. were in terms of the differential mass scattering coefficient.

#### 4.1.2 CALIBRATION OVERVIEW

Our calibration method is a simple process. The scattering from a known aerosol is measured along with its average mass concentration during the scattering measurement. The

experimental result is scaled to the theoretical result for the calibration aerosol. Polystyrene spheres are the best calibration particles for this purpose, as they are available in various sizes from commercial manufacturers and are well characterised (Marx and Mulholland, 1983; Mulholland et al., 1985a). The scattering by polystyrene spheres is calculated from Mie theory. This is also the necessary theory since the laser power and wavelength used in this study are not suitable for Rayleigh scattering measurements. A benefit of the method developed here is that it is application to light scattering systems based on laser diodes, which currently operate at the longer visible and infrared wavelengths.

Determination of the mass concentration is accomplished by a gravimetric means. Knowing the flow rate of calibration aerosol onto a pre-weighed high efficiency filter, the collection time, and the collected mass gives the average mass concentration during the collection period. The collection period is the time it takes to measure the angular scattering of calibration aerosol at the two polarisations VV and HH, about 12 minutes at a flow rate of  $1.67 \times 10^{-4} \text{ m}^3 \cdot \text{s}^{-1}$  ( $10 \text{ L} \cdot \text{min}^{-1}$ ). The mass of polystyrene spheres collected was usually about 0.2 mg to 0.5 mg and weighed with a balance having microgram sensitivity.

The following sections describe in more detail the theoretical basis of the calibration, the methodology of the calibration particle preparation and mass concentration measurement. A calibration verification process has been used to test the calibration and determine the best means of determining the calibration constant. This calibration verification is analogous to calibration of a microscope's image scale by a particle of known size. The calibration verification has also been used to assess the uncertainties of making light scattering measurements. The second half of this chapter is largely dedicated to the uncertainty analysis.

## 4.2 CALIBRATION THEORY

To scale the detector signal to the differential mass scattering cross section, a calibration constant needs to be determined. The calibration constant,  $K$ , is determined by scattering light from the calibration particles and normalising the detected signal by the theoretical result for these particles. The detector signal is the result of scattering by a cloud of particles. Instead of the number concentration of the cloud we are making use of the mass concentration to reduce the data (Sec. 2.4.1). Mathematically,

$$K \equiv \frac{u(\theta)}{M\sigma_{th}(\theta)}, \quad (4.1)$$

where  $M$  is the average mass concentration of the scattering particles determined from measurements made by a gravimetric method (Sec. 4.3.1.2). The scattering signal from the aerosol in the scattering volume is measured by the volume corrected detector signal,  $u(\theta)$  (Sec. 3.3.4). The theoretical value,  $\sigma_{th}(\theta)$ , is derived from the differential scattering cross section which is calculated for a single calibration particle using Mie theory (**note:**  $\sigma_{th}(\theta) = \sigma_{msca}(\theta)$  in Sec. 2.4). The theoretical differential mass scattering cross section for a monodisperse collection of particles is expressed as,

$$\sigma_{th}(\theta) = \frac{\sigma_{sca}(\theta)}{V_p \rho_p}, \quad (4.2)$$

where the values  $V_p$  and  $\rho_p$  are the volume and density respectively of the calibration particles; the product of which is a single calibration particles mass. Mie calculations have made use of the FORTRAN program BHMIE of Bohren and Huffman (1998). The single particle mass is used in Equ. 4.2 since the calibration particles are monodisperse. That is to say their size distribution is a delta function (GSD = 0.987, see Sec. 2.2.1 and Table 4.1).

As outlined in **Equ. 4.1** the calibration constant is determined from a set of experimental data and a set of theoretical data for an ensemble of known particles. This data reduction was completed using three different least-mean-square methods (LMS or modified Chi-square). The first method used to determine the a calibration constant,  $K_1$ , was the standard LMS,

$$Q = \sum_{i=1}^N (E_i - K_1 T_i)^2, \quad (4.3)$$

which calculates the  $K$  that minimises  $Q$ ; i.e.  $dQ/dK = 0$ . In **Equ. 4.3** the experimental result is given by  $E_i = u(\theta_i)/M$  and the theoretical result by  $T_i = \sigma_{th}(\theta_i)$  for all data points  $i = 1, 2, 3, \dots, N$ . There are  $N$  discrete angular measurements in an experimental scan from  $\theta = 5 \dots 135^\circ$ . After minimisation, the calibration constant given by the standard LMS is,

$$K_1 = \frac{\frac{1}{M} \sum_i^N u(\theta_i) \sigma_{th}(\theta_i)}{\sum_i^N \sigma_{th}^2(\theta_i)}. \quad (4.4)$$

Two more calibration constants were determined using weighted least-mean-squared methods (WLMS), both aimed at reducing the dominance of the small angle scattering signal on the standard LMS estimate of **Equ. 4.3**. The first weighting was logarithmic and the other was sinusoidal. The calibration constants are given by,

$$\text{Logarithmic,} \quad \ln K_2 = \frac{1}{N} \sum_i^N [\ln(u(\theta_i)) - \ln(M \sigma_{th}(\theta_i))] \quad (4.5)$$

$$\text{Sinusoidal,} \quad K_3 = \frac{\frac{1}{M} \sum_i^N [u(\theta_i) \sigma_{th}(\theta_i) \sin(\theta_i)]}{\sum_i^N [\sigma_{th}^2(\theta_i) \sin(\theta_i)]} \quad (4.6)$$

Another method, the fourth, initially used (Weinert et al., 2001; Weinert and Mulholland, 2001) was based on an angular calibration function,  $K(\theta)$ , which mapped the experimental results directly onto the theoretical. However it was found that this function was not appropriate when applied to other aerosols. This was a consequence of minima in the calibration particle Mie results being heavily weighted and subsequently appearing in the experimental result of another aerosol. The angular average of this function was then used as the calibration constant, that is

$$K_4 = \langle K(\theta_i) \rangle = \frac{1}{NM} \sum_i^N \frac{u(\theta_i)}{\sigma_{th}(\theta_i)} \quad (4.7)$$

Thus four possible calibration constants are available after data reduction of the light scattering calibration. These four calibration constants were assessed to identify the most appropriate for this study by identifying the calibration constant with the lowest deviation from Mie theory.

In a normal series of experiments a calibration constant is determined from the scattering signal of the calibration particles for each polarization state,  $K_{VV}$  and  $K_{HH}$ . An experiment with an unknown smoke aerosol is then conducted where both the volume corrected detector signal,  $u(\theta)$ , and the mass concentration of aerosol particles,  $M$ , are determined.

The differential mass scattering cross section at a given polarisation is then,

$$\sigma_{VV}(\theta) = \frac{u_{VV}(\theta)}{M K_{VV}} \quad \text{and} \quad \sigma_{HH}(\theta) = \frac{u_{HH}(\theta)}{M K_{HH}}. \quad (4.8)$$

Here,  $\sigma_{VV}(\theta)$  and  $\sigma_{HH}(\theta)$ , are the measured differential mass scattering cross sections for vertical-vertical (perpendicular) and horizontal-horizontal (parallel) polarisations of the aerosol under examination. Quite simply they give the strength of the particle scattering at a

given scattering angle per mass of particles present in the scattering volume (Sec. 2.4). In this way the calibration has resulted in a means of determining in an absolute sense the differential mass scattering cross section [ $\text{m}^2 \cdot \text{g}^{-1} \cdot \text{ster}^{-1}$ ] of the aerosols under investigation. The experimental method of the calibration is described in the following sections and the four calibration constants are assessed. They are compared and the most appropriate method is then identified and applied to the smoke aerosol scattering data presented and discussed in later chapters.

### 4.3 CALIBRATION METHOD

#### 4.3.1 PROPERTIES OF CALIBRATION PARTICLES

Calibration of a light scattering instrument requires the use of a well-characterised calibration particle; polystyrene spheres are an excellent choice for this purpose. Polystyrene spheres are also called polystyrene latex spheres, which identify their means of production. The spheres are products of an emulsion polymerisation (O'dian, 1991) where water, a surfactant, styrene monomer and free radical initiator are mixed together. The emulsion polymerisation leads to a monodisperse pure polystyrene sphere colloid. The final size can be varied from as small as  $0.03 \mu\text{m}$  to as large as  $10 \mu\text{m}$ , by varying the reactant concentration and reactor conditions. These particles are commercially available from a number of sources such as Duke Scientific Inc.

The experimental approach in this study is to perform a primary calibration of the LAOF to determine the calibration constants of the apparatus using polystyrene spheres. Verification of the calibration has been conducted by a comparison between Mie theory,  $\sigma_{\text{th}}(\theta)$ , and experimental results,  $\sigma(\theta)$ , for polystyrene spheres of a different size from that of the calibration particles. This section covers in detail the method used in the preparation of the calibration particles, as well as the measurements made to determine the mass concentration,

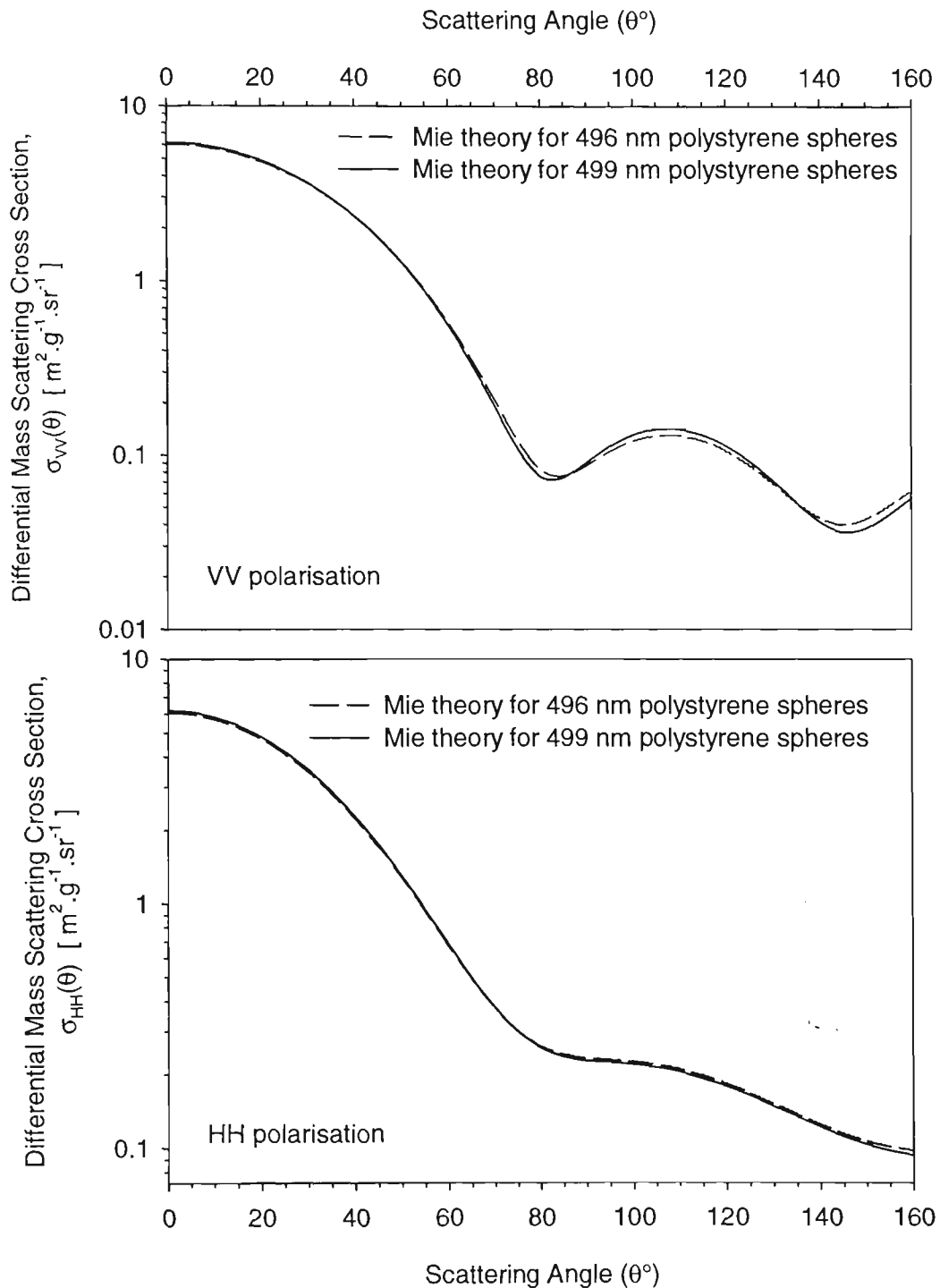
$M$ , of the calibration particles. The steps required to measure the scattered light signal,  $u(\theta)$ , are dealt with in **Appendix I**.

The calibration particles were polystyrene spheres of two different sizes, 496 nm and 499 nm in diameter. Two different sizes were necessary because the 496 nm diameter particles used initially stopped being manufactured. The specific characteristics of these nominally 500 nm diameter particles are shown in **Table 4.1**. This size is chosen because it is similar to that of smoke aerosols, but more importantly the Mie theory for this size and type of material shows that the scattering features have broad maxima and minima, see **Figure 4.1**. Another particle could have very sharp and deep features that would be hard for the detector to resolve due

**Table 4.1:** Physical properties of polystyrene (PS) spheres used in the calibration and verification experiments.

Physical Properties	Calibration Particles		Calibration Verification Particle
Nominal Diameter (nm)	500		800
Mean Diameter (nm)	$496 \pm 5$	$499 \pm 5$	$802 \pm 6$
Standard Deviation (nm)	6.5	6.5	9.6
Coefficient of Variation (%)	1.3	1.3	1.2
Density ( $\times 10^3 \text{ kg.m}^{-3}$ )	1.05		
Index of Refraction @ $\lambda = 632.8 \text{ nm}$	1.59		

**Figure 4.1:** Differential mass scattering cross section calculated from Mie theory for 499 nm and 496 nm diameter polystyrene spheres as an aerosol for polarisation perpendicular (VV) and parallel to the scattering plane (HH).



stray light, background signal noise, etc. This would also lead to higher uncertainties in the calibration constant near the scattering angles of those deep minimums. The difference in the Mie theory results for 496 nm and 499 nm diameter polystyrene spheres is as shown in **Figure 4.1**, with a maximum relative difference of about 12 % occurring at  $\theta = 75^\circ$ .

#### 4.3.1.1 Calibration Aerosol Generation

The first step in the calibration is the production of the calibration particles as an aerosol. The measurement of the light scattered from these particles is then made along with a measurement of the total mass of calibration particles passing through the LAOF. The data is then analysed to determine the calibration constant.

The mean diameter of the calibration particles, see **Table 4.1**, is the key component of the Mie calculations and is usually determined by the manufacturer using transmission electron microscopy (TEM) for the size ranges used in this study. The size measurement technique is traceable to the US National Institute of Standards and Technology through use of standard reference material (SRM) micro-spheres certified by NIST. These SRM particles are polystyrene spheres in suspension available in sizes of nominally 1000 nm and 100 nm (SRM 1960 and 1963 respectively) (Mulholland et al., 1985a; Mulholland et al., 1999). The other factor of importance in Mie calculations is the refractive index of the polystyrene spheres and this has been determined as 1.59 at 623 nm from comparison of experimental and theoretical results for single particle light scattering (Marx and Mulholland, 1983).

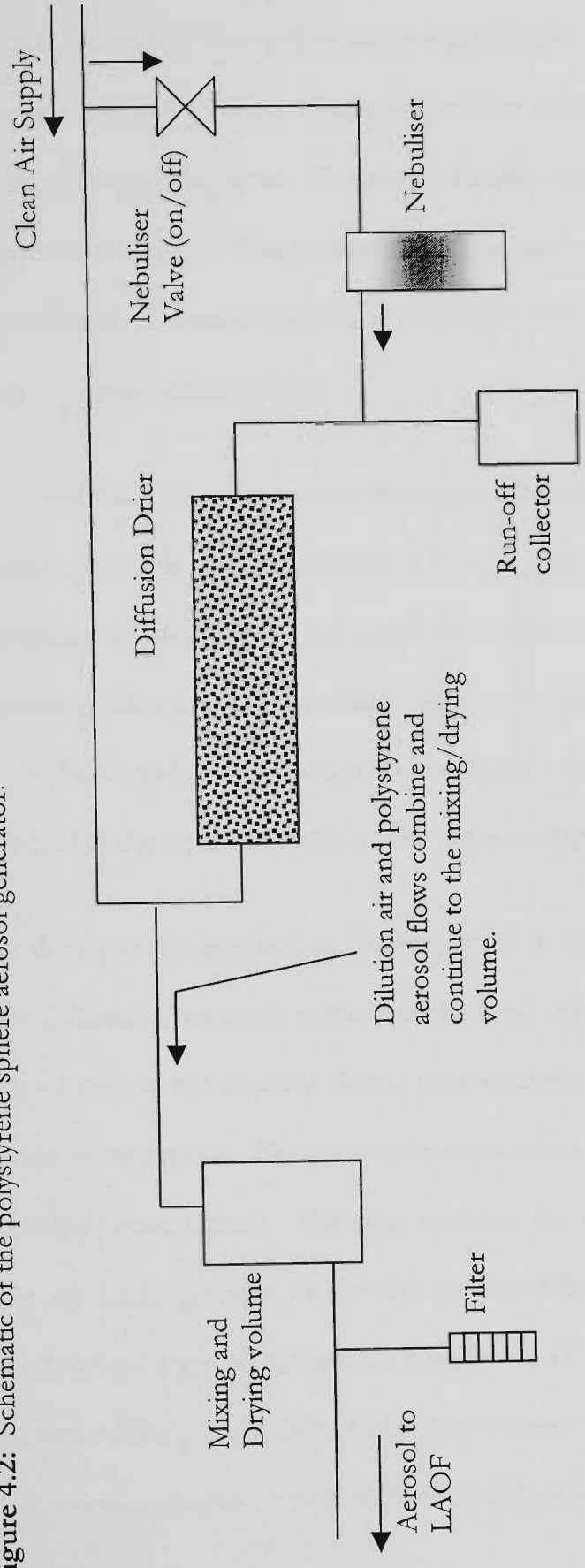
The density of the polystyrene material is  $1.05 \times 10^3 \text{ kg.m}^{-3}$  ( $1.05 \text{ g.cm}^{-3}$ ). The polystyrene spheres are packaged in an aqueous medium usually containing an anionic surfactant, which the manufacturer uses to ensure a high degree of dispersion and minimise agglomeration of the spheres. The spheres are contained in a 15 ml bottle with a drop-tip. The larger spheres do settle out of this solution when the bottle has been standing for some time, but the

solution is designed such that the spheres do not agglomerate after settling. They have a finite shelf life specified by the manufacturer.

To determine the calibration constant, the spheres must be introduced as an aerosol into the scattering volume where the incident laser light and particles interact. To do this the polystyrene spheres must be converted from an aqueous based suspension (hydrosol or colloid) to an airborne one (aerosol). The intermediate step in this process is to form droplets of water containing polystyrene spheres then to dry the water off of the spheres leaving an aerosol consisting of just polystyrene spheres. This is the standard means of producing an aerosol of polystyrene spheres followed in this study.

**Figure 4.2** show's a schematic diagram of the polystyrene aerosol generator used to produce both the calibration and calibration verification aerosol. The generator consists of a free air supply line that is split to supply dilution air and drive the nebuliser flow. An in-line valve to the nebuliser controls its on/off state. When the valve is closed only the clean air flows through to the LAOF with no aerosol. When the valve is open the nebuliser produces an aerosol spray. The nebuliser itself contains the polystyrene spheres in a dilute suspension of polystyrene spheres in particle-free (filtered with 0.22  $\mu\text{m}$  pore size filter) distilled and deionised water. This working suspension is produced by mixing between 30 and 40 drops, about 1 ml to 1.3 ml, of the polystyrene sphere base suspension and diluting it with 50 ml of filtered and de-ionised water. The working suspension was then briefly agitated in an ultrasonic bath for about 1 minute to mix the polystyrene spheres into the water, before being poured into a larger container (250 ml). This larger storage container was used to store the working polystyrene suspension so that a large quantity was at hand for multiple experiments. An amount of about 35 ml of the working suspension was poured into the clean reservoir of the nebuliser when a calibration aerosol was needed. **Figure 4.3** shows the nebuliser, which makes use of a Venturi effect to draw the polystyrene suspension into the jet

Figure 4.2: Schematic of the polystyrene sphere aerosol generator.



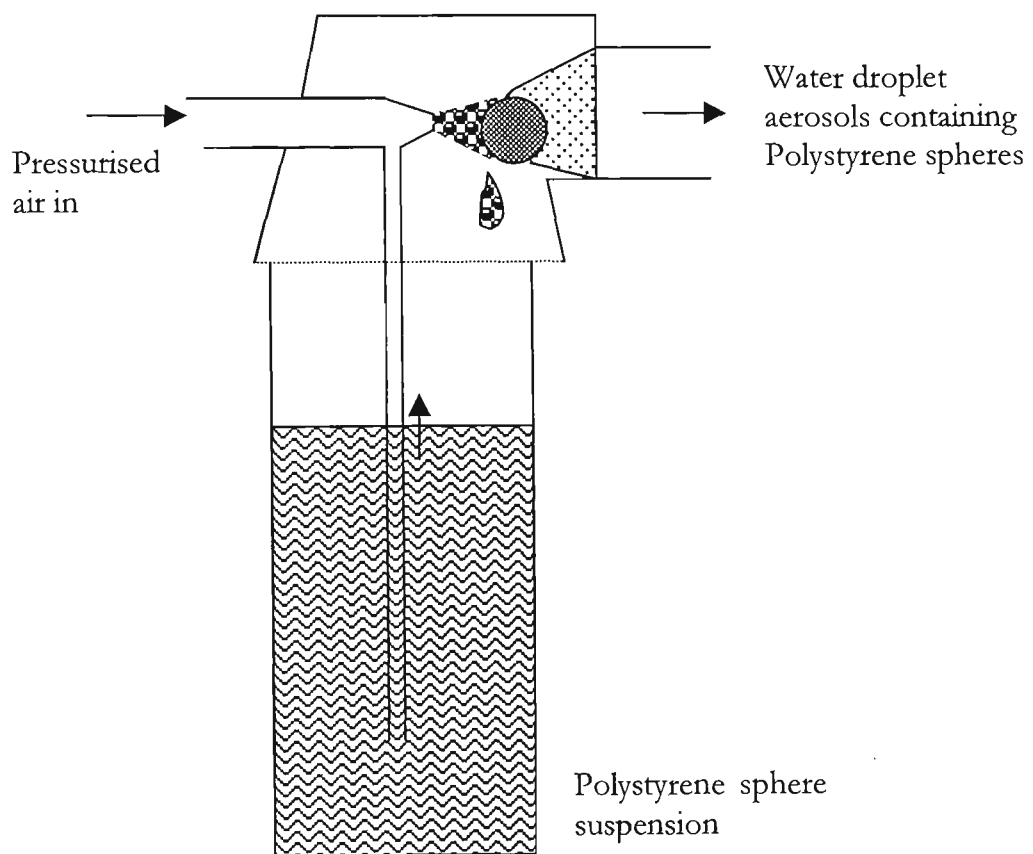
flow. The flow breaks up into droplets in the jet flow and is aimed at a small ball construction that acts like an impactor and removes larger droplet particles from the flow by impaction. There is a net airflow out of the nebuliser that contains water droplets which themselves contains polystyrene spheres. Some large droplets that fail to make the turn at the T-section impact on the walls. This polystyrene sphere and water mix then simply runs down the tubing walls into an attached bottle. The smaller droplets containing polystyrene spheres continue towards the diffusion drier.

To dry the water off of the polystyrene sphere, the entire nebulised aerosol is transported by the airflow through a diffusion drier, see **Figure 4.2**. The drier construction consists of a concentric arrangement of two cylinders, the centre one having a mesh wall. Between these cylinders is a granulated silica gel desiccant that creates a very low water vapour pressure in the centre tube. As the aerosol travels through the central tube, water vapour from the liquid droplets is transported to the region of lower vapour pressure, drying the particles.

The local vapour density is not constant as the amount of nebulised water and subsequent evaporation in the diffusion drier tends to increase the local ambient vapour pressure about the droplets. This increases the required drying time since the silica gel desiccant cannot instantly take up the water vapour. As operation time increases the desiccant itself starts to saturate with absorbed water vapour. This also increases the required residence time for drying. Typically for water particles of the size produced by the nebuliser the droplet life-time would be less than a second at a relative humidity of about 50 % (Hinds, 1982). The average residence time of the particle through the drier is about 0.7 seconds as the flow rate from the nebuliser was measured at about  $8.3 \times 10^{-5} \text{ m}^3 \cdot \text{s}^{-1}$  (5 L.min<sup>-1</sup>).

A fine mist of water particles can be seen coming from the exit of the diffusion drier as the drier saturates. To evaporate the remaining liquid a 3 L volume is connected to the end of

**Figure 4.3:** Schematic of the nebuliser used to produce an aerosol of water droplets containing polystyrene spheres.



the drier before the aerosol flow moves into the LAOF. A flow of dry (RH 10%) air joins the aerosol flow just before it enters the 3 L mixing and final drying volume and no water droplets are observed flowing out of this volume, see Figure 4.3. The dilution air flow rate is set to about  $8.33 \times 10^{-5} \text{ m}^3 \cdot \text{s}^{-1}$  (5 L.min<sup>-1</sup>) and the flow drawn through the LAOF runs at about  $1.67 \times 10^{-4} \text{ m}^3 \cdot \text{s}^{-1}$  (10 L.min<sup>-1</sup>). The flow from the nebuliser makes up the difference. Any excess aerosol from the generator is released via an overflow tee connection placed after the mixing volume; this overflow line terminates at a filter. Similarly, if the system air to the aerosol generator should be shut off while the LAOF is still running, then the filter allows clean airflow into the system so that there is no negative pressure builds up.

By the time the aerosol has left the mixing volume and entered the LAOF, the water in the droplets has evaporated leaving the polystyrene spheres as an aerosol. In a small fraction of droplets, the polystyrene spheres do not necessarily exist in the droplets as single spheres and it is possible that two or more spheres are in one droplet. This depends on the initial size of the water droplet relative to the polystyrene sphere size. Bigger droplets from the nebuliser result in a higher probability that it contains more than one polystyrene sphere, doublets, triplets etc. An optical microscope was used at a magnification of 100x to image particles collected by holding a clean glass microscope slide at the exit flow of the mixing volume. A survey of glass slides viewed under the microscope gives a doublet to singlet ratio of 0.065.

Once the aerosol of polystyrene spheres leaves the mixing/drying volume it enters the LAOF and is drawn down and through the scattering volume. Immediately after the scattering volume, the aerosol is drawn onto a filter for determination of the aerosol average mass concentration over the time of the experiment. The particulars of the scattering volume and the associated optics are covered in the earlier chapter, see Sec 3.3.4 and 3.3.1.

### 4.3.1.2 Mass Concentration Measurement

To determine the experimental differential mass scattering cross section,  $\sigma(\theta)$ , it is necessary to know the mass concentration in the scattering volume. The gravimetric method used determines the average mass concentration of the aerosol particles over the sampling time of the experiment. By measuring the mass of particles collected on a filter over a known time period and knowing the flow rate over the filter the average mass concentration [ $\text{mg}\cdot\text{m}^{-3}$ ] is given by,

$$M = \frac{\Delta w}{\dot{V}t}. \quad (4.9)$$

Here  $\Delta w$  is the weight of the aerosol collected on the filter,  $\dot{V}$  is the volumetric flow rate through the LAOF and  $t$  is the length of time the aerosol was collected on the filter. In most experiments the time period corresponds to an angular scan of the scattered light for two polarisation configurations (VV and HH), which is between 10 and 15 minutes of uninterrupted collection time. As noted in **Sec. 4.1.2**, the mass of aerosol samples weighed was typically in the range of 0.2 mg to 0.5 mg, and the standard uncertainty in the balance of  $\pm 0.005$  mg. This led to a relative standard uncertainty of about 2 %. The flow rate was determined with a bubble flow meter (Giliblator-2 Primary Flow Calibrator, Gilian Instruments Inc), at typical values of about  $1.67 \times 10^{-4} \text{ m}^3 \cdot \text{s}^{-1}$  (10  $\text{L}\cdot\text{min}^{-1}$ ), with a relative standard uncertainty of 2 %. The uncertainty in the time of aerosol collection is negligible compared with the other parameters. The relative standard uncertainty in the mass concentration measurement is about 3 %. This was obtained by combining in quadrature the relative standard uncertainties of the mass and flow.

Filters are weighed individually in batches before the light scattering experiment begins. A clean filter is kept and weighed periodically as a check as to the uncertainty in the weighing

process and to alert in case of any errors in operation. The filters themselves are circular, 47 mm diameter, polyfluorocarbon membrane supported by a second membrane of the same material (Zeflour<sup>TM</sup>). The filter pore size is 2  $\mu\text{m}$  and the filter is quoted by the manufacturer as having an aerosol retention of 99.99% for 0.3  $\mu\text{m}$  DOP aerosol at a flow rate to filter area ratio of 32 Lpm/100  $\text{cm}^2$ . The filters were stored in disposable plastic petri dishes. Stacking of these petri dishes was avoided after the filter was placed inside since it could result in electrostatic charges lifting the filters onto the inside of the lid of the petri dish. This in turn could mean the loss of some deposited particle mass.

Weight measurements (see **Appendix I**) were repeated three times for each filter when new (pre-weighing) and three times for each filter after aerosol collection. The three filter measurements were then used to determine an average weight, both an initial (clean) and final (collected particles). The mass of aerosol particles collected is given by the difference between the initial and final average weights. The aerosol mass is then used along with the measured flow rate through the LAOF and the time of aerosol collection to determine the average mass concentration during the sampling period.

## 4.4 LIGHT SCATTERING CALIBRATION MEASUREMENTS

### 4.4.1 METHOD

When the calibration aerosol is flowing through the LAOF and the laser is on, the scattering by the aerosol is visible to the eye due to the beam power and the large number concentration of polystyrene spheres, which is nominally  $10^3$  to  $10^5$  particles per  $\text{cm}^3$ . This has an advantage in that it is very easy to see whether the calibration particles are flowing through the scattering volume in a relatively uniform manner. The light scattering measurements are made as they are for any aerosol following the procedure detailed in **Appendix I**.

Once the light scattering measurements are made the data is reduced. The scattering volume,  $u(\theta)$ , and the average mass concentration,  $M$  [ $\text{mg}\cdot\text{m}^{-3}$ ], over the period of the calibration experiment, are used as outlined above to determine the calibration constants,  $K_1$  through to  $K_4$  (Sec. 4.2). In **Figure 4.4** experimental results shown have been scaled by applying the calibration factors,  $K_1$  and  $K_2$ , from standard and log weighted LMS respectively. In essence the experimental results shown in **Figure 4.4** are the result of a “best fit” applied to the corrected detector signal. The calibration constants were calculated from the scattered signal and then used to scale that signal data to the correct units of the differential mass scattering cross section. The analysis shown in **Figure 4.4** does act as a good check in the first instance of the scattering calibration.

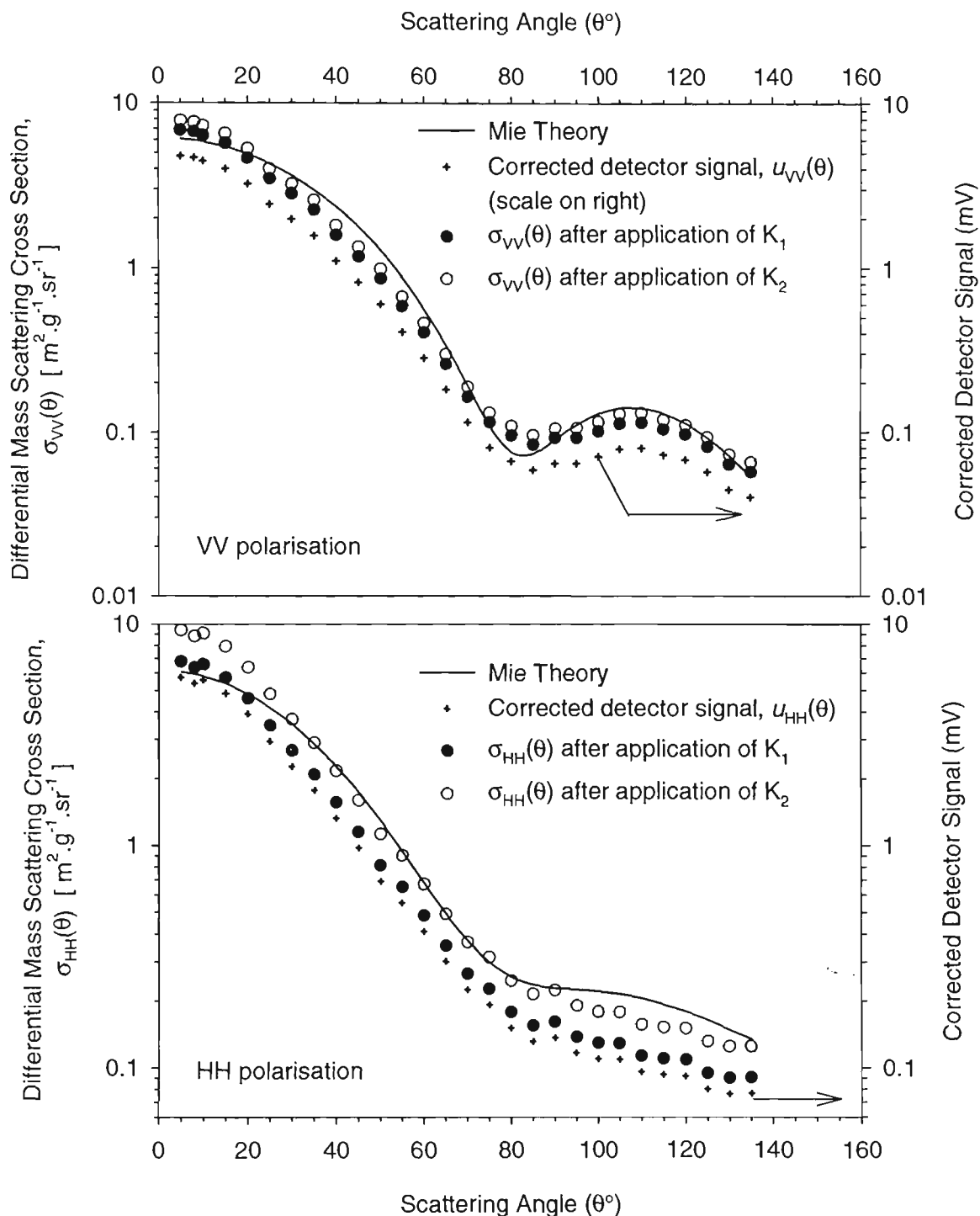
A verification of the calibration process is used to determine the calibration constants,  $K_1$  through to  $K_4$ , and then apply the calibration constants to the scattering signal of different polystyrene spheres, nominally 800 nm in diameter. The results of these verification tests are compared to the theoretical result and used to determine the best calibration constant of the four to be used in this study. The comparison with theory was also used to analyse the uncertainty in the scattering measurements. The calibration verification is discussed in the next section.

## 4.5 CALIBRATION VERIFICATION

### 4.5.1 METHOD

Applying the results of a calibration to polystyrene spheres of different diameter makes it possible to investigate the applicability of the calibration method and to assess the uncertainty in determining the differential mass scattering cross section. This section presents the method and results of a verification of the calibration experiments using nominally 800 nm diameter polystyrene spheres as the scattering particles. The calibration factors from the

**Figure 4.4:** Comparison of Mie theory and experimental results for 499 nm diameter polystyrene (PS) spheres at **a)** VV polarisation and **b)** HH polarisation. Two calibration constants used on the experimental results are the (1) standard and (2) log-weighted least-mean-square methods; they represent a best fit to the theoretical result. The graph is indicative of the variations of the experimental results about the theory and the differences in the two calculated calibration constants.



nominally 500 nm diameter polystyrene spheres are applied to the scattering results for these 800 nm diameter verification particles. These verification particles are as well characterised as the calibration particles themselves, see Table 4.1, and similarly Mie theory gives an exact result for the light scattering. This gives an excellent method of scrutinising the calibration method used in this study, and provides a means of assessing the method of LAOF operation to determine the differential scattering cross section per unit mass, for particles other than the calibration particle. The methods are the same no matter what aerosol is introduced into the LAOF and the only aspect that changes for different particles is the method of generation and their subsequent transport into the LAOF.

The calibration verification particles used in this study are 802 nm diameter polystyrene spheres. As with the calibration particles a suspension of 802 nm diameter particles was mixed with 50 mL of particle-free deionised distilled water at a dilution of about 2 % to 2.5 % polystyrene solution to water. Once this nebuliser suspension was prepared an aerosol of polystyrene spheres was generated as detailed above (Sec. 4.3.1.1). The light scattering measurements were then made as described for any aerosol in **Appendix I**.

#### 4.5.2 RESULTS

Analysis of the calibration data leads to four different calibration constants, but it is necessary to determine which of these calibration constants is the appropriate one to be used in this study. By investigating the deviation of the 802 nm diameter polystyrene spheres when compared with the exact result from Mie Theory the appropriate calibration constant can be identified: the criterion being that the calibration constant chosen should cause the smallest deviation from theory. This assessment made use of nine sets of calibrated 802 nm diameter experiments at both polarisations. This data as a whole is referred to as the “verification data set”, one for each calibration constant under consideration. The analysis of deviation of each

set with respect to the Mie theory result is accomplished by a least-mean-squared method.

This approach is helpful in the sense that it is the same as an uncertainty analysis.

The uncertainty analysis aimed at identifying the appropriate calibration constant, calculates the standard deviation of the verification data set about the Mie theory, such that

$$s(\theta) = \sqrt{\frac{\sum_j^m (\sigma_j(\theta) - \sigma_{th}(\theta))^2}{m-1}}, \quad (4.10)$$

where  $s(\theta)$  is the standard deviation of the experimental value,  $\sigma_j(\theta)$ , of the  $j$ th verification experiment about the theoretical value,  $\sigma_{th}(\theta)$ , at the scattering angle,  $\theta$ . The summation is over the number,  $m = 9$ , of experiments making up the calibration verification data set at a given angle. This results in a standard deviation as a function of scattering angle. The standard deviation function is computed for the each verification set determined by the four different calibration constants.

It is beneficial to define the angular average of the standard deviation relative to the theoretical value as,

$$\langle s(\theta) / \sigma_{th}(\theta) \rangle = \frac{1}{m} \sum_{j=1}^m \frac{s(\theta_j)}{\sigma_{th}(\theta_j)}. \quad (4.11)$$

Thus the relative standard deviation of the experimental about the absolute result is a single number, for a given polarisation.

In **Figure 4.5** the approximate 95 % confidence limit about the theory,  $\sigma_{th}(\theta) \pm 2s(\theta)$ , for each set of verification results generated by using different calibration constants is presented.

**Figure 4.5a** and **4.5b** present the polarisation results for VV and HH respectively. For

clarity twice the standard deviation is used instead of the single standard deviation. The HH plot has more clarity when graphically comparing the deviations associated with different calculation methods of the calibration constants. In the case of the VV plot the lowest confidence limit occurs about the minimum at  $\theta=110^\circ$ . Normally at this minimum, the detector fails to resolve the depth of the minimum. In **Table 4.2** the angular average of the standard deviation relative to the theoretical value,  $\langle s(\theta)/\sigma_{th}(\theta) \rangle$ , is shown for all the calibration analysis methods and polarisation settings.

**Table 4.2:** The angular average of the relative standard deviation,  $\langle s(\theta)/\sigma_{th}(\theta) \rangle$ , calculated for the different calibration constant methods.

Polarisation	Standard LMS	Logarithm weighted LMS	Sin( $\theta$ ) weighted LMS	Angular average
VV	0.245	0.195	0.205	0.185
HH	0.255	0.12	0.185	0.115

The logarithm weighted LMS method, **Equ. 4.5**, is selected for determining the calibration constant since it provides the lowest deviation from Mie theory of the other LMS likelihood estimates. It is curious that simply computing a calibration constant for each angle and then averaging the values produces  $s(\theta)$  almost identical to the Logarithm weighted LMS method.

With the appropriate method of determining the calibration constant identified, the results of a verification experiment can be compared directly with the theoretical result. **Figure 4.6** presents the results of a verification experiment conducted immediately after the calibration experiment in **Figure 4.4** and uses the calibration constant,  $K_2$ , from that experiment. Mie theory results are also present for comparison. A comparison of the experimental and

**Figure 4.5:** The 95 % confidence limits (standard deviation multiplied by 2) about the theoretical result for 802 nm diameter polystyrene spheres of the calibration verification sets for the different methods of calibration constant calculation. Only the HH plot shows all of the methods for clarity.

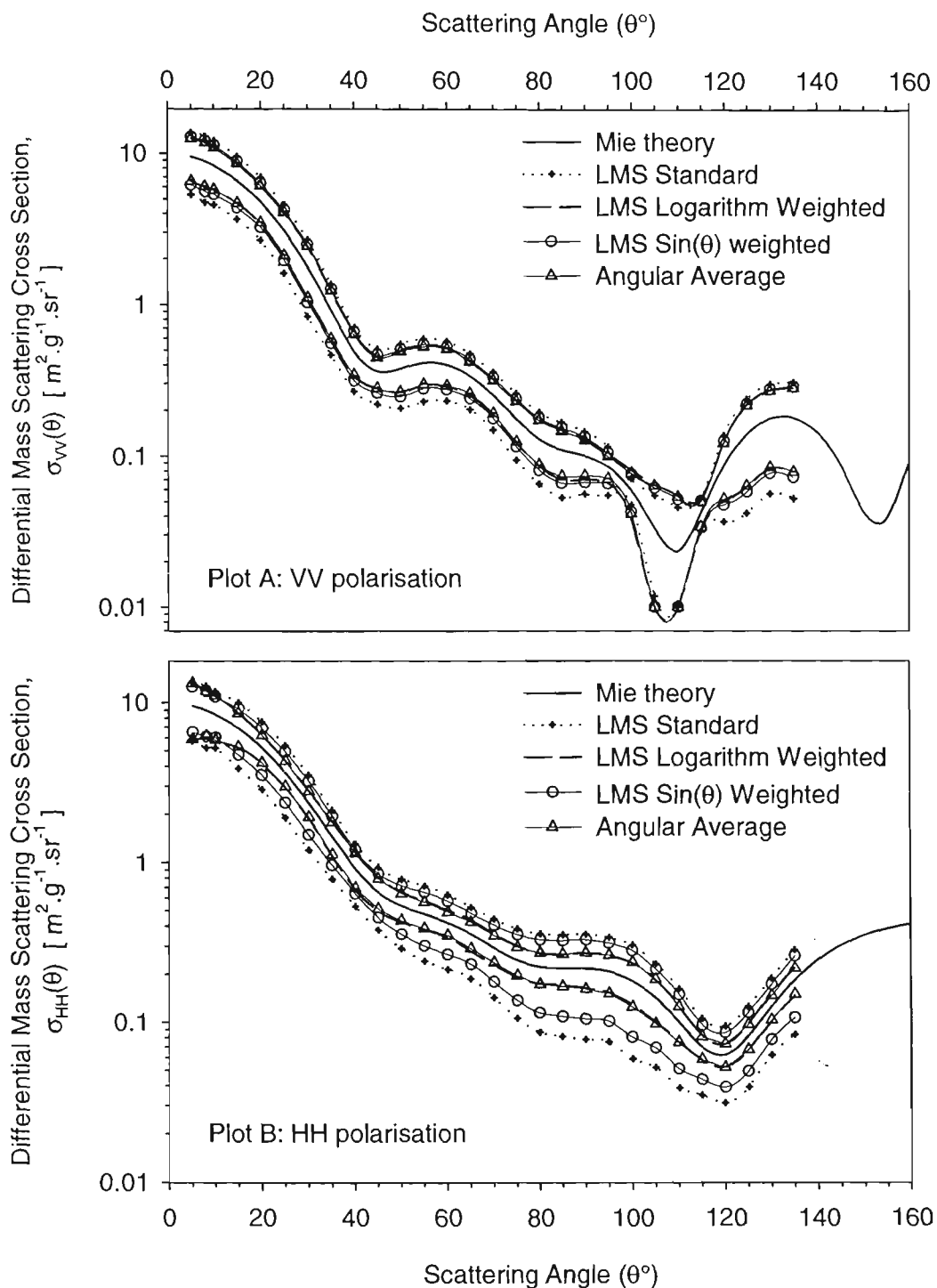
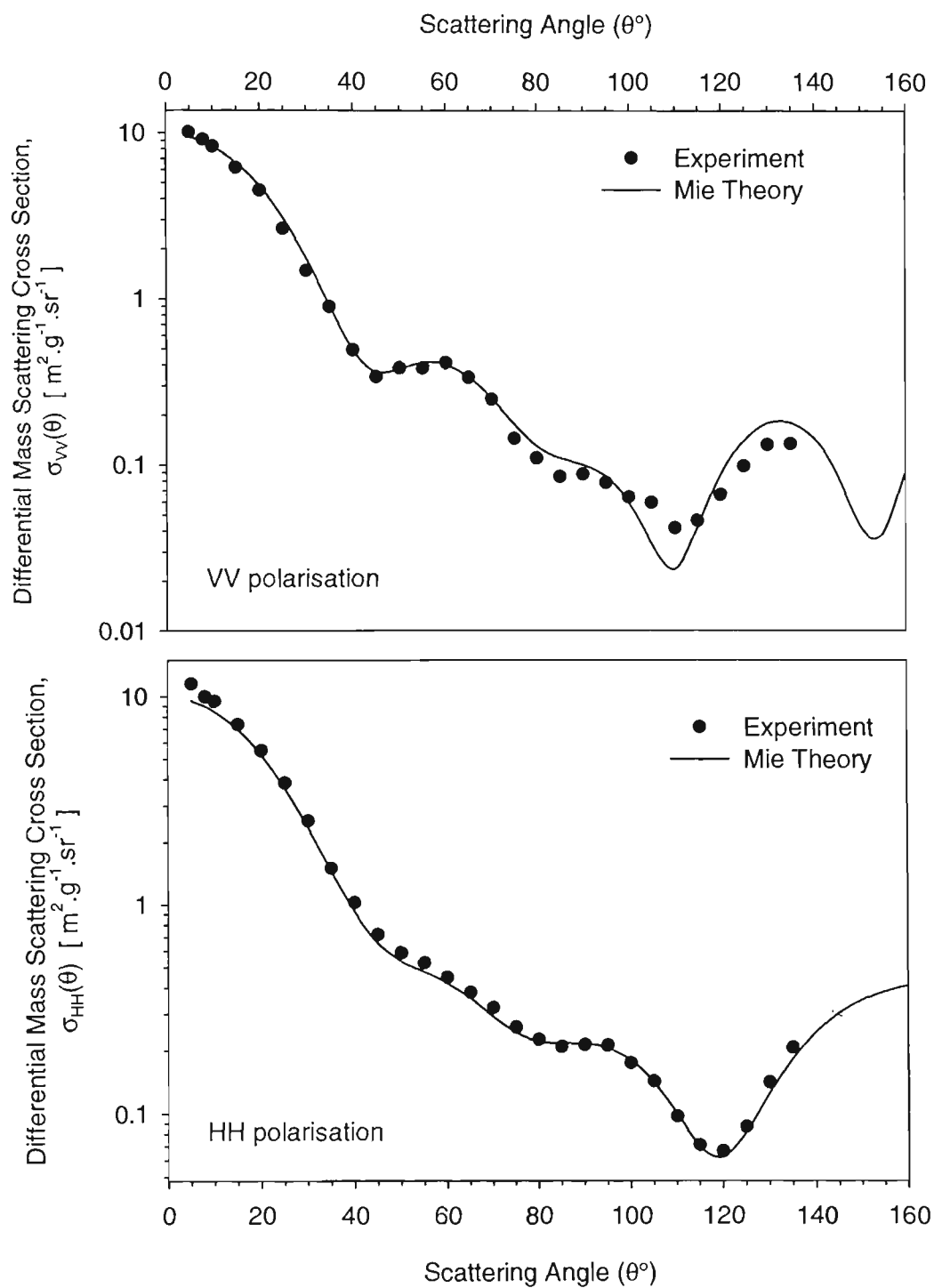


**Figure 4.6:** Results of a calibration verification experiment using 802 nm diameter polystyrene spheres along with the Mie theory results for comparison. The calibration constant applied was determined using the logarithm weighted LMS (i.e.  $K_2$ ).



theoretical results in **Figure 4.6** indicates that overall the calibration is good with the exception of the minimum at  $110^\circ$  for VV polarisation. To get a better understanding of the factors that influence measurement of  $\sigma(\theta)$  and quantifying the uncertainty in its measurement. A thorough analysis of the uncertainty is presented below.

## 4.6 UNCERTAINTY ANALYSIS

### 4.6.1 TYPE A AND TYPE B UNCERTAINTIES

The uncertainty analysis conducted here includes Type A and Type B uncertainties (Taylor and Kuyatt, 1993). The former is based on statistical methods of data assessment, the latter is based on a scientific judgment of the standard uncertainty using all relevant available information other than statistical analysis. That means that a Type B analysis makes use of various data sources including manufacturer information and previously published studies. As an example, a Type A analysis was used to identify the best method for computing the calibration constant, in **Sec. 4.5.2**.

The basic uncertainty presented in this study is referred to as the standard uncertainty of a measurement or calculated result. The following summarises the uncertainty evaluation used in this study and follows the NIST guidelines (Taylor and Kuyatt, 1993). Once all the component standard uncertainties are determined, the law of propagation of uncertainty, the “root-sum-of-squares” or quadrature rule is used to combine them. This combined uncertainty is then multiplied by an appropriate factor to specify a region of confidence about the measurand (the quantity to be measured) in which the measurements made are likely to actually be. The multiplier used in this study is 2, which gives approximately the 95 % confidence limits. Once applied the uncertainty is referred to as the expanded uncertainty. This study presents uncertainties as a relative uncertainty (a ratio, usually expressed as a percentage) about a mean measurement or theoretical result. In this study it is convenient to use an angular average over the scattering angles of relative standard

uncertainty, usually with respect to the calculated Mie result. This result is beneficial for two reasons: firstly it gives a direct comparison with the ideal result and secondly the detection system is not calibrated for absolute irradiance measurement but for the absolute Mie result.

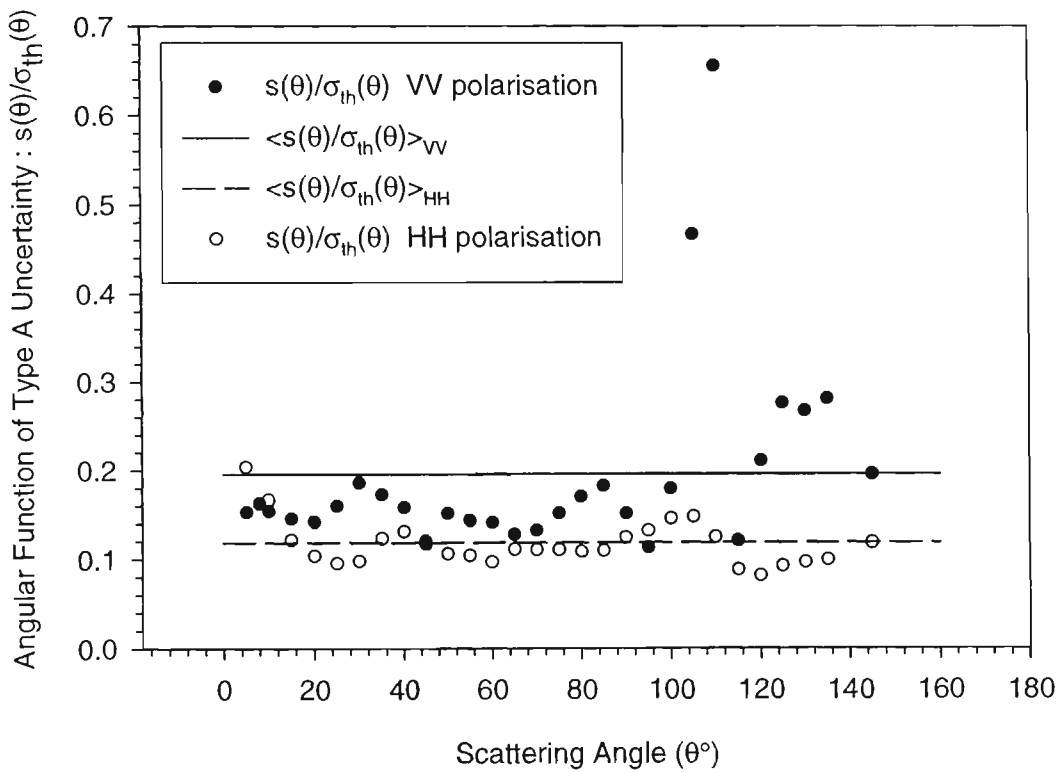
#### 4.6.2 UNCERTAINTY IN THE CALIBRATION VERIFICATION

Uncertainty in the calibration verification experiments is analogous to determining the uncertainty in an unknown aerosol generated and transported to the LAOF in the same manner as the calibration verification particles.

##### 4.6.2.1 Type A Uncertainty

As mentioned above the analysis used to determine the appropriate method of calculating the calibration constant is an uncertainty analysis. Specifically a Type A analysis as it is statistically based. The relative standard deviation is an angular function given by  $s(\theta)/\sigma_{th}(\theta)$ , where  $s(\theta)$  is determined by Equ. 4.11 and  $\sigma_{th}(\theta)$  is the Mie theory result. The relative standard uncertainty is defined as the angular average of the angular function, that is  $\langle s(\theta)/\sigma_{th}(\theta) \rangle$ . This result is a quantity that is easily compared with other uncertainties. However, the angular average results in a loss of detail that is important to the assessment of the factors influencing the uncertainty. In Figure 4.7 the angular function of the relative standard deviation has been presented so that the angular behaviour can be examined. One fact that becomes immediately apparent in Figure 4.7 is the outliers at  $\theta = 105^\circ$  and  $110^\circ$  in the VV polarisation data. These outliers are a result of detection system and size distribution uncertainties affecting resolution of the minima at  $\theta = 110^\circ$ . The value of the relative standard uncertainty has been determined as 19.5 % and 12 % for VV and HH polarisation settings respectively, see Table 4.2 and shown in Figure 4.7 as the solid lines. If the two outliers are removed from the VV verification data set and the uncertainty recalculated then the result is about 16.7 % relative to the Mie theory result. This is more

Figure 4.7: Plot of the relative standard deviation,  $s(\theta)/\sigma_{th}(\theta)$ , and the relative standard uncertainty,  $\langle s(\theta)/\sigma_{th}(\theta) \rangle$ , for both polarisations.



representative of the majority of the data points at angles  $\theta < 100^\circ$ . A difference exists between the HH and the VV uncertainties the cause of which will become more apparent after an uncertainty analysis of the components of the measurement are examined below.

The Type A uncertainty of the calibration verification data is an uncertainty that includes all of the uncertainties that go into that measurement. What has not been accounted for is the uncertainty in the theoretical calculations with which experiments are compared. The Type A and calculation uncertainties (Type B) will then be combined into the combined uncertainty.

#### *4.6.2.2 Type B: Polystyrene sphere uncertainty*

This section and the one following it, on the refractive index, examine the uncertainties associated with the characteristics of polystyrene spheres used in the Mie calculations. The basic assumption of the theoretical calculation is that a cloud of particles of the same diameter, 802 nm, scatters the light. In reality the particles passing through the scattering volume are distributed over a narrow range about a mean size close to 802 nm in diameter. The data supplied by the manufacturer, see **Table 4.1**, is used in this section as sensitivity data for the upper and lower bounds of the polystyrene sphere size. The data source means that it is a Type B uncertainty analysis. This is an important examination as all the verification data is compared with the scattering expected from single sized particles with a specific refractive index. These uncertainties have to be combined with the Type A analysis above, to account for the overall uncertainties.

The effects of widening the size distributions leads to averaging effects that reduce the depth of minima (Kerker, 1969; Holland and Gagne, 1970; Hobbie and Sung, 1996) that occur in single-sized particle scattering. This is due to integration over different sized particles present in the scattering volume. The effect of a narrow (monodisperse, in this case  $GSD = 0.988$ )

size distribution of polystyrene sphere used in this study will be less than the effect due to a wide (polydisperse, say  $GSD = 1.2+$ ) distribution. The Mie theory result is calculated for scattering over an ensemble of polystyrene spherical particles with a size distribution defined by the information in **Table 4.1**. Bounds of the size distribution effects are calculated using a mean size of the distribution that corresponds to a standard deviation either side of 802 nm. Therefore two cases made use of mean diameters based on the upper and lower limits of the size measurement uncertainty in **Table 4.1** (i.e.  $\pm 6$  nm) at the same standard deviation of the distribution,  $s_d = 9.6$  nm. Integration of the scattering signal over the size distribution was based on a Gaussian quadrature using Gausse-Hermite abscissa and weights (**Sec. 2.4.3**) (Press et al., 1995; Germer, 2001). Relative uncertainties determined from these calculations were determined as angular averages of the angular dependent result  $\sigma(\theta)$  for  $\theta = 5$  to  $135^\circ$ . Uses of higher (backward) angles tended to increase the uncertainty, but are ignored since they lie out of our range of measurement. Angles less than the experimental limit of  $\theta = 5^\circ$  had negligible effect on the calculations. The two upper and lower bound cases ( $802 \pm 6$  nm) were used to assess both the effect of a monodisperse distribution and the uncertainty in the actual mean diameter of the particles by comparison with the calculated result from a single-sized polystyrene sphere of 802 nm diameter.

Results of the calculations for the monodisperse cases are shown in **Figure 4.13** along with the results of a single 802 nm diameter sphere and experimental results. The first monodisperse case used a mean diameter  $d_n = 796$  nm, and distribution standard deviation of  $s_d = 9.6$  nm. This case gave a relative standard uncertainty of 3.8 % and 2.5 % for VV and HH polarisation respectively. The second case used the data set,  $d_n = 808$  nm and  $s_d = 9.6$  nm. In this second case the standard uncertainty relative to the single 802 nm diameter results are 4.7 % and 2.1 % for VV and HH respectively. In **Figure 4.8** the results

**Figure 4.8:** The results of Mie calculation for single ( $d_p = 802$  nm) and monodisperse ( $d_p = 796$  nm and  $808$  nm,  $s = 9.6$  nm) polystyrene spheres. The experimental results from Figure 4.7 are also included for comparison.

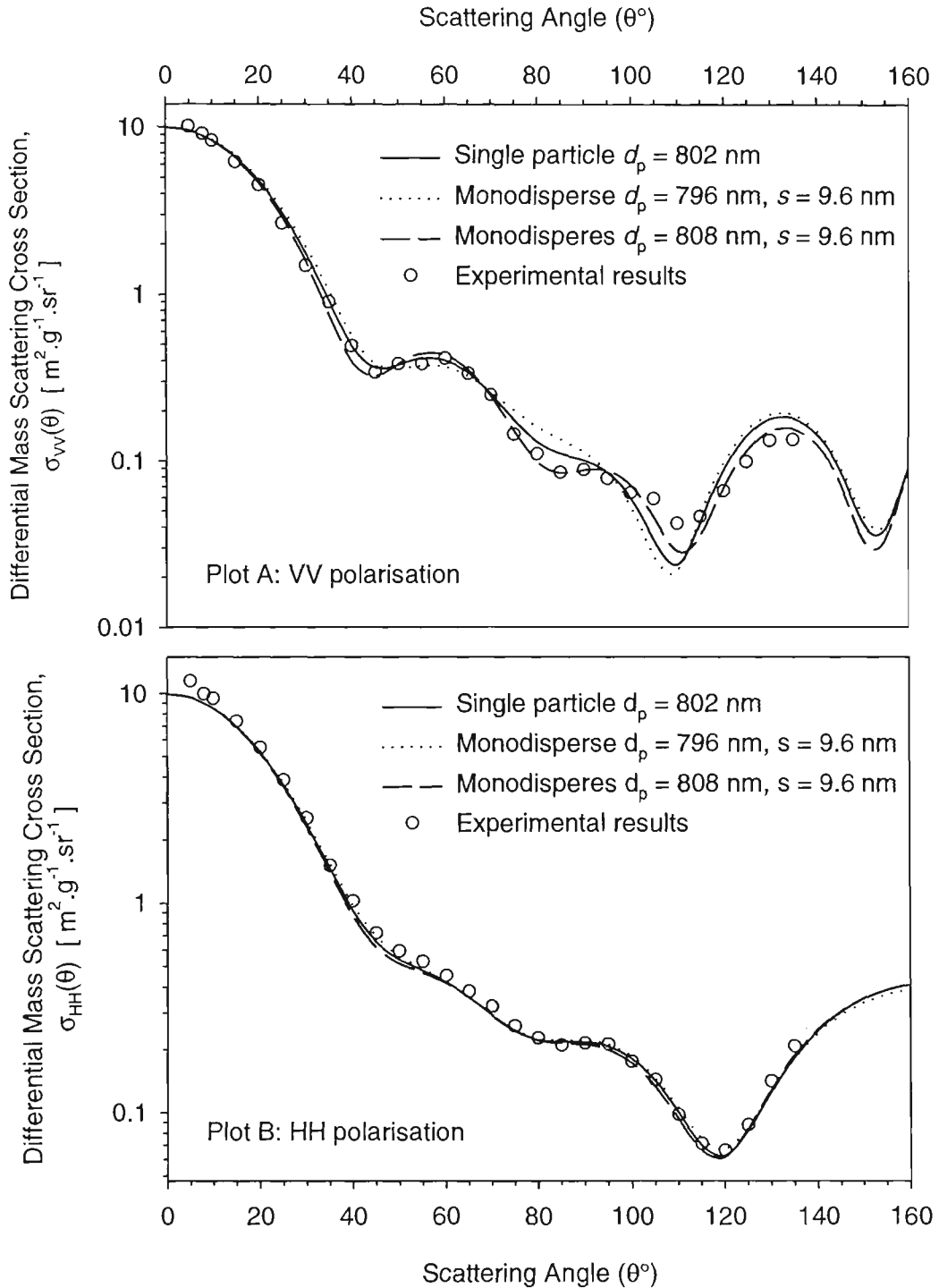


**Table 4.3:** Relative standard uncertainty results for size, distribution, and refractive index calculation with respect to Mie theory for a single 802 nm diameter polystyrene sphere, for  $\theta = 5$  to  $135^\circ$ .

Case	Calculation	Relative standard uncertainty, VV (%)	Relative standard uncertainty, HH (%)
$d_n = 802 \pm 6$ nm $s_d = 9.6$ nm	Monodisperse	4.25	2.3
$d_n = 802$ nm $s_d = 9.6$ nm	Monodisperse	0.6	0.02
$d_n = 802$ nm $n = 1.577$ to $1.595$	Single Particle	0.4	1.23

of these calculations are shown graphically. An analysis of the monodisperse distribution for  $d_n = 802$  nm and  $s_d = 9.6$  nm was also conducted and resulted in a relative standard uncertainty with respect to single scattering case of 0.6 % and 0.002 % for VV and HH respectively. From this it can be concluded that monodispersity in the polystyrene spheres has a small effect compared with the uncertainty in actual mean diameter. This study will make use of the uncertainties determined from the monodisperse cases,  $d_n = 796$  nm and  $d_n = 808$  nm, and average them to arrive at the relative standard uncertainties 4.25 % and 2.3 % for VV and HH polarisation settings respectively. The results of this analysis are summarised in Table 4.3.

#### 4.6.2.3 Type B: Refractive index uncertainty

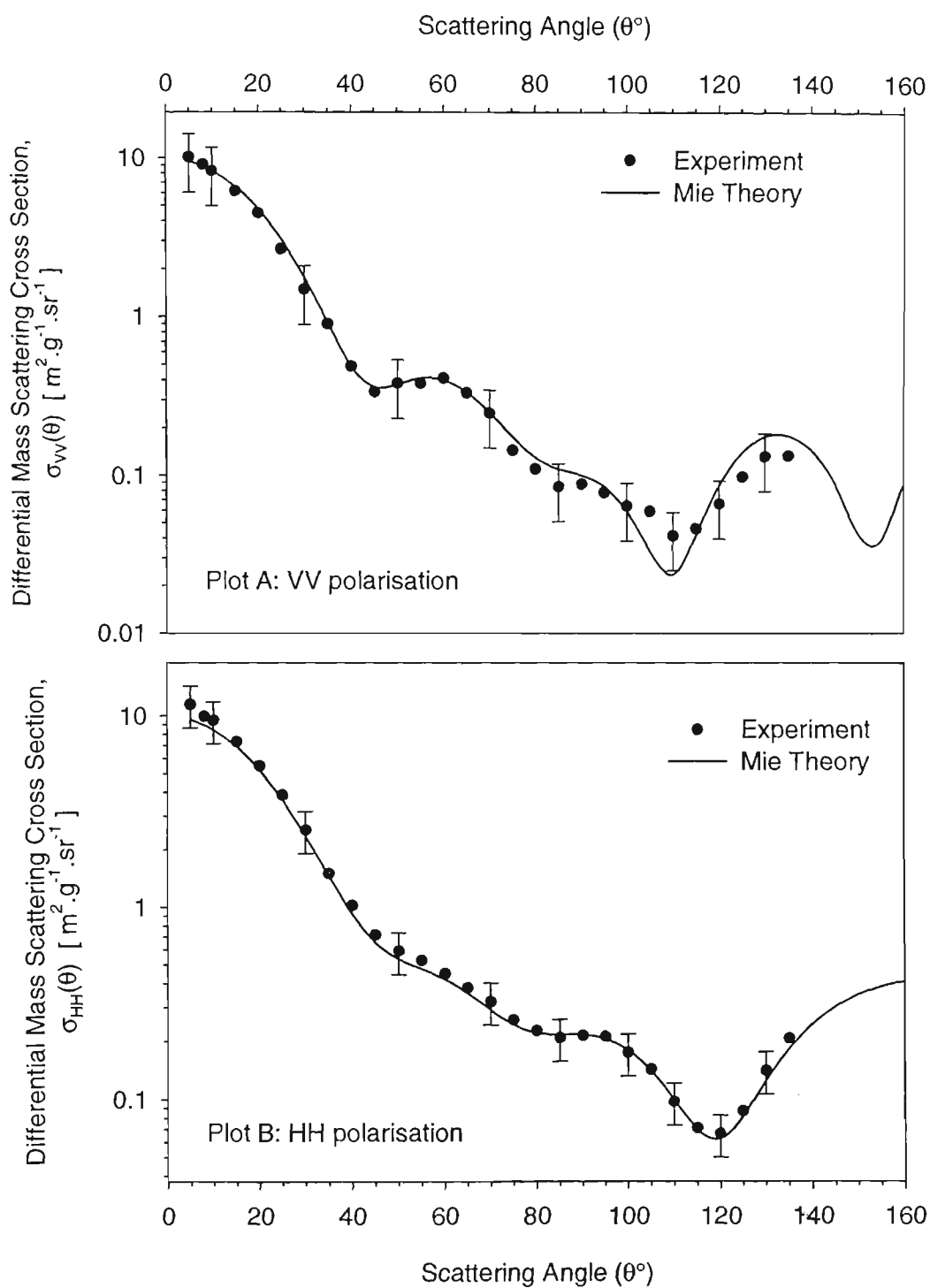
Refractive index is a material optical property upon which light scattering is intimately dependent, so any deviation from the value quoted in Table 4.1 must be considered. Marx

and Mulholland (1983) have assessed the refractive index of single polystyrene spheres for use as a standard reference material (SRM). Later a simple dispersion relation was applied to extrapolate the refractive index to HeNe (632.8 nm) wavelengths (Mulholland et al., 1985a). To assess the influence of the refractive index on the calculated result a Type B approach is used similar to what was done in the last section. This was achieved by taking the extreme values of the various published refractive indices (Marx and Mulholland, 1983; Mulholland et al., 1985a), namely 1.577 and 1.595, and applying each to the Mie calculation for a single sphere of 802 nm diameter for both polarisations. This range of values was not calculated from a propagation of uncertainty analysis but an addition of expected uncertainties. Subsequently the range of refractive indices is closer to two standard deviations. The relative uncertainty due to this range of refractive indices is averaged for a given polarisation and the factor of two removed. The results are 0.4 % and 1.23 % for VV and HH polarisations respectively, the results are also shown in **Table 4.3**.

#### ***4.6.2.4 Calibration verification: combined and expanded uncertainty***

Including both the Type A and Type B uncertainties determined in the above sections the law of propagation of uncertainty, that is a root-sum-of-squares, gives the uncertainty in the calibration verification experiments. The combined standard uncertainty is then determined as 20 % and 12.3 % for VV and HH polarisation settings respectively. The expanded (two standard deviations, 95 % confidence limit) of the uncertainty is then 40 % and 24.6 % for VV and HH polarisation settings respectively. The data from the experiment shown in **Figure 4.6** is shown along with error bars in **Figure 4.9**, where the error bars indicate the 95 % confidence limits.

**Figure 4.9:** Plot of the data in Figure 4.6 with error bars showing the expanded uncertainty determined in Sec. 4.6.2.4.



### 4.6.3 COMPONENT UNCERTAINTY ANALYSIS: TYPE A

The uncertainty analysis described in the last few sections relies heavily on the Type A uncertainty of the calibration verification. To see how the different components of the measurement contribute to the uncertainty above each must be investigated separately where possible. The following uncertainty analysis separates components of the measurement and tries to quantify their magnitude for comparison. By later combining the component uncertainties a comparison can be made with the combined and expanded uncertainty result in the last section, **Sec. 4.6.2.4**.

Type A uncertainty analysis is used where enough data is available to allow meaningful statistical analysis of the variation in the measured quantity. An example of this is the variation in repeatable results of the calibration verification experiments, which examines the variation of multiple experiments about the mean quantity resulting from that set of experiments. The subject of the following sections is a Type A uncertainty analysis of the uncertainty in repeat experiments, detector signal and mass concentration.

#### *4.6.3.1 Uncertainty in repeat experiments*

One aspect that is important to an experimental measurement is the ability to repeat that measurement. The uncertainty of repeating experiments is dependent on the combined uncertainties in an experiment. This quantity has been assessed by determining the standard deviation of the verification experiments about the average of those experiments. A method that is analogous to **Equ. 4.11**. Except that the result is relative to the experimental average and not the calculated Mie result as in **Equ. 4.11**. The analysis is mathematically expressed as,

$$\langle \sigma(\theta_j) \rangle = \frac{1}{N} \sum_{v=1}^N \sigma_v(\theta_j) \quad (4.12)$$

which gives the average result at an angle  $\theta_j$ , for the data set of,  $\nu = 1..N$ , verification experiments. The standard deviation,  $h(\theta_j)$ , is then given by,

$$h(\theta_j) = \sqrt{\frac{1}{N-1} \sum_{\nu=1}^N [\sigma_{\nu}(\theta_j) - \langle \sigma(\theta_j) \rangle]^2}, \quad (4.13)$$

which finally leads to the relative standard uncertainty of repeat experiments,  $h$ , by simplifying the functional form by determining the angular average, that is

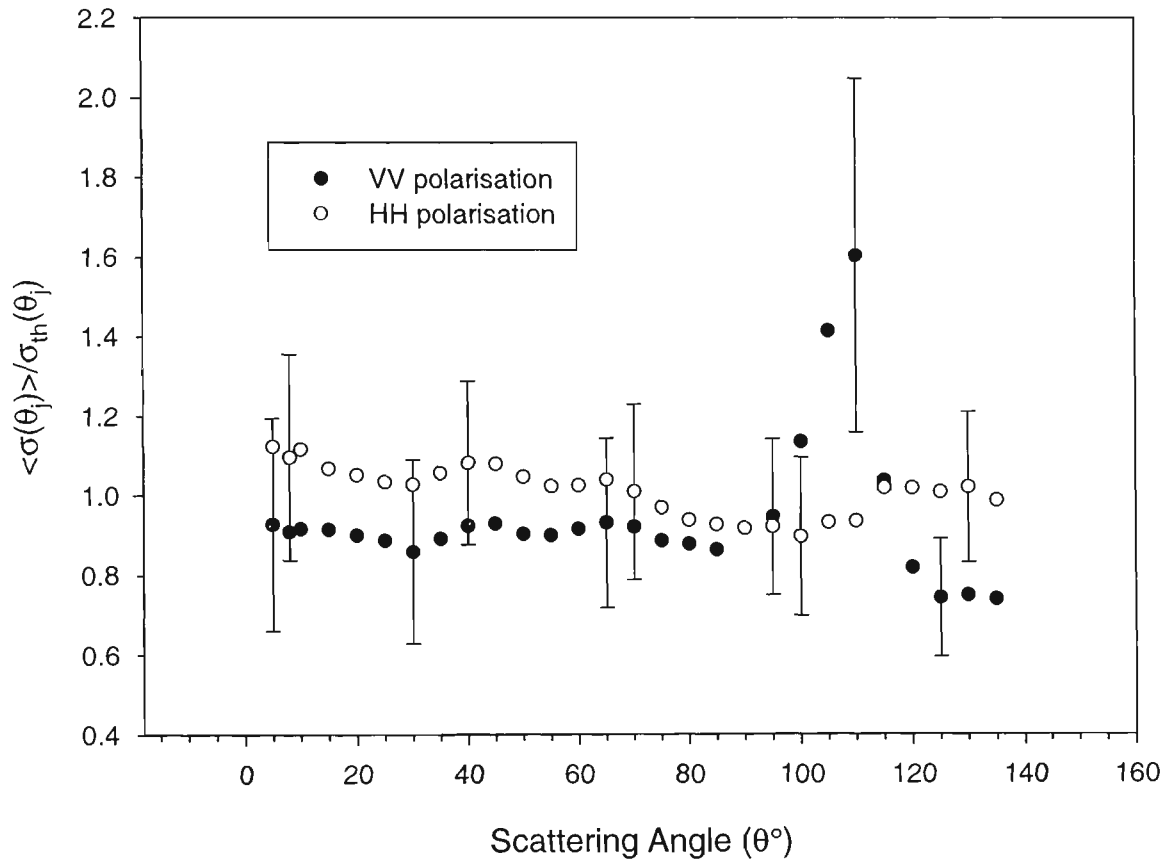
$$h = \frac{1}{k} \sum_{j=1}^k \frac{h(\theta_j)}{\langle \sigma(\theta_j) \rangle}. \quad (4.14)$$

The functional form of the relative standard uncertainty of repeat experiments is given by  $h(\theta_j)/\langle \sigma(\theta_j) \rangle$ , where  $h$  is the angular average of the functional form in **Equ. 4.13**. The relative standard uncertainty in repeat experiments,  $h$ , of the verification experiments has been calculated at about 12.2 % and 10.0 % for the polarisation settings of VV and HH. This is relative to the average of the experiments. In **Figure 4.10** the average of the verification experiments, **Equ. 4.12**, has been normalised with respect to the calculated result for 802 nm diameter spheres. **Figure 4.10** shows the variation of the experimental average about the Mie theory result as the data points, error bars in **Figure 4.10** represent  $2h(\theta_j)/\sigma_{th}(\theta_j)$ . The standard uncertainty of repeating experiments changes only slightly over the angles, but is pronounced at an angle of about  $110^\circ$ .

#### 4.6.3.2 Detected Signal Uncertainty

The uncertainty in the detection system has a  $1/\sqrt{N}$  dependence, where  $N$  is the number of events underlying the measurement, such as the number of photons reaching the detector or the number of particles in the scattering volume. By their nature these processes are

**Figure 4.10:** This plot shows the average of the verification experiments relative to the calculated result, that is  $\langle \sigma(\theta_j) \rangle / \sigma_{th}(\theta_j)$ . Error bars give the relative standard uncertainty of repeat experiments at the 95 % confidence limit,  $2h(\theta_j) / \sigma_{th}(\theta_j)$ .



independent of polarisation. The two main noise processes are due to the photon flux to the photomultiplier and fluctuations in the number of particles in the scattering volume. The photon flux is very high and as a source of uncertainty it is considered negligible. For the particle number fluctuations, the contribution is important since the scattering signal is directly proportional to the number of particles in the scattering volume. A typical number concentration calculated from the gravimetrically determined mass concentration of  $1.89 \text{ mg.m}^{-3}$ , is about  $7 \times 10^9 \text{ particle.m}^{-3}$  ( $7 \times 10^3 \text{ particles.cm}^{-3}$ ) or around 300 particles in the smallest scattering volume at  $\theta = 90^\circ$ , which gives a  $1/\sqrt{N}$  standard uncertainty of about 6 %.

By making use of actual detector signal data the uncertainty of a measurement at a given scattering angle can be determined. Since the detector signal measured and recorded at a particular scattering angle is the average of ten quick measurements, the standard uncertainty of this average is  $s_1/\sqrt{N_m}$ , where  $s_1$  is the standard deviation of the measurements about the average and  $N_m$  in this case is 10. Examining the \*.RAW data file containing all the detector data, a relative standard uncertainty of detector signal measurements ranges from about 0.5 % to 2 % of the measured average detector signal. In **Figure 4.11** an example of this signal detection standard uncertainty is shown as the bars about data points that demonstrate the variation in the aerosol mass flow over time, the subject of the next section. The two to three orders of magnitude range in the detected signal affects the uncertainty, which changes as the angle increases and the noise floor of the detector is approached. This resolution floor is reduced by increasing the sensitivity of the lock-in amplifier as the detector moves through a scan (**Sec. 3.3.2**).

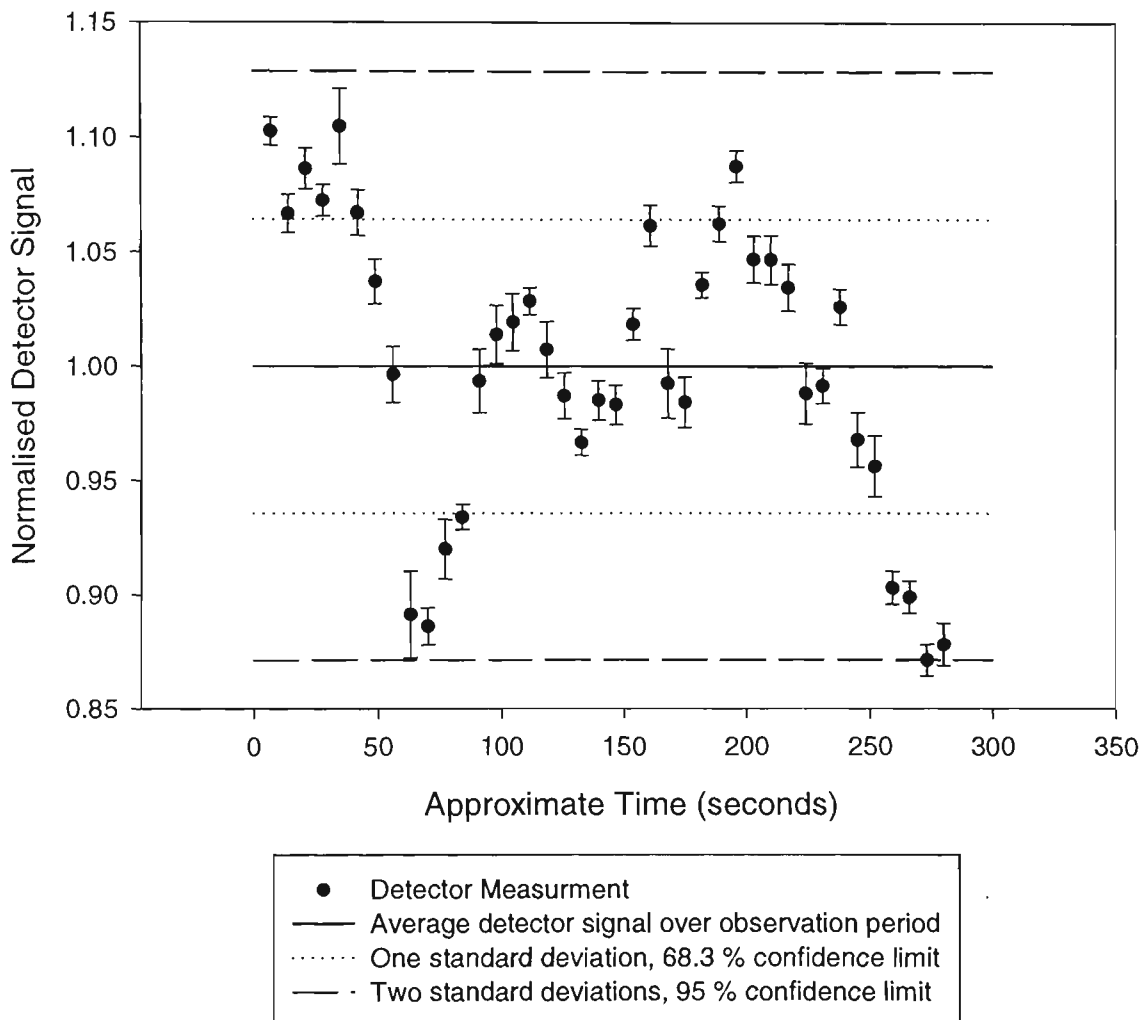
### 4.6.3.3 Mass concentration time dependence

As has been discussed above there are no differences in method between the light scattering measurements made for different aerosols, see **Appendix A1**. The differences are in the aerosol generation and transport to the LAOF. The effects of different smoke aerosol production methods will be dealt with when their results are discussed in later chapters. For the calibration and verification experiments, the polystyrene sphere generator in **Figure 4.2** is considered in this section.

In general the aerosol generated and supplied to the LAOF influences the number of particles present in the scattering volume over a relatively longer time period than that considered in the faster signal uncertainties above. This means that mass concentration measurement and detector signal over the time of an actual angular scan will be affected. That is to say, drift in the aerosol generator will affect scattering signal measurements made at different angles. Variation in mass flow control also plays a role in this uncertainty but is not isolated in the analysis that follows; to a degree it is included in the actual weighing of the filtered aerosol sample, see **Sec 4.3.1.2**.

The mass concentration measurement made in an experiment is an average over the period of sampling. The mass concentration is not measured as a function of time. The detector signal is more sensitive to these variations while it is making many measurements over the experimental period and “sees” these fluctuations. The mass concentration fluctuations were observed by making use of scattering data collected while the detector was stationary at  $\theta = 10^\circ$  and an aerosol of polystyrene spheres was flowing through the LAOF. The results of this experiment are shown in **Figure 4.11** where they have been normalised to the average detector signal over the total period of all the observations. This corresponds to the mass concentration determined by the gravimetric measurement method, as the average over all the observations is proportional to the mass concentration measurement. Subsequently the

**Figure 4.11:** Results demonstrating mass fluctuations in the calibration aerosol generator, the detector has been held at  $10^\circ$  while polystyrene sphere aerosol flows through the LAOF. The average detector signal for the period of observation and the 95% confidence limits of this average are shown. The error bars correspond to the detector signal uncertainty.



fluctuation in aerosol mass flow from the generator, results in a standard Type A uncertainty of about 6 % relative to the mass concentration from the gravimetric measurement. This result is independent of the polarisation setting.

#### 4.6.4 COMPONENT UNCERTAINTY ANALYSIS: TYPE B

The following sections are concerned with the Type B uncertainty analysis of components of the calibration verification. In the case of an analysis of uncertainty in the polariser settings, a set of experiments were analysed using a Type A assessment. This analysis did not faithfully represent the real experimental procedure, although they did set a minimum level of uncertainty. Subsequently some judgement was used in determining the polariser setting uncertainty, making it a Type B uncertainty. The uncertainties from multiple scattering and scattering angle deviations are also considered.

##### 4.6.4.1 *Scattering angle deviations*

Angular uncertainties are coupled to the position of the detector based on components such as the rotation stage, its controller, the central positioning of the scattering volume, and the uncertainty in the initial zeroing of the detector. The rotation stage and controller were designed for extremely high precision and give uncertainty in the angular position of  $\pm 0.0035^\circ$ . The zero position is found by examining the incident beam at close to  $\theta = 0^\circ$ , where the detector then moves through a coarse arc (arc  $\pm 2^\circ$ , step  $\Delta\theta = 0.23^\circ$ ) and then a fine arc (arc  $\pm 1^\circ$ , step  $\Delta\theta = 0.1^\circ$ ) looking for the largest peak signal (Sec. 3.3.1). A Gaussian beam distribution has been assumed and the effect of the optical elements on this assumption has been ignored. Thus peak values might not necessarily occur at the centre of the beam since aberrant effects such as dust on optical elements and interactions with these elements themselves can lead to deviations from the Gaussian form. Nevertheless, an estimated standard uncertainty of about  $\pm 0.25^\circ$  is acceptable given the zeroing procedure.

The uncertainty caused by misalignment of the scattering volume, which should have a centre common to both the incident and scattered beam, was not directly quantified. Analysis of the verification experiment data, such as the HH minimum between  $115^\circ$  and  $120^\circ$ , indicates that the overall standard uncertainty in the angular position is  $< 2.5^\circ$  as an upper bound.

The maxima and minima typical of the aerosols examined in this study do not have fine angular widths, see **Figures 4.1** and **4.6**. So they should be easily resolved by the acceptance half-angle of  $\pm 0.3^\circ$ . Integrating the Mie scattering result, which is ideally for an infinitesimal detector, over the acceptance angle and dividing by the total view width,  $0.6^\circ$ , gives the result for the detectors angular view. The integration has been performed numerically after the Mie result was calculated for a single 802 nm polystyrene sphere. The Mie result was calculated for an angular step of  $\Delta\theta = 0.1^\circ$  and then integrated using Simpson's rule from  $+0.3^\circ$  to  $-0.3^\circ$  of commonly used measurement angles within the range of  $\theta = 4.7^\circ$  to  $135^\circ$ . The relative standard uncertainty of this acceptance angle was determined at  $\leq 0.002\%$  with respect to the Mie result for an infinitesimal detector. The uncertainty of the acceptance angle of  $\pm 0.3^\circ$  is negligible for the slowly varying scattering patterns observed in this study.

An estimate of standard uncertainty in the angular position of about  $\pm 0.5^\circ$  seems appropriate. This leads to an angular average standard uncertainty of about  $4\%$  relative to the Mie theory solution, independent of polarisation.

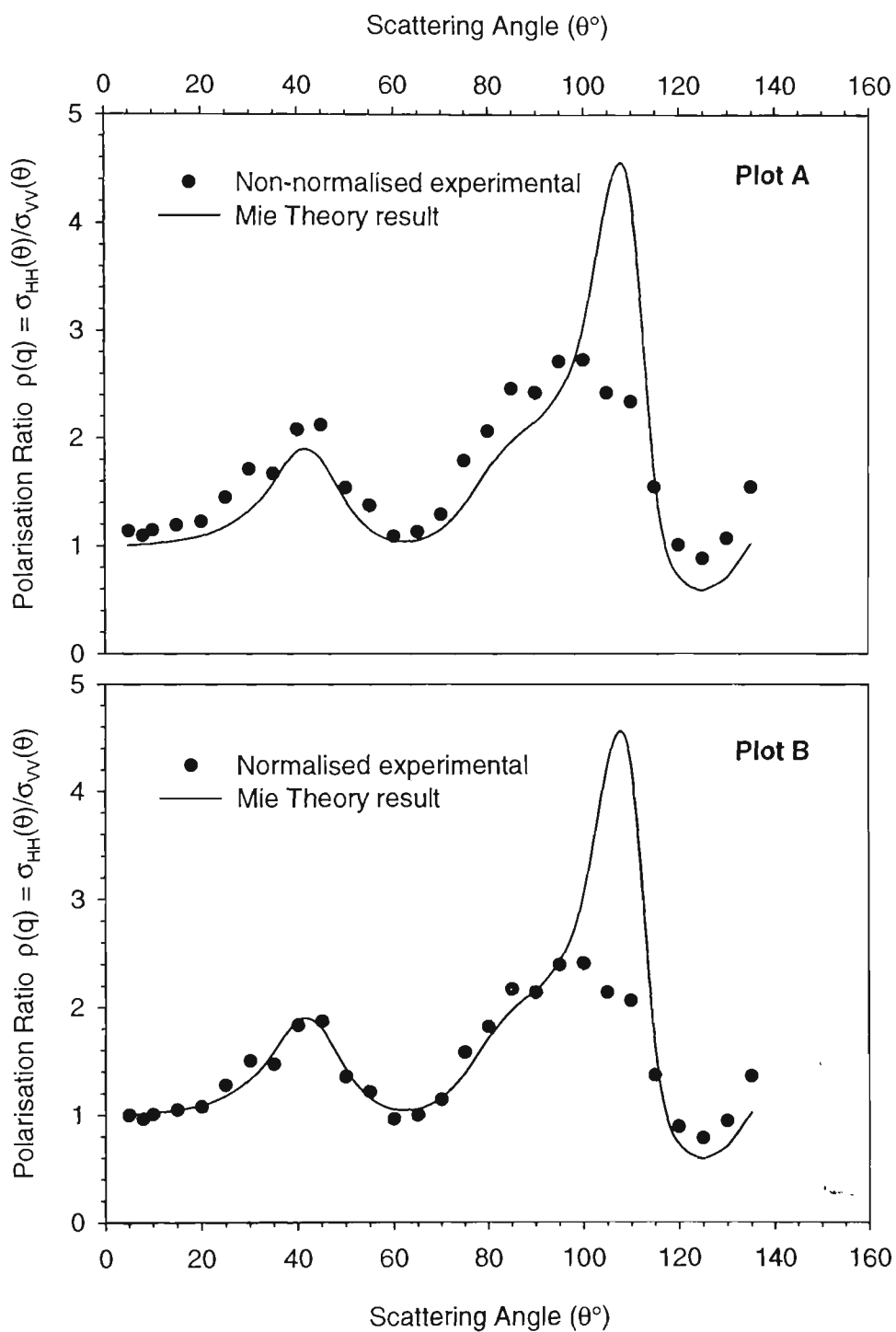
#### *4.6.4.2 Uncertainty in polariser setting*

Some experimental tests have been conducted with the polariser elements to understand the magnitude of the uncertainties they contribute. To test the manual movement of the polarisers the detector and its optical train were positioned at  $\theta = 0^\circ$  with a neutral density filter reducing the incident beam magnitude to a measurable level. The analyser optic before the detector and the halfwave plate were then rotated from HH to VV settings and back

many times, the detected signal being recorded after each movement. The standard uncertainty of these measurements was about 2 % for both polarisation settings. The time constant on the lock-in amplifier was increased substantially to average out noise effects. A larger deviation appears when the HH and VV data are examined at the near forward angles. For angles  $< 20^\circ$  the polarisation ratio,  $\rho(\theta) = \sigma_{HH}(\theta) / \sigma_{VV}(\theta)$ , is on average about 1.25 for the experiments in the verification set, whereas theoretically the polarisation ratio should be less than 1.1 at these angles. **Figure 4.12** presents a non-normalised and normalised (set to 1 at  $\theta = 5^\circ$ ) polarisation ratio for comparison, where data used is the same as that presented in **Figure 4.7**. As in the Type A data shown in **Figures 4.7**, large divergence from Mie theory occurs at the angles associated with the minima in the VV polarisation data. The normalisation at  $\theta = 5^\circ$  of the experimental data corrects well for the systematic over and under estimation of the HH and VV polarisation settings respectively.

One test was made of this under and over estimation with the detector sitting at  $\theta = 8^\circ$  while 802 nm diameter polystyrene aerosol was flowing through the LAOF. The analyser optic and halfwave was then manually moved between HH and VV polarisation settings. Again a 2 % variation in the average detector signal was observed but an average polarisation ratio of 1.14 was measured for nearest pairs of settings. Mie theory gives a polarisation ratio of 1.01 at this angle. Examination of the calibration verification data shows that the VV component is generally lower than the exact result unlike the HH result, which is typically close to or higher than the exact result, see **Figure 4.12**. The result of the typically lower VV and higher HH makes the polarisation ratio much higher than exact theory. This systematic deviation is believed to have two possible causes. One possible cause believed to contribute substantially to the uncertainty is the analyser optic (before the detector) causing some beam refraction. This optical element is not perfectly mounted with its faces at  $90^\circ$  to the incident scattered beam and is also a thick optical element (**Sec. 3.3.1**). The refraction causes the

**Figure 4.12:** The **a)** non-normalised and **b)** normalised (at  $\theta = 5^\circ$ ) Polarisation ratio,  $\rho(\theta) = \sigma_{HH}(\theta)/\sigma_{VV}(\theta)$ , of the calibration verification experiment shown in Figure 4.7. The non-normalised Mie result is also shown.



scattered beam entering the detector assembly to shift slightly away from the final aperture (1 mm diameter). While this effect is small for the HH polarisation setting it is apparently larger for the VV setting after rotation of the analyser, which is believed to refract the scattered beam away from the final aperture causing a larger deviation from Mie theory in the VV case. The other influence is the polarisation dependence of a photomultiplier, which has a bias towards horizontal polarisation. This photomultiplier effect is expected to be about 1 % to 2 % of the signal. While these factors are difficult to quantify the future approach would be to improve the optical elements, detector performance and scattering vessel design. As is often the case with optical apparatus the best solution is prevention.

For manual setting of the polariser the relative standard uncertainty of 2 % based on the measurements made above are utilised. There is obviously some component contributing to a difference in the VV and HH polarisations that is responsible for a deviation about 13 % in the polarisation ratio when not normalised at  $\theta = 5^\circ$ . From these a relative standard uncertainty of 7 % and 5 % about the detector signal for VV and HH polarisation settings is adopted.

#### 4.6.4.3 *Multiple scattering*

Consider the effects of multiple scattering that occur when light scattered from one particle interacts with one or more particles before reaching the detector. Mie theory is an exact theory for single scattering events and any multiple scattering will cause a deviation. Multiple scattering is driven by the separation distance of particles in the scattering volume and, if present, results in a disproportionate scattering signal compared with particle concentration, whereas Mie theory is directly proportional to the scattering signal. A condition of multiple scattering (Napper and Ottewill, 1964) is that if the ratio of the average separation of particles,  $L$  ( $L \propto \rho_n^{-1/3}$ , where  $\rho_n$  is the number concentration given the assumption that

the particles are in a cubic lattice), and the particle diameter,  $d_p$ , is greater than 100, then the effect of multiple scattering is insignificant. In this study, typical ratios of  $L/d_p$  are many times greater than 100, based on the mass and number concentrations determined in the sections above (around 600). The condition put by Napper and Ottewill (1964) is quite stringent when compared with those proposed by Quirantes et al. (2001), who have shown that particles with small size parameter,  $x < 5.5$ , are very sensitive to separation distances. The 802 nm diameter polystyrene spheres used in this study have a size parameter of  $x = 3.95$ . A rule of thumb is that the volume fraction (Quirantes et al., 2001),

$$\phi_c = \frac{\pi}{6} \left( \frac{d_p}{L} \right)^3, \quad (4.15)$$

be less than 0.01 is necessary to ensure that inter particle separations are large enough to avoid multiple scattering. Again this condition is easily met in the experiments conducted in this study, with typical volume fractions of about  $2 \times 10^{-9}$ . A visual clue to the presence of multiple scattering is a halo about the scattering beam. This halo was never observed in any experiments conducted with the LAOF. On the basis of this analysis effects of multiple scattering can be ignored in this study.

#### 4.6.4.4 Polystyrene sphere doublets

There is another complicating process that might also contribute to uncertainties related to the nature of the particles and that is the presence of agglomerated doublets. Deviation from single particle scattering due to the presence of agglomerated polystyrene spheres represents a deviation from the symmetrical sphere modelled by Mie theory. Bottiger et al. (1980) have shown that the main deviation from Mie theory caused by doublet agglomerates occurs in the amplitude of the maxima and minima not the angular dependence. Fortunately, the ratio of doublets to single spheres in the aerosol flowing through the LAOF is small with an

estimated value of 6.5 % of the total number of singlet polystyrene spheres (Sec. 4.3.1.1). A sensitivity test of the effects of these doublets was investigated but not pursued as it was considered impractical. Principally because the number of doublets is a small fraction of the singlets the effects have been considered to be negligible in comparison to other experimental sources of uncertainty.

#### 4.6.5 COMBINED COMPONENT UNCERTAINTY

Combining and expanding the component uncertainties determined in the last sections can help identify some of the dominant sources of uncertainty in the experimental measurements. The Type A standard uncertainties of the calibration verification experiment in Sec. 4.6.2.4, are 20.0 % and 12.3 % for the VV and HH polarisation settings respectively. The standard uncertainties of the individual components examined are summarised in Table 4.4. The combined standard uncertainties for the components are 10.7 % and 9.5 % for the VV and HH polarisations respectively. This component uncertainty compares well with the measured uncertainty in repeat experiments, 12.2 % and 10.0 % for the VV and HH polarisations respectively. The component and repeat experiment uncertainties are comparable since they are not relative to the Mie theory result as the verification experiment uncertainties are. Figure 4.10 shows the difference between the average verification experiment and the Mie theory result as the vertical axis. The angular average uncertainty represented by this difference is the 6 % and 1.2 % for the VV and HH polarisation settings. In the case of the VV component combination with the uncertainty in repeat experiments results in an uncertainty of about 13.6 %, the HH component has a negligible effect. Uncertainty in VV has a strong contribution in the angular average analysis adopted in this study due to an inability to fully resolve the minima near  $110^\circ$ .

All the combined uncertainties can be expanded to their 95 % confidence levels by multiplying by 2.

**Table 4.4:** A summary of the component Type A and Type B uncertainty analysis.

Uncertainty	Relative standard uncertainty, VV (%)	Relative standard uncertainty, HH (%)
Detector Signal (Type A)	2.0	2.0
Polariser Settings (Type B)	7.0	5.0
Scattering angle (Type B)	4.0	4.0
Aerosol Mass Flow (Type A)	6.0	6.0
Gravimetric (Equ. 4.9) (Type B)	3.0	3.0
<b>Component Combined Uncertainty</b>	<b>10.7</b>	<b>9.5</b>
Repeat Experiments (Type A)	12.2	10.0
Combined uncertainty in Verification Experiments	<b>20.0</b>	<b>12.3</b>

## 4.7 DISCUSSION

The calibration method presented above is novel in that it uses an aerosol of polystyrene spheres to determine the angular distribution of scattered light in mass units as opposed to being normalised to arbitrary units. The use of normalised units simplifies the measurements in that a determination of the number of scatterers in the scattering volume is not necessary. A gravimetric approach makes an indirect measurement of the number of particles by determining the mass concentration of aerosol in the scattering volume, which directly formulates the volume scattering problem in terms of mass units. The use of a number-size distribution would put a weighting on small but numerous particles that are not strong scatterers. A mass scattering approach is thus more conceptually representative of the underlying aerosol size distribution relevant to light scattering. Mass units also have relevance in fire science and engineering where the yields of produced smoke are dealt with

in units of fuel mass loss and smoke mass concentration. Similarly mass units greatly enhance the ability to compare experimental and theoretical aerosol light scattering studies.

The gravimetric method at the heart of this calibration technique is easier to implement than the method developed by Holland et al. (Holland and Draper, 1967; Holland and Gagne, 1970). They had to map the particle jet flow and distribution through their scattering volume as well as calibrating in terms of absolute intensity (Prichard and Elliot, 1960). The gravimetric method relies on thorough mixing in the scattering volume, the ability to weigh relatively small aerosol samples and to control the aerosol mass flow through the scattering volume onto a high efficiency filter.

The benefit of using the verification experiments for the uncertainty analysis is that it reproduces many of the uncertainty components that affect measurements of  $\sigma(\theta)$  on unknown aerosols. The only uncertainty component that is not analysed for other aerosols is the aerosol generation and transport particular to those unknown aerosols. The uncertainties in the calculated Mie scattering are small compared with the uncertainties in the measurement of the differential mass scattering cross section (Sec. 4.6.2.4). Analysis of the components contributing to the uncertainty in the measurements indicates two main sources of uncertainty: the polariser settings and the aerosol mass flow rate through the scattering volume. Future work with the Large Agglomerate Optical Facility should aim at minimising the effects of these two measurement components. An improved optical train and a scattering reference channel would be of use in reducing these uncertainties. The accepted combined and expanded uncertainties in a scattering experiment on polystyrene spheres in this study are 40 % and 25 % for VV and HH polarisation settings.

## SMOKE AEROSOL FROM NON-FLAMING FIRES

### 5.1 INTRODUCTION

#### 5.1.1 OVERVIEW

An overview of light scattering theory, a description of the light scattering apparatus and calibration of that apparatus has been discussed in earlier chapters. The following chapters present the results of experiments conducted to characterise the smoke aerosols generated by different fuels. The characterisation focuses primarily on the angular light scattering by the smoke aerosols generated in non-flaming fires (Sec. 1.3). This is measured and quantified in terms of the differential scattering cross section per unit mass per steradian. An overview of the characteristics of smoke aerosols generated in non-flaming fires in other studies is discussed before moving on to the methods of the experiments conducted. The methods describe the means particular to non-flaming smoke aerosol generation. Smoke particle size distribution is also presented and this information is used along with previously published information on smoke refractive index to compare the experimental results with Mie theory (Sec. 2.4.3). The number and mass concentrations of the smoke aerosols were also measured at their source, the Fire Emulator/Detector Evaluator (FE/DE) at NIST.

#### 5.1.2 SMOKE AEROSOLS FROM NON-FLAMING FIRES

The environment in which non-flaming smoke aerosols are generated is very different from that of smoke aerosol from a flaming fire, and for this reason the smoke aerosols produced are quite different. The differences in environment have fundamental effects on the chemistry and physics of formation and subsequently the morphology of generated particles. These differences are the basis on which this study addresses its hypothesis of discriminating between the smoke aerosols generated by the two modes of fire: flaming and non-flaming.

Smouldering combustion is quite different from forced pyrolysis, as it comprises a true self-sustaining propagating combustion wave that has three distinct zones (Ohlemiller, 1995; Moussa et al., 1979). First is the pyrolysis zone, where heat from the adjacent reaction zone is thermally decomposing the fuel and producing gaseous products. Some fraction of these gaseous products condenses forming an aerosol. The second zone is the reaction zone where combustion is the dominant process. The products of this zone are oxidised gases, some of which could condense or react with surfaces of condensed phase particles. The third zone is the char zone, which could produce some solid airborne char material. Many of the aerosol products produced in smouldering combustion are similar to those in forced pyrolysis, in that they are a condensed phase of hydrocarbon decomposition products. This is due mainly to the processes at work in the pyrolysis zone of the smouldering combustion. Smouldering combustion is defined as being a self-sustaining process. Essentially this means that the heat loss rate from the smouldering fuel is less than the combustion heat release rate. If heat needs to be applied, then this is not smouldering combustion but forced pyrolysis.

Forced pyrolysis is pyrolysis of a fuel by an external heat flux and has an important place as an incipient stage of some fires. The term “non-flaming” fire is stretched in this study to include forced pyrolysis as well as smouldering combustion since forced pyrolysis is a cause of fire ignition in many situations and thus related to early detection (Sec. 1.2). The heat flux present in forced pyrolysis thermally decomposes the fuel material evolving monomers, polymer fragments, and partially oxidised species. Some of these components are high boiling point species, which cool as they move away from heat sources, finally condensing to form an aerosol composed of small droplets. Whether a liquid or solid particle is formed is dependent on the chemistry of the pyrolysis products and the environment.

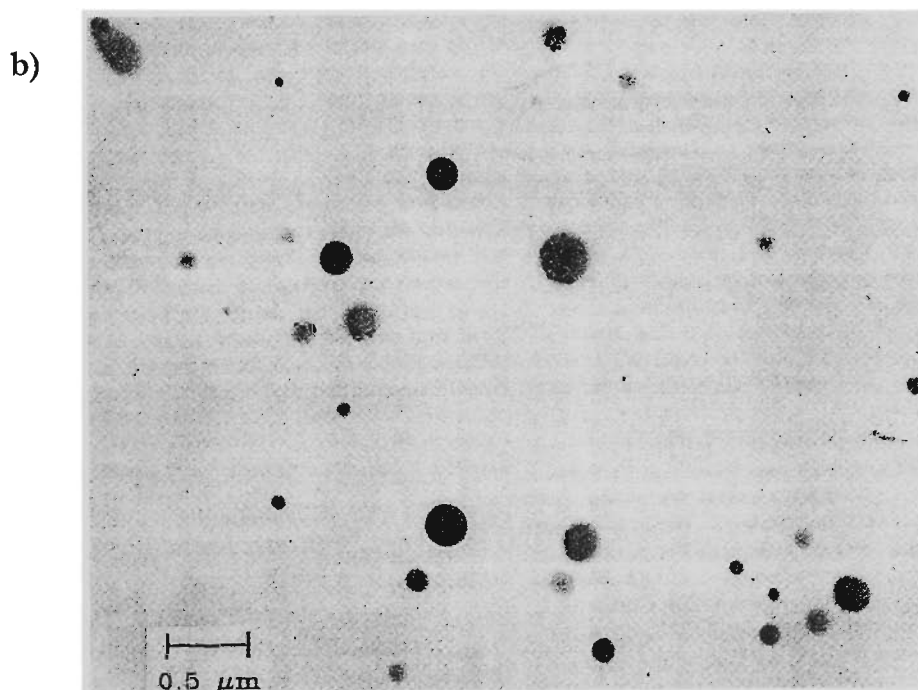
The formation processes above leads to a simple conclusion that smoke aerosols from non-flaming fires are condensed phase hydrocarbon compounds. Rau (1989) conducted a very

interesting study of the chemical composition of the smoke aerosols from a household wood burner operating in various modes of combustion. The smoke aerosols from the non-flaming wood fires were found to be predominantly organic carbon, 55% to 60%, and water with very few trace elements.

The chemistry and physics of aerosol particle formation puts constraints on shapes that resultant particles form. As has been discussed above these particles are a condensed phase of hydrocarbons and as such they tend to form droplet-like particles. **Figure 5.1** shows a scanning electron microscope image of some smoke particles from smouldering wood (Colbeck et al., 1997) and a transmission electron microscope image of incense smoke (Cheng et al., 1995). Bankston et al. (1981) obtained SEM images of smoke particles generated by non-flaming fires of smoke from wood, polyurethane foam and polyvinyl chloride plastic. Even though their images were from an impaction plate on which many particles had landed on one another, the droplet nature of the particles was recognised. The droplet shape of smoke particles from non-flaming fires is often simply considered to be that of a sphere, a valid assumption given the images of **Figure 5.1**. This has meant that past studies for response modelling of light scattering smoke detectors (Meacham and Motevalli, 1992; Aggarwal and Motevalli, 1997) could utilise Mie theory, as well as those that characterise the particles (Mulholland et al., 1985b).

The phase behaviour of pyrolysis products can vary a great deal, which in some circumstances can lead to exceptional behaviour. For example, polytetrafluoroethylene with a high pyrolysis temperature produces a solid-like aerosol with agglomerate structure, while cooking oil produces droplets. **Figure 5.2** shows a situation where an aggregated smoke aerosol is produced by forced pyrolysis of a polytetrafluoroethylene insulated wire in low gravity. This image was collected by Paul et al. (1997) when they were examining

**Figure 5.1:** a) Scanning electron microscope micrograph of smoke aerosol from smouldering wood, the scale represents 2 $\mu\text{m}$  (Colbeck et al., 1997). b) Transmission electron microscope image of incense smoke particles (Cheng et al., 1995).

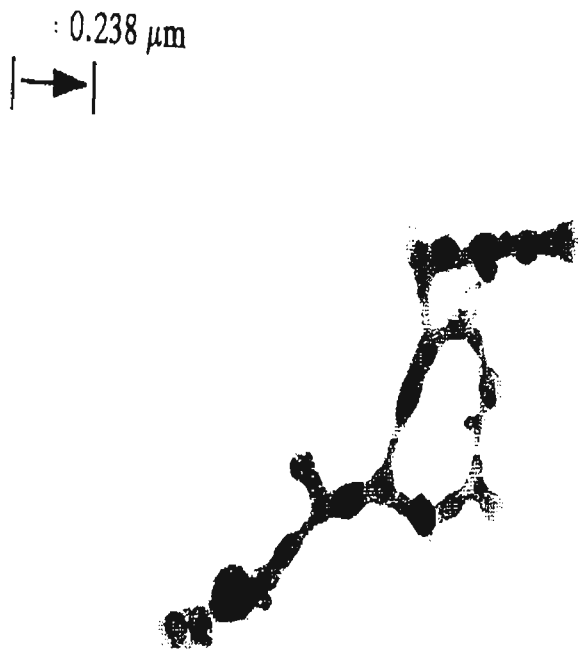


the smoke aerosols produced in overheating electrical wires used on spacecraft. They were characterising the smoke particle morphology for smoke detection purposes. Paul et al. (1997) noted that the elongation of the primary particles was due to the large vector of force that occurred when the insulation of the wire burst allowing the hot pyrolysis product near the wire to escape. These elliptical primary particles were a result of this particular material and environmental condition.

Comparison of light scattering studies with theory for spherical aerosols is feasible given knowledge of the size distribution and refractive index of the particles. Particle diameter is a key parameter controlling the light scattering and of importance to aerosols kinetics. Subsequently, there have been a number of studies carried out to characterise the size distributions for smoke aerosols produced by non-flaming fires. The characteristic diameters of smoke aerosol size distributions have been found to range between 0.1  $\mu\text{m}$  to 5  $\mu\text{m}$  (Rau, 1989; Phalen et al., 1976; Mulholland and Ohlemiller, 1982; Helsper et al., 1980; Cheng et al., 1995; Bankston et al., 1981; Lee and Mulholland, 1977; Mulholland et al., 1989). The refractive index is also an important parameter though there have been relatively few measurements of refractive index for smoke. Mulholland et al. (1985b) found the refractive index of smoke produced by smouldering  $\alpha$ -cellulose to have a value of about 1.5 at a wavelength of 442 nm.

This study includes size distribution measurements of smoke aerosols from non-flaming fires so that the contributions of this parameter to the light scattering results could be accounted for. In the past the tendency has been to rely on an anecdotal generalisation: smoke aerosols

**Figure 5.2:** Transmission electron microscope micrograph of a Teflon smoke particle, the source was an overheating of Teflon wire insulation in micro-gravity (Paul et al., 1997) (the image has been distorted by copying).



from non-flaming fires are larger than those from flaming fires (Meacham and Motevalli, 1992), common in the smoke detector community. This generalisation is discussed further in **Chapter 8**. Lack of size and shape information about the smoke aerosols examined in previous light scattering studies has hampered clear descriptions of findings. The generalisation has come from the research into ionisation and photoelectric detectors and the fact that the two detectors have different responses to different moments of the particle size distribution (Mulholland and Liu, 1980). Ionisation detectors are more responsive to smoke aerosols from flaming fires than non-flaming fires because the flame-generated particles are small and very high in number. A photoelectric detector will respond better to smoke aerosol generated by non-flaming fires since these fires *generally* produce larger particles. For light scattering studies of smoke aerosols the morphology (sphere or agglomerate) of the particles is a very important factor (Sec. 2.5). These points will be demonstrated in the results that follow in this and the subsequent chapters, which will be finally compared in **Chapter 8**.

## 5.2 METHODS

### 5.2.1 NON-FLAMING FUELS AND SMOKE AEROSOL GENERATION

This section presents the method and particular experimental details by which data on the light scattering properties and size distribution were collected. The generation of aerosols is detailed first, followed by descriptions of the methods used for sampling and measuring the size distribution, mass and number concentration.

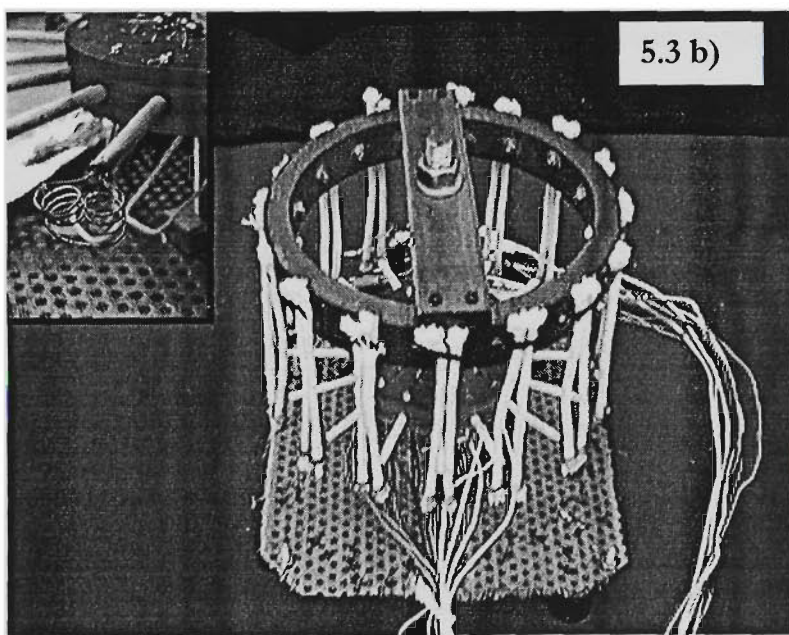
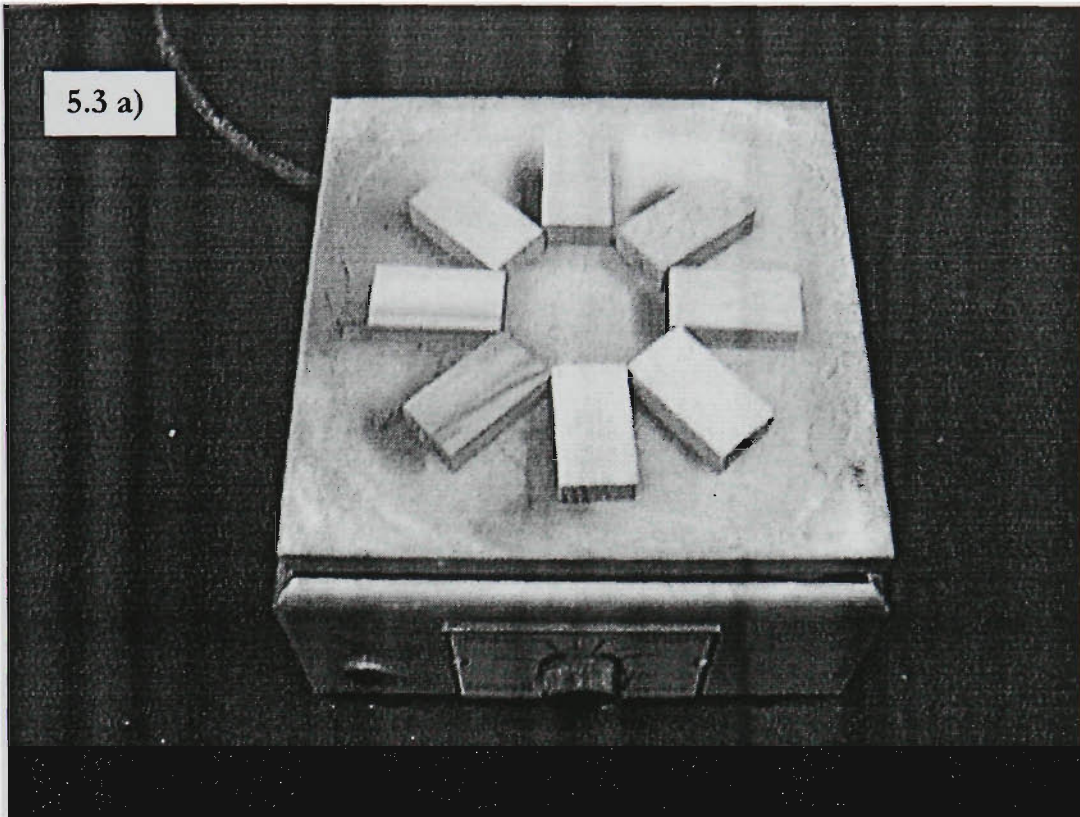
Three non-flaming fuels have been examined in this study, two of which are commonly used in fire detector standards. One fuel is small beech wood blocks common to the European fire detector standard EN54 Part 9 (EN54, 1982). These wood blocks are 35 mm x 20 mm x 10 mm in dimension and have been kept in a conditioning room when not in use, as required by EN54-9. The second fuel common to smoke detector standards is a cotton lamp wick,

very similar in appearance to shoe laces, that is used in both EN54 and the UL217 (UL 217, 1993). The cotton lamp wick material was cut from a long roll into wicks each about 210 mm in lengths that were burnt in the Fire Emulator/Detector Evaluator (FE/DE) (Sec. 3.4.1.2). Both the original roll and the cut lengths were stored in the same conditioning room as the beech wood blocks. The final fuel used was fire retarded polyurethane foam taken from the seat cushion of an armchair. The main factor behind the use of this polyurethane as a fuel was its use in a series of large-scale tests that were being conducted at NIST as part of an investigation of residential fire detectors (Bukowski et al., To be published). Polyurethane foam is common in seating furnishings and a common fuel ignited in some residential fires.

The FE/DE was used to generate all the smoke aerosols from non-flaming fires for this portion of the study. The FE/DE is used for this purpose since there were no facilities near the Large Agglomerate Optical Facility (LAOF) to burn solid fuels in a controlled environment with appropriate sensor instrumentation. The wood blocks and the cotton lamp wicks were commonly used in the FE/DE to test fire detectors for the very reason that they are standard test fire fuels used in detector certification. This study was able to examine the light scattering and size characteristics of smoke particles generated in the FE/DE adding to the knowledge of the FE/DE's standard operation.

The sequence for operating the FE/DE and collecting the smoke is as follows: the fuel with appropriate heating system was positioned in the test section of the FE/DE (see **Figure 3.4**). About 60 seconds of background data were collected before the fuel under examination was ignited or heat applied. In the case of the beech wood, blocks of the wood were arranged on a 250 cm<sup>2</sup> (750 kW) hot plate in the test section of the FE/DE. The hot plate and beech wood blocks used to generate smoke aerosols are shown in **Figure 5.3a**. Each block of beech wood has dimensions of nominally 35 mm x 20mm x 10 mm. Eight of the blocks

**Figure 5.3:** a) The arrangement of wood blocks on the hot plate used to pyrolyse them, and b) the staged-wick-ignition device developed at NIST (Cleary et al., 2001) and used to produce the cotton lamp wick smoke aerosol. The insert shows the wire ignition coils.

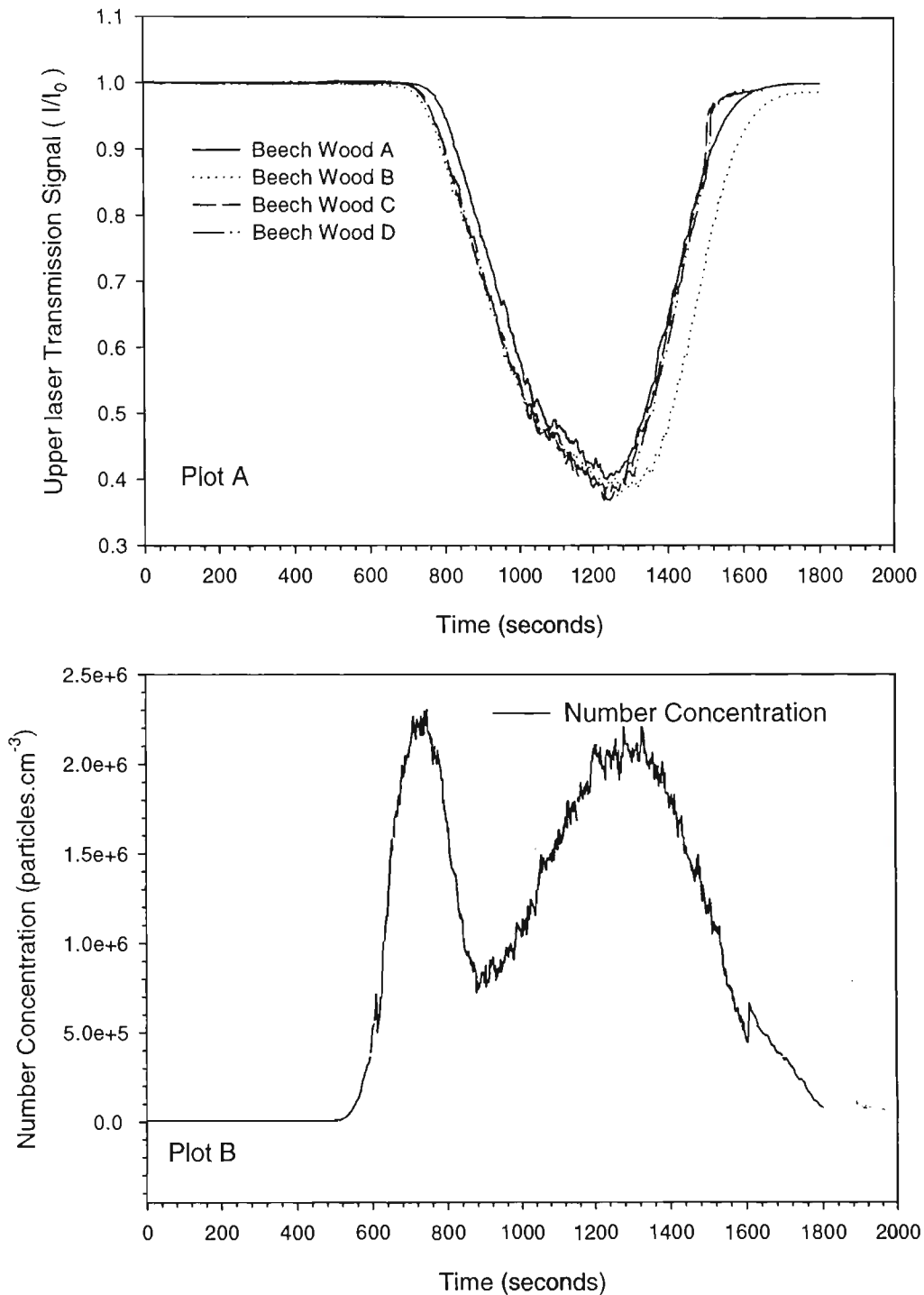


were arranged on the hot plate for an experiment. The beech wood was then placed on the hot plate turned to full power, a setting of 500°C, subjecting the wood blocks to forced pyrolysis (Sec. 1.3). **Figure 5.3** shows a photograph of the beech wood blocks arranged on the hot plate.

**Figure 5.4a** shows the light transmission measured by the upper laser of the FE/DE while pyrolysing beech wood blocks. The repeatability of the smoke generation is apparent in the closeness of the transmission curve and the similarity of form. This is the point of utilising the FE/DE, which has been designed for repeatable operation, particularly with the beech wood and cotton lamp-wick standard test-fuels. The surface of the hot plate was washed down after the wood was pyrolysed on it. It had been found that when reused uncleaned bursts of residual wood tars were vaporised from the hot plate surface. These vapours would then recondense to form very small particles. This did not impact significantly on the smoke aerosol as these small particles evolved from the hot plate surface before the wood began to produce smoke aerosols. In **Figure 5.4b** the number concentration versus time measured by the condensation particle counter (CPC, to be discussed in the next section) contains two peaks: the first for the very small particles and the second for the smoke aerosol. Once these very small particles were observed, the hot plate cleaning process was changed to include a number of wet wipes while at its operating temperature. It was then left for a time at full power before being turned off to cool. The hot plate cleaning was particularly important during continuous monitoring of aerosol equipment sensitive to small particles such as the CPC. The light scattering by particles this small is negligible at the wavelength used in this study,  $\lambda = 632.8$  nm. As can be seen in **Figure 5.4a** the response of the lasers in the FE/DE are insensitive to small particles when compared with the CPC (**Figure 5.4a**).

The smoke aerosol generated by the pyrolysed beech wood blocks was sampled from 800 seconds after turning on the hot plate, till about 1600 seconds. The laser transmission

**Figure 5.4:** a) Transmission measured by the upper laser of the FE/DE while pyrolysing the beech wood blocks. b) The number concentration as measured by the CPC showing the evolution of the very small particles before the wood smoke is produced.

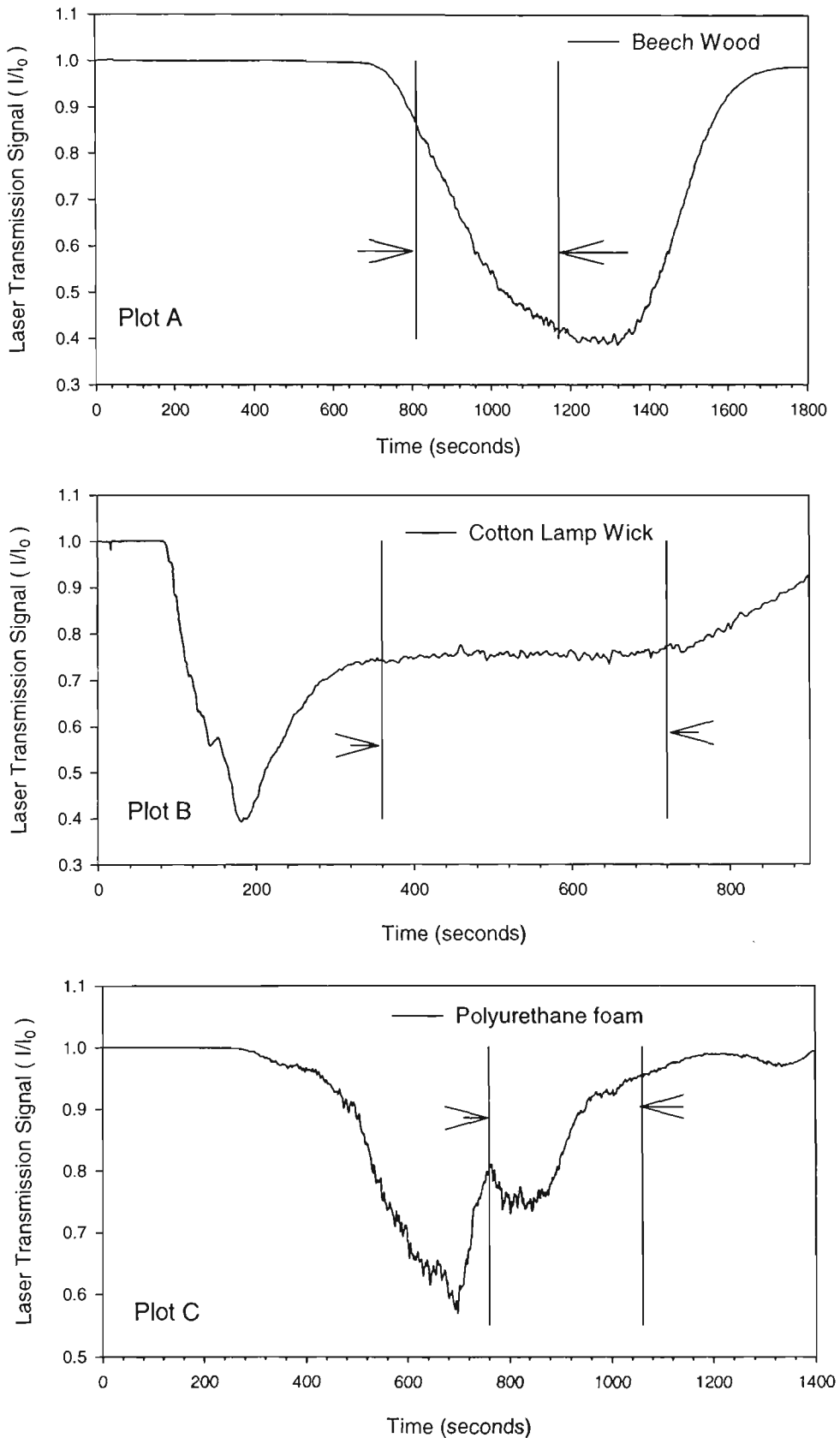


and sampling times are shown in **Figure 5.5a**. This sample corresponds to the smoke aerosol to be used in the light scattering measurements.

In **Figure 5.3b** the staged-wick ignition device that was used to smoulder cotton lamp wick is shown (Cleary et al., 2001). The ignition device is shown loaded with a total of 32 cotton lamp wicks as used in this study. This device allows various ignition sequences to be used. The FE/DE computer controls the sequence as the power to electrical heating wires at the bottom of the cotton wicks is applied, as shown by the insert in **Figure 5.3b**. The smoulder propagation is in the upward direction. In the case of light scattering and size distribution measurements four sets of eight wicks were ignited with a 12 second interval between ignition of each set. After about 180 seconds the wicks were known to be out of the influence of the hot ignition coils and in a true smoulder state, i.e. self-sustained. The self-sustained propagation rate is about  $0.17 \text{ mm.s}^{-1}$ . Smoke aerosol generated by the cotton lamp wick was sampled while at a steady state as can be seen in **Figure 5.5b**.

The polyurethane was cut directly from the chair cushion in relatively large pieces. These pieces were then cut down to smaller bricks of approximately  $15 \text{ cm} \times 10 \text{ cm} \times 7 \text{ cm}$ . A cut was made in one side of the polyurethane brick and a nichrome wire pushed through the cut into the polyurethane. This wire was then connected to a variac so that the nichrome wire would act as an ignition source. The polyurethane sample was placed on a simple tray of aluminium foil to catch any liquid products; this was all placed on a piece of cement-fibre board. The power was first applied with the variac on a setting of 5 V. This allowed the wire to warm up. After 60 seconds the variac voltage was increased to 10 V. Once the polyurethane foam was believed to have reached a self-sustained smoulder, the power was cut off. If the smoulder did not self sustain, then the test was stopped. Only smoke aerosol from self-sustaining smoulder was collected for light scattering and size distribution

**Figure 5.5:** A plot of the typical transmission measured by the upper laser of the FE/DE for non-flaming fuels: a) beech wood, b) cotton lamp wick and c) polyurethane. The vertical bars show the sampling period.



measurements. After generating the smoke aerosol and sampling for measurements there was still some polyurethane left although most of its core was consumed. The laser transmission in **Figure 5.5b** shows the evolution of smoke and the sampling period.

## 5.2.2 SMOKE AEROSOL SAMPLING AND MEASUREMENT

Aerosols were sampled from the FE/DE for characterisation measurements aimed at light scattering and size distribution measurements, as well as for number and mass concentration measurements. Mass-size distribution measurements were made with a cascade impactor directly sampling from the FE/DE. Light scattering and number-size distribution measurements were made in another laboratory by moving a sample of aerosol to the LAOF (Sec. 3.4) and a separate laser particle-sizing instrument. Other aerosol measurements made use of two aerosol measuring instruments sampling from the FE/DE, a condensation particle counter (CPC) and tapered element oscillating microbalance (TEOM). These aerosol measurements were all conducted at different times, in some cases days and even months apart. As outlined in Sec. 3.4.1.2, smoke aerosol sampling was done in the test section of the FE/DE. The instruments were connected to this sampling port and then made use of either their own internal pumps or an external pump to draw the aerosol through the sampling tube into the aerosol instrument. This section describes the method of the smoke aerosol sampling and measurements.

### 5.2.2.1 *Sampling for Size Distribution*

While the main emphasis of this study is the angular light scattering characteristics of the smoke aerosols, the availability of aerosol instruments represented an important addition of particle characteristics. It allowed the gathering of other information about the nature of the particles by independent methods. This also meant that the light scattering data could be compared with the Mie theory using the measured size distribution. As discussed above these aerosol characterisation instruments have not been available in other studies where light

scattering measurements were made (Meacham and Motevalli, 1992; Loepfe et al., 1997; Aggarwal and Motevalli, 1997). The lack of direct measurement of size distribution information has meant that common generalisations tend to be relied upon when interpreting light scattering information, which can lead to over-simplification in some circumstances. This study represents one of the few studies combining angular light scattering and size characterisation of examined aerosols of non-flaming fire generated aerosols.

The main method used in this study for size distribution measurement has been by impaction methods. Another particle sizing instrument became available due to a visit to the laboratory at NIST by a visiting professor, Dr. Da-Ren Chen, who kindly left a light scattering based particle spectrometer (Particle Measurement System's, High Sensitivity Laser Aerosol Spectrometer, HSLAS) at our disposal for a short time.

#### *5.2.2.1.1 Mass Distribution*

The cascade impactor that was used in this study was a 10 stage Micro-Orifice Uniform Deposit Impactor (MOUDI, Model 110 without rotator) (Marple et al., 1991). It is an inertial impaction device that separates aerosol particles into size bins based on their aerodynamic diameter (Hinds, 1982). The aerodynamic diameter is an equivalence measure; that is, the particles are sized based on their aerodynamic behaviour being equivalent to that of a sphere of unit density. For this study, the aerodynamic diameter is close to the actual physical diameter because the smoke aerosols have densities of about 0.9 to 1 based on monomer composition or like materials and because the aerodynamic diameter is proportional to the square root of the density. The aerodynamic diameter is an over estimate by no more than about 5 %.

Inertial impaction makes use of the fact that small mass particles follow streamline trajectories more readily than larger particles that tend to continue in a straight line as the

flow direction changes. As the flow velocities increase it becomes harder for larger particles to follow bending streamlines that pass around obstacles. In a cascade impactor the obstacles are impaction plates. Depending on the incident flow velocity and the particle diameter, the aerosol particles either make the turn around the impaction plate or they are impacted onto it. In this manner a cascade impactor removes large mass particles first and sequentially smaller particles as the aerosol flows through the impactor. The mass on a particular impaction plate is associated with the 50% collection efficiency aerodynamic diameter (fundamentally corresponding to a particle's Stokes number) of a particular impactor stage (Hinds, 1982). The aerodynamic diameters of the MOUDI impaction stages are shown in **Table 5.1**.

**Table 5.1:** List of MOUDI impact cascader stage aerodynamic (cut) diameters.

Stage	Aerodynamic Diameter ( $\mu\text{m}$ )	Stage	Aerodynamic Diameter ( $\mu\text{m}$ )
0	$\geq 18$	6	0.56
1	10	7	0.32
2	5.6	8	0.18
3	3.2	9	0.1
4	1.8	10	0.056
5	1.0	11	Everything else $< 0.056$

The MOUDI inlet was connected to the FE/DE test section using the 10 mm copper tube (Sec. 3.4.1.2). A pump was connected to the MOUDI outlet, with a bleed valve between the pump and MOUDI to control the operating flow that was checked and confirmed at about  $5 \times 10^{-4} \text{ m}^3 \cdot \text{s}^{-1}$  (30 L.min<sup>-1</sup>). A differential pressure gauge was connected between the inlet and 9<sup>th</sup> stage to monitor the flow as described by Marple et. al. (1991). An experiment using the

MOUDI to measure the size distribution was usually 300 seconds in duration. The MOUDI sampling occurred over about the same period as sampling into the drum did. The beech wood, cotton lamp wick and polyurethane smoke particle size distributions were measured with the MOUDI sampling from the FE/DE. The intention was to approximate the size distribution of particles generated for the light scattering experiments.

Each impaction stage had a pre-weighed aluminium foil. A final stage filter was also weighed and placed in the MOUDI. The weighing procedure made use of the technique and equipment described in **Appendix I**, and was the same for initial and final measurements. In the case of the MOUDI the aluminium foil was placed in a plastic petri dish after removal from the impaction plate. Electrostatic charging of the aluminium foils in their plastic petri dishes could result in the foils being attracted to the upper surface of the petri dish. This would result in a loss of mass and thus invalidate the data. Another point of operation concerned the final stage of the MOUDI when dismantling to remove the aluminium foils. Dismantling the higher stages sometimes caused a negative pressure due to constricted airflow by the lower stages and final filter. If the final filter stage was not unscrewed from the impactor before the higher stages, the slight vacuum was enough to lift some impaction plate and foils from their resting posts, thus losing mass to the surfaces they came in contact with.

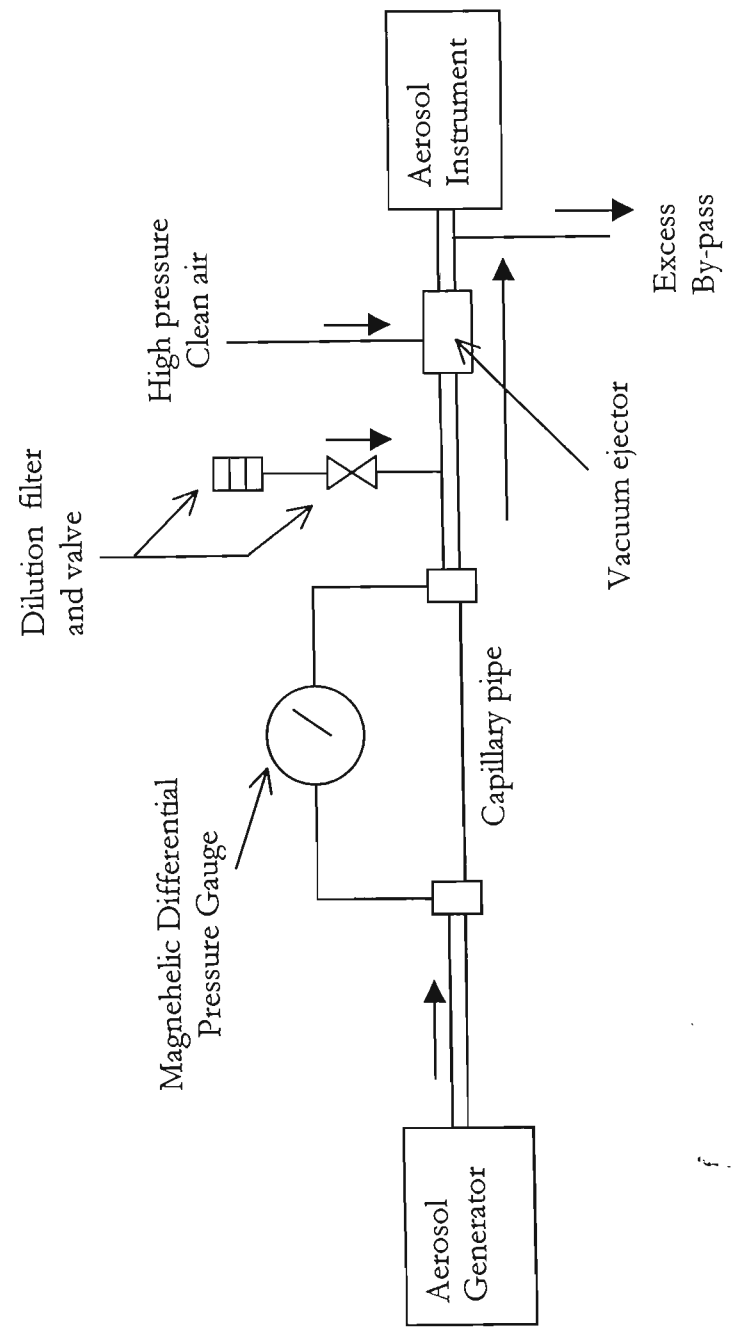
#### *5.2.2.1.2 Number Distribution*

The number distribution as a function of particle size was measured by the aerosol spectrometer (Particle Measurement Systems Inc., High Sensitivity Laser Aerosol Spectrometer, HSLAS). This instrument is known as an optical particle counter-spectrometer. It measures the scattered light from a particle passing through a laser beam, counts this pulse and relates its area to the size of particles. It utilises an active cavity laser scattering cell and focused jet of particles to determine the particle's number size distribution

from the scattered light signal of individual particles. The manufacturer calibrates the instrument with monodisperse polystyrene spheres to relate the detector output to the particle size. The detected scattered light pulse height or area caused by a single particle passing through the laser beam is associated with a calibrated size. In this way an accumulated count of the number of particles falling into a size bin is made. These instruments provide reliable results if there is only a single particle in the scattering volume. To obtain this condition, the aerosol concentration has to be diluted to less than  $10^{10}$  particles.m<sup>-3</sup> ( $10^4$  particles.cm<sup>-3</sup>); above this level there would be more than one particle in the scattering volume causing coincidence errors. To dilute the flow into the HSLAS from the drum, a system designed by Dr. Da-Ren Chen and Dr. George Mulholland was used to dilute the aerosol from the drum by about 50 times (particle concentrations of about  $4 \times 10^9$  particles.m<sup>-3</sup> [ $4 \times 10^3$  particles.cm<sup>-3</sup>]). The diluter is shown in **Figure 5.6**. It makes use of a capillary tube together with an ejector pump to cause a small flow from the aerosol side to mix with clean air. Collection of the aerosol into the drum also resulted in dilution. The dilution was checked before each measurement of the number distribution by drawing ambient air into the instrument for a total particle count. One measurement was made without the diluter, ambient conditions being about  $10^4$  to  $10^5$  particles.cm<sup>-3</sup>, and a second measurement was made with the diluter connected to the HSLAS. Then the dilution factor is calculated from the ratio of the two measurements. This same procedure was used with the CPC when necessary.

The HSLAS was in the same laboratory as the LAOF and so the smoke aerosol was collected into the drum from the FE/DE and transported. Only the number distributions of smoke aerosol from beech wood and cotton lamp wicks were measured using the HSLAS since the instrument was only available for a short time.

Figure 5.6: Schematic of the diluter used in the aerosol measurement experiments.



### 5.2.2.2 Sampling for Number and Mass Concentrations in the FE/DE

A series of experiments were conducted to measure the number and mass concentration as the smoke aerosol was produced in the FE/DE. The number concentration was measured by a condensation particle counter (CPC, TSI Model 3022a) while the mass concentration was measured by a tapered element oscillating microbalance (TEOM, Rupprecht & Patashnick Co.). Data from these measurements and mass-size distributions were used to examine the moments of the aerosols distributions (Cleary et al., ). Results from that study also made use of data from a measuring ionisation chamber (MIC) and a residential ionisation chamber (RIC), an instrument based on an adapted residential ionisation chamber. The data from the number and mass concentrations are useful to this study in putting the concentrations of smoke aerosol sampled for light scattering experiments into context. The light scattering measurements rely on time averaged mass concentration and not those in the FE/DE.

A condensation particle counter (CPC) is another light scattering particle counting instrument except that it will not size the particles. This instrument makes use of a controlled flow of particles and a pulse height or area analyser to count the number of particles passing through the beam in a given time; this time and a controlled flow rate allows the volume sampled to be determined. The CPC increases its responsiveness to small particles by condensing a volatile, such as butanol, onto the particles thus making them larger. As with other optical particle counting instruments the aerosol particles often need to be diluted. The unit used in this study had an operating concentration of less than about  $10^{13}$  particles.m<sup>-3</sup> ( $10^7$  particles.cm<sup>-3</sup>). The diluter used on the HSLAS was used to dilute the aerosol from the FE/DE by about 70 times. In this case the diluter was connected to the sampling tube from the FE/DE test section then to the CPC. The dilution ratio was determined as it was for the HSLAS in Sec. 5.2.2.1.2 above.

The tapered element oscillating microbalance (TEOM) (Hinds, 1982) was connected to another sampling line that was positioned next to the CPC sampling tube inlet. The TEOM has a lowest mass concentration sensitivity of about  $0.2 \text{ mg}\cdot\text{m}^{-3}$  (high uncertainty) and a maximum of  $10 \text{ mg}\cdot\text{m}^{-3}$ . It operates by drawing aerosol onto a filter at the end of a hollow oscillating element. At the high mass concentrations the filter quickly saturates. The airflow through the filter is internally controlled at a flow rate of about  $8.3 \times 10^{-6} \text{ m}^3\cdot\text{s}^{-1}$  to  $8.3 \times 10^{-7} \text{ m}^3\cdot\text{s}^{-1}$  ( $0.5$  to  $5 \text{ L}\cdot\text{min}^{-1}$ ). Since the element and attached filter is transversely oscillating any aerosol deposited on the filter will cause a change in the resonance frequency, which can be detected and converted to a mass concentration.

The sampling for both the CPC and TEOM was done with sampling tube velocities higher than the FE/DE tunnel velocity. This results in some anisokinetic sampling of the aerosol, which is to say that preferentially smaller particles are sampled. This bias is considered negligible given the relatively small size of the particles being sampled.

### 5.2.2.3 Sampling for Light Scattering

Sampling aerosols for the light scattering experiments was relatively straightforward in the sense that no intrinsically complex instruments were necessary. In fact there is little more detail to add to the overview given in Sec. 3.4.1.2, but these details may be of interest and are presented here for completeness with a little repetition from earlier.

Smoke aerosol sampled for the light scattering experiments had to be transported to the LAOF, which was situated in another laboratory. To do this a  $0.2 \text{ m}^3$  (200 L) drum, see Figure 3.5, was filled with a sample of the aerosol flowing through the FE/DE. The drum was connected to the sampling tube inserted into the FE/DE test section and a rotary pump was connected to the other side of the drum. Valves were used to isolate the inlet and outlet ports of the drum. These valves and tubing were also of nominally 10 mm outer diameter

(7 mm i.d.). The pump had to be throttled down as its normal flow rate was far higher than that required for the approximate aerosol concentration required for the experiments, about  $11 \text{ mg.m}^{-3}$ . The final sampling flow rate was set and measured by using a bubble flow meter in line between the drum and pump; the rate was  $333 \text{ cm}^3.\text{s}^{-1}$  ( $20 \text{ L.min}^{-1}$ ). The sampling period was usually about 360 seconds. The main factor influencing this time was the rate associated with a particular fuel's smoke production. In the case of the beech wood and cotton lamp wick this time was always used, as the smoke aerosol supply was abundant. For polyurethane, the time available to collect smoke aerosols did vary and some abortive attempts were made to generate the smoke aerosol. This occurred because the intention was to collect smoke from a self-sustained smoulder, but as mentioned earlier this was not always successful and was probably not the case in the strict sense. The smoke aerosol from the polyurethane used in the light scattering experiment was collected over a 300 second interval. In **Figure 5.5** the light transmission for non-flaming fire generated smoke aerosols are shown along with sampling times. These data correspond to the smoke aerosol collected for the light scattering experiments detailed later in this chapter.

Once the smoke was in the drum, it was unceremoniously dragged down the corridor and into the lift, whence after a drop of one floor it was propelled along another corridor, around a corner and into the laboratory containing the LAOF. This period is an important consideration in the experimental procedure as transported aerosols can undergo coagulation or agglomeration collisions during the transport and set up period. Simple calculation indicates that settling will mainly affect particles bigger than about  $3 \mu\text{m}$  (Hinds, 1982). It is known from past studies that aging of the smoke particle has a large impact on the number of particles (Lee and Mulholland, 1977). Affects on the volume or mass of the smoke particles to which light scattering is sensitive is small in comparison with the aging effects on number concentration. For the light scattering measurement, aging will have minimal

influence, but the number size distribution measurements described below might be affected more substantially. There is also a possible bias towards collection of small particles due to the fast inlet velocity of the sampling tube in the test section of the FE/DE. Again this bias has little effect on light scattering but might affect number-size distribution measurement.

Once in the laboratory with the LAOF the drum was connected via its outlet valve and a filter was connected to its inlet valve. In this manner smoke aerosol was drawn into the LAOF, while clean air passed through the filter making up lost air. This meant that the remaining smoke aerosol in the drum was being continually diluted as it was drawn into the LAOF. This aspect of the aerosol transport is an important source of uncertainty in the light scattering measurements. A discussion and analysis of this uncertainty is delayed until the light scattering result section below.

### **5.2.3 THEORETICAL LIGHT SCATTERING METHODS**

From the above it is apparent that smoke aerosols generated by non-flaming fires are spherical particles to which Mie theory is applicable. This theory requires knowledge of the size of the particles or in this case, as we are dealing with an ensemble of particles of different size, the parameters of the size distribution. These parameters are available via the mass-size distributions of the smoke aerosols measured by the MOUDI cascade impactor, and the assumption made in this study that the smoke aerosols are lognormally distributed. The details of the size distributions and the effect this has on the light scattering have been detailed in the earlier theory chapter (Sec. 2.2.1 and 2.4.3).

The other main light scattering parameter that is of importance is the refractive index of the smoke particles. This study does not make direct measurement of the refractive index but relies on findings of an earlier study of smoke particles generated by smouldering alpha-cellulose (Mulholland et al., 1985b). This is justified by the fact that the majority of organic

compounds have a relatively small range of refractive indices (real part) in the range of about 1.4 to 1.6. Mulholland et al. (1985b) trapped and suspended single smoke particles in an electrostatic field and applied methods developed previously (Mulholland et al., 1985a; Marx and Mulholland, 1983). They fitted theoretical scattering curves to observed light scattering results and thus determined an average real part of the refractive index as 1.5 at a wavelength of 442 nm. The complex component was measured at about  $8 \times 10^{-4}$ , which has a relatively small affect on scattered light. The 632.8 nm incident wavelength used in this study is not expected to influence the refractive index, given the low complex component. Thus the refractive index used in Mie theory calculations for this study is assumed to be  $m = 1.5 + i0$ .

A polydisperse adaptation of Mie theory, described in Sec. 2.3.1, and the size parameters measured in this study have been used for comparison with the light scattering results below. The computational code used in this study is based on the class library SCATMECH (Germer, 2001).

### 5.3 RESULTS

The following sections present size distribution information from the HSLAS and MOUDI so that light scattering data can be more readily interpreted and size information used in calculation for comparison with theory. Size distribution information is also of interest in other fields of study where particle size is necessary for transport calculations, such as smoke aerosol penetration into a detector. The angular light scattering measurements of the smoke aerosols generated by pyrolysed beech wood, smouldering cotton lamp wick and smouldering polyurethane foam are presented in terms of the differential (angular distribution) mass scattering cross section, which is made possible by the calibration method described in Sec. 4.4.1. A comparison is made with Mie theory using size distribution data and the refractive index information from Mulholland et al. (1985b) as discussed in the previous section. The truncated scattering cross section is determined from the angular results. These results are

also used in various single ratio approaches to probe the particle morphology. Finally the scattering results are expressed in terms of the scattering parameter,  $q$ .

### 5.3.1 SIZE DISTRIBUTION

#### 5.3.1.1 *Mass and Number Distribution*

The smoke aerosols examined in this study are an ensemble of many different sized particles, i.e. they are polydisperse. A lognormal distribution provides a good fit to the measured size distributions as it does for other aerosols (Hinds, 1982; Mulholland, 1995). Three parameters characterise the distribution: a total quantity corresponding to the area under the distribution curve, a mean diameter and distribution width or geometric standard deviation (GSD). The mass distribution of particle sizes is determined using the MOUDI characterised by the mass median aerodynamic diameter (MMAD) and GSD, while the HSLAS measured the number distribution characterised by the mean number diameter. The mass-size distribution is used in generating theoretical data from Mie theory. The total mass is not necessary for this computation only the characteristic diameter and geometric standard deviation. The MOUDI was used to sample smoke aerosol directly from the FEDE while the HSLAS was used to sample smoke aerosol that had been transported to it in the drum. A comparison of results from these instruments will be insightful to the effects of drum transportation.

The data treatment of the weighed stages of the MOUDI was done using two theoretically equivalent methods, the histogram and log-probability method. For the histogram method the weight of the collected particles is divided by  $\Delta \log D$  of the two adjacent bin aerodynamic diameters (i.e. their 50 % cut diameters), then plotted against the mid-range diameter of the stage to give the mass distribution as a function of aerodynamic diameter. The log-probability method plots the aerodynamic diameter of an impaction stage against the percentage of total mass less than the stage diameter on a log-probability graph. As the particle size distribution is assumed to be lognormal (Sec. 2.2.1), the histogram method

should show an almost Gaussian distribution and the log-probability method should result in straight-line plots. In **Figure 5.7** the histogram of the mass-size distribution is shown for the smoke aerosols from non-flaming beech wood, cotton lamp wick and polyurethane. Similarly in **Figure 5.8** the log-probability graph of the mass distribution is shown. In practical terms, if the data from about 5 % to 95 % is a straight line then the distribution is lognormal. In the case of the cotton lamp wick data, the upper four stages, which carried no mass, have been ignored. Similarly with the polyurethane, two of the upper stages carried negligible mass, and for this reason those stages do not appear as data in **Figure 5.8**. These stages would be at 100 % on the probability axis.

In the case of the log-probability plot, 50<sup>th</sup> percentile of the probability axis gives the mass median aerodynamic diameter, while 16<sup>th</sup> or 84<sup>th</sup> percentiles define the standard deviation or width of the distribution. The geometric standard deviation (GSD) is given by the ratio of the 84<sup>th</sup> to the 50<sup>th</sup> percentile diameters. It is implicit in this analysis that the distributions are lognormal. The relatively linear behaviour of data in **Figure 5.8** indicates that lognormal behaviour is a satisfactory assumption. In **Table 5.2** the results of the mass-size distribution analysis are shown for both methods. The main difference between the two in this study is in the determination of the GSD. The GSD is sensitive to the line of best fit in the log-probability method.

One aspect of the MOUDI is that the particles less than 0.056  $\mu\text{m}$  in aerodynamic diameter are collected on a final filter. In previously published results of this study (Weinert et al., 2001) it was found that about in 42 % of the total mass (8.2 mg total, collected over all the stages) of the cotton lamp wick smoke aerosol in the MOUDI was on this final filter. In a

**Figure 5.7:** Histogram of the mass-size distribution of the non-flaming fuel smoke particles. The data has been normalised by the peak value for ease of comparison of the distributions.

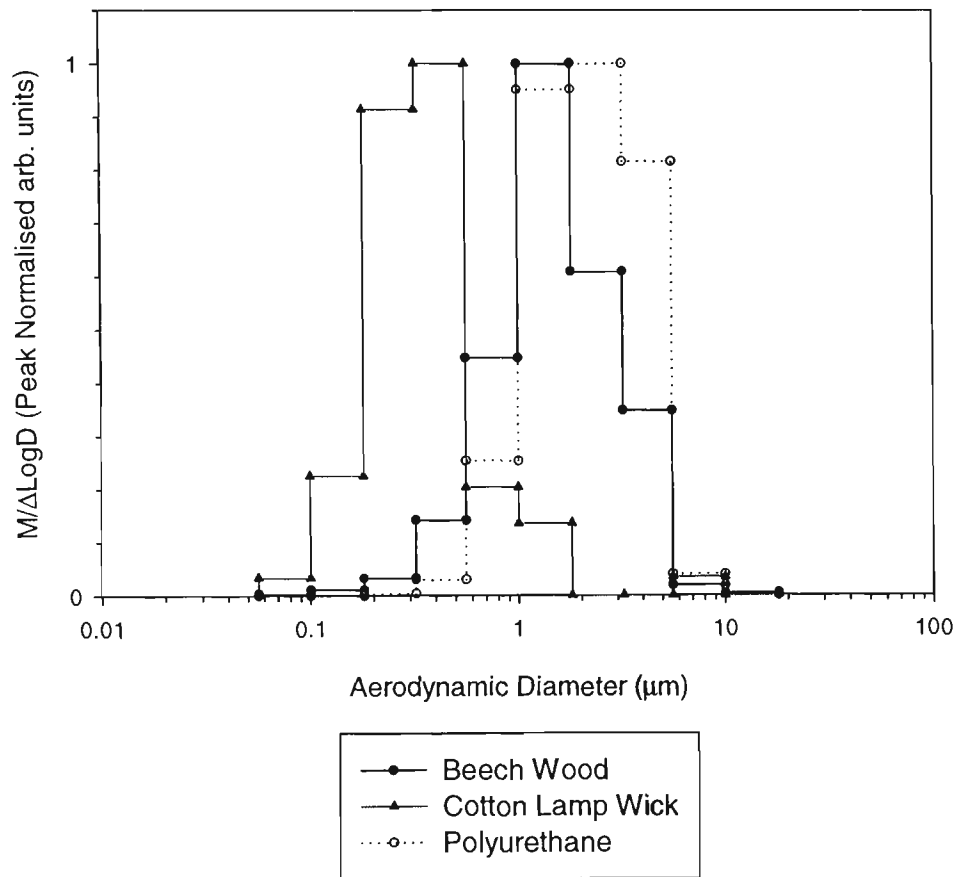


**Figure 5.8:** Log-probability plot of the mass-size distribution of the non-flaming fuel smoke particles.

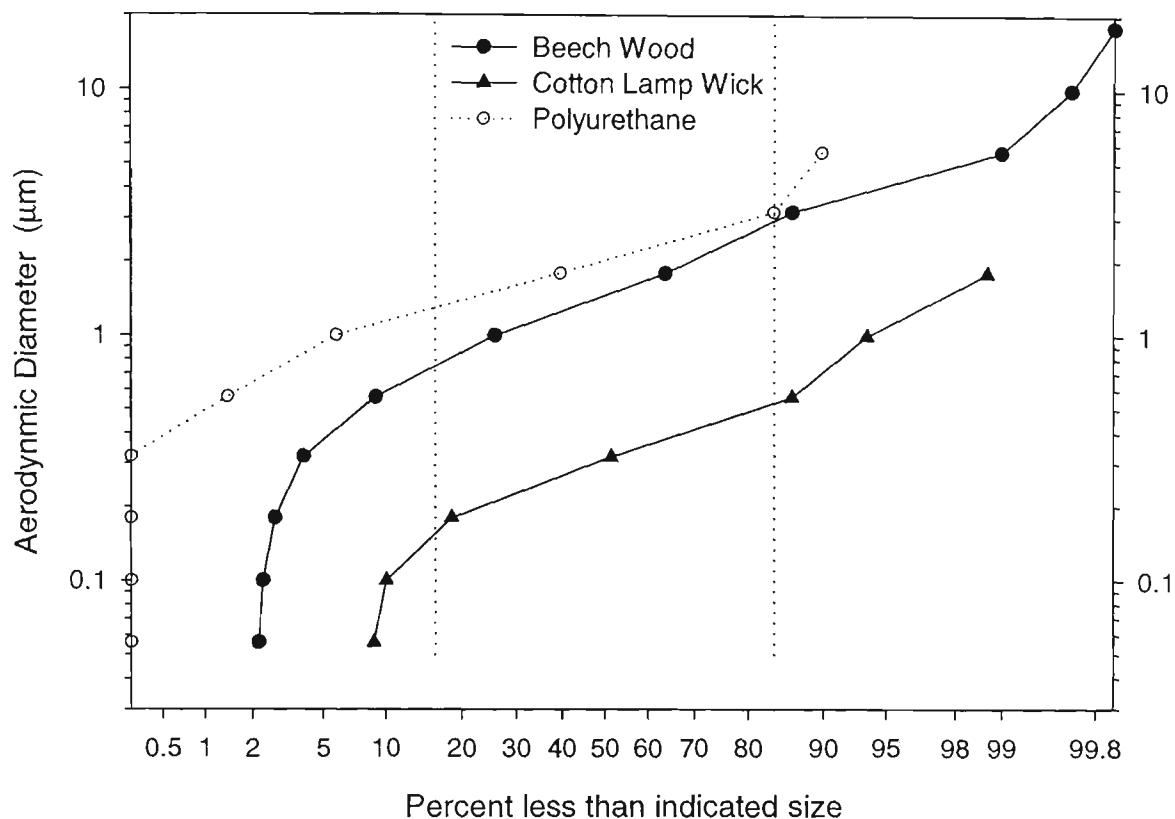


**Table 5.2:** Tabulated results of the mass median aerodynamic diameter and geometric standard deviations from the histogram and log-probability analysis methods.

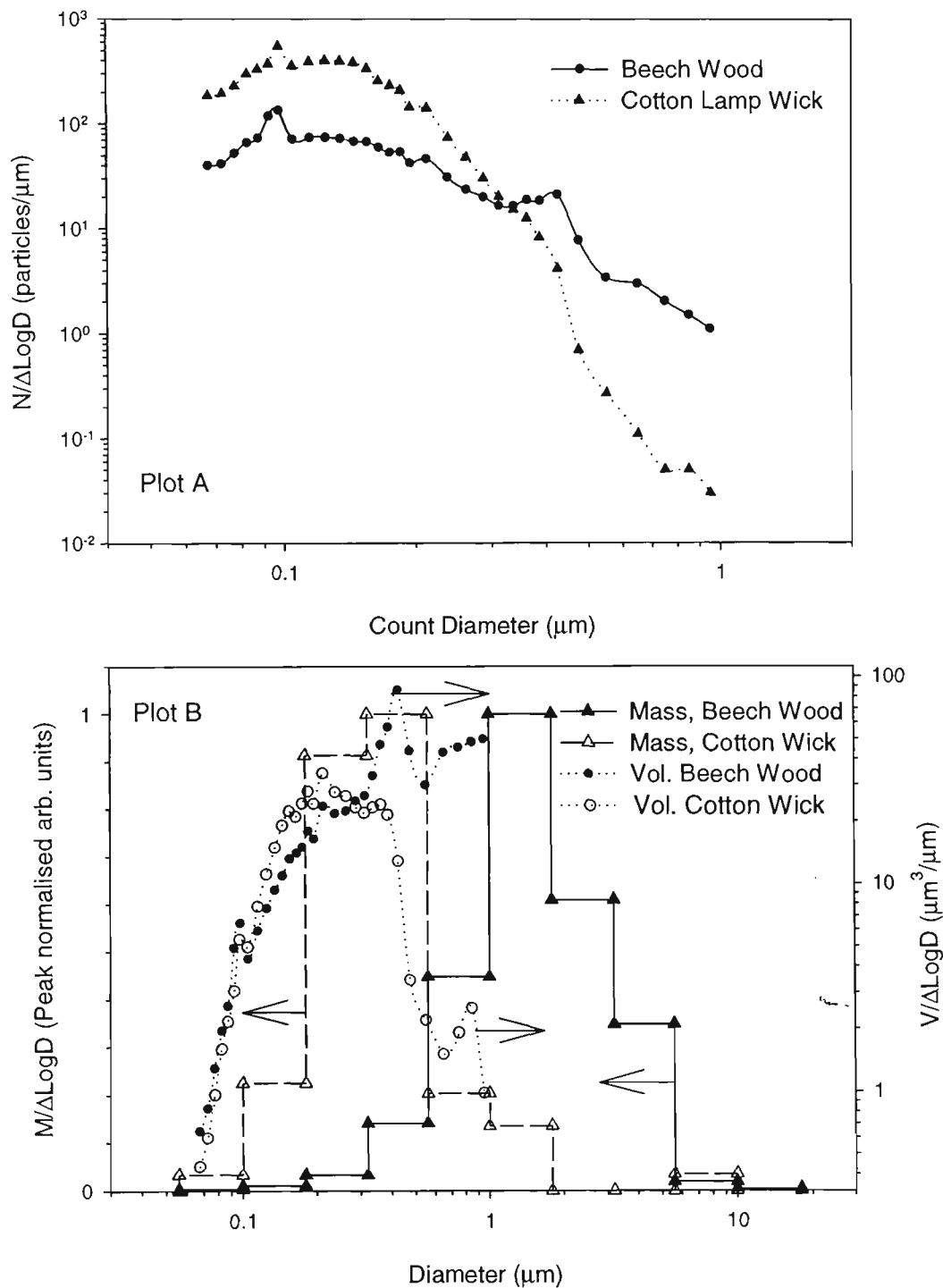
Fuel	Histogram		Log-Probability	
	Median Diameter ( $\mu\text{m}$ )	GSD	Median Diameter ( $\mu\text{m}$ )	GSD
Beech Wood	1.5	1.95	1.5	1.9
	1.5	2.0	1.5	2.0
Cotton Lamp Wick	0.35	2.0	0.31	1.7
Polyurethane	2.2	1.9	2.0	1.7
	2.3	1.8	1.85	2.3

later series of measurements (Weinert et al., 2002) the final filter of the MOUDI contained 8.8 % of the total mass (8.8 mg collected over all the stages) of the cotton smoke aerosol sampled. The distribution is still bimodal but only the larger mode is considered in this study as it is clearly characterised. The beech wood and polyurethane smoke aerosols were found to have only 2.2 % and 0.3 % of their total mass collected in the impactor, 16.3 mg and 5.6 mg respectively, on the final stage. Both of these fuels are considered single mode distributions.

Number distribution data for the beech wood and cotton lamp wick sampled from the drum and measured by the HSLAS is shown in **Figure 5.9a**. Unfortunately the HSLAS does not have the size range (lowest is  $0.0675\ \mu\text{m}$ ) to investigate the bimodal behaviour of cotton lamp wick smoke aerosol. Similarly the upper range stops at  $1\ \mu\text{m}$  so the number distribution of beech wood is truncated at the upper bound. Peaks in the HSLAS data are a result of changes in the width of the size channel from as small as widths of  $0.005\ \mu\text{m}$  for the  $0.07\ \mu\text{m}$  size bin, to  $0.1\ \mu\text{m}$  width for the  $0.7\ \mu\text{m}$  bin. In **Figure 5.9b** the number distribution has been converted into the volume distribution, the third moment of the distribution function (Hinds, 1982). The volume distribution is proportional to the mass distribution, related by the density, which allows the two to be compared as in **Figure 5.9b**. The volume distribution of the cotton lamp wick is in good agreement with the mass distribution, even considering that the volume distribution is of smoke sampled from the drum and not directly from the FE/DE, as the mass distribution was.

The beech wood volume distribution is inconclusive since a portion of the distribution lies outside the range of the HSLAS. The median volume diameter of the beech wood smoke aerosol is most likely larger than the cotton lamp wick. Any smoke aerosol coagulation or “aging” in the barrel would mainly effect the number-size distribution. The number of

**Figure 5.9:** (a) Number distribution of beech wood and cotton lamp wick smoke aerosol. (b) Comparison of mass and volume distribution data for the same fuels. The peaks have been normalised to aid comparison.



particles in an ensemble is sensitive to coagulation; however, the effect on volume or mass distribution is much less. Light scattering by particles is sensitive to the particle volume or mass.

The size distribution parameters from the log-probability graph are used as the input data for the Mie theory calculations. The assumption that the particles are of unit density is applied to all of the smoke aerosols from non-flaming fires.

### **5.3.1.2 Mass and Number Concentration**

The mass concentrations as measured in the FE/DE are shown in **Figure 5.10**. These data were collected during separate experiments conducted some time after the light scattering and size distribution experiments. These data and the number concentration data were used to demonstrate a distribution moment method for extracting size distribution information from an ionisation detector (Cleary et al., To be published). That study is attached as an appendix (**Appendix II**). Note that in that study the cotton lamp wick was ignited in a different pattern from the one used in this study. Cleary et al. used 32 wicks loaded in the wick-ignition device and ignited them in the following pattern. After a 60 second delay, four sets of 2 wicks were ignited at 200 second intervals, followed 200 seconds later by two sets of 4 wicks in a 200 second interval. This different sequencing resulted in a more gradual build up of smoke in the FE/DE and made dilution easier for CPC operation. The number concentration measured with the CPC is shown for the beech wood in **Figure 5.4b** and for the mass concentration in **Figure 5.10**. Both number and mass concentration for smoke aerosol from cotton lamp wick and polyurethane are presented in **Figure 5.11**.

**Figure 5.10:** The continuous mass concentration of the smoke aerosol from non-flaming fires measured in the FE/DE.

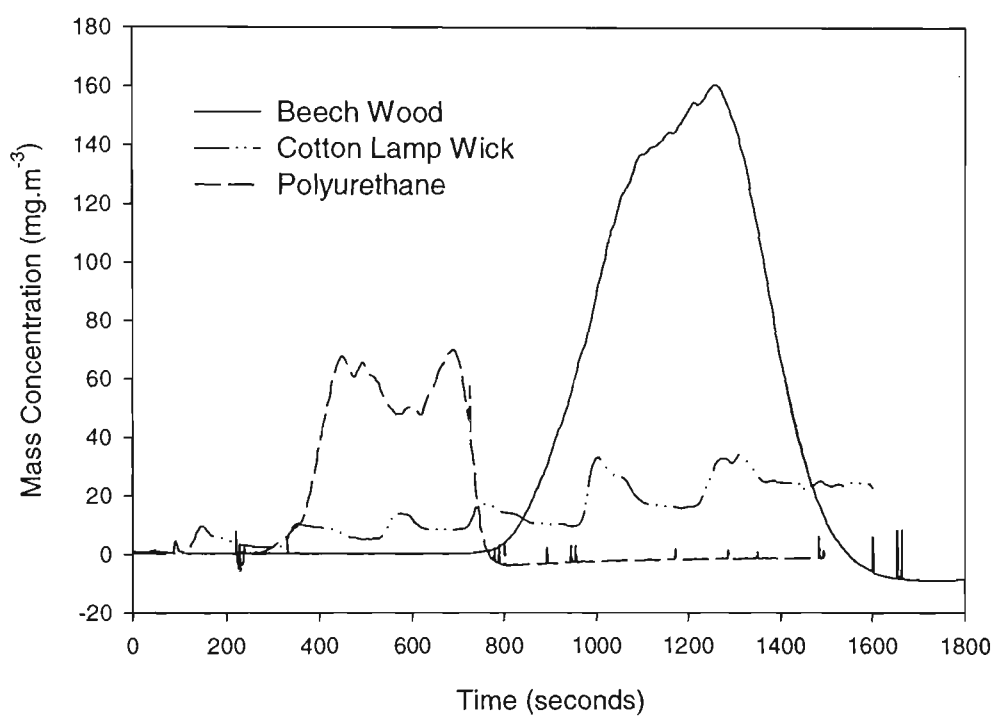
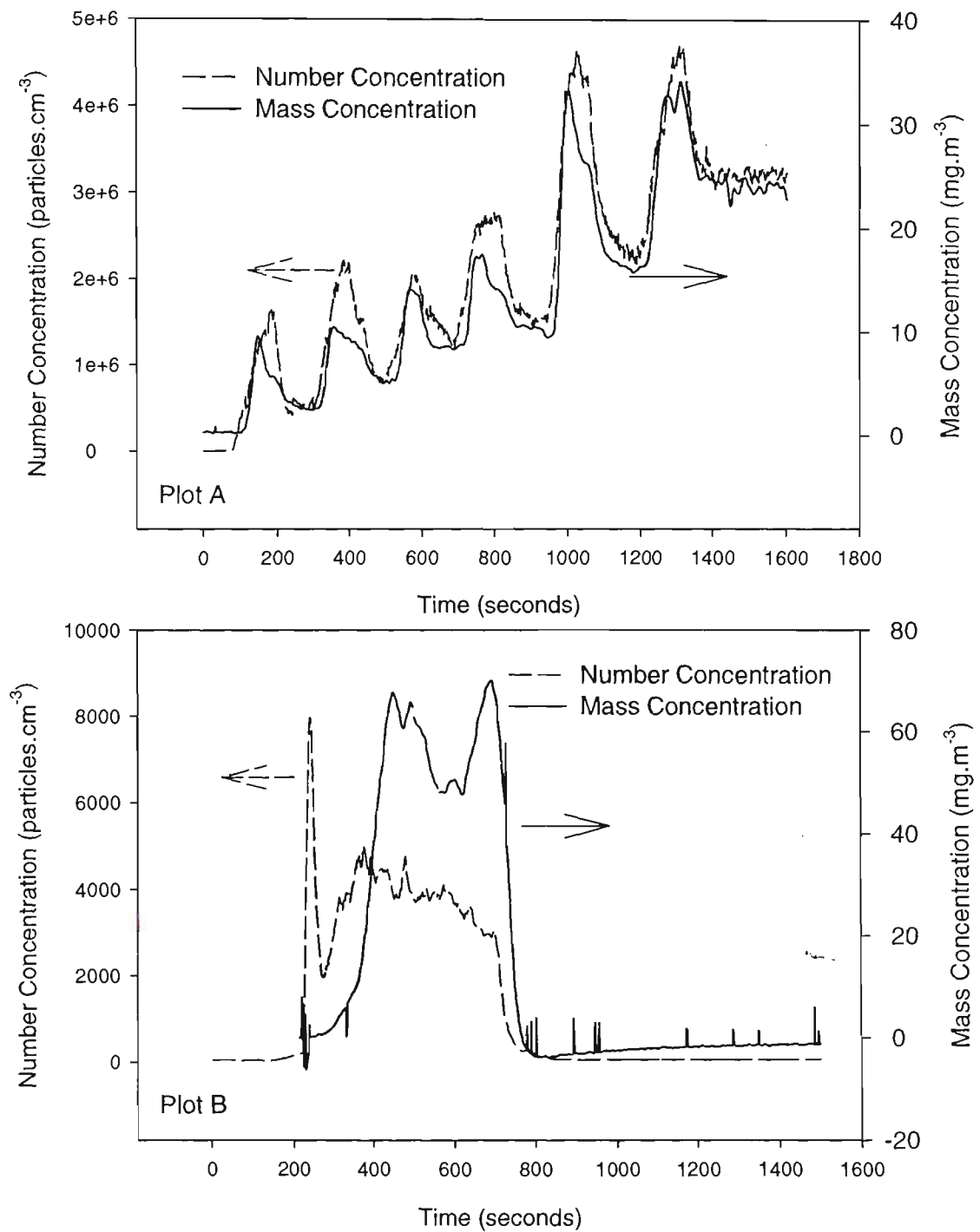


**Figure 5.11:** The continuous mass and number concentration of smoke aerosol from **a)** cotton lamp wick and **b)** polyurethane generated by Cleary et al (Cleary et al., To be published).



### 5.3.2 MASS EXTINCTION CROSS SECTION

Since the smoke particles from non-flaming fires have negligible elemental carbon content or other trace elements (Rau, 1989), then these particles will have a complex component of refractive index close to zero. Thus these particles will not absorb light but only scatter it. This means that the extinction cross section will be equal to the total scattering cross section, see **Equ. 2.21**. The total scattering cross section is not measured by the LAOF due to its truncated angular range. The extinction cross sections can be compared with the truncated scattering cross section determined in a later section, **Sec. 5.3.5**.

To determine the extinction cross section, which is one dependent parameter of “obscuration” measurements in the fire fields, the attenuation of a light beam passing through smoke needs to be made. The FE/DE has two such measuring instruments: the upper and middle lasers in the test section which record the attenuation ratio,  $I/I_0$ , as the smoke flows past. Where  $I$  is the laser signal at the detector after the beam has passed through the smoke, and  $I_0$  is the signal at the detector when no smoke is present. This ratio is then used to determine the mass extinction cross section since the path length of the laser is known and the mass concentration is given by the total mass in the MOUDI. The mass in the MOUDI has been sampled at a rate of about  $5 \times 10^{-4} \text{ m}^3 \cdot \text{s}^{-1}$  ( $30 \text{ L} \cdot \text{min}^{-1}$ ) for a known time, which gives a time averaged mass concentration. Using this information the average extinction cross section has been determined and presented in **Table 5.3**, from available data. The values in **Table 5.3** compare well with the results of Seader and Einhorn (Seader and Einhorn, 1976) who measured the mass extinction cross section at about  $4.4 \text{ m}^2 \cdot \text{g}^{-1}$  for various non-flaming smoke aerosols.

**Table 5.3:** Results of extinction coefficient estimates.

Fuel	Mass Extinction Cross Section (m <sup>2</sup> /g)
Beech Wood	4.2
	3.9
Cotton Lamp Wick	4.4
Polyurethane	2.8
	3.1

### 5.3.3 ANGULAR LIGHT SCATTERING

The angular light scattering results of smoke aerosols generated in this study are presented in the following sections. The presentation starts with angular scattering data presented in terms of the differential mass scattering cross section. These results are compared with results computed from Mie theory using the size distribution information above (Sec. 5.2.3). Following this the angular data is analysed using various methods to extract information about the particles scattering the light. Then truncated light scattering cross sections are determined and compared with extinction measurements detailed above. The angular data is then presented in terms of the scattering parameter. This builds a database from which the light scattering characteristics of non-flaming smoke aerosols can be compared with the other smoke and nuisance aerosols.

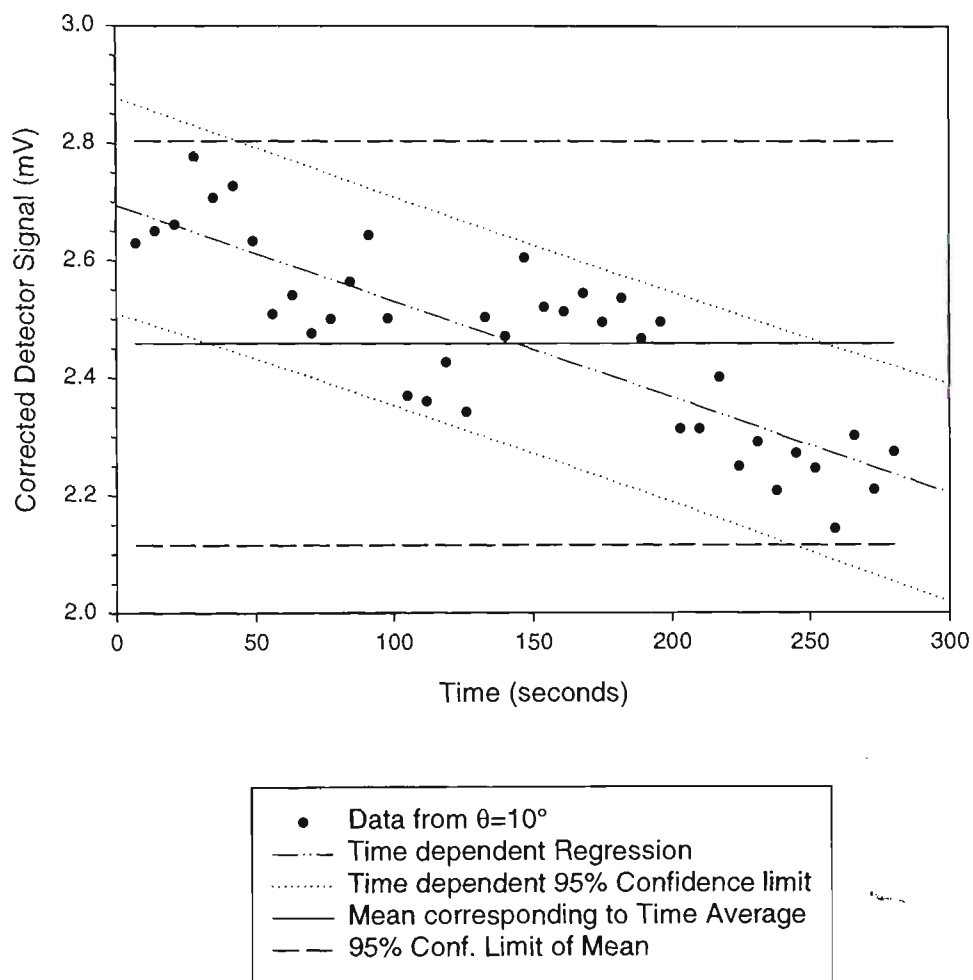
#### 5.3.3.1 Uncertainty analysis of drum dilution

Before proceeding with the angular scattering results it is important to understand the effects of sampling aerosols from the drum into the LAOF. To quantify the effects of this dilution and to understand the uncertainty it introduces into the scattering cross section measurements two simple tests were performed. The first was to collect some smoke aerosol in the drum, and then follow the procedure described above for connecting it to the LAOF.

The LAOF was set to monitor the scattering at an angle of  $\theta = 10^\circ$  for a relatively long period of time as smoke aerosol was drawn out of the drum. The results of this test are shown in **Figure 5.12**. The time averaged mean corresponds to the mass concentration measurement on which the differential mass scattering cross section is dependent (see **Equ. 4.8**). A decrease in particle number in the aerosol flowing through the scattering volume of the LAOF is clearly visible. This can be seen because scattering by a cloud of particles is directly proportional to the number of particles in the scattering volume and thus the mass concentration (**Sec. 2.4.3**). The time of this test data collection corresponds to approximately one third of the time over which a mass concentration measurement is normally made. From the data shown in **Figure 5.12** the relative standard uncertainty (one standard deviation) about the time averaged mean is estimated at 7 %, while the same quantity for the decreasing regression is nominally 4 %. If this analysis is extended over the full period of a mass concentration measurement, that is two scans of the two polarisation settings or about 12 minutes, by extrapolating the time dependent regression the time averaged mass concentration will have a relative standard uncertainty of about 18 %. This means that the uncertainty is increasing as the experiment continues for measurement of the differential mass scattering cross section. A typical scattering experiment would consist of two scans per time averaged mass concentration measurement. One scan takes about 6 minutes, and both polarisations took about 12 to 13 minutes for a single time averaged mass concentration measurement.

The second method of assessing the effect of dilution caused by using the drum made use of 802 nm diameter polystyrene spheres that had been introduced into the drum from the aerosol generator used in the calibration verification experiment. The drum was then connected to the LAOF and a total of five consecutive scans were made at the vertical-vertical polarisation setting. In **Figure 5.13** the volume corrected detector signal is

**Figure 5.12:** Light scattering results from the drum tests, aimed at quantifying the uncertainty in the mass concentration when using the drum as a means of aerosol transport to the LAOF. This figure shows the results for aerosol flowing through the scattering volume with the detector positioned at  $\theta = 10^\circ$ .



shown for consecutive scans of the polystyrene spheres from the drum. Mie theory results have been normalised to the first and fifth runs at a scattering angle of  $\theta = 5^\circ$  for comparison. From this data it can be seen that the main effect on the scattering signal is an increase in noise apparent in the scattering for  $\theta > 60^\circ$  in later runs from the drum. A consequence of this is a decrease in mass concentration after successive runs. Two mass concentration filter measurements were made during these five scans. The first corresponds to the average mass concentration for the first, second and third runs, and was determined at  $0.52 \text{ mg.m}^{-3}$ . The second mass concentration was made for runs four and five, and was found to be  $0.21 \text{ mg.m}^{-3}$ . A typical calibration verification experiment with 802 nm diameter spheres generated using the polystyrene sphere aerosol generator (Sec. 4.3.1.1) would have an average mass concentration of about  $2 \text{ mg.m}^{-3}$ , so there is substantial dilution of the polystyrene spheres. A threshold mass concentration of  $1 \text{ mg.m}^{-3}$  has been assumed in this study, all light scattering measurements were usually made at mass concentrations greater than this threshold.

In **Figure 5.14** the first run from the drum has been corrected in an approximate manner. The dilution rate from **Figure 5.12**,  $1.6 \times 10^{-3} \text{ mV.s}^{-1}$ , has been used along with an estimate of the time step between detector measurements. It was also necessary to normalise all the data in **Figure 5.14** to one at  $5^\circ$ , since the initial mass values are not known. The correction is an over estimate of the theory at large angles. The preferred method of examining the uncertainty in a light scattering measurement is by determining the standard uncertainty in repeat measurements, analogous to **Sec. 4.6.3.1**. This approach was used on the beech wood smoke to be discussed in the next section and has the benefit of containing the other components of uncertainty in the differential mass scattering cross section.

**Figure 5.13:** This plot shows the results of successive angular scans of polystyrene aerosol flowing from the drum into the LAOF.

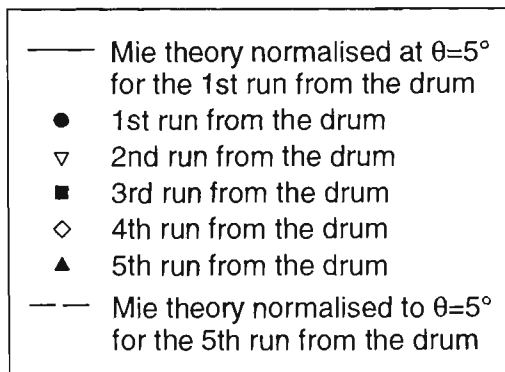
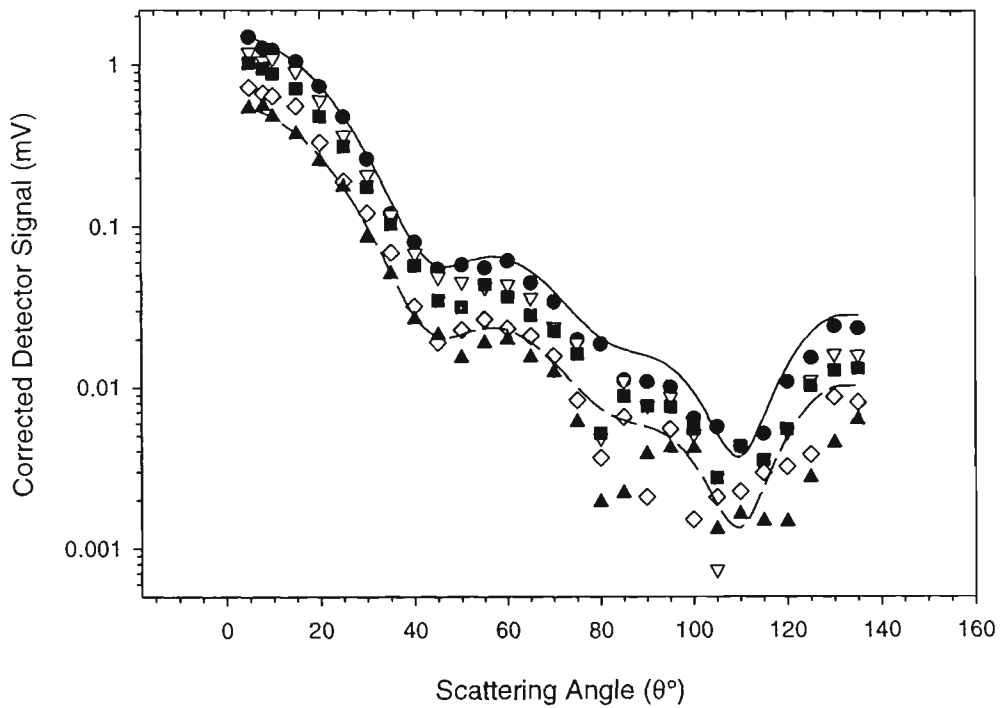
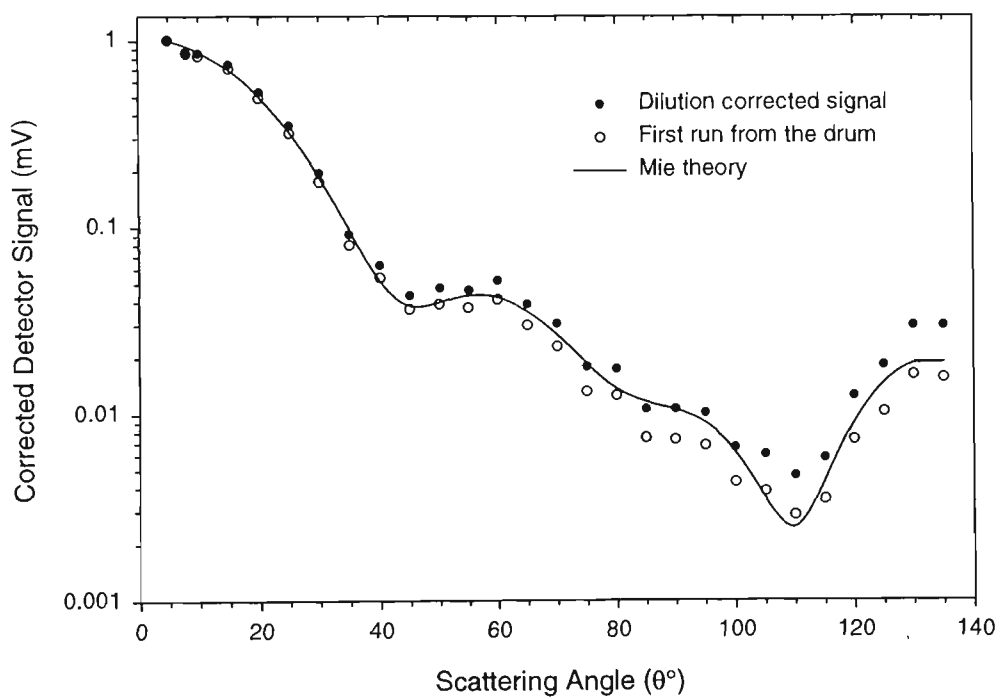


**Figure 5.14:** This figure shows a correction estimate for dilution of the first run from the drum.



### 5.3.3.2 Smoke aerosol from beech wood

Beech wood is a fuel that has been used successfully and often in the FE/DE due both to the ease of working with it and its connection to smoke detector standards. The result of the light scattering measurement from one of these experiments is shown in **Figure 5.15**. The average mass concentration of this smoke aerosol was  $4.2 \text{ mg}\cdot\text{m}^{-3}$ . One feature that is apparent in this result shown in **Figure 5.15** is that there is very little scattering structure in the experimental results. This is a direct consequence of the polydisperse nature of the natural aerosol and the averaging that occurs over the size distribution of particles (Sec. 2.4.3). Interestingly, there is interference structure in the Mie theory calculations shown in **Figure 5.15** although quite muted as a result of averaging over the size distribution when compared with monodisperse polystyrene spheres (see **Figure 2.1**). This is a result of the large number of interference features common to larger particles within the ensemble of particles.

The Mie theory has a steeper gradient for  $\theta > 5^\circ$  and under-predicts the experiments at higher angles. This is most likely due to uncertainty in the size distribution measurement and idealisation of a lognormal size distribution. Also the assumed refractive index could be affecting this result. These differences will affect comparison of observed and calculated data at specific angles. Both the functional form of the experimental results and the magnitude of the scattering are comparable with the calculated result. This is a good result given the two to three orders of magnitude variation in the signal.

A consequence of the ease of generating beech wood smoke aerosol is that a number of scattering experiments were completed. These results can then be analysed according to the variation in the measured differential mass scattering cross section. A total of six beech wood scattering experiments had been conducted and the repeatability calculated as defined in Sec. 4.6.3.1, Equ. 4.12 and 4.13. The standard uncertainty in repeat experiments of the

**Figure 5.15:** A plot of differential mass scattering cross section of smoke aerosol generated by pyrolysing beech wood blocks (point data). The results of Mie calculation are also shown (lines), calculated using the size parameters from log-probability plot, see **Table 5.2**, and  $m = 1.5 + i0$ .

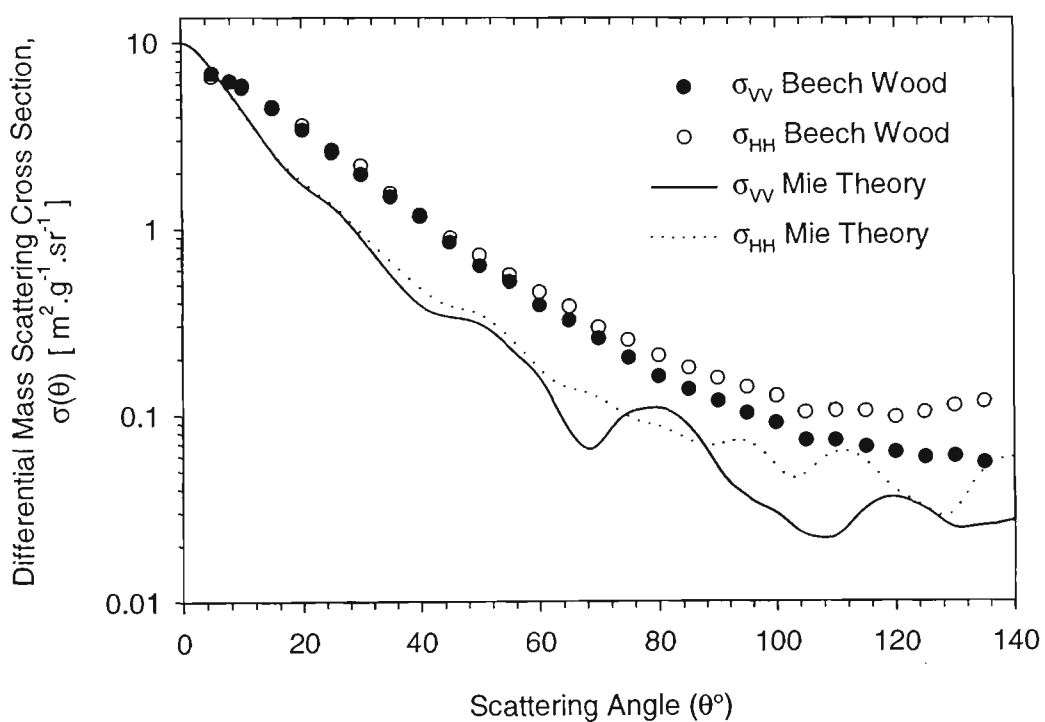


**Figure 5.16:** A plot of the average differential mass scattering cross section measurement for smoke aerosol from pyrolysed Beech Wood blocks based on repetitions. An experimental result, from **Figure 5.9** is also shown along with the 95% confidence limits of the repeatability.

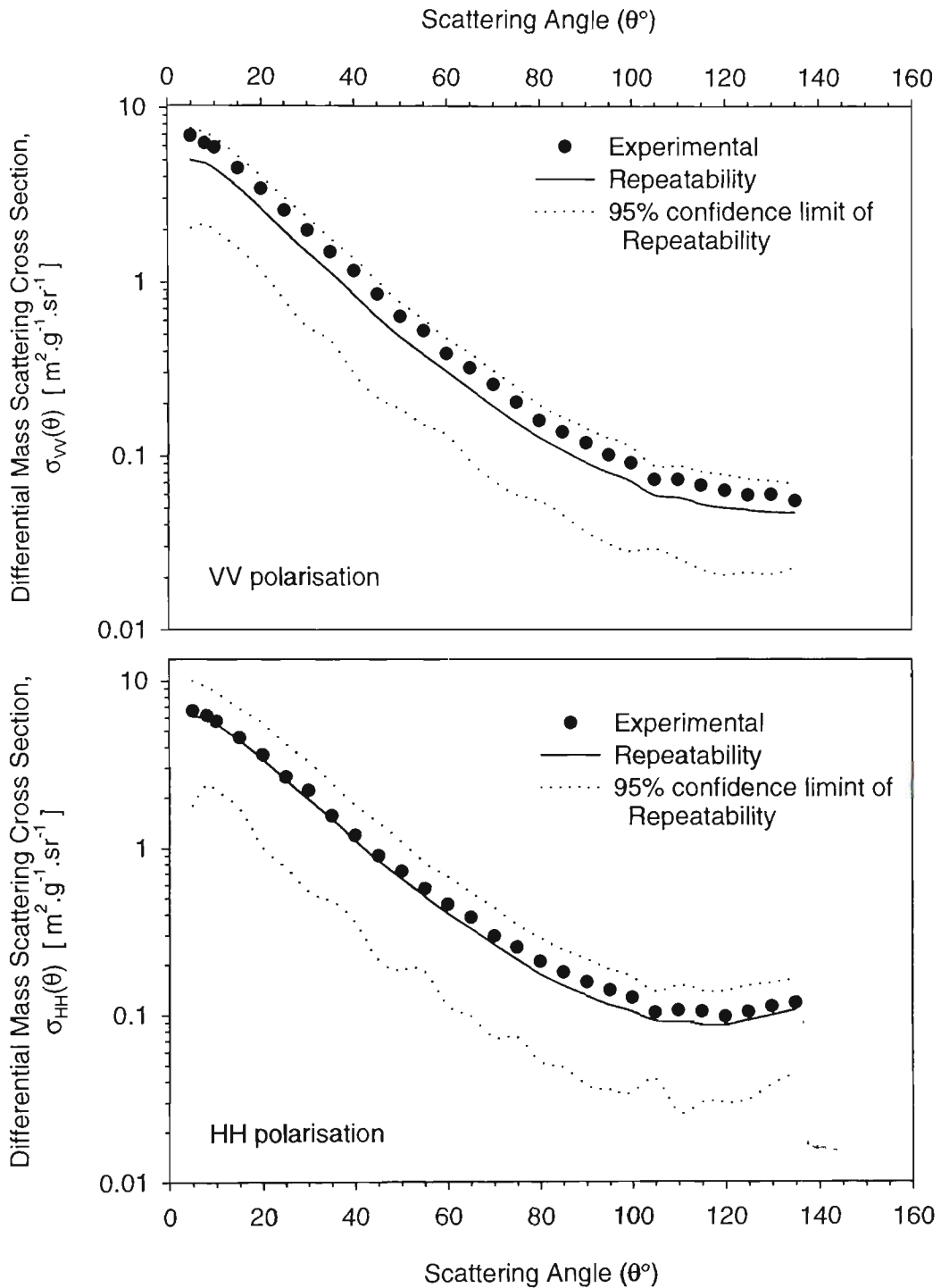


**Table 5.4:** Average mass concentrations for the Beech wood experiments used in the repeatability experiments.

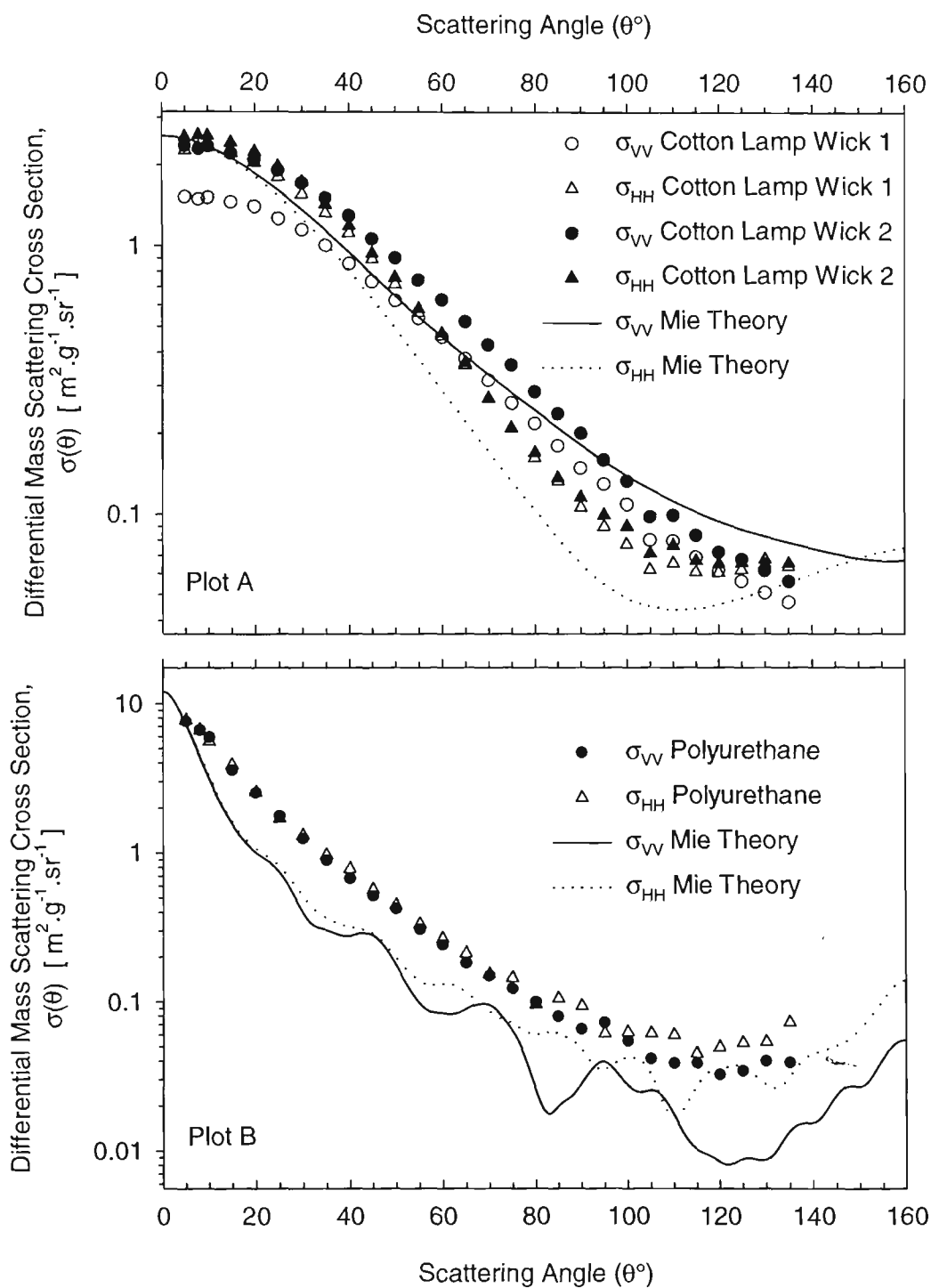
Beech Wood Experiment	Average Mass Concentration ( $\text{mg.m}^{-3}$ )
1	4.2
2	3.8
3	5.6
4	3.8
5	7.7
6	2.9

differential mass scattering cross section for the vertical and horizontal polarisation settings is about 28 % and 31 % respectively. The average of the scattering is shown in **Figure 5.16** along with the 95 % confidence limits of the repeatability. In addition results of one experiment from **Figure 5.15** are shown for comparison. A drop in mass concentration during mass sampling from the drum causes the great majority of this variation, as described in **Sec. 5.3.3.1**. It can be expected that similar variation would occur in other smoke aerosol experiments using the drum as a means of transport. The average mass concentrations of experiments used in this uncertainty analysis are given in **Table 5.4**. The relative standard deviation of this data set is about 37 %.

### **5.3.3.3 Smoke aerosol from smouldering cotton lamp wick**

Light scattering results for cotton lamp wick smoke aerosols are shown in **Figure 5.17a**, which shows two consecutive experiments sampling from the transport drum. The average mass concentration of these two experiments was measured at  $4.9 \text{ mg.m}^{-3}$  and  $5.0 \text{ mg.m}^{-3}$  for experiments 1 and 2 respectively. The first results were measured by making a scan of VV and then one for HH polarisation, which was then repeated. The smoke aerosol examined

**Figure 5.17:** A plot of the differential mass scattering cross section of smoke aerosol from a) smouldering cotton lamp wicks and b) smouldering polyurethane. Mie theory used the diameters from **Table 5.2** and  $m = 1.5 + i0$ .



had been collected from the same cotton lamp wick burn in the FE/DE. The first VV experiment (Expt. 1) deviates substantially from the other results for cotton lamp wick. Though whether this is due to an uncertainty in setting the polariser position or some other uncertainty, such as sampling from the drum, is not clear.

The general trend of the Mie theory results is in close agreement with the observed result for cotton lamp wick experiment number 2. The variation between the calculated result and the observed data occurs at larger angles, where VV and HH data cross. Comparison of the observed scattering magnitude (Expt. 2) is excellent over the range of scattering angles. The Mie results show no interference structure in the scattering at large angles as seen in the case of the beech wood. This is a result of the smaller sizes making up the cotton lamp wick distribution and the comparative lack of larger particles. These smaller particles scatter light as an ensemble in such a way that “averaging out” of interference features in the scattering is nearly complete. The interference features common to larger particles are not as efficiently averaged out. Another feature of these experimental results compared with those from beech wood is the smaller gradient in the forward scattering direction. This is a consequence of the small mean diameter of the particles when compared with the beech wood smoke aerosol.

#### *5.3.3.4 Smoke aerosol from smouldering polyurethane foam*

In **Figure 5.17b** the angular scattering result of smoke aerosol from smouldering polyurethane is presented along with the same data as a function of the scattering parameter in **Figure 5.17b**. The average mass concentration of smoke aerosol that resulted in this scattering result was only  $2.0 \text{ mg.m}^{-3}$ . This is a relatively low figure for the smoke aerosol experiments. The data shown in **Figure 5.17b** is from the first set of scans from the drum, a second set of polarisation scans from the drum were completed at an average mass concentration of about  $1.0 \text{ mg.m}^{-3}$ . This second run from the barrel is not shown as it

contains a strong noise effect due to the relatively low mass concentration. The onset of this mass-related noise can be seen in the data of **Figure 5.17b** at the larger angles,  $\theta \geq 100^\circ$  where the scattering cross section fluctuates.

The scattering results in **Figure 5.17b** indicate that the particles in the polyurethane smoke aerosol are polydisperse and definitely larger in mean size than the cotton lamp wick smoke aerosol. The indicator of the larger size is the steep slope of the data in the near forward direction. The size distribution results in **Table 5.2** show that the polyurethane also has a mass median aerodynamic diameter (MMAD) larger than the beech wood smoke aerosol. Influences of reduced mass concentration at the higher angles are probably the dominant factor over any possible interference features. The effect on light scattering of a reduced mass concentration is demonstrated above in **Figure 5.13**.

The comparison with Mie theory shows similar general behaviour to the beech wood results above. The Mie theory predicts a steeper gradient than is observed in the experimental results and that at scattering angles greater than  $5^\circ$  the theory under-predicts the observed scattering. The experimental results are also smoother than the Mie results that show interference features because of the large particles in the ensemble.

### 5.3.4 ANALYSIS OF ANGULAR SCATTERING

#### 5.3.4.1 *Forward scattering and asymmetry ratios*

In **Sec. 2.4.5** two ratios were introduced: the forward scattering ratio,  $\sigma_{vw}(5^\circ)/\sigma_{vw}(20^\circ)$ , and the asymmetry ratio defined as  $\sigma_{vw}(45^\circ)/\sigma_{vw}(135^\circ)$ . The forward scattering ratio allows the relative size of the scattering particles to be examined, and the asymmetry ratio is a measure of the relative strength of the forward to backward scattering.

The influence of relative smoke particle size on the light scattering results is presented in **Table 5.5**. The cotton lamp wick has a smaller mean particle size as the scattering is approaching that of Rayleigh scattering over the range of the ratio angles. Polyurethane aerosol is apparently slightly larger than beech wood smoke aerosol. These light scattering results are confirmed when compared with the size distribution parameters given in **Table 5.2**. The same ratio calculated from Mie theory is also given in **Table 5.5**.

**Table 5.5:** Forward scattering and asymmetry ratio for smoke aerosols generated in non-flaming fires.

Fuel	Forward Scattering Ratio		Asymmetry Ratio	
	Experimental	Theoretical	Experimental	Theoretical
Beech Wood	2.0	4.2	15.5	13.2
Cotton Lamp Wick (Expt.1)	1.1	1.3	15.7	10.0
(Expt. 2)	1.2		18.9	
Polyurethane	3.0	7.2	13.2	20.7

The other ratio that is of interest is the asymmetry ratio that represents the relative amounts of light scattered into a forward angle of  $45^\circ$  and a backward angle of  $135^\circ$ . The asymmetry ratio is also presented in **Table 5.5** along with the result from Mie theory. Traditionally it is a measure used by those interested in Mie scattering to determine if Mie theory is applicable to the particles that they are studying. This means that it is a recognised means of identifying very non-spherical particles and will become of more interest to this study as more non-spherical particles are examined in later chapters. There is no great difference between the experimental asymmetry ratios of non-flaming smoke aerosols in **Table 5.5**.

### 5.3.4.2 Polarisation Ratio

A means of discrimination that has been used in the recent past is the approach of polarisation light scattering as a means of differentiating soot from other aerosols. The work by Loepfe et al. (Loepfe et al., 1997) has examined the smoke aerosols generated in EN54 test fires: pyrolysed beech wood and smouldering cotton lamp wick. As mentioned previously, they used the degree of linear polarisation, a measure related to the polarisation ratio used in this study (see **Equ. 2.34**).

In **Figure 5.18** the normalised polarisation ratio results are shown. These results have been normalised to 1 at the scattering angle of  $\theta = 5^\circ$  to adjust for the differences seen between HH and VV signals. **Table 5.6** gives the polarisation ratio at an angle of  $\theta = 90^\circ$  for both experimental and theoretical values. The comparison between experiment and theory is not satisfying given the differences between these results for the differential mass scattering cross sections. For the cotton lamp wick, experiment number 1 has been used as shown in **Figure 5.17** and as well as used in **Table 5.6**. The polarisation ratio plotted in **Figure 5.17** does also indicate the relative size of the particles (Kerker, 1991). The smaller cotton lamp wick smoke results are those of smaller particles with a valley developing near  $90^\circ$ . The two larger smoke aerosols are generally similar to each other over the angular range. The polyurethane is affected by reduced mass concentration towards the higher angles, where the polarisation ratio shows large variations between the two (VV and HH) polarisation settings. By inspection of the results in **Figure 5.17b** it is clear that the effects are due to mass concentration falling below acceptable levels for those angles. The dotted line in **Figure 5.17** is for indication of data point location.

**Figure 5.18:** The polarisation ratio of smoke aerosol generated by beech wood blocks, cotton lamp wick (Expr. 1) and polyurethane foam. The ratio is normalised to 1 at  $\theta = 5^\circ$ .

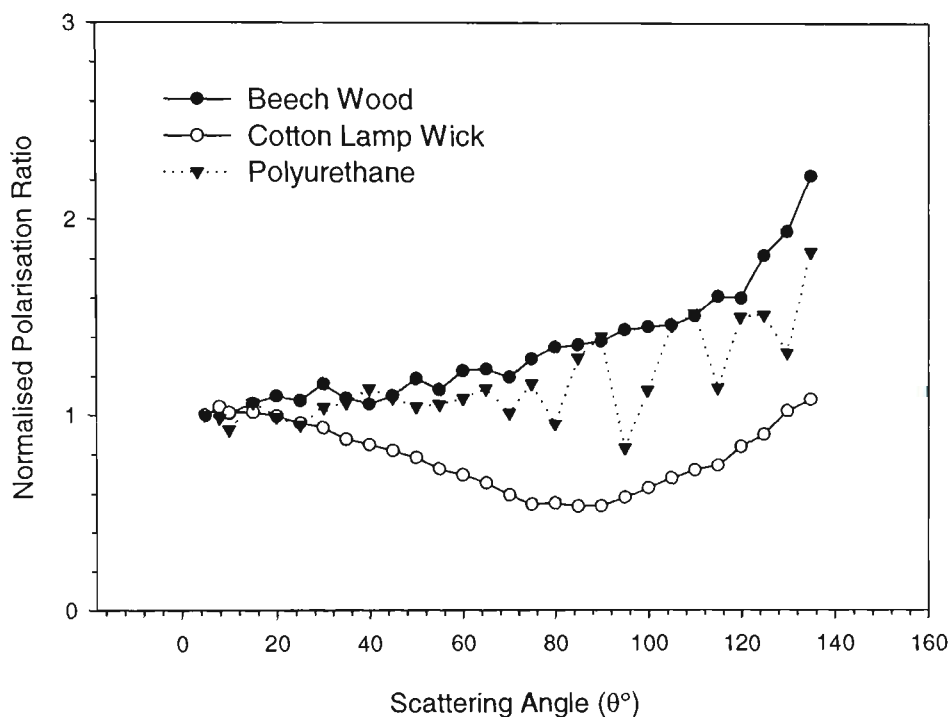


**Table 5.6:** Polarisation ratio at  $\theta = 90^\circ$  for the non-flaming fire generated smoke aerosols normalised to 1 at  $\theta = 5^\circ$ .

Non-Flaming Fuel	Polarisation Ratio	
	Experimental	Theoretical
Beech Wood	1.37	0.75
Cotton Lamp Wick (Expr.1) (Expr. 2)	0.48 0.57	2.77
Polyurethane	1.4	0.59

### 5.3.5 TRUNCATED LIGHT SCATTERING

The differential mass scattering cross section has been measured and presented above. That information is useful when angular scattering information is necessary, such as in the design of photoelectric smoke detectors and deciding at what angles to place the detector. The total scattering is another measure of interest, say when dealing with integrating light scattering instruments (nephelometers). The total scattering cross section is also equivalent to the extinction cross section when the particles scattering the light are non-absorbing. The extinction and the total scattering cross sections and their relationship to each other have been defined and discussed in **Sec. 2.4.2, Equ. 2.21**. The angular scattering measured for the three smoke aerosols above has been integrated by Simpsons Rule (Press et al., 1995), for the form

$$C_{T_{sca}} = 2\pi \int_5^{135} \frac{(\sigma_{VV}(\theta) + \sigma_{HH}(\theta))}{2} \sin(\theta) d\theta \quad (5.1)$$

which gives the truncated ( $5^\circ$  to  $135^\circ$ ) mass scattering cross section,  $C_{T_{sca}}$ , of the smoke particles. The summation of the two polarisation components gives  $C_{T_{sca}}$  as the cross section of scattered unpolarised light, with linear components of polarisation in the vertical and horizontal planes. In **Table 5.7** the truncated mass scattering cross section is presented for the smoke aerosols from the non-flaming fuels examined above. In the case of the beech wood a calculation of  $C_{T_{sca}}$  has been made using the mean of the repeat experiment data set; the mean of the experiments is the solid line in **Figure 5.16**. Also presented in **Table 5.7** are the Mie theory results for the particles based on the size distribution results from the log-probability plots, see **Table 5.2**. Both the truncated ( $\theta = 5$  to  $135^\circ$ ) and total ( $\theta = 0$  to  $180^\circ$ ) mass scattering cross sections are given in **Table 5.7**.

The measured scattering cross sections in **Table 5.7** are predominantly larger than the computed values. This is particularly the case for the larger smoke aerosols, beech wood and polyurethane. A trend that is apparent in **Figure 5.15** and **Figure 5.17b** as the experimental results tend to larger values for  $\theta \leq 40^\circ$ . The value determined for repeat experiments of beech wood compared with the single experimental result indicates clearly the effect of uncertainty.

**Table 5.7:** Experimental and Theoretically calculated total ( $\theta = 0$  to  $180^\circ$ ) and truncated ( $\theta = 5$  to  $135^\circ$ ) mass scattering cross section for the smoke aerosols from the non-flaming fuels. Mie theory used the diameters from **Table 5.2** and  $m = 1.5 + i0$ .

Fuel	Experimental Truncated ( $\text{m}^2/\text{g}$ )	Theoretical Truncated ( $\text{m}^2/\text{g}$ )	Theoretical Total ( $\text{m}^2/\text{g}$ )
Beech Wood	6.2	3.11	3.46
Beech Wood (repeatability)	5.2	as above	as above
Cotton Lamp Wick R1	4.3	4.17	4.34
Cotton Lamp Wick R2	5.3	as above	as above
Polyurethane	4.2	1.99	2.3

### 5.3.6 SCATTERING PARAMETER

#### 5.3.6.1 *q-slope*

Another method of presenting light scattering information is in terms of the scattering parameter,  $q$ , discussed in **Sec. 2.6** along with expected scattering behaviour in terms of that parameter. The scattering parameter is traditionally not applied to spherical (Mie theory) particles, but in this study it is proposed as a possible means of smoke aerosols discrimination. The scattering parameter use is traditionally limited to the VV component for soot agglomerates, dealt with in the next chapter. For dipoles the HH component is

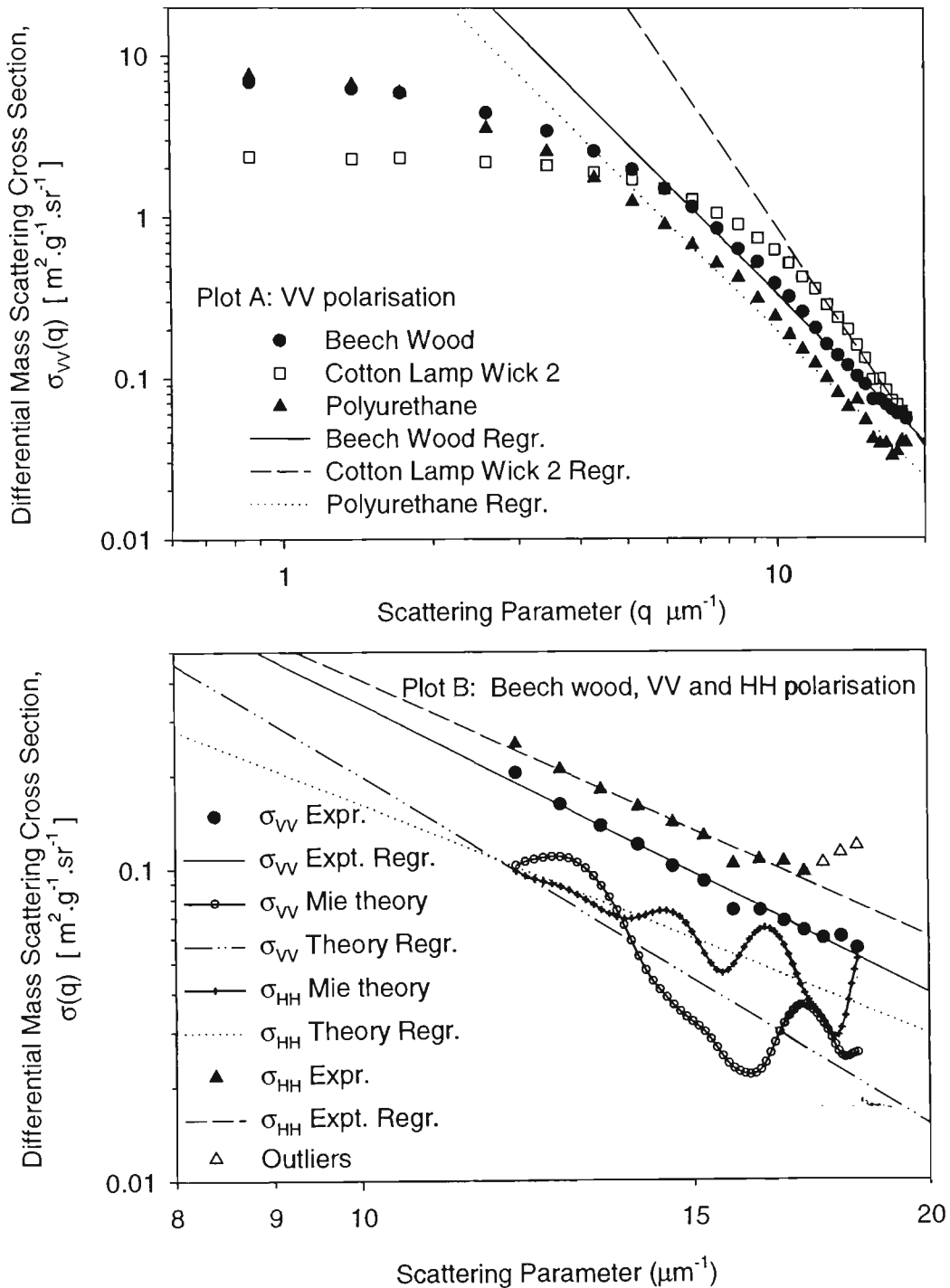
simply related to the VV component, that is Rayleigh scattering. In the case of larger spherical scatterers this simplification does not exist although the results above indicate that the experimental measurements of VV and HH will not vary dramatically in overall form when represented in terms of the scattering parameter.

In **Figure 5.19a** the results of the differential mass scattering cross section as a function of scattering parameter for the three non-flaming fire generated smoke aerosols are shown. This plot also includes linear regression lines (first order) for the scattering parameter range of  $12 \leq q \leq 18.3 \mu\text{m}^{-1}$  ( $75^\circ \leq \theta \leq 135^\circ$ ), for graphical comparison of the slopes of the regressions. The slope generated by the regressions over this range is simply referred to as the q-slope in this study. In **Figure 5.19b** the regressions analysis for the case of beech wood, both experimental and theoretical, is shown for the two polarisation settings, HH and VV. The q-slopes of each non-flaming smoke aerosol are determined in the manner demonstrated in **Figure 5.19b**. The slopes of this regression analysis are tabulated in **Table 5.8**.

Note that the regression for  $\sigma_{HH}(q)$  of beech wood in **Figure 5.19b** has had the last three points removed for demonstration only. If they were not removed the q-slope would be -2.1 instead of -3.1, which highlights the sensitivity of the q-slope to the range over which it is determined. The range of  $12 \leq q \leq 18.3 \mu\text{m}^{-1}$  is chosen simply because it is a fixed range at large q for which the aerosols can be compared. It also avoids the transitions at smaller q values (see **Equ. 2.47**).

In **Table 5.8**, q-slope analysis results of the non-flaming smoke aerosols are shown for both experimental and theoretical scattering data at VV and HH polarisation settings. The regression correlation coefficients are also shown for the regression analysis range, which in all cases was  $12 \leq q \leq 18.3 \mu\text{m}^{-1}$ . As can be seen in **Figure 5.19b** the theoretical results for

**Figure 5.19:** A plot of the differential mass scattering cross section of smoke aerosols from non-flaming fires as a function of the scattering parameter for polarisation settings a) VV and b) both experimental and calculated results beech wood for VV and HH polarisations.



the larger particles leads to rather substantial interference features that weaken the regression analysis of this data, leading to smaller correlation coefficients in the case of the HH polarisation. The experimental HH results are also subject to variation due to an increase in  $\sigma_{HH}(q)$  at larger values of the scattering parameter. Thus the regression analysis has a lower correlation coefficient for each smoke aerosol. Determining the q-slope of the HH data after removing some of these outlier values of  $\sigma_{HH}(q)$  leads to q-slope values closer to the VV result as demonstrated for beech wood in the last paragraph.

**Table 5.8:** Results of q-slope regression analysis for experimental and theoretical scattering results at both polarisation settings, VV and HH. The linear correlation coefficient of each q-slope regression analysis is given in brackets next to each q-slope.

Fuel	Experimental q-slope (negative)		Theoretical q-slope (negative)	
	VV	HH	VV	HH
Beech Wood	3.1 (0.98)	2.1 (0.83)	3.7 (0.73)	2.5 (0.79)
Cotton Lamp Wick (Expt. 1)	4.2 (0.99)	2.9 (0.88)	3.2 (0.99)	2.2 (0.7)
Cotton Lamp Wick (Expt. 2)	4.6 (0.99)	2.9 (0.94)	3.2 (0.99)	2.2 (0.7)
Polyurethane	3.1 (0.9)	2.1 (0.7)	3.8 (0.66)	2.3 (0.59)

### 5.3.6.2 Envelope approach to the q-slope

The range used to determine the q-slope above is subjectively restricted, essentially chosen to avoid the transition region at smaller q values (and to make use of all of the data at large angles. The set range is also useful, as fixed position detectors are more easily applicable to smoke detector applications. The range of q values can be chosen to emphasise the envelope of the scattering function. This range is chosen specifically to avoid any features of the

scattering that deviate from a straight line in the experimental data, which occurs at large angles. This procedure widens the  $q$  range in most cases compared to the range used above since these ranges include smaller values of  $q$  in the calculation of the slope. Also, only the VV component is used in this envelope analysis. The resulting values from the experimental and calculated results are given in **Table 5.9**.

In **Table 5.9**, pyrolysed beech wood blocks and smouldering polyurethane have experimental and Mie theory results that are closer than those in **Table 5.8**. This is due to ignoring fitting of the linear regression to the calculated results. Choosing an envelope of the scattering data from polyurethane smoke aerosol in this manner has dramatic effect on the  $q$ -slope. The cotton lamp wick data converges for both experiments using their very similar ranges, a good result. The correlation coefficients for the Mie theory improve, as more data is made available by extended ranges of  $q$ , reducing the influence of the interference features in those results.

**Table 5.9:** Results of  $q$ -slope envelope analysis using linear regression for experimental and theoretical scattering results at polarisation setting, VV. The linear correlation coefficient of each  $q$ -slope regression analysis is given in brackets.

Fuel	Scattering Parameter, Range in $q$ ( $\mu\text{m}^{-1}$ )	Experimental $q$ -slope (negative) VV	Theoretical $q$ -slope (negative) VV
Beech Wood	6.79 to 18.3	3.2 (0.99)	3.1 (0.91)
Cotton Lamp Wick (Expt. 1)	11.4 to 18.3	4.1 (0.99)	3.1 (0.99)
Cotton Lamp Wick (Expt. 2)	9.92 to 18.3	4.1 (0.99)	3.1 (0.99)
Polyurethane	8.4 to 17.2	3.6 (0.99)	3.5 (0.83)

## 5.4 DISCUSSION

The light scattering results above demonstrate the feasibility of measuring the differential mass scattering cross section,  $\sigma(\theta)$ , for non-flaming fire generated smoke aerosols. The uncertainties in the results have increased in comparison with the uncertainties determined in the last chapter. The time averaged mass concentration measurement from the transport drum is the main contribution to this uncertainty. Introducing a reference channel by which the mass concentration variation can be monitored would reduce the mass concentration uncertainties. This approach has been used by Holland and Gagne (1970) although their methods were different.

The Mie theory calculations are based on the measured size distribution parameters, **Table 5.2**, and refractive index of  $m = 1.5 + i0$ . Uncertainties in these quantities lead to differences in the calculated results when compared with the observed scattering results. Deviation of the smoke aerosol's size distribution from lognormal might be a factor in this uncertainty. The magnitude of the scattering by smoke aerosols generated by beech wood and polyurethane is over and under-predicted at small and large angles respectively, by the Mie theory. These differences make comparison of theory and experiment difficult for the forward scattering, asymmetry and polarisation ratios. The general trend and magnitude of the experimental results is in fair agreement with the theory. For the smaller smoke aerosol particles from cotton lamp wick, the agreement is particularly good.

Using the observed scattering, differentiation of smokes with respect to relative size is apparent with use of both the forward scattering ratio and the polarisation ratio. The polarisation ratio results are in agreement with the study completed by Loepfe et al. (Loepfe et al., 1997), where they observed a similar difference between beech wood and cotton lamp wick smoke aerosols as was observed in this study. The asymmetry ratio does not

discriminate between the smoke aerosols generated by non-flaming fires examined in this study.

A regression analysis of the differential mass scattering cross section over a restricted range of the scattering parameter has yielded the q-slope ( $12 \leq q \leq 18.3 \mu\text{m}^{-1}$ ). The q-slope of the envelope is a range chosen to highlight linear behaviour. One fact that is particularly apparent from this analysis is that the range of q values over which the slope is determined has significant affect on the result. Apparently the VV polarisation results are better fitted with the regression analysis method for the fixed range and envelope q-slope. The HH results increase at large q values complicating the regression analysis. Interestingly the interference structure in the theoretical results complicates the regression analysis for the fixed range q-slope. Using an approach aimed at highlighting the envelope of the scattering function a variable range reduces the influence of the interference features. For the larger smoke aerosols defining a set range reveals a tendency of larger particles to approach q-slope values of about -3, while a variable range defining an envelope slope results in values between -3 and -4. In the case of the small cotton lamp wick smoke particles the q-slope is about -4. What remains to be seen is how this quantity will compare with the same measure for soot and nuisance aerosols. These aerosols are dealt with in the following chapters and finally compared in the penultimate discussion chapter (**Chapter 8**).

## SMOKE AEROSOL FROM FLAMING FIRES

### 6.1 INTRODUCTION

This chapter presents the results of light scattering measurements of smoke aerosol generated by flaming fuels, simply called soot. Smoke aerosol is the generic term used in this study to include gas borne solid and liquid particulate in smoke from fires. The term soot is specific to graphitic light-absorbing smoke aerosol generated in flames. This study limits itself to over-ventilated conditions where the oxygen supply is high, as opposed to under-ventilated fire conditions where the oxygen supply to the combustion zone is limited in some way. Flaming fires generate carbonaceous black soot when combustion conditions in the flame do not completely oxidise the fuel. Soot from a laminar diffusion flame will change from graphitic-carbon to partly organic as the flame becomes fuel rich. The agglomerate structure becomes more agglutinated, and the elemental carbon content decreases from 90 % to about 50 % (Leonard et al., 1994). Burning vegetated wood will produce predominantly “whitish” smoke aerosol in a flaming fire since the content of water and condensable organics is usually high (Mulholland et al., 1989). An under-ventilated closely packed crib test (a standard fire used in laboratories) produces whitish smoke due to pyrolysis dominating over flaming combustion (Bryner and Mulholland, 1991). In the case of smoke detection an under-ventilated fire represents a fire that has usually grown to a size beyond detector based warning. The design basis of a smoke detector is an over-ventilated fire, a small flaming fire in a much larger space. Thus the post-flame soot from this type of fire is studied here.

The chemical formation of soot has been of interest for many years and it is not the place of this study to provide a review of that work as many such reviews are already available (Wagner, 1979; Haynes and Wagner, 1981; Glassman, 1988; Simmons, 1995). What follows below is a summary of the general aspects of soot formation of interest to this study, which

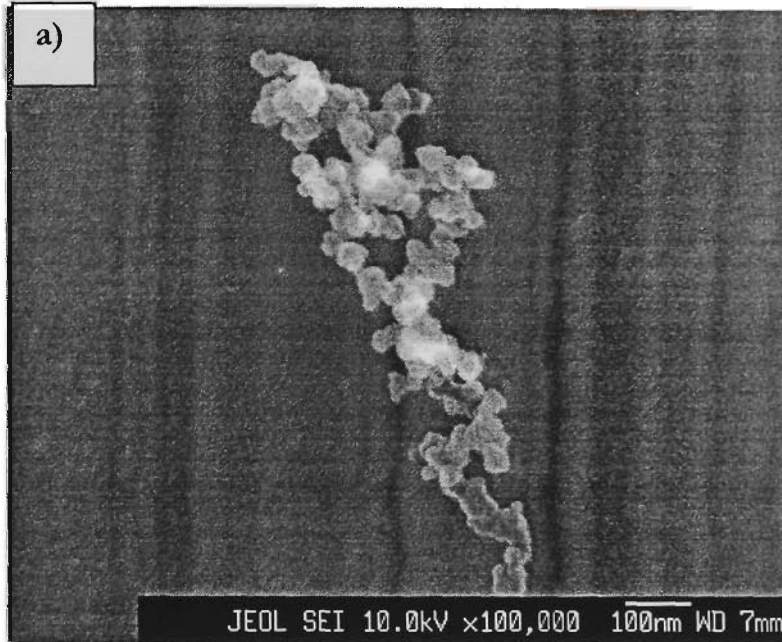
tends to be physical as opposed to chemical. The physics of soot formation is now well understood as will be discussed below, but the role of chemistry in the very early stages of soot formation is complex and an area of on-going research.

The formation of soot starts with the thermal decomposition (pyrolysis) of the fuel into gaseous products. These gases undergo high temperature reactions which produce many saturated and unsaturated hydrocarbon radicals and ions. These compounds then go through different processes of cyclisation and polymerisation, with the possibility of subsequent fragmentation, to form incipient soot particles. Additional growth of the spherule occurs through surface growth and then coalescent collisions. Finally dehydrogenation strips the hydrogen from the hydrocarbons increasing their viscosity and producing the graphitic soot primary particle (Palmer and Seery, 1973; Calcraft et al., 1975; Dobbins et al., 1998). Which of the chemical processes are dominant and under what conditions is yet to be fully determined (Simmons, 1995).

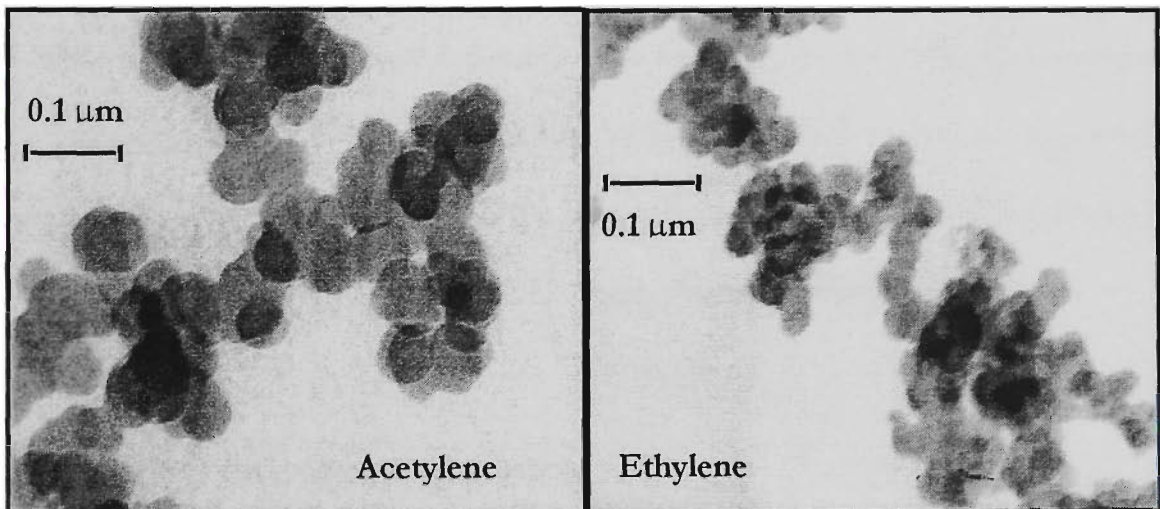
All these processes are likely to be occurring in parallel to some extent and by any sequence of these events the primary soot particles are formed. The morphology of the primary soot particle is often described as a graphite-like spherical particle, ranging from 10 to 80 nm in diameter. The term graphite-like is only applicable in the sense that the particle's microstructure has graphitic layering in shells rather than plates. The primary particles look like onions with discontinuities through the layers (Palmer and Seery, 1973). These primary particles collide with other primary particles or small clusters in the flame to form chain-like soot agglomerates, as seen in **Figure 6.1**.

The shape of the soot agglomerates is not trivially equivalent to a sphere for which the aerodynamic diameter can be determined (Cleary, 1989). Electron microscopy methods are

**Figure 6.1:** (a) A field emission scanning electron microscope image of a small soot particle from flaming polyurethane foam (this study). (b) Transmission electron microscope image of soot from turbulent acetylene and ethylene flame burners (Mulholland and Choi, 1998).



b)



perhaps the best method of determining soot agglomerate size distributions. The radius of gyration of soot agglomerates can be obtained through small angle scattering and the fractal dimension can be obtained from scattering at larger angles. The radius of gyration is examined in this study with post-flame agglomerates as a function of fuel flow rate and as a function of time as the soot agglomerates grow.

There have been a substantial number of studies of light scattering by soot agglomerates; those related to post-flame soot are of particular interest to this study. Zhang et al. (1988) conducted a light scattering study of the fractal dimension during agglomerate growth of soot extracted from a premixed methane flame. Mulholland and Choi (1998) have conducted extinction cross section and total scattering to extinction ratio measurements for acetylene and ethylene using the TCRN capability of the LAOF. Koylu and Faeth (1994) have conducted experiments measuring differential, total and extinction cross sections of post-flame soot of propylene, acetylene, ethylene and propane. Their differential scattering results are normalised and based on absolute intensity calibration using Rayleigh scattering. The differential data was also used to determine the fractal dimension of the soots generated. The measurement of the fractal dimension of the flame generated soot is also important in our study as it is one potential method for discriminating soot from the other smoke and nuisance aerosols examined, analogous to the q-slopes determined in the last chapter.

## **6.2 METHOD**

### **6.2.1 SOOT GENERATION AND TRANSPORT**

Soot generated for this study was from acetylene, ethylene, propylene and heptane, all burning in over-ventilated conditions. The majority of these fuels are gaseous, while the heptane is a liquid fuel. As discussed in **Sec 2.5.1** the universality of soot means that as long as the fire is well ventilated then the soot particles formed will be carbonaceous agglomerates with fractal dimensions characterising their morphology. The use of the gas fuels is quite

representative of the great majority of flaming fires when concerned with the production and investigation of soot. Solid fuels will also produce soot agglomerates as shown in **Figure 6.1a** when burning with an over-ventilated flame.

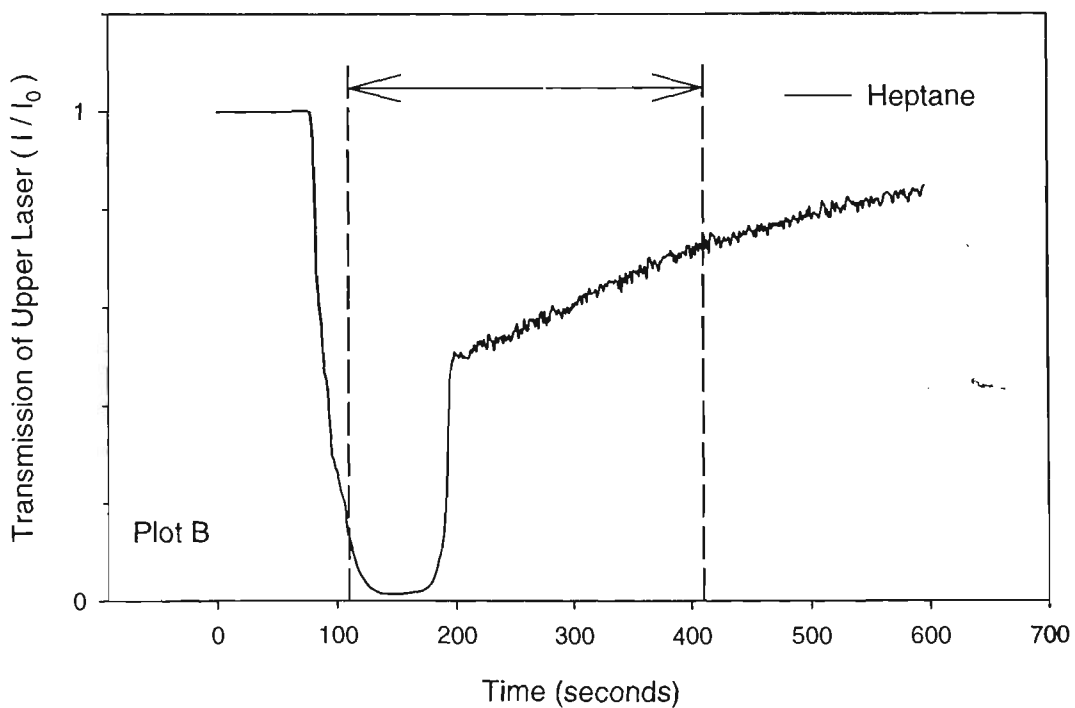
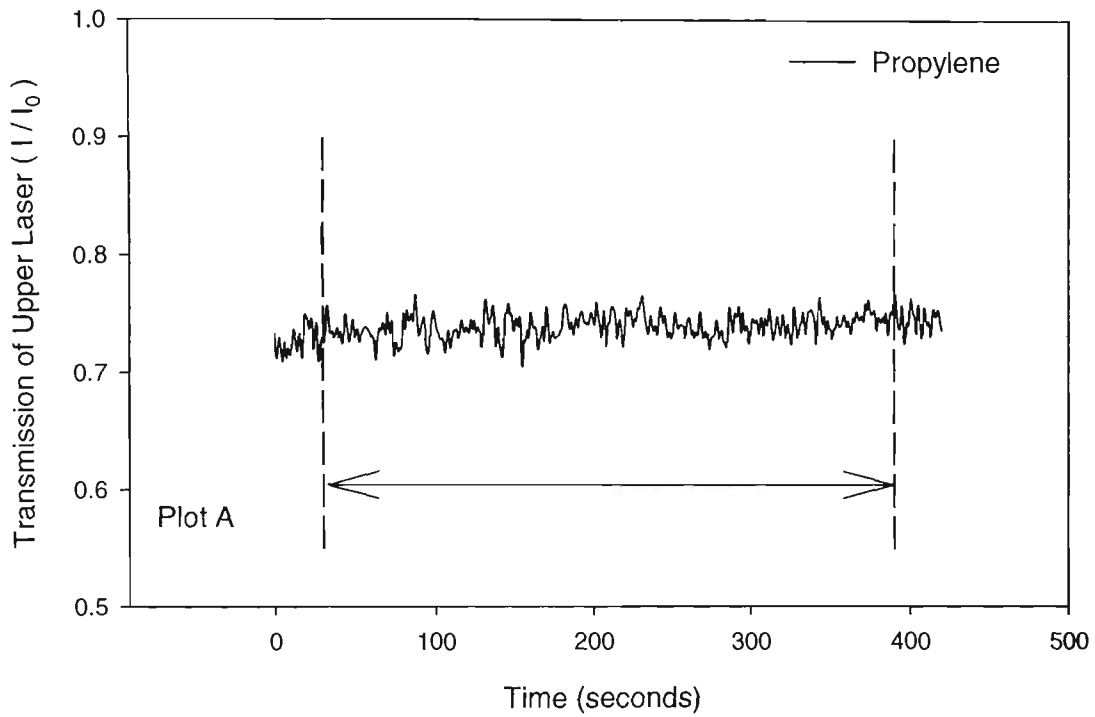
Acetylene and ethylene soots were generated in a co-flow laminar burner developed for an earlier investigation (Samson et al., 1987) and later modified with the addition of a tripper plate followed by a mixing section (Mulholland and Choi, 1998). This burner was positioned next to the LAOF so that a small sample of soot could be tapped off the main buoyant soot flow. This sample was drawn off by the vacuum pump of the LAOF and diluted with the addition of clean air. The soot that was not drawn into the LAOF was exhausted through the laboratory exhaust. The soot produced by this burner was continuously sampled through the LAOF for light scattering measurements. The typical fuel flow rate was about  $0.79 \text{ cm}^3 \cdot \text{s}^{-1}$  and  $7 \text{ cm}^3 \cdot \text{s}^{-1}$  for acetylene and ethylene respectively. While the acetylene and ethylene were sampled directly into the LAOF, the propylene and heptane had to be transported to the LAOF using the drum system (**Sec. 3.4.1** and **Sec 5.2.2**).

A co-flow burner was also used with propylene but at a higher flow rate resulting in a pulsating flame structure. In the case of the propylene the burner was attached to the FE/DE at the vertical riser section above where the solid non-flaming fuels were burnt. The great majority of soot generated was allowed to flow straight out via an exhaust duct; a small amount was allowed to pass into the FE/DE. A damper between the burner and the FE/DE controlled this soot flow into the FE/DE. The fuel flow rate used was about  $10 \text{ cm}^3 \cdot \text{s}^{-1}$  ( $0.6 \text{ L} \cdot \text{min}^{-1}$ ). The smoke concentration in the FE/DE reached steady state conditions before the soot was collected in the drum. This took about 30 seconds. The collection of soot into the drum started at 30 seconds and ended at 360 seconds.

The heptane was the only non-gaseous fuel examined in these soot experiments and produced a turbulent diffusion flame. The heptane soot was generated by a small pool fire located in the same section of the FE/DE as the non-flaming fuels. A 25 cm<sup>3</sup> pool of heptane was poured on top of 100 cm<sup>3</sup> of water contained in a Pyrex petri dish surrounded by a metal overflow dish. The water helped reduce the effects of the heptane boiling and splashing out of the dish. It also raised the heptane to the lip of the dish so that lip effect was reduced on this small pool fire. The time available for sampling was much reduced in the case of the heptane, but this was compensated for by the large amount of soot produced by heptane. To slow the flow of the heptane soot through the FE/DE it was necessary to turn off the driving fan of the FE/DE, and allow the buoyancy of the hot plume and the small air pump effect of the FE/DE exhaust fan to carry the soot through the FE/DE. This approach worked well, since the heptane would often burn out before all the soot had moved out of the FE/DE. In the light scattering experiment presented below the heptane was ignited at 60 seconds and the collection of smoke into the drum was started at 110 seconds. The heptane flame extinguished at about 140 seconds, and the drum collection was finished at about 410 seconds.

In **Figure 6.2** the FE/DE trace of the transmittance of the upper laser shows both propylene and heptane during sampling into the drum. The laser transmission for propylene was nearly constant while for heptane there was a rapid decrease in transmission due to intense soot production. This was followed by a continuous increase in the transmission as the smoke aerosol moved out of the FE/DE. The sampling of the soot generated by the FE/DE followed the same procedure used in sampling smoke aerosols from non-flaming fires (**Sec. 5.2.2**). The drum was connected to the FE/DE via the 10 mm copper sampling line. A pump was connected to the outlet valve on the drum along with a bubble flow meter so that the flow rate into the drum was known. Because the soot from the

**Figure 6.2:** Light transmission of the upper laser in the FE/DE for propylene and heptane soot generation. The sampling times of collection into the drum are shown.



propylene and heptane was collected into the drum, light scattering measurements were susceptible to the uncertainty caused by mass concentration decrease in the drum (Sec. 5.3.3.1). The results for acetylene and ethylene have less uncertainty because the steady-state burner was attached to the LAOF.

## 6.2.2 LIGHT SCATTERING METHODS

The differential mass scattering cross section,  $\sigma(\theta)$ , was the major quantity of interest in this study. This quantity has been measured following the procedures described in **Appendix I**. The results are presented in the following sections where they are used to determine the forward scattering ratio, asymmetry ratio and polarisation ratio. The differential scattering data is then examined in terms of the scattering parameter. Since improved characterisation is possible with steady state soot generation using the laminar diffusion burners attached to the LAOF, other soot experiments were conducted to measure the radius of gyration. These measurements are detailed later in this chapter. Mie theory calculations were not conducted since the theory is not applicable to the agglomerate structure of the soot particles.

## 6.3 LIGHT SCATTERING RESULTS

### 6.3.1 ANGULAR SCATTERING

The differential mass scattering cross section [ $\text{m}^2 \cdot \text{g}^{-1} \cdot \text{sr}^{-1}$ ] has been measured for the soots produced by propylene and heptane in the FE/DE as well as for acetylene and ethylene soot generated in a co-flow laminar burner attached to the LAOF. The differential mass scattering cross section has been measured for the two polarisations perpendicular (vertical in – vertical out, VV) and parallel (horizontal in – horizontal out, HH) to the scattering plane.

In **Figure 6.3** the results for propylene and heptane are shown. Similarly in **Figure 6.4** the results for acetylene and ethylene are shown. The most striking point of all these results is

**Figure 6.3:** Differential mass scattering cross section [ $\text{m}^2 \cdot \text{g}^{-1} \cdot \text{sr}^{-1}$ ] for propylene and heptane generated in the FE/DE and transported by drum.

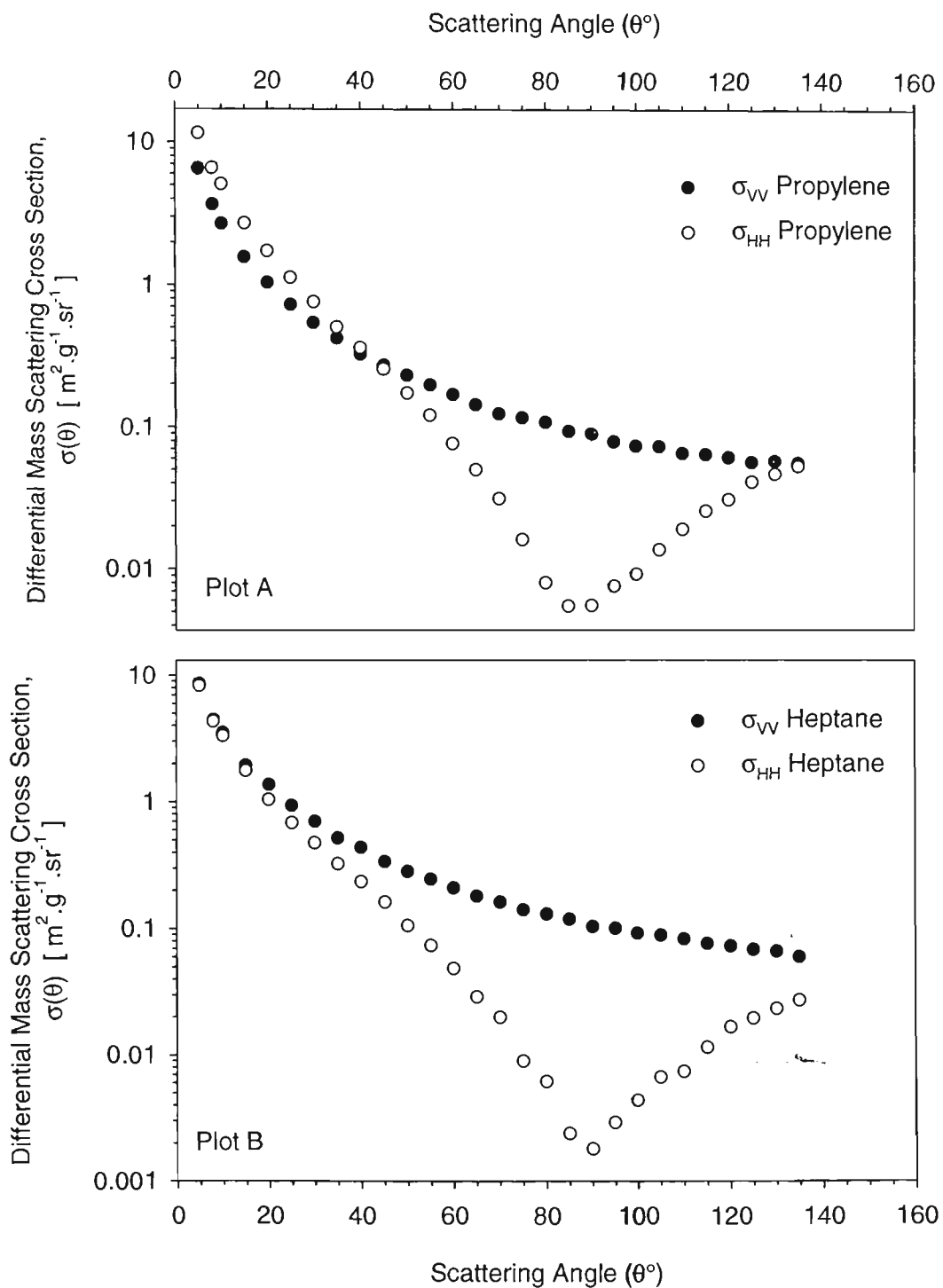


**Figure 6.4:** Differential mass scattering cross section [ $\text{m}^2 \cdot \text{g}^{-1} \cdot \text{sr}^{-1}$ ] for acetylene and ethylene generated in the co-flow laminar burner attached to the LAOF.

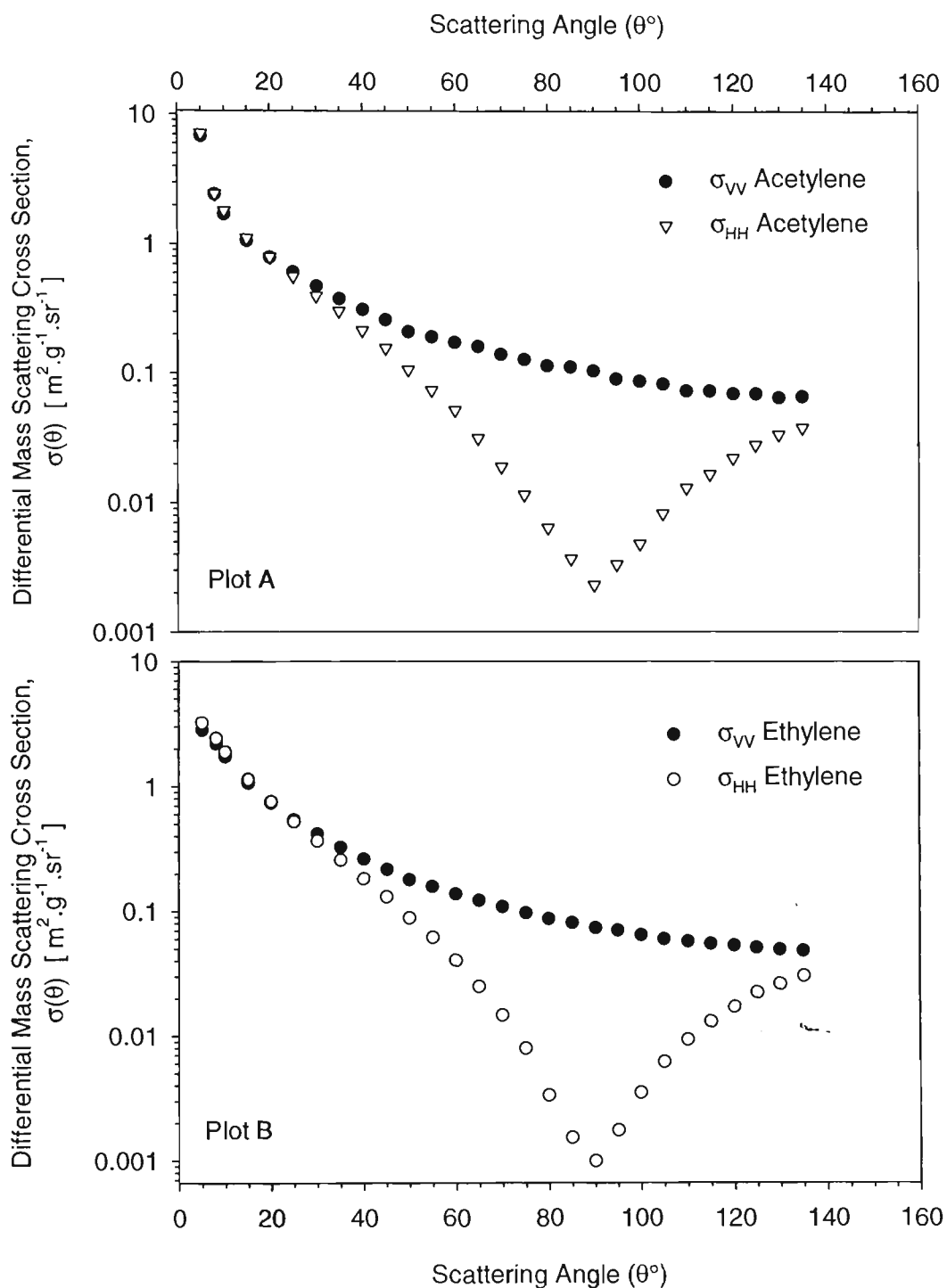
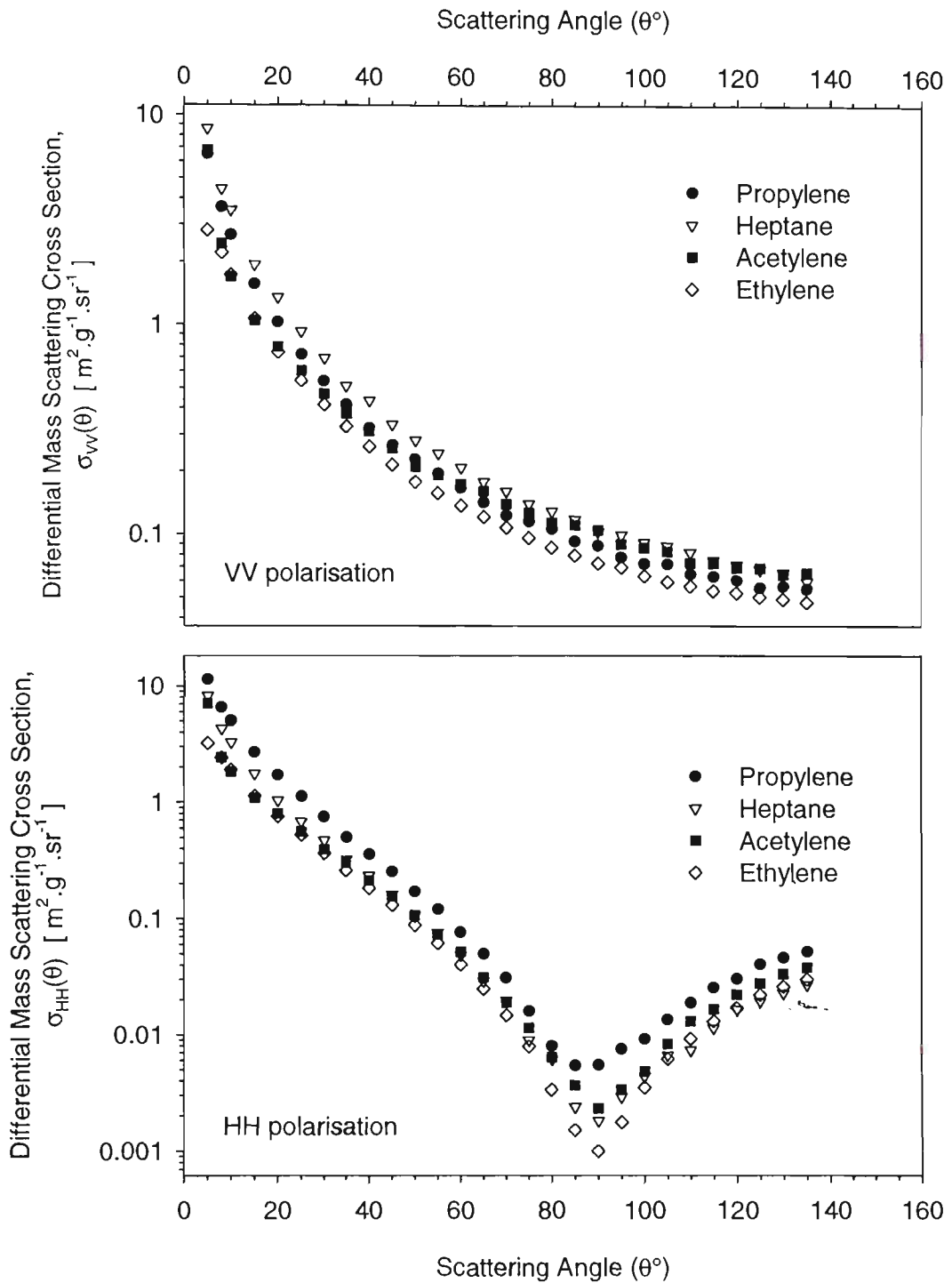


**Figure 6.5:** Comparison of differential mass scattering cross section [ $\text{m}^2 \cdot \text{g}^{-1} \cdot \text{sr}^{-1}$ ] for all of the soots.



that they are similar in functional form. Their agglomerate morphology is the cause of this similarity and is similar from soot particle to soot particle no matter what organic fuel created the soot particle. As the results in **Figures 6.3** and **6.4** are analysed in this section the similarities will become more apparent.

To compare the scattering data in **Figures 6.3** and **6.4** the polarisations have been separated and plotted in **Figure 6.5**. The similarity in the angular distribution of scattered light is striking. This is a result of the universal nature of soot agglomerate structure. The small primary particles making up the agglomerate scatter light individually as Rayleigh scatterers then combines in the far field as described in detail in **Sec. 2.5**.

### *6.3.1.1 Forward scattering and asymmetry ratio*

The forward scattering ratio,  $\sigma_{VV}(5^\circ)/\sigma_{VV}(20^\circ)$ , is a measure of the relative size or number of primary particles making up the soot agglomerates. The forward scattering ratio will have small values that approach 1 for small particles and larger values for larger agglomerates. The size refers to an average size over the ensemble of soot agglomerates produced by the respective sources. Forward scattering ratio results are presented in **Table 6.1**. The ethylene soot it is the smallest agglomerate with a value of 3.8, and acetylene with a result of 8.7 is the largest. Propylene and heptane are comparable, having values of 6.3 and 6.4 respectively.

The asymmetry ratio,  $\sigma_{VV}(45^\circ)/\sigma_{VV}(135^\circ)$ , is also given in **Table 6.1**. The asymmetry ratio ranges from 4.0 to 5.6, which does not indicate any large differences between the different soots. This is to be expected given the scattering parameter dependence of the scattering curves and the post-flame nature of the soot that leads to large radii of gyration. Under such conditions the scattering dependence can be described by **Equ. 2.45**. For example, determining the asymmetry ratio in terms of the scattering parameter at  $45^\circ$  and  $135^\circ$  using **Equ. 2.45** the result is about 4.9 for a fractal dimension of 1.8.

**Figure 6.6:** The normalised ( $\rho(5^\circ)=1$ ) polarisation ratio from the data shown in figure 6.3 and 6.4 for propylene, heptane, acetylene and ethylene.

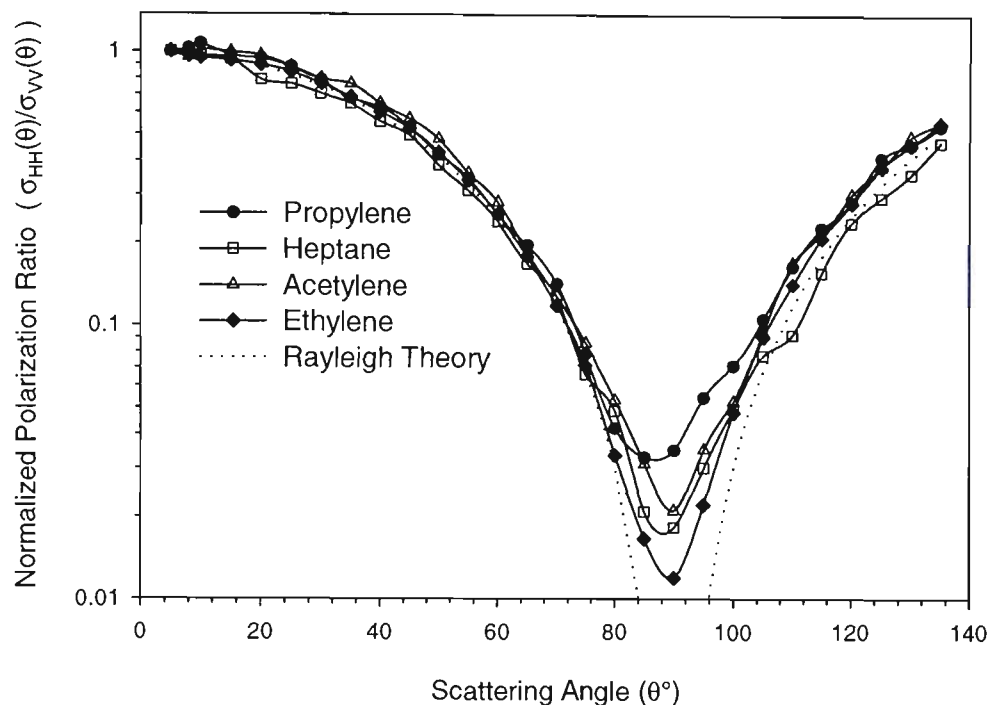


**Table 6.1:** Results of analysis of differential mass scattering cross section.

Fuel	Forward Scattering Ratio	Asymmetry Ratio	Polarisation Ratio at 90°	Truncated Scattering cross section (m <sup>2</sup> .g <sup>-1</sup> )
Propylene	6.3	4.9	0.035	2.3
Heptane	6.4	5.6	0.018	2.2
Acetylene	8.7	4.0	0.021	1.6
Ethylene	3.8	4.5	0.012	1.4

### 6.3.1.2 Polarisation ratio

The similarity in the form of the scattering curves shown above is also apparent when considering the polarisation ratio, defined by  $\rho(\theta) = \sigma_{HH} / \sigma_{VV}$ , shown in **Figure 6.6**. The polarisation ratio results shown in **Figure 6.6** have been normalised to  $\rho(5^\circ) = 1$  for comparison. The polarisation ratio is dominated by the large difference between VV and HH about  $\theta = 90^\circ$ . Since the scattering caused by the agglomerate morphology is not strongly dependent on polarisation, the polarisation ratio,  $\rho(\theta)$ , reflects the Rayleigh-like scattering by the primary spheres and results in a minimum at  $\theta = 90^\circ$  (**Sec. 2.5.2**). The polarisation ratio result for a Rayleigh scattering particle has been included in **Figure 6.6** for comparison.

### 6.3.1.3 Truncated scattering cross section

The truncated mass scattering cross section ( $5^\circ \leq \theta \leq 135^\circ$ ) determined from the data of **Figures 6.3** and **6.4**, has been determined using the same method as that used for the smoke aerosol from non-flaming fires, see **Equ 5.1**. The results are presented in **Table 6.1** and are in fair agreement with Mulholland and Choi (1998) for acetylene and ethylene,  $1.65 \text{ m}^2 \cdot \text{g}^{-1}$  and  $1.58 \text{ m}^2 \cdot \text{g}^{-1}$  respectively, using the same laminar burner as the one used in this study.

## 6.3.2 SCATTERING PARAMETER

The universality in morphology seen in **Figures 6.3** and **6.4** is also revealed by re-plotting the data in these figures against the scattering parameter,  $q = (4\pi/\lambda)\sin(\theta/2)$ . The wavelength used through out this study is that of the HeNe laser,  $\lambda = 632.8 \text{ nm}$ .

**Figure 6.7** shows this re-plotted data the slope of which gives the fractal dimension of the soot aggregates,  $\sigma(q) \sim q^{-D}$  for  $qR_g > 1$  (**Sec. 2.5.2.3**). The fractal dimension of the

**Figure 6.7:** Shows the scattering of propylene, heptane, acetylene and ethylene re-plotted against the scattering parameter.

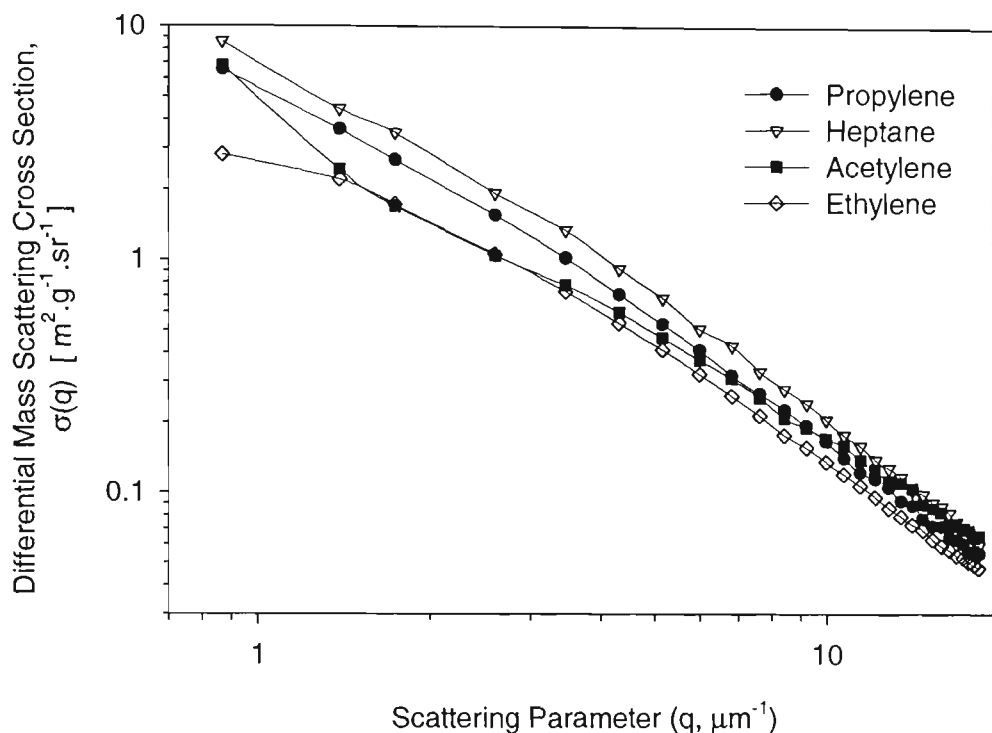


**Table 6.2:** Soot fractal dimension and q-slope measured from lights scattering measurements of this study and those of post-flame soot measured by (Koylu and Faeth, 1994)

Fuel	Fractal Dimension $8.3 \leq q \leq 18.3 \mu\text{m}^{-1}$	q-slope (negative) $12 \leq q \leq 18.3 \mu\text{m}^{-1}$	Fractal Dimension (Koylu and Faeth, 1994)
Propylene	1.8	1.8	1.84
Heptane	1.9	2.0	---
Acetylene	1.6	1.7	1.85
Ethylene	1.7	1.7	1.83

soots examined in this study are given in **Table 6.2** for the range  $8.4 \leq q \leq 18.3 \mu\text{m}^{-1}$  ( $50^\circ \leq \theta \leq 135^\circ$ ). We find that the fractal dimension for the four soots is in the range 1.7 to 2.0 as given in **Table 6.2**. This is to be compared with a range of 1.7 to 1.85 for soot for light scattering studies (Koylu et al., 1995; Sorensen and Feke, 1996). The q-slope is also computed over the same range as used for the non-flaming smoke,  $12 \leq q \leq 18.3 \mu\text{m}^{-1}$  ( $75^\circ \leq \theta \leq 135^\circ$ ). The values of the q-slope are equal to or less than 2. The linear correlation coefficient,  $r^2$ , for both the fractal dimension and the fixed range q-slope in **Table 6.2** is not less than 0.98 in all cases.

## 6.4 SCATTERING MEASUREMENT OF THE RADIUS OF GYRATION

### 6.4.1 METHOD

In the course of doing the scattering measurements we noted interesting behaviour associated with the radius of gyration for soot generated at lower fuel flow rates of acetylene and ethylene. Measurement of the radius of gyration of a soot agglomerate fits well with a study of agglomerate fractal dimensions. It is also beneficial to have some measure of the agglomerate mean size. The following sections describe the methods and results from examination of post-flame soot agglomerate radius of gyration.

The morphology of soot agglomerates is described by various parameters some of which are directly accessible via light scattering data, see **Sec 2.5.2**. The average radius of gyration,  $\langle R_g \rangle$ , of the polydisperse ensemble of soot agglomerates can also be determined from angular light scattering information (Sorensen et al., 1992). This average radius is simply referred to as the radius of gyration in the following text. The theoretical basis of this has been described in a previous chapter, **Sec. 2.5.2.1**, as a consequence of the Guinier equation, **Equ. 2.43**, that applies for  $qR_g < 1$ . If the radius of gyration is large then the Guinier regime requires small angle measurements for the fixed wavelength used in these studies.

The smallest angle available in this study for measurement is  $\theta = 5^\circ$  and this puts a limit on the largest radius of gyration measurable. This limit is exceeded for the results presented above so that for those cases the radius of gyration cannot be determined from the light scattering measurements. Small agglomerates are characterised by  $\sigma(q) \rightarrow 1$  for small values of  $q$ . As  $\langle R_g \rangle$  becomes large  $\sigma(q)$  has a form approaching a straight line over a wider range of  $q$ .

To overcome this limitation the gas fuel burner attached to the LAOF was used to produce relatively small soot particles by reducing the fuel flow rate into the flame under the same oxygen conditions. The small soot particles were generated to meet the optical requirement that the scattering signal at  $\theta = 5^\circ$  was about three times the background scattering at that angle. These measurements would then give an indication of the largest soot particles from which the scattering could be reasonably observed.

The radius of gyration in this study was measured using the Guinier expression, **Equ. 2.43**, rearranged to the following form,

$$\frac{u(0) - u(q)}{u(0)} \approx \frac{q^2 \langle R_g \rangle^2}{3}. \quad (6.1)$$

The radius of gyration can be obtained from the slope,  $\langle R_g \rangle^2 / 3$ , at small angles when plotted as a function of  $q^2$ . The equation above has made use of the proportionality between the detected signal,  $u(q)$ , and the differential mass scattering cross section,  $\sigma(\theta)$ . Also, given that the smallest scattering angle is  $\theta = 5^\circ$  the detector reading at this angle was used for  $u(0)$  in **Equ. 6.1**.

#### 6.4.1.1 *Acetylene and Ethylene at different fuel flow rates*

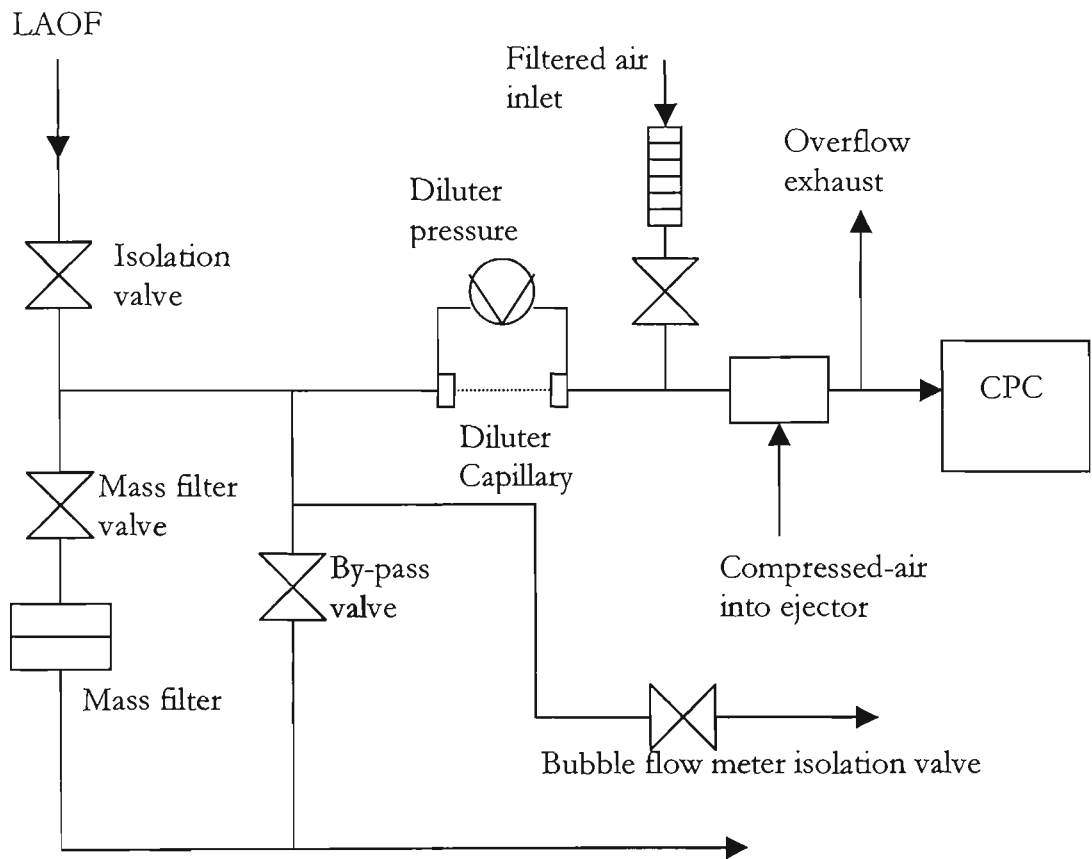
The scattering signal was measured for soot produced by ethylene and acetylene for a range of fuel flow rates. It is known that the agglomerate size increases as the fuel flow rate increases (Samson et al., 1987). This is thought to result from the increased soot yield as the fuel flow conditions increase. The flame changes from producing no post-flame soot to the first evidence of soot, to progressively more intense sooting. The soot generated under different burner conditions was allowed to flow through the LAOF, where the scattering signal was measured in the forward direction. In these experiments only the angles from  $5^\circ$  to  $55^\circ$  were measured. Since the interest is in the scattering signal only, there is no need to measure the mass concentration. These experiments with varying fuel flow rates characterized the forward scattering as the soot continuously flowed through the LAOF.

#### 6.4.1.2 *Agglomerate post-flame growth of Acetylene and Ethylene*

Experiments were also performed to study affects of agglomeration on the angular scattering. These experiments were carried out at low fuel flows:  $0.67 \text{ cm}^3\cdot\text{s}^{-1}$  and  $6.6 \text{ cm}^3\cdot\text{s}^{-1}$  for acetylene and ethylene respectively. These low flows resulted in relatively small agglomerates. Closing a valve between the burner and the LAOF inlet as well as the pneumatic isolation valve at the lower end of the LAOF isolated the soot. The soot was held in the LAOF to undergo agglomeration at essentially standard temperature and pressure conditions. Differential scattering measurements were then made.

The scattered light signal at the forward angles ( $\theta = 5^\circ$  to  $20^\circ$ ,  $\Delta\theta = 1^\circ$ ) was measured at recorded intermittent times during the isolation of the soot. In this way the change in radius of gyration could be measured as the soot grew, this was why the initial soot isolated in the LAOF was of the smallest starting size. A measurement of the number concentration of the

**Figure 6.8:** Schematic of condensation particle counter connection to the LAOF.



soot agglomerates was also made on separate occasions to the scattering measurements. These measurements were made before and after soot was isolated for a one-hour period. Measurements were made with the CPC that was also used in measurement of the number concentration in the FE/DE (Sec. 5.2.2.2). The ratio of the number concentrations before and after isolation gave a measure of the amount of agglomeration that had taken place. To make the number concentration measurements it was necessary to connect the diluter between the LAOF and the CPC, as shown in **Figure 6.8**. The pressure across the diluter was kept at about 20 Pa. This results in a dilution of about two orders of magnitude across the dilution circuit in **Figure 6.8**.

## 6.4.2 RESULTS

### 6.4.2.1 *Radius of gyration at different fuel flow rates*

In **Figure 6.9** the results of light scattering by acetylene and ethylene soot generated at different fuel flow rates has been measured. The data has been normalised at a scattering angle of  $20^\circ$  and presented in terms of the measured detector signal corrected for the scattering volume angular dependence. In the case of the low fuel flow rates it was necessary to make five scans over the angular range and to then average over the scans to reduce the noise. The bar in **Figure 6.9b** is the 95 % confidence limit of this averaging. In the case of the acetylene the uncertainty was the size of the data point. This highlights the repeatability of the acetylene even at low fuel flow rate. The ethylene data vastly improves in repeatability at higher fuel flow rates.

The effect of high and low fuel flow rates can be seen in the forward scattering region. A large radius of gyration of the soot agglomerate leads to stronger scattering in the forward direction. The radius of gyration limit is apparent when comparing the acetylene results for the fuel flow rates of  $0.73 \text{ cm}^3 \cdot \text{s}^{-1}$  and  $0.79 \text{ cm}^3 \cdot \text{s}^{-1}$ . At these settings there is little difference in

**Figure 6.9:** The results of light scattering measurements in the forward direction from a) acetylene and b) ethylene generated soot.

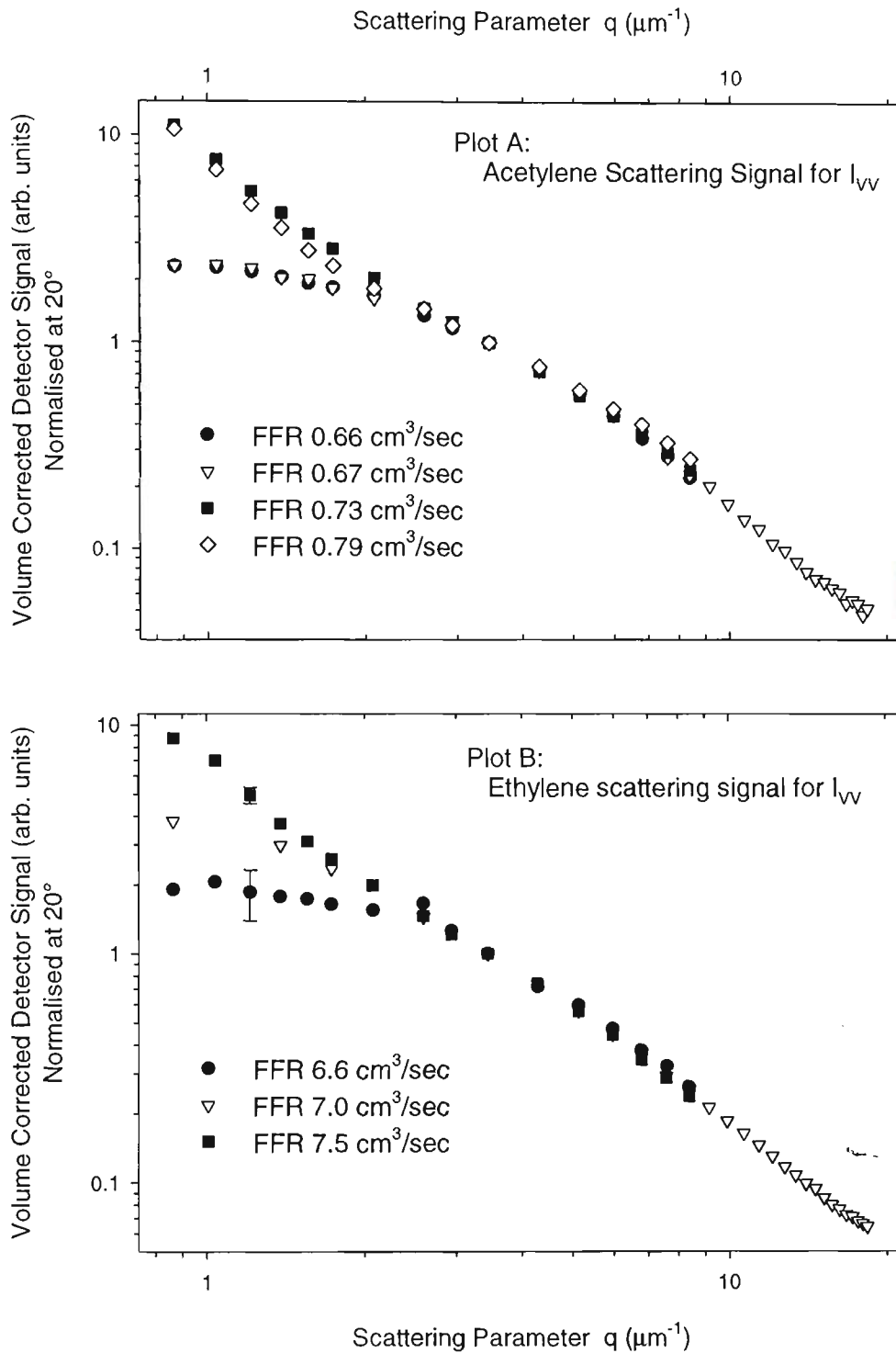


**Figure 6.10:** Results of radius of gyration analysis for acetylene and ethylene using **Equ. 6.1**.

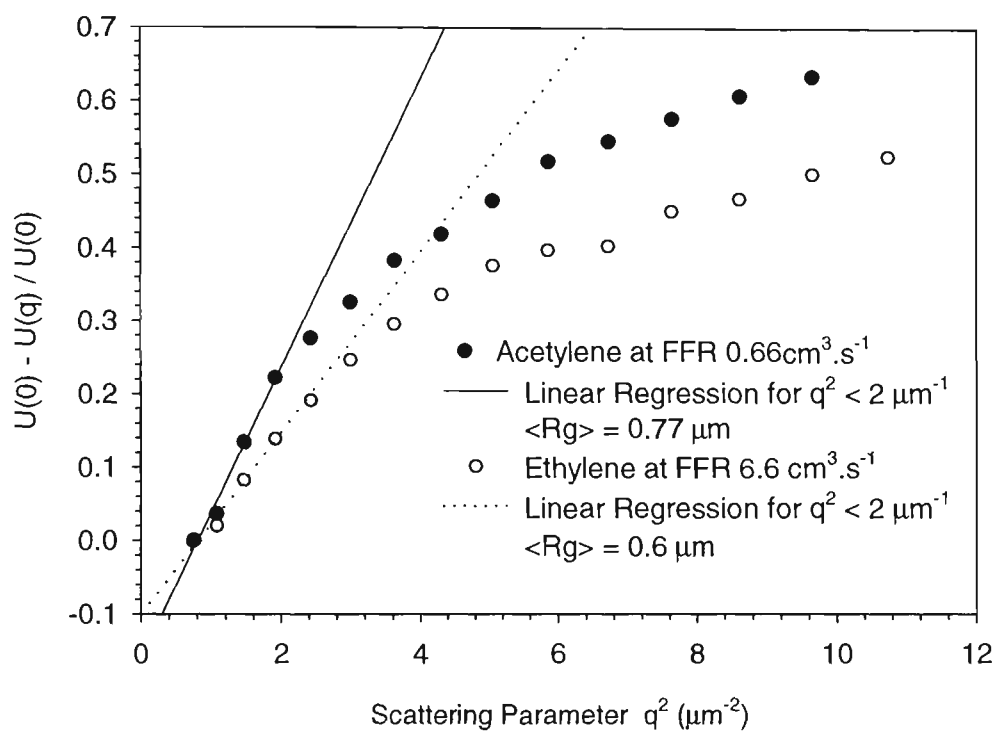


**Table 6.3:** The radius of gyration for different fuel flow rates of acetylene and ethylene used to generate soot.

Acetylene FFR ( $\text{cm}^3/\text{sec}$ )	$\langle R_g \rangle$ ( $\mu\text{m}$ )	Ethylene FFR ( $\text{cm}^3/\text{sec}$ )	$\langle R_g \rangle$ ( $\mu\text{m}$ )
0.66	0.8	6.6	0.6

the scattering at small angles. Very small angle data would be necessary to see any possible differences in the average radius of gyration.

**Figure 6.10** illustrates the method of analysing the forward scattering signal from the acetylene and ethylene soot (**Sec. 6.4**). The data used to calculate the radius of gyration were the average of five angular scattering experiments determined for acetylene and ethylene each. The radius of gyration was computed from the linear region which consists of the first four data points measured at scattering angles of  $\theta = 5^\circ, 6^\circ, 7^\circ, 8^\circ$ . In some data even these four points were not in the linear region. The non-linear region is a consequence of a breakdown of the approximation in the Guinier region due to the effects of the large radius of gyration. This is why the approximation in **Equ. 6.1** is used. It gives a strong visual clue as to the appropriateness of the approximation. In **Table 6.3** the results for the radius of gyration are presented for the different fuel flow rates of acetylene and ethylene. The acetylene soot,  $0.8 \mu\text{m}$ , is larger than the ethylene soot,  $0.6 \mu\text{m}$ . The radius of gyration could only be computed for the lowest flow rates for each fuel, because the other fuels flow rates did not have linear results at the small angles measured.

#### **6.4.2.2 Post-flame agglomerate growth of acetylene and ethylene**

The results that follow show the increase in radius of gyration of the soot agglomerates as they grow by coagulation kinetic collisions in an isolated volume. The radius of gyration is measured at forward angles as has been done in the last section. In **Figure 6.11a** and **6.12a** the results of the forward scattering measurements at different times after isolation are shown for acetylene and ethylene respectively. As the isolation time increases the number of large soot agglomerates increases due to collisions. The change in the shape of the  $q$ -scattering plot for ethylene smoke suggests that agglomerate growth is taking place. For acetylene on the other hand, there does not appear to be a consistent change in the shape of the scattering curve as a function of  $q$ . The scattering magnitude for the acetylene soot is increasing but the

**Figure 6.11:** The light scattering results for acetylene soot growing by coagulation (aging) in an isolated volume: **a)** volume corrected detector signal **b)** plot of  $t = 5$  min and  $t = 45$  min using Equ. 6.1.

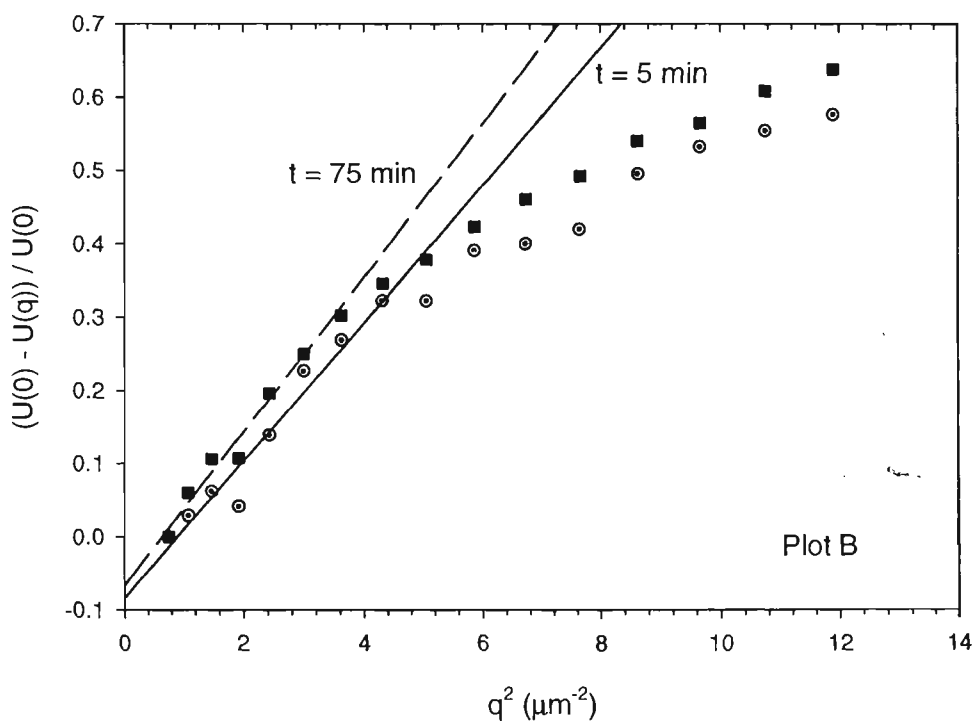
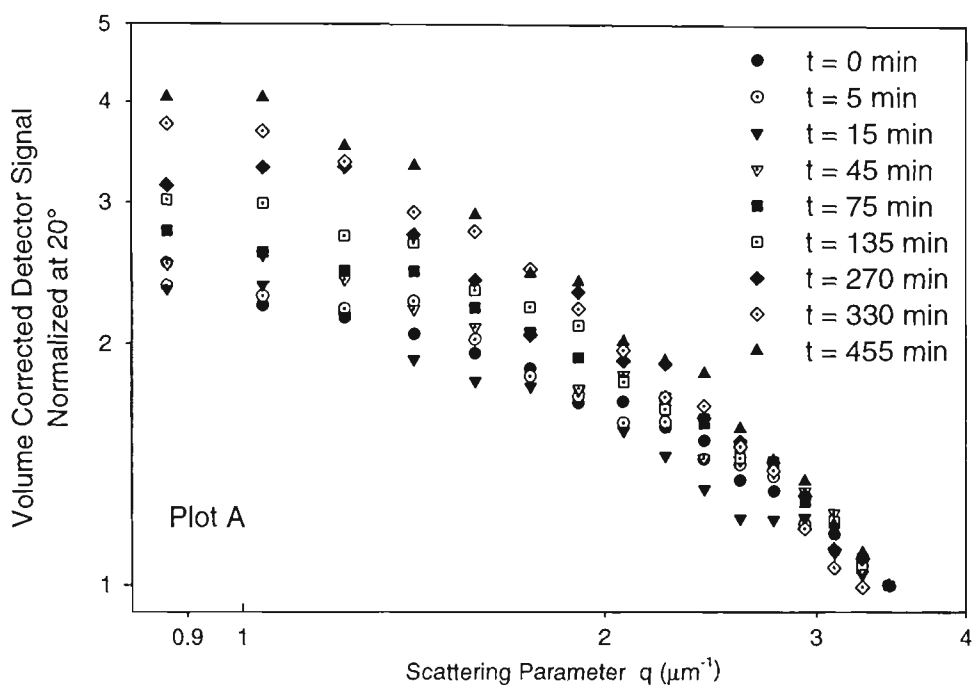
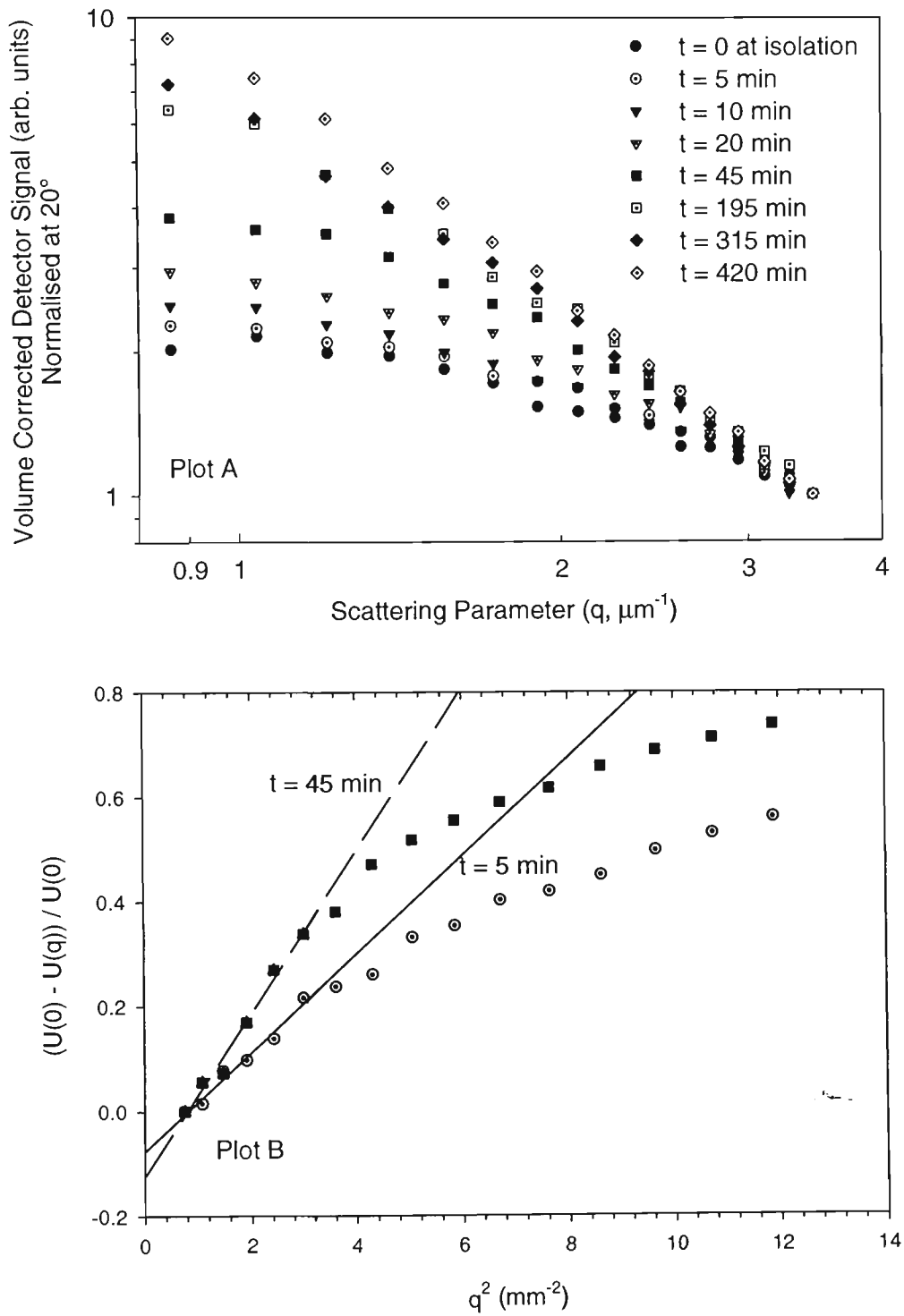


**Figure 6.12:** The light scattering results for ethylene soot growing by coagulation (aging) in an isolated volume: **a)** volume corrected detector signal **b)** radius of gyration plot using Equ. 6.1.



changes in the scattering curve are not pronounced as seen in the ethylene results. The acetylene flame creates a large soot agglomerate to start with and growth can result in even larger ones that dominate the light scattering signal at smaller values of  $q$ . In this case, particle settling and transport to the walls might also be a significant process.

In **Figure 6.11b** and **6.12b** selected scattering results have been transformed as per **Equ. 6.1**. The first six angles have been used to calculate the radius of gyration of the ensembles. **Table 6.4** shows the calculated average radius of gyration of the soot agglomerates as a function of isolation time. In **Table 6.4** the growth of the ethylene from 0.49 to 0.67  $\mu\text{m}$  is more substantial than that of the acetylene. Acetylene growth from 0.55 to 0.57  $\mu\text{m}$  is not significant enough to be considered indicative of growth. Both soot results are affected by uncertainty generated by noise from large agglomerates in the scattering volume. Acetylene is the most affected by this uncertainty as demonstrated by the results in **Table 6.4**.

The results are the ratio of initial to final number concentrations after an hour of isolation are presented in **Table 6.5**. Isolating ethylene generated by fuel flow rates of 6.6  $\text{cm}^3\cdot\text{s}^{-1}$  and 7  $\text{cm}^3\cdot\text{s}^{-1}$  resulted in decreases of 13.4 and 12.4 times the number concentration before isolation, respectively. This is significant compared with the reduction in initial number concentrations of 5.6 and 8.1 times for acetylene generated at fuel flow rates of 0.67  $\text{cm}^3\cdot\text{s}^{-1}$  and 0.79  $\text{cm}^3\cdot\text{s}^{-1}$  respectively. How the loss of soot agglomerates to the walls or settling on surfaces affects these figures is unknown. The number concentrations and ratios have a relative standard uncertainty of about 5 %. The low fuel flow rates were used in the soot growth experiments while the larger fuel flow rates were used in the light scattering experiments presented in **Sec. 6.3.1**.

**Table 6.4:** Tabulated results of the radius of gyration for different fuel flow rates of acetylene and ethylene used to generate soot.

Acetylene Time (min)	$\langle R_g \rangle$ ( $\mu\text{m}$ )	Ethylene Time (min)	$\langle R_g \rangle$ ( $\mu\text{m}$ )
0	0.55	0	0.49
5	0.52	5	0.52
10	0.62	15	0.6
45	0.55	20	0.57
75	0.57	45	0.67

**Table 6.5:** Acetylene and Ethylene soot number concentrations for steady state, and ratio of initial to final number concentration after one hour of isolation.

Acetylene FFR ( $\text{cm}^3 \cdot \text{s}^{-1}$ )	Steady State Num. Conc. ( $\text{p} \cdot \text{cm}^{-3}$ )	Ratio of Num. Conc. Ratio	Ethylene FFR ( $\text{cm}^3 \cdot \text{s}^{-1}$ )	Steady State Num. Conc. ( $\text{p} \cdot \text{cm}^{-3}$ )	Ratio of Num. Conc. Ratio
0.67	$1.2 \times 10^6$	5.6	6.6	$5.5 \times 10^6$	13.4
0.79	$4.1 \times 10^6$	8.1	7.0	$1.65 \times 10^7$	12.5

## 6.5 DISCUSSION

The differential mass scattering cross section has been measured and used to analyse various aspects of scattering by soot agglomerates. The forward scattering ratio indicates that ethylene has the smaller mean agglomerate size. Radius of gyration measurements supports this. The fuel flow rate influences the size of soot agglomerates produced and the number, see **Table 6.3** and **Table 6.5**. The truncated scattering cross section calculations compare well with those measured by Mulholland and Choi (1998) (**Sec. 6.3.1.3**).

The polarisation ratio in **Figure 6.6** shows the distinct minimum typical of Rayleigh scattering; although the scattering by soot agglomerates is not Rayleigh scattering (**Sec. 2.5**).

The minimum at  $90^\circ$  in **Figure 6.6** is a result of the removal of the agglomerate structure factor from the polarisation ratio due to its relative insensitivity to polarisation (**Sec. 2.5.2**). The results in **Figures 6.5** and **Figures 6.6** display the typical universality expected of soot agglomerates.

The asymmetry ratio is related,  $\sigma(q(45^\circ))/\sigma(q(135^\circ)) \approx [q(135^\circ)/q(45^\circ)]^{D_f}$ , to the fractal dimension of the soot agglomerates and both measures do not vary over a large range. This is another implication of the universal morphology of soot agglomerates and a result of their large radii of gyration. The fractal dimensions in **Table 6.2** compare well for propylene measured in this study and that measured by Koylu and Faeth (1994) for their turbulent burner. The fractal dimension result for acetylene is smaller and that for heptane larger than what might be expected, given the typical range of 1.7 to 1.85 (Koylu et al., 1995; Sorensen and Feke, 1996). The heptane has a fractal dimension of 1.9 and a q-slope of 2. The fractal dimensions and q-slopes for the other soot agglomerates are slightly less than 2. As a generalisation of these results the flame-generated aerosols have a q-slopes of about 2 or less. Their fractal dimensions vary about 1.8.

Measurement of the mean radius of gyration for post-flame soot has been demonstrated for acetylene and ethylene, with values of  $0.8 \mu\text{m}$  and  $0.6 \mu\text{m}$  respectively. The forward scattering ratio for soot at higher fuel flow rates indicates the same difference in size. The growth in the mean radius of gyration from about  $0.49 \mu\text{m}$  to  $0.57 \mu\text{m}$  of post-flame ethylene soot is observed. Growth is also observed for acetylene soot but is not as conclusive due to losses and scattering noise.

## NUISANCE AEROSOLS

### 7.1 INTRODUCTION

Common nuisance aerosols include steam, cooking generated aerosols, cigarette smoke and dust. While cigarette smoke has been well characterised and studied (Phalen et al., 1976), the other nuisance aerosols have attracted far less light scattering attention until the last decade or so. The majority of attention (anecdotal) has been from smoke detector manufacturers, who rarely publish their results. In fact, there are only two light scattering studies that have used what are classified in this study as nuisance aerosols for smoke detection research (Aggarwal and Motevalli, 1997; Loepf et al, 1997). Both of these studies did not measure the size distribution of the aerosols they investigated.

Aggarwal and Motevalli (1997) demonstrated some discrimination of different non-flaming fire generated aerosols by light scattering by different smokes at about the same mass concentration. They made use of a multiple-angle light scattering apparatus (Meacham and Motevalli, 1992) although they limited their reported work to a scattering angle of  $\theta = 20^\circ$ . They considered cooking oil (corn based) and bread (toasted) as aerosol sources. Aggarwal and Motevalli (1997) did not have any instruments for size analysis at their disposal, although because the data were collected at an angle ( $\theta = 20^\circ$ ) they would be sensitive to relative size differences.

Another study by Loepfe et al. (1997), using a more advanced light scattering apparatus of similar design to that of Aggarwal and Motevalli (1997), examined specifically the ability of polarised light scattering to differentiate fire and nuisance aerosols. To do this they measured the degree of linear polarisation, **Equ. 2.34**, for the EN54 (1982) test fires and nuisance aerosols steam, toasting bread, cooking oil and candle wax. They could separate the nuisance

aerosols based on their degree of polarisation and identified a spike in this measure at about  $155^\circ$  for steam which might be used to differentiate water aerosol from fire generated aerosols. They had mixed success separating other nuisance aerosols from the non-fire aerosols, cooking oil and pyrolysed beech wood blocks in particular.

In this study two of the nuisance aerosols, burning toast and overheating cooking oil, are generated by pyrolysis. The third and final nuisance aerosol was ISO Fine dust or Arizona road dust, a standardised dust (ISO 12103-1; A2). In this chapter the results of light scattering and size characterisation are presented. Light scattering results are presented in terms of the differential mass scattering cross section [ $\text{m}^2\cdot\text{g}^{-1}\cdot\text{sr}^{-1}$ ]. Such information can be used for predicting the response of a given detector to these three aerosols. The size distribution measurements are made for the first time in this study to enable comparison between Mie theory predictions and our measured cross sections. In the following chapter the results from all of the smoke and nuisance aerosols are compared to examine different methods of discriminating between smoke and nuisance aerosols.

## **7.2 METHOD**

### **7.2.1 NUISANCE AEROSOL GENERATION, SAMPLING AND TRANSPORT**

All of the nuisance aerosols, burning toast, overheating cooking oil, and dust, were generated in the FE/DE, where they are commonly used as nuisance alarm aerosols for smoke detector evaluation. The conditions under which they were generated are discussed here. The sampling and transport of the nuisance aerosols follows the same procedures as described in **Sec. 5.2.2** and **Sec. 3.4**.

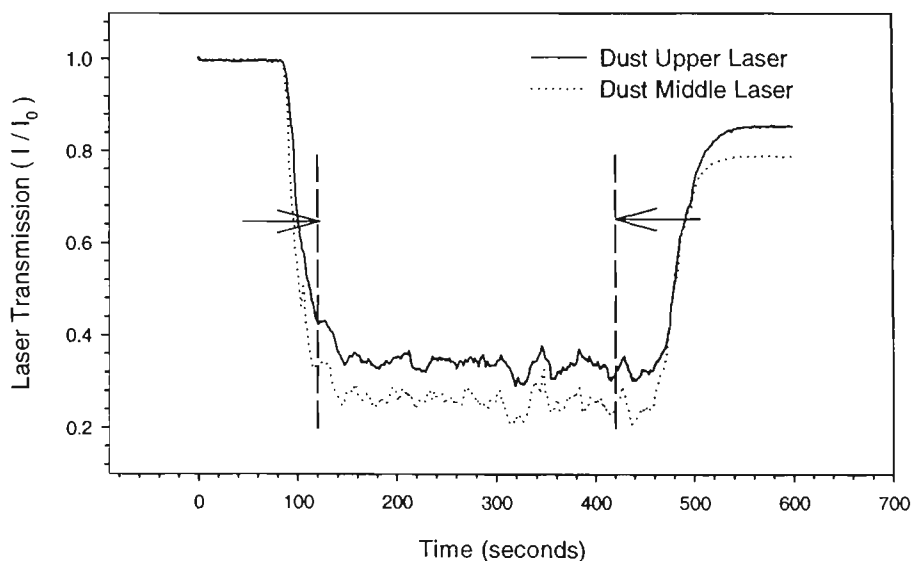
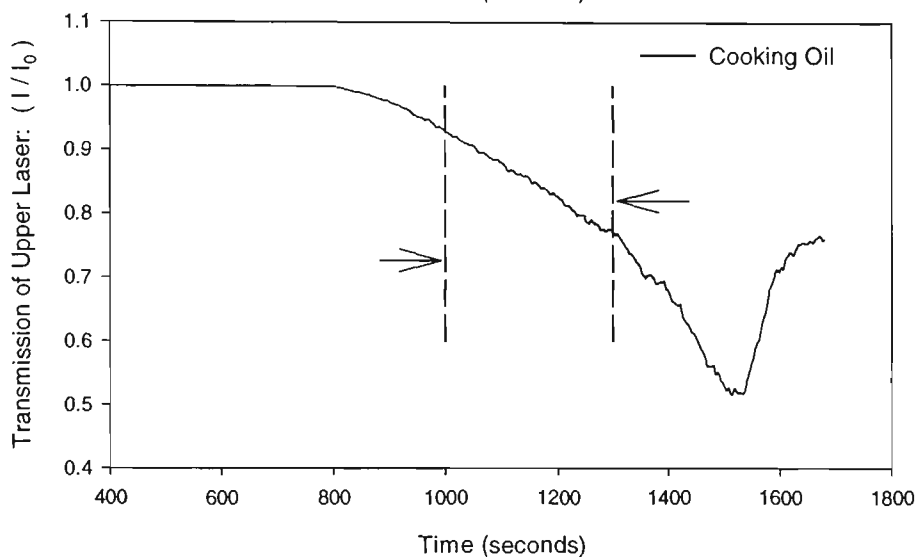
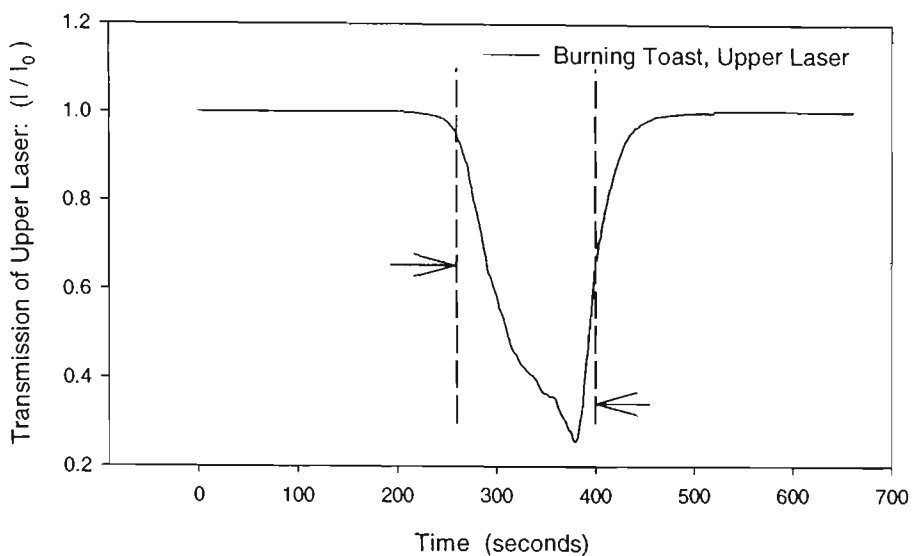
To generate the burning (pyrolysing) toast aerosol, a simulation of the normal occurrence taking place in many kitchens all over the world, two slices of white bread were placed in a standard two-slice pop-up toaster. The toaster had been wired on so that the toast would not

pop up. The smoke concentration produced by the burning toast had a rapid rate of rise. The toaster was only powered for a short period compared with the sampling time, to avoid a transition to flaming. It is the early stage of burning toast that is of interest in this study, not the transitional smoke aerosol. The CO level in the FE/DE was monitored as a check on the state of the burning toast. If the CO level rose too high then the toast was beginning to blacken and a transition to flaming would usually follow quickly. In the experiments of this study, smoke was collected at very low CO levels, indicating no carbonaceous aerosols. The other aspect of using the FE/DE is that the source behaviour is well understood and repeatable.

In **Figure 7.1** the transmission curves for the upper laser in the FE/DE duct are shown for the nuisance aerosols. The vertical lines on the plots indicate the time over which aerosol sampling into the barrel took place. The transmission of the upper laser for the burning toast is seen in **Figure 7.1a** where the rapid reduction in light transmission corresponds to the fast evolution of smoke from the burning toast. The toaster was powered at 60 seconds and sampling took place from 260 to 400 seconds. To avoid the transition to flaming the power to the toaster was shut off at 360 seconds. The production of nuisance aerosol caused by burning toast is rapid as can be seen in **Figure 7.1a**. This tends to increase uncertainties of measurements based on use of average mass concentrations in the FE/DE, such as in extinction measurements. The FE/DE fan rate used throughout this study was set to 7 Hz, which resulted in an air velocity of about  $0.2 \text{ m}\cdot\text{s}^{-1}$ .

To generate the over-heating cooking oil aerosol, a  $5 \text{ cm}^3$  sample of corn-based cooking oil was placed in a petri dish and pyrolysed on the hotplate, which was set at full power. It was the same hotplate used to pyrolyse the beech wood blocks (**Sec. 5.2.1**). Again the CO level in the FE/DE was monitored to ensure that the oil vapour was not close to ignition. The CO level during the oil vaporisation did not increase in our experiments. In **Figure 7.1b**

**Figure 7.1:** Light transmission through the nuisance aerosols generated by burning toast, over-heating cooking oil, and dust. The time of sampling into the transportation drum is also shown.



the upper laser transmission is shown along with the sampling period marked. It took a relatively long period to generate the cooking oil aerosol. Sampling into the drum began at 1000 seconds and lasted for 300 seconds.

The dust used as a nuisance aerosol was ISO Fine Dust (12103-1; A2), manufactured by Powder Technology Inc. This dust has a mass mean diameter of about 25  $\mu\text{m}$ . It was dispensed into the FE/DE flow before the fire test section by a screw feeder (AccuRate Inc., Dry Material Feeder), and a pressurised ejection head, which used a compressed air line to inject the dust into the FE/DE duct. The screw speed was kept quite slow, a dial speed setting of 1 was used and the compressed air line was set at a pressure of 550 kPa (80 PSI). The FE/DE has honeycomb before the sensor section, which leads to a loss of particles larger than about 10  $\mu\text{m}$ . Gravity fractionation of the dust was also observed by differences in the transmitted light beams at the top and middle heights of the sensor section. The net effect was that sampled dust aerosol had a different size distribution compared with the original ISO fine dust at the source. Some settling in the barrel also occurred and further changed the size distribution of the final dust sample entering the LAOF. The gravity fractionation can be seen in **Figure 7.1c** along with the sampling period to draw the dust into the drum. The dust dispenser was started at 60 seconds and sampling into the drum started at 120 seconds and lasted 300 seconds.

## 7.2.2 MASS SIZE DISTRIBUTION, MASS AND NUMBER CONCENTRATION

The aerosol characteristics of the nuisance aerosols were measured while sampling from the FE/DE. The procedure and equipment used for the characterisation have been detailed in the earlier chapters on the apparatus and smoke aerosol from non-flaming fires, see **Sec 5.2**. Those aspects are summarised here with attention to differences specific to the nuisance aerosols. Unlike the smoke aerosol from non-flaming fires, no number distribution

measurements were made of the nuisance aerosols since the High Sensitivity Laser Aerosol Spectrometer (HSLAS, Particle Measurement Systems Inc.) was not available. Mass size distributions were measured using the Micro-Orifice Uniform Deposit Impactor (MOUDI) (Sec. 5.2.2.1). The continuous mass and number concentrations were also measured in the FE/DE for the burning toast and overheating cooking oil nuisance aerosols. The same equipment and methods as detailed in Sec. 5.2 were used.

### 7.2.3 LIGHT SCATTERING MEASUREMENTS

The light scattering measurements follow the same procedure as those presented for non-flaming fire generated smoke aerosol. The drum is transported to the LAOF and a calibration experiment is conducted as described in **Appendix I**.

#### 7.2.3.1 *Theoretical light scattering methods*

Light scattering calculations have been made using Mie theory for comparison with the experimental measurements of the differential mass scattering cross section. The computer code used is the polydisperse algorithm developed from SCATMECH (Germer, 2001) and described in Sec. 2.4.3. Approximate refractive indices of  $1.5 + i0$  and  $1.47 + i0$  are used for burning toast and overheating cooking oil nuisance aerosols, respectively (Mulholland et al., 1985b; National Toxicology Program, 2002). The ISO Fine Dust is estimated to have a refractive index of  $m = 1.47 + i4.8 \times 10^{-3}$ . The real part of the refractive index is assumed to be dominated by  $\text{SiO}_2$  ( $m = 1.47$ ), and the imaginary component is taken from a list of three values ( $7.0 \times 10^{-3}$ ,  $4.8 \times 10^{-3}$ ,  $2.1 \times 10^{-3}$ ) by a multi laboratory test (Gerber and Hindman, 1982). The dust particles are irregular in shape and as such are only expected to follow Mie theory at forward angles (Holland and Gagne, 1970).

## 7.3 RESULTS

### 7.3.1 SIZE DISTRIBUTION, MASS AND NUMBER CONCENTRATIONS IN THE FE/DE

The mass median aerodynamic diameter and geometric standard deviation have been measured for the nuisance aerosols using the MOUDI while sampling the aerosols as they flowed through the FE/DE. The mass distributions are presented as histograms in **Figure 7.2** and a log-probability plot is given in **Figure 7.3** (Sec. 5.3.1.1).

The mass based log-probability plot has been analysed to determine the size distribution parameters of the nuisance aerosols used in the Mie theory calculations. The log probability graph is linear over the range of the upper (95%) and lower (5%) confidence limits and indicates that the size distributions of the nuisance aerosols are close to lognormal. The mass median aerodynamic diameter of the nuisance aerosols produced by toast, cooking oil and dust are 0.43  $\mu\text{m}$ , 1.6  $\mu\text{m}$ , and 2.2  $\mu\text{m}$  respectively. The quantified results of the size distributions are shown in **Table 7.1**. Repeat size distribution measurements were made for the dust and both results are given in **Table 7.1**.

Results of the continuous monitoring of number and mass concentrations for toast and cooking oil in the FE/DE are shown in **Figure 7.4**. The large peak in the number concentration for the cooking oil at about 600 seconds is caused by the evolution of condensable species from the hot plate as described in Sec. 5.2.1. A time delay exists between the mass sampling and the number concentration results because of the different transport lines of to the respective instruments and the relatively long time response of the TEOM.

**Figure 7.2:** The size-mass distribution as a histogram of nuisance aerosols from **a)** burning toast as well as cooking oil and **b)** ISO fine dust measured in the FE/DE.

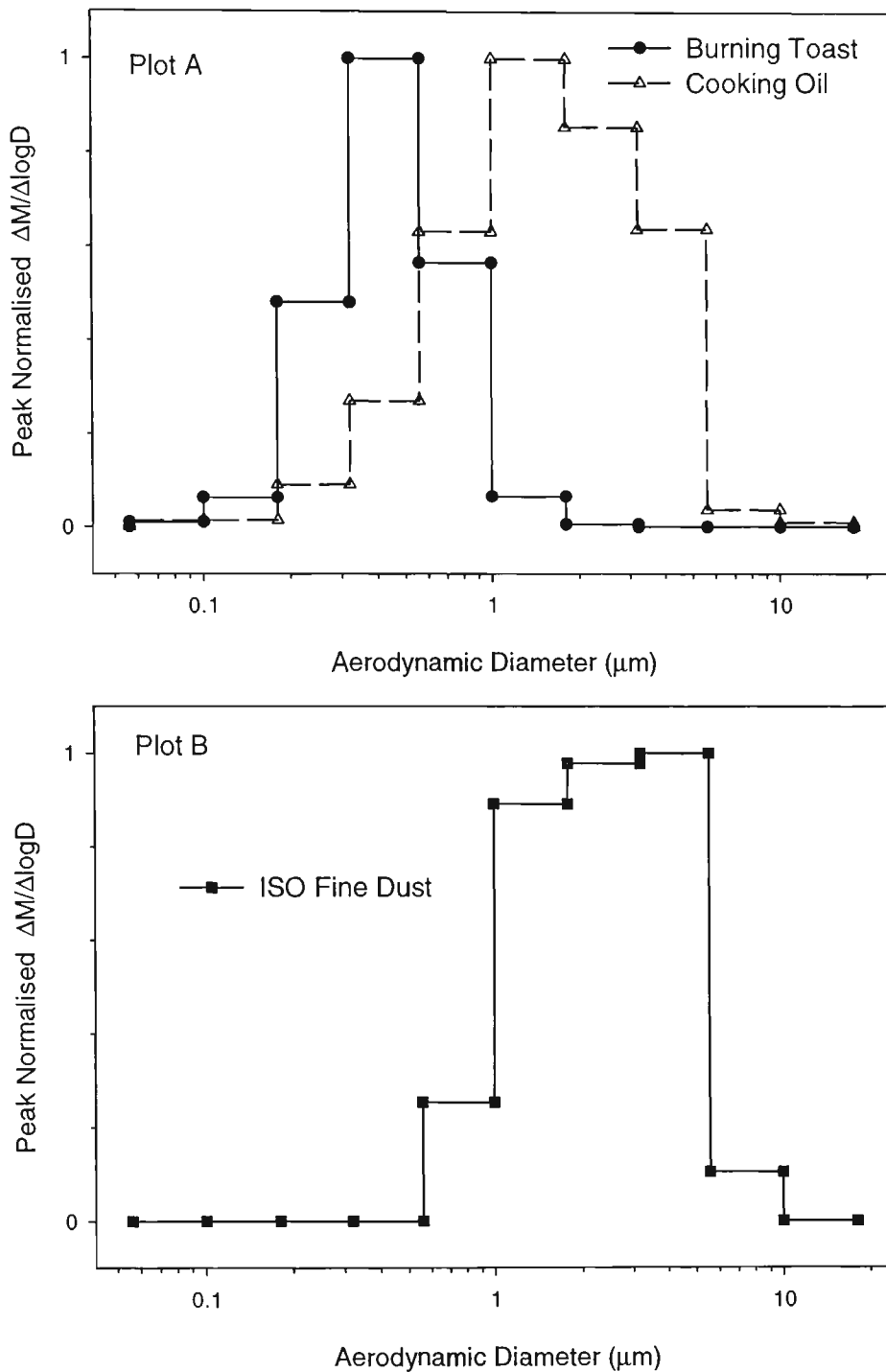


**Figure 7.3:** The log-probability graph of the size-mass distribution of nuisance aerosols measured in the FE/DE.

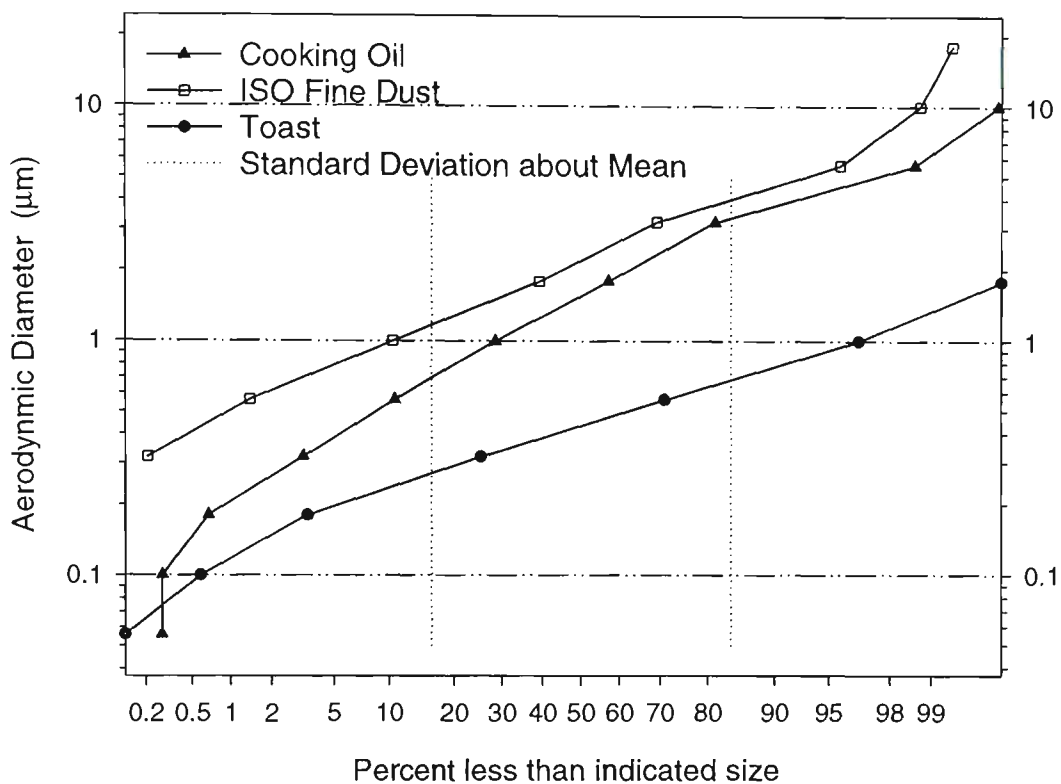
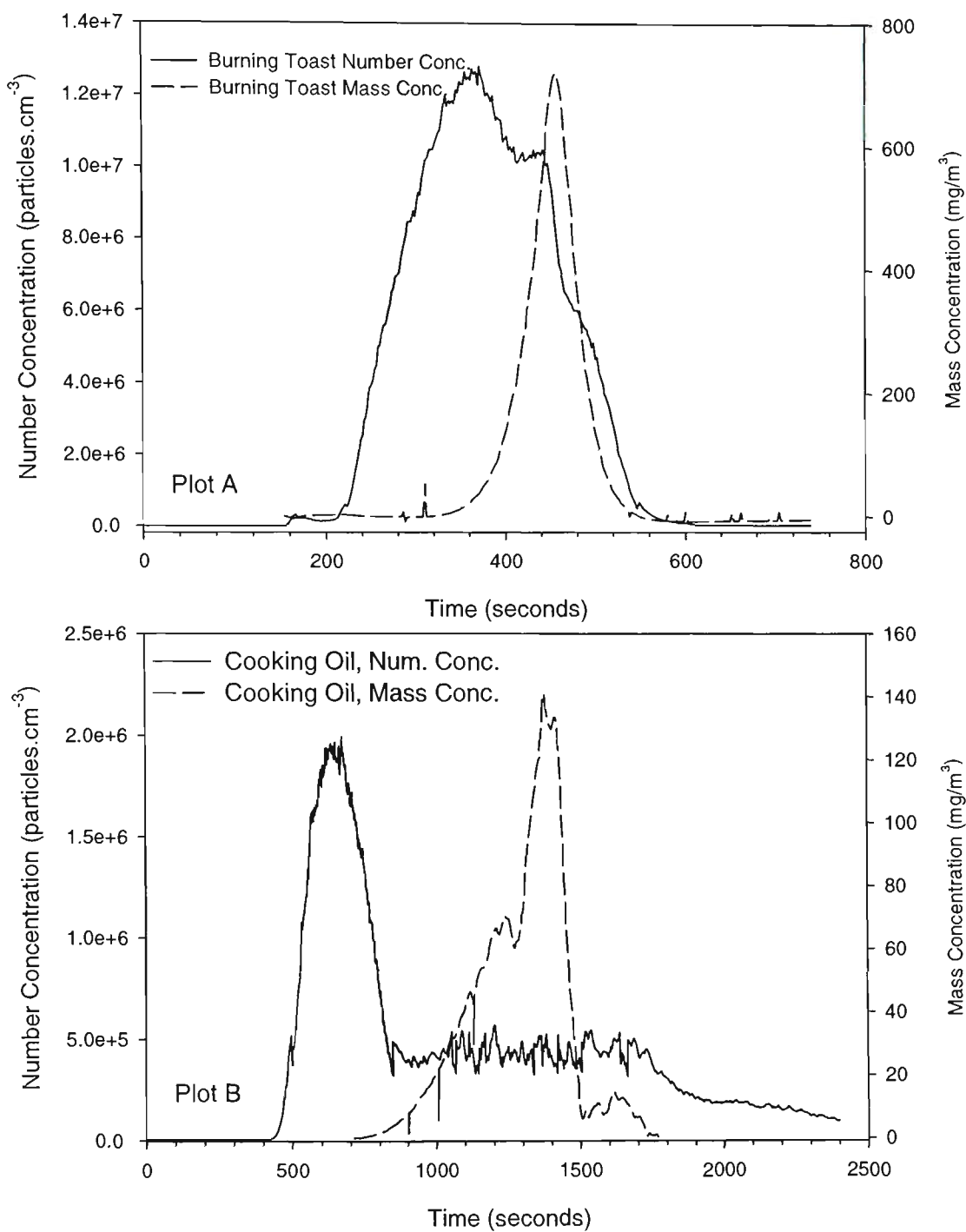


**Table 7.1:** Size distribution parameters determined from the MOUDI.

Nuisance Aerosol	Histogram		Log-probability	
	Mass median aerodynamic diameter (µm)	Geometric standard deviation (GSD)	Mass median aerodynamic diameter (µm)	Geometric standard deviation (GSD)
Toast	0.43	1.7	0.43	1.6
Cooking oil	1.5	2.2	1.6	2.2
Dust	2.3	1.8	2.2	1.8
	2.2	1.9	2.2	2.0

Figure 7.4: Results of the continuous number and mass concentration monitoring of toast and cooking oil aerosols in the FE/DE.



### 7.3.2 EXTINCTION MASS CROSS SECTION

As has been described in Sec. 5.3.2, the extinction mass cross section has been determined for the nuisance aerosols generated. The results of this calculation are presented in Table 7.2 for the experiments conducted. Comparison of the organic aerosols from burning toast and cooking oil can be made with the results of Seader and Einhorn's (1976). They found the smoke aerosols from non-flaming fires that they examined had an extinction mass cross section of  $4.4 \text{ m}^2 \cdot \text{g}^{-1}$  for incident white light. This equivalence argument makes use of the similar organic nature and spherical shape of burning toast and cooking oil. The result for dust has not been reported before.

**Table 7.2:** Results of extinction coefficient estimates.

Fuel	Mass Extinction Cross Section ( $\text{m}^2 \cdot \text{g}^{-1}$ )
Burning Toast	3.5
Cooking Oil	4.1
Dust	4.0
	4.5

### 7.3.3 ANGULAR LIGHT SCATTERING OF NUISANCE AEROSOLS

Differential mass scattering cross section,  $\sigma(\theta)$  [ $\text{m}^2 \cdot \text{g}^{-1} \cdot \text{sr}^{-1}$ ], at the both VV and HH polarisation settings have been measured for the nuisance aerosols. The Mie theory and experimental results are presented together. The refractive indices used in the calculated results are detailed above in Sec. 7.2.3.1 and the size parameters used are from the log-probability plot summarised in Table 7.1.

The angular scattering results for burning toast are given in Figure 7.5a. The same measurements for overheating cooking oil and dust are shown in Figure 7.5b and

**Figure 7.6**, respectively. The forms of the scattering curves agree well between the experimental and calculated differential scattering cross sections. The observed scattering by the nuisance aerosols results in smooth curves, while Mie calculations predict interference features for the larger particles from cooking oil and dust that are not observed.

Light scattering calculations for aerosols generated by burning toast over-predicts the observed scattering result at small angles and under-predicts the scattering magnitude at the larger scattering angles, see **Figure 7.5a**. The general form of the observed and calculated angular distribution of the scattered light is very good for these smaller aerosol particles.

In the case of the overheating cooking oil and the aerosol dust the calculated results are lower than observed results at small scattering angles. The two polarisation experimental results for dust separate at larger angles more than the theory. This is probably due to irregular particle shape (Holland and Gagne, 1970). The mass concentration over time is also likely to have some influence as discussed in **Sec. 5.3.3.1**. The differences between calculated and observed results are to a degree, a consequence of uncertainty in the size distribution and to some extent the assumption that it is lognormal.

### **7.3.3.1 Forward scattering and asymmetry ratios**

The toast nuisance aerosol shows typically low forward scattering indicative of a small particle when compared with the result for cooking oil and dust nuisance aerosols. The forward scattering ratio,  $\sigma_{vw}(5^\circ)/\sigma_{vw}(20^\circ)$ , has been quantified in **Table 7.3**. It is a simple measure of the slope of the scattering curve in the forward direction, and a means of determining the relative size of particles. The results in **Table 7.3** show that burning toast generates a small particle since the forward scattering ratio is 1.3. The overheating cooking oil and dust aerosols are relatively larger with values of 3.4 and 7.1 respectively. This relative

**Figure 7.5:** Differential mass scattering cross section results for a) burning (pyrolysing) toast and b) overheating (pyrolysing) cooking oil at both VV and HH polarisations. Mie calculations use the diameters from Table 7.1 and  $m = 1.5 + i0$ .

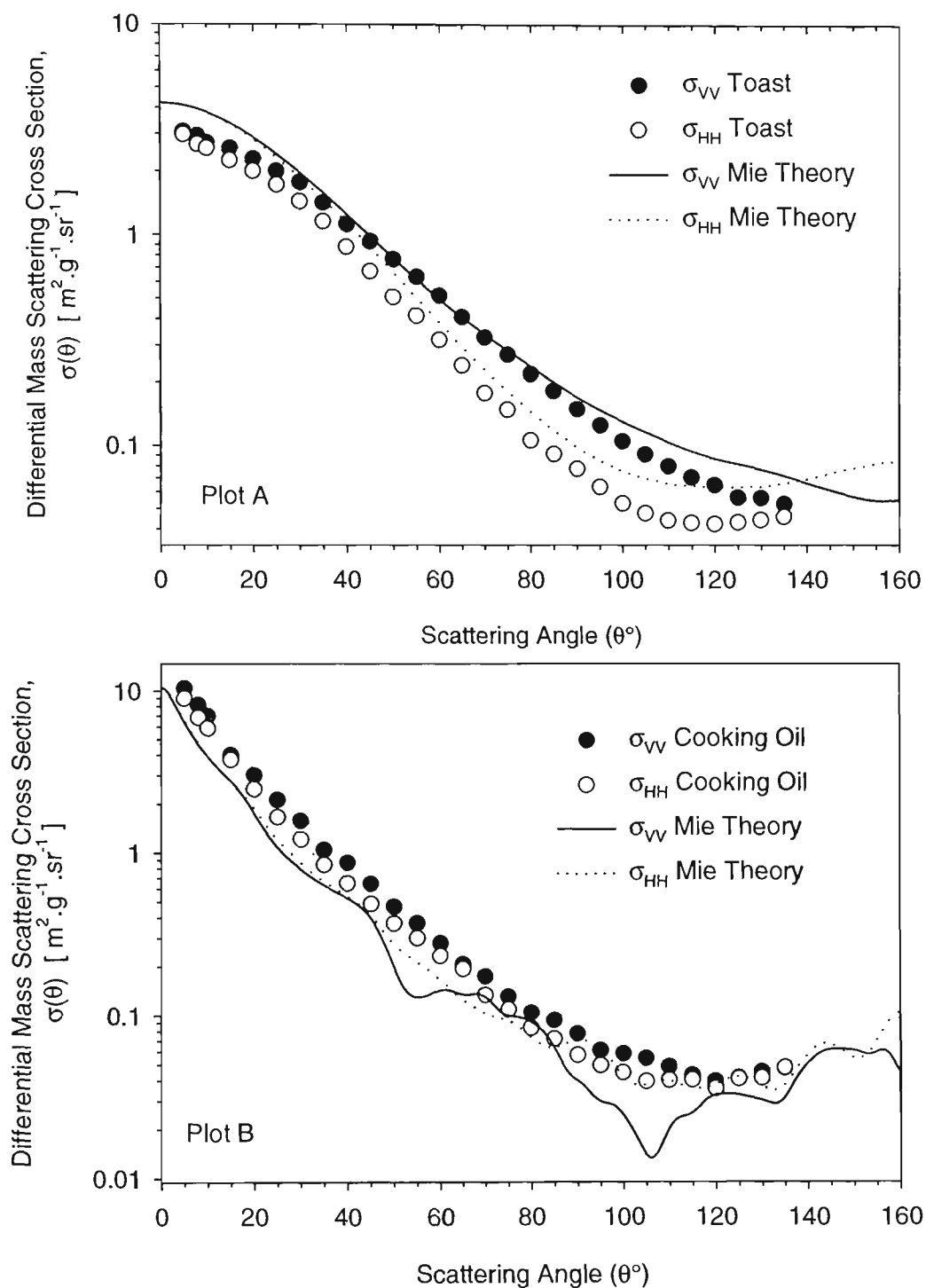


**Figure 7.6:** Differential mass scattering cross section results for ISO Fine Dust at both polarisation settings after sampling from the FE/DE and drum transport. Mie calculations use the diameters from **Table 7.1** and  $m = 1.5 + i0$ .

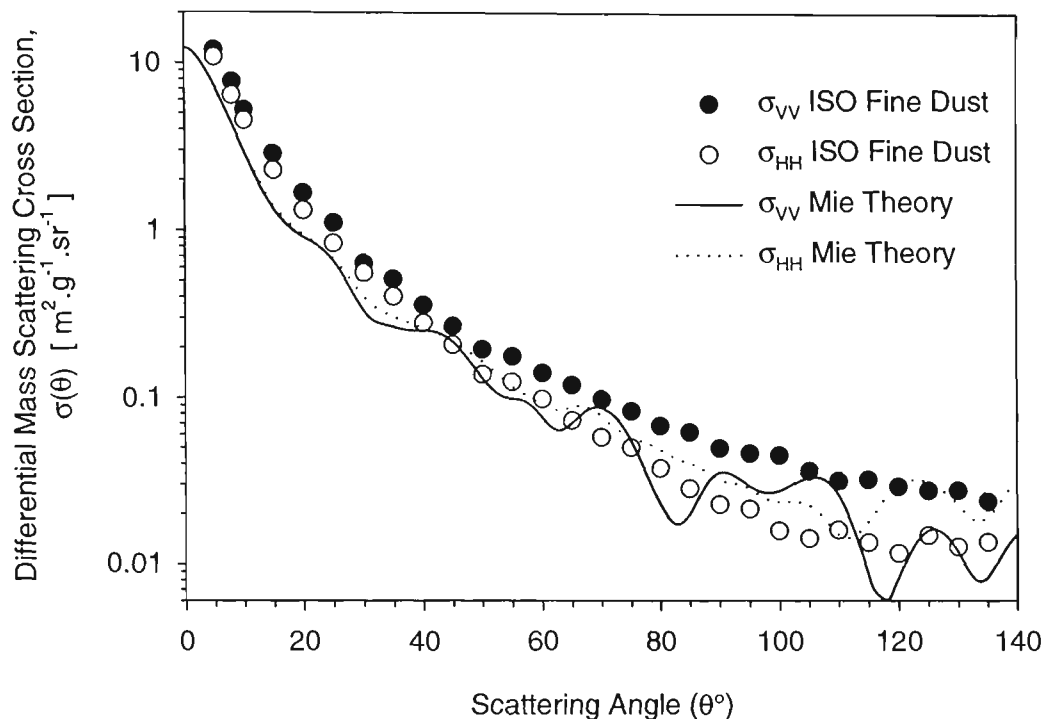


**Table 7.3:** Forward scattering ratio and asymmetry ratio for nuisance aerosols.

Nuisance Aerosol	Forward Scattering Ratio		Asymmetry Ratio	
	Experimental	Theoretical	Experimental	Theoretical
Toast	1.3	1.4	17.8	13.8
Cooking Oil	3.4	3.6	13.6	12.5
Dust	7.1	7.9	11.3	26.0

sizing has high confidence given the size distribution information above. Comparison with the forward scattering ratio calculated from the theoretical results is also good.

The asymmetry ratio,  $\sigma_{vw}(45^\circ)/\sigma_{vw}(135^\circ)$ , for the nuisance aerosols are also given in **Table 7.3**. The asymmetry ratio burning toast (17.8) is larger than both the cooking oil (13.6) and the dust (11.3) asymmetry ratios. The interference features in the calculated scattering results strongly influence comparison with the experimental asymmetry ratio. This leads to differences between the experimental and theoretical asymmetry ratios. The experimental asymmetry ratio of dust is interesting since these particles are irregular in shape. Decisive discrimination of the dust from the other nuisance aerosols is not conclusive given the results in **Table 7.3** and as it is the only irregular shaped particle present in the particle set.

### 7.3.3.2 Polarisation Ratio

The polarisation ratio,  $\rho(\theta) = \sigma_{HH}(\theta)/\sigma_{VV}(\theta)$ , normalised at  $\theta = 5^\circ$  for the nuisance aerosols is plotted in **Figure 7.7** and given in **Table 7.4** for  $\rho(90^\circ)$ . The polarisation ratio of toast is typical of smaller particles due to the HH component being smaller than the VV. In the case of the large dust particles the HH component also falls below VV as the scattering angles increase, see **Figure 7.6**, giving a polarisation ratio that also drops similar to the smaller toast particle. A comparison with the theoretical polarisation result at  $90^\circ$  is difficult because of the presence of interference features not observed in the experiments.

### 7.3.3.3 Truncated and total light scattering

The experimental data in **Figure 7.5** and **Figure 7.6** is used to determine the truncated mass scattering cross section (**Sec. 5.3.5**). The Mie theory results are also calculated for comparison. In **Table 7.5** these experimental and theoretical values of the truncated scattering cross section are shown. As a function of the total scattered light most of the light is scattered into forward angles, demonstrated by the peak at small angles in the angular

**Figure 7.7:** The normalised (at  $5^\circ$ ) polarisation ratio of the nuisance aerosols.

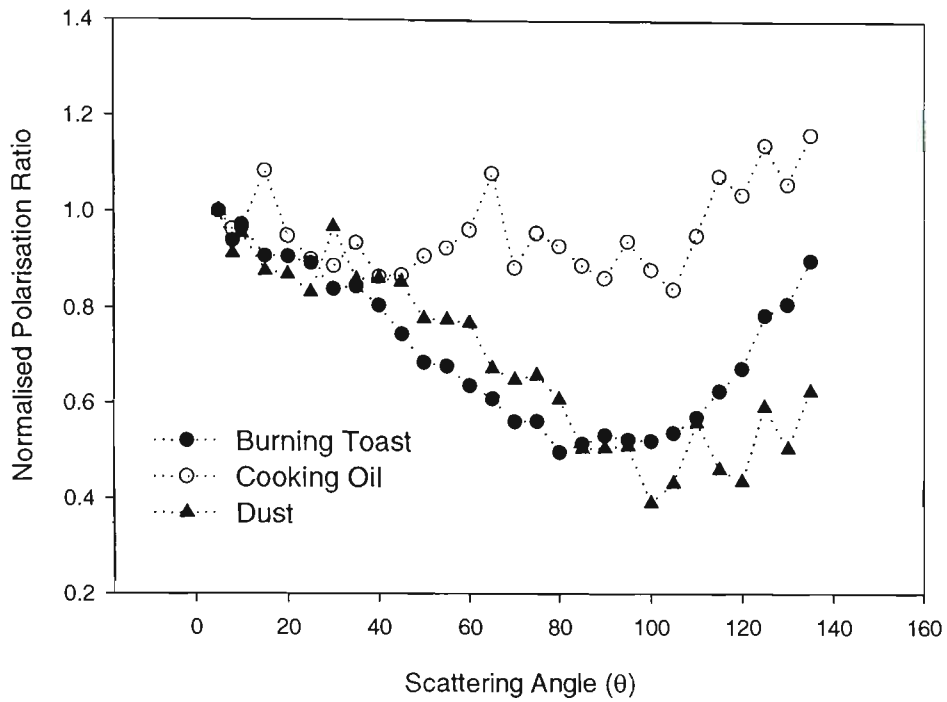


**Table 7.4:** Polarisation ratio at  $90^\circ$  for the nuisance aerosols

Nuisance Aerosol	Polarisation Ratio	
	Experimental	Theoretical
Toast	0.53	0.58
Cooking Oil	0.86	1.77
Dust	0.51	0.91

**Table 7.5:** Truncated and total mass scattering cross sections for nuisance aerosols.

Nuisance Aerosol	Truncated mass scattering cross section ( $\text{m}^2 \cdot \text{g}^{-1}$ )		Total mass scattering cross section ( $\text{m}^2 \cdot \text{g}^{-1}$ )
	Experimental	Theoretical	Theoretical
Toast	4.6	5.76	5.89
Cooking Oil	4.3	3.16	3.29
Dust	2.4	1.95	2.05

scattering results. So agreement between experiment and theory at these angles is crucial to agreement of truncated or total scattering cross sections.

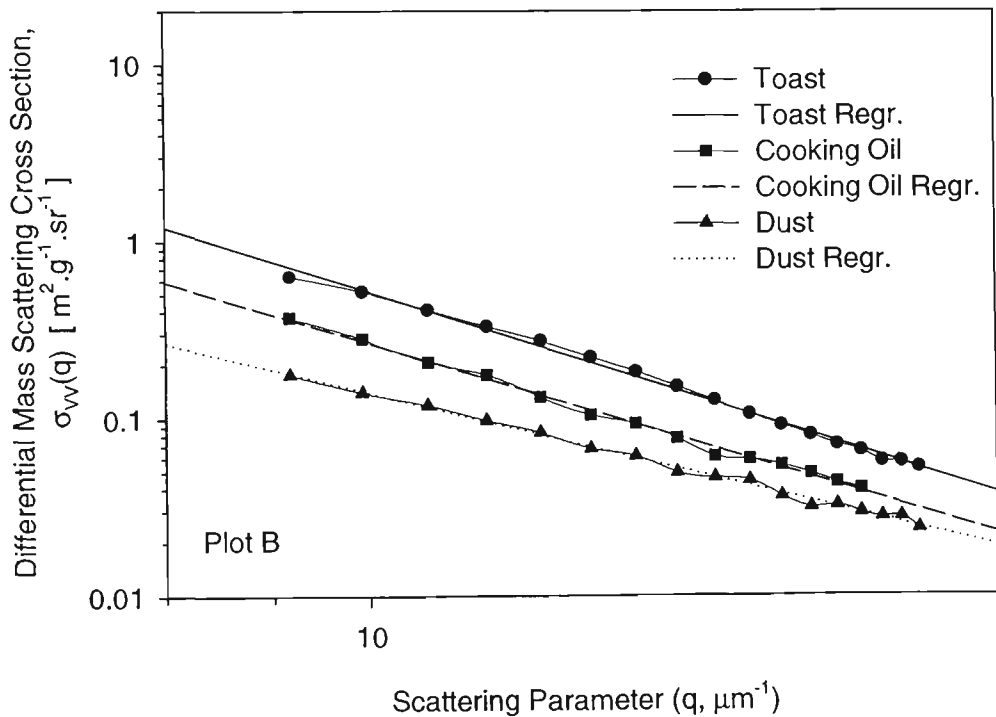
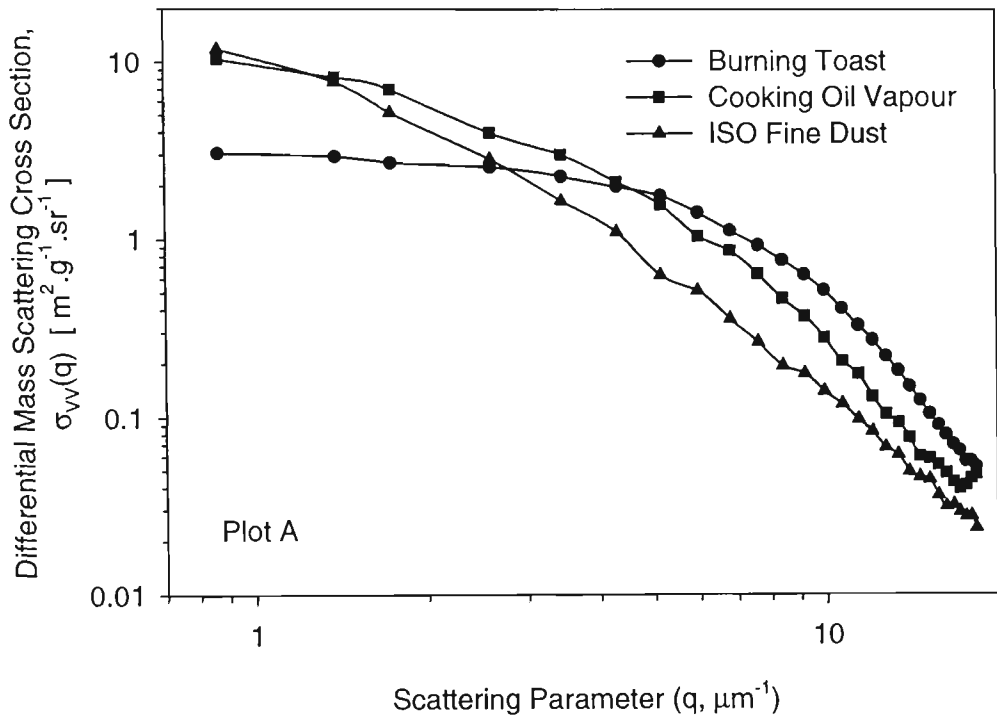
The calculated result for the aerosol generated by burning toast overestimates the scattering intensity at small angles. Thus the theoretical truncated mass scattering cross section,  $5.76 \text{ m}^2 \cdot \text{g}^{-1}$ , over-estimates the experiments,  $4.6 \text{ m}^2 \cdot \text{g}^{-1}$ . In the case of the cooking oil and dust nuisance aerosols the theory under-estimates the experimental values. The cooking oil has a measured scattering cross section of  $4.3 \text{ m}^2 \cdot \text{g}^{-1}$  and the dust a measured value of  $2.4 \text{ m}^2 \cdot \text{g}^{-1}$ .

### 7.3.4 SCATTERING PARAMETER

#### 7.3.4.1 *q-slope*

In **Figure 7.8** the differential mass scattering cross section for the VV polarisation has been plotted against the scattering parameter. The results emphasise the forward scattering slope and linear behaviour at large  $q$ . The small toast generated aerosol has a scattering curve typical of small particles. The dust aerosol results have less curvature than the toast and cooking oil aerosols. This is a result of the larger mean size of the dust aerosols and some irregular shape effects might also be present. In **Table 7.6** the  $q$ -slopes calculated from VV

**Figure 7.8:** Differential mass scattering cross-section as a function of scattering parameter for nuisance aerosols at VV polarisation setting. **a)** the full data plot and **b)** the “envelope” (variable range) data with regressions.



and HH experimental and theoretical data are shown. The q-slopes have been determined over the range of  $12 \leq q \leq 18.3 \mu\text{m}^{-1}$ .

The experimental q-slope results for the nuisance aerosols indicate that the larger particles have VV polarisation q-slopes approaching -3 while the smaller burning toast generated particles are closer to -4. The HH results of the regression analysis are lower than the VV results for toast and cooking oil; the larger dust particles have comparable q-slopes for the two polarisation settings. However, in the case of the HH the correlation coefficients are much worse than in the VV case. This poor correlation is also present in the q-slope analysis of the results from Mie theory. The difference between the experimental and calculated results is most likely due to the interference features in the calculated large particle results.

**Table 7.6:** Results of q-slope regression analysis for experimental and theoretical scattering results at both polarisation settings, VV and HH. The linear correlation coefficient of each q-slope regression analysis is given in brackets next to each q-slope.

Fuel	Experimental q-slope (negative)		Theoretical q-slope (negative)	
	VV	HH	VV	HH
Toast	4.1 (0.99)	2.9 (0.89)	3.3 (0.99)	2.5 (0.89)
Cooking Oil	2.7 (0.92)	2.2 (0.71)	3.4 (0.54)	2.2 (0.85)
ISO Fine Dust	2.9 (0.98)	3.1 (0.89)	3.2 (0.48)	2.2 (0.55)

#### 7.3.4.2 Envelope approach to q-slope

In **Figure 7.8** the VV data for each nuisance aerosol has been edited to best present the linear-envelope of the scattering function to which a linear (first order) regression has been applied. The range of q values for which there is a strong first-order linear behaviour defines the linear envelope. The envelope range is chosen to avoid deviations from the straight line.

The ranges used for the regression and the measured slopes are given in **Table 7.7**, only the VV polarisation data are used.

**Table 7.7:** Results of q-slope envelope regression analysis for experimental and theoretical scattering results (VV). The linear correlation coefficient of each q-slope regression analysis is given in brackets next to each negative q-slope.

Fuel	Experimental q-slope (negative)		Theoretical q-slope (negative)	
	q Ranges	VV	VV	VV
Toast	10.7 to 18.3	3.9 (0.99)		3.3 (0.99)
Cooking Oil	9.17 to 17.2	3.5 (0.99)		3.98 (0.85)
ISO Fine Dust	9.17 to 18.3	2.9 (0.99)		3.4 (0.77)

The following compares the results from **Table 7.6** with those from **Table 7.7** considering the different ranges of q used. The toast q-slope has not moved appreciably from a slope of -3.9 to -4.1. The cooking oil is the most affected by the envelope range as three points at the largest scattering angles have been removed, the slope shifting from -2.7 to -3.5. The ignored points are apparently a result of backward scattering phenomena. A very linear tendency in the dust data is apparent, as there has been no appreciable change in the slope.

Comparison of theoretical results in **Table 7.7** with those in **Table 7.6** are both influenced by the interference features in the calculated scattering results. The correlation coefficients indicate clearly a reduction in the variation about the regression that results from using an envelope approach.

## 7.4 DISCUSSION

The differential mass scattering cross section for three types of nuisance aerosol have been measured. The measurement of those particle size distributions and reliance on previously

reported refractive indices has allowed a comparison with calculated results based on Mie theory. Agreements in general trend and magnitude between the calculated and experimental results is good overall. In the case of the larger mass median diameter particles generated from overheating cooking oil and dust, the calculated results show interference features (peaks and valleys) that are not observed in the experimental results. This is most likely a result of uncertainties associated with the size distribution measurements entered into the calculation. Factors associated with the detector, sensitivity and stray light will also reduce the resolution of the peaks and valleys expected from calculated results.

The analysis of the angular scattering data in terms of the scattering parameter,  $q$ , is insightful. A fixed range approach, the  $q$ -slope as defined above, has the disadvantage of being sensitive to scattering artefacts at larger scattering angles near  $130^\circ$ . The use of ranges subjectively chosen to emphasise the “envelope” appears the best way to highlight general behaviour of the scattering mechanisms as described by Sorrensen and Fischbak (2000). A smoke detector is more likely to operate with a fixed range. The principal result of the light scattering experiments on nuisance aerosols indicates that the power of the scattering parameter dependence varies between about -3 and -4.

Relative size is being measured with light scattering data quite reliably using forward scattering angles. The size distribution of the dust must contain particles that are substantial forward scatterers. These large particles result in a large forward scattering ratio that can separate the dust from the other nuisance aerosols. The experimental asymmetry ratio for irregular dust particles is slightly lower than that of the calculated result for burning toast and overheating cooking oil. What is difficult to say is whether this is also a means of discriminating the irregular particle from the spherical without investigating further. Given the results above there are no substantial differences in the asymmetry ratio of the nuisance aerosols. The differences in the calculated and experimental results are most apparent with

the dust. Investigation of the aerosol dust shape would address this. Consideration of calculated asymmetry ratio results from Mie theory is complicated by the presence of interference features.

The size distribution information in the log-probability plot, **Figure 7.3b**, indicates a good first order approximation of a lognormal distribution given the linearity of the plotted data. However, it is possible that deviation could affect the interference behaviour predicted for the corn oil and dust aerosols. The effects of the particle material densities are not known and the shape factor of the dust particles has not been taken into account. In the case of cooking oil the density of the oil can be estimated to be closer to  $0.9 \text{ g.cm}^{-3}$  than to  $1 \text{ g.cm}^{-3}$ . Thus a corrected MMAD corresponding to a density of  $0.9 \text{ g.cm}^{-3}$  corresponds to a change in MMAD of about 5 % resulting in a median diameter of  $1.52 \text{ }\mu\text{m}$  from the measured  $1.6 \text{ }\mu\text{m}$ . This does not have significant affect on the scattering calculations. The same dust has been examined by other studies (Yoshiyuki et al., 1998) but its size and possibly shape distributions are changed by its production as an aerosol in this study. Yoshiyuki et al. (1998) have estimated the shape factor of 1.5 (ie. lying somewhere between aluminium oxide and talc, not measured) and the density of  $2.2 \text{ g.cm}^{-3}$  for Arizona road dust, an earlier version of ISO Fine Dust. These quantities reduce the aerodynamic diameter measured in this study by about 32 %, from  $2.2 \text{ }\mu\text{m}$  to about  $1.5 \text{ }\mu\text{m}$ . The smaller mean diameter does not correlate well with the large slope in the forward scattering observed in this study, subsequently the measured aerodynamic diameter is used. The analysis of both shape and density of dust aerosol generated in this study is an area for future work.

## DISCUSSION

### 8.1 INTRODUCTION

A consequence of the angular scattering measurements is that the nuisance aerosols and non-flaming and flaming smoke aerosols can all be compared and their scattering behaviour used to investigate means of discriminating between them. When such means of discrimination are realised, then a detector can identify types of fires or nuisance events. This would lead to different responses to the fire events if necessary and avoiding nuisance alarms. The results of the last few chapters dealt separately with the different light scattering characteristics of the aerosols; here they are brought together and compared.

This chapter focuses on bringing the light scattering results together and comparing them in terms of the main aim of this study: the measurement of angular light scattering characteristics of flame generated smoke, non-flaming smoke, and nuisance aerosols, and to assess the similarities and differences in their characteristics. This means that this study is analogous to a survey of the light scattering characteristics of smoke and nuisance aerosols, with the subsequent analysis focusing on discrimination of the aerosols based on the surveyed data. This has been accomplished by measurement of the differential mass scattering cross section, which was made possible after the development of an appropriate calibration method. Subsequent analysis by various means has demonstrated some of the different characteristics that are accessible in the light scattering data. These methods of analysis have used both fixed angle ratios, truncated scattering cross sections and linear slope over a scattering parameter range. Where appropriate such comparisons have included results from Mie theory. The fixed angle methods are the forward scattering (Sec. 8.3.3), asymmetry ratio (Sec. 8.3.4) and polarisation ratios (Sec. 8.3.5). The results of the truncated scattering cross sections and extinction cross sections are also compared between aerosols

(Sec. 8.3.6). The scattering parameter range approach has used essentially two ranges: one fixed range and the other a variable range chosen to ignore data with high variation about a fitted linear regression (Sec. 8.4). This latter method is referred to as the envelope approach. A recently developed intuitive model for light scattering by spherical particles (Sorensen and Fischbach, 2000) has direct relevance to this study. In fact, the data from this study provides an excellent experimental examination of that model over a broader range of scattering parameter values and aerosol phase shift parameters than originally published by Sorensen and Fischbach (2000). This chapter presents a comparison of the results of this study with those of Sorensen and Fischbach (2000). Finally, comment is made on the analysis methods as means of discrimination in smoke detection.

## 8.2 DIFFERENTIAL MASS SCATTERING CROSS SECTION

### 8.2.1 CALIBRATION AND MEASUREMENT

This study has taken the opportunity to further develop a light scattering apparatus, the Large Agglomerate Optical Facility, that has in the past examined mass specific light extinction of soot agglomerates (Mulholland and Bryner, 1994; Mulholland and Choi, 1998). This development was the means of measuring the angular scattering of an aerosol in a mass specific manner by reference to an absolute calibration. That is to say, a calibration method based on an exact light scattering theory for a known aerosol to which that theory is completely applicable.

The differential mass scattering cross section,  $\sigma(\theta)$  [  $\text{m}^2 \cdot \text{g}^{-1} \cdot \text{sr}^{-1}$  ], has been measured by calibrating the LAOF with polystyrene spheres in a method analogous to that used by Mulholland and Choi (1998), who used polystyrene spheres to calibrate the LAOF for light extinction measurements. Other work (Holland and Draper, 1967; Holland and Gagne, 1970) has also made differential mass scattering cross section measurements based on a

complex calibration method substantially different from the method used in this study, see Chapter 4.

The mass scattering approach has the benefit of being easily related to standard measurements used in fire science for smoke concentration. For example, the mass concentration of smoke is measured by light extinction methods (Mulholland, 1995). The total scattering cross section is equivalent to an extinction measurement provided the particles do not absorb light (Sec. 2.4.2). Measurement of the angular distribution of scattered light finds direct application in the design and testing of light scattering smoke detectors. The benefit of a mass specific scattering measure is that the design stage can incorporate typical smoke mass concentrations to predict detector response. For example, the European fire detector standard EN54 (EN54, 1982) stipulates that a sensitive detector must operate at extinction (obscuration) levels corresponding to smoke concentrations of less than  $26 \text{ mg.m}^{-3}$  of non-flaming fires and about  $14 \text{ mg.m}^{-3}$  for soot (Seader and Einhorn, 1976; Mulholland, 1995; Mulholland and Croarkin, 2000). Very sensitive detection designs (commercial “mission critical” protection) aim to operate in the range of about  $0.02 \text{ mg.m}^{-3}$  to  $0.2 \text{ mg.m}^{-3}$  for non-flaming smoke aerosol and  $0.01 \text{ mg.m}^{-3}$  to  $0.12 \text{ mg.m}^{-3}$  for soot. To determine the angular scattering per unit volume one needs only to multiply the mass specific scattering cross section by the aerosol mass concentration. The scattering volume needs to be known to determine the actual differential scattering cross section in units of  $\text{m}^2$ .

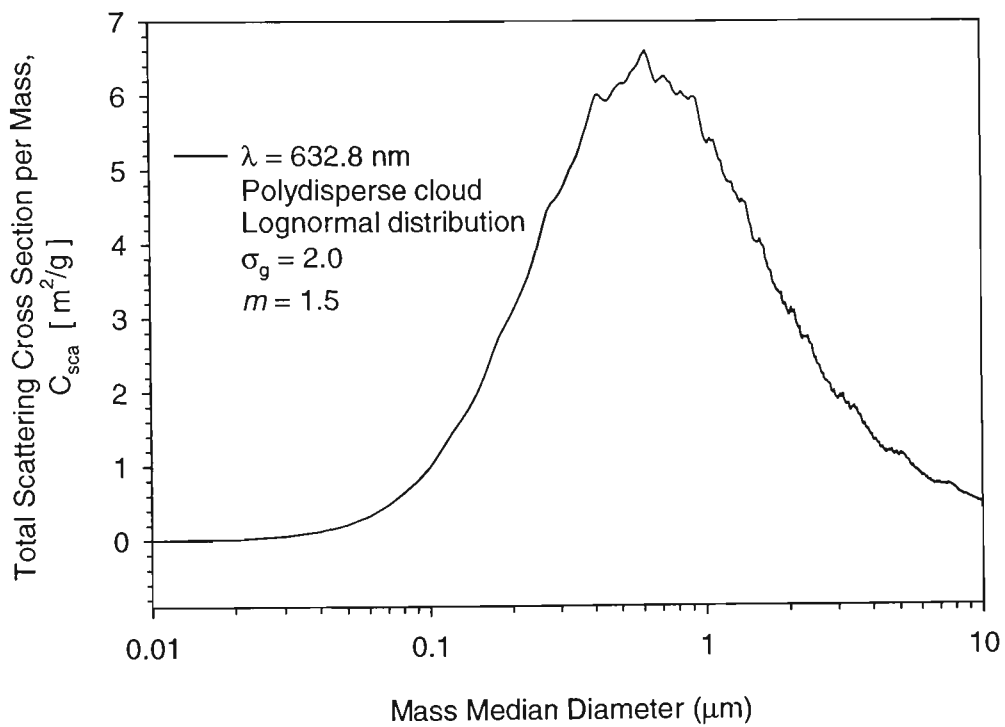
The calibration method has demonstrated that measurement of  $\sigma(\theta)$  results in good agreement with theory. In particular for the nominally 800 nm diameter polystyrene spheres used to test the calibration, the standard combined uncertainty (one standard deviation) of these measurements has been determined at 20 % and 12 % for the vertical-vertical and horizontal-horizontal polarisations respectively. The dynamic range of the measurements was typically two to three orders of magnitude. The higher uncertainty for the vertical-

vertical polarisation indicates that there is some systematic uncertainty in this polarisation measurement. That uncertainty is believed to be associated primarily with the optical and polarisation direction alignment (Sec. 4.6.4.2). The other main component of the uncertainty independent of polarisation settings is the mass concentration variation with time in the polystyrene sphere rate of production as an aerosol.

The use of this calibration method has been well demonstrated in this study and the utilisation of it relies wholly on the well-characterised polystyrene spheres commonly available and the application of Mie theory to them (Marx and Mulholland, 1983; Mulholland et al., 1985a). This approach requires a relatively modest cost because of the availability of stable, low-cost lasers and monosize polymer spheres. This is a particularly accessible and relatively straightforward means of characterising the optical properties of aerosols. In a practical field version of the LAOF it would be possible to characterise extinction, total scattering and differential scattering cross section (Mulholland and Choi, 1998; Weinert et al., 2002). From this information the absorption cross section would follow and thus an indication of the aerosol particles complex component of the refractive index (Equ. 2.21).

The measurement of an orientation averaged scattering cross section per unit mass directly provides the quantity needed for radiative transport analysis. This is to be contrasted with the widely used method of estimating the refractive index and determining an effective sphere size and then using Mie theory to compute the cross section. The uncertainty in the cross section computed in this manner can be much greater than for this experimental approach. The standard uncertainty (one standard deviation) in the repeat light scattering experiments drawing from aerosol the drum was determined at 28 % and 31 % for vertical-vertical and horizontal-horizontal polarisations respectively (Sec. 5.3.3.2). This uncertainty is dominated by the change in time of the mass concentration.

**Figure 8.1:** The total scattering cross section per mass of a polydisperse ( $\sigma_g = 2.0$ ) ensemble of particles with refractive index of  $m = 1.5$ . The mass median diameter of the ensemble is given by the abscissas. The scattering is plotted against the logarithm of the mass median diameter.



The specific mass scattering approach is more beneficial to smoke aerosols than number based measurements. The variation in the total scattering cross section per unit mass of a polydisperse cloud of aerosols as a function of the mass median diameter (MMD) of the ensemble is given in **Figure 8.1**. The results in **Figure 8.1** were calculated by placing the SCATMECH (Germer, 2001) based algorithm in a loop to change the MMD of the distribution, then by recording each distributions total scattering result. The geometric standard deviation of the size distribution was 2.0 and the refractive index was set at 1.5 with no complex component. The total scattering by a polydispersion with MMD of between 0.1  $\mu\text{m}$  and 0.4  $\mu\text{m}$  varies dramatically over that range. Less sensitive response occurs between 0.4  $\mu\text{m}$  and about 1.0  $\mu\text{m}$  and the total scattering per unit mass reaches its maximum in this range. When computed as a function of the number concentration this region is more sensitive to the logarithm of the number diameter. As the particle size increases beyond a MMD of 1.0  $\mu\text{m}$  the sensitivity of the total scattering cross section per mass also increases until about 10  $\mu\text{m}$ .

The measurement of the differential mass scattering cross section is particularly useful in the fire science and engineering fields. The natural size range of smoke aerosols also highlights the versatility of the mass specific measurement.

## **8.3 LIGHT SCATTERING CHARACTERISATION**

### **8.3.1 OVERVIEW**

The following sections address the results of this study with the aim of comparing the light scattering characteristics of soot agglomerates, non-flaming fire generated smoke aerosols, and nuisance aerosols. This comparison makes use of the measured size distributions and analysis of the angular scattering data. Smoke aerosol from non-flaming fires can vary dramatically in size due to variation in the amount of condensable vapour available to form smoke particles. Factors that affect this include the air flow rate over a smouldering fuel

(Mulholland and Liu, 1980; Hotta and Horiuchi, 1985) or the magnitude of heating applied to a pyrolysed material (Bankston et al., 1981). The fuels examined in this study cover a reasonable range of sizes.

In the case of possible nuisance aerosols the variability is high in both the source of the aerosols and the particle characteristics. This study has made use of some examples of the most common nuisance aerosols, principally those associated with cooking. The dust was included as an example of an irregularly shaped nuisance aerosol that might occur in say an industrial situation. There are many other types of irregularly shaped nuisance aerosols, such as dust from inside a building that would be different from the silica (sand) based dust (ISO Fine dust) used in these studies. While the aerosols used in this study are not representative of all possibilities the methods used and developed in this study make other aerosols and their light scattering characteristics accessible.

The agglomerate structure of soot from flaming fires has been studied in the past decades and techniques have been applied in this study to characterise the light scattering by soot. Much of this knowledge about light scattering by soot agglomerates is not well known to the fire science/engineering community.

Discrimination using the magnitude of light scattered at a particular angle is the most commonly used method in smoke detection. This is driven by the fact that low cost strategies can be implemented when based on a single angle, as opposed to relying on multiple detectors that increase costs in the detector and associated electronics. The main point of research into fixed angle smoke detector design is whether the signal of the light scattering smoke particles is in a measurable range and is common to a large range of smoke aerosols types (Meacham and Motevalli, 1992; Aggarwal and Motevalli, 1997; Nagashima et al., 1999). This generally requires that the detector be placed in a position such that

$5^\circ < \theta \leq 90^\circ$ , where signal-to-noise and gain aspects are manageable at relatively low cost. The great majority of home installed photoelectric smoke detectors make use of this type of detector design. Other systems such as aspirated detectors are aimed at getting the highest sensitivity at low concentrations. Thus some have used integrating techniques. Increasingly sophisticated and cheaper optoelectronics is leading to other approaches involving multiple angle and polarisation detection methods. Subsequently, it is becoming more common in prototype designs to use polarised angular light scattering.

### 8.3.2 AEROSOL PARTICLE SIZE

It has also been a common approach in smoke detector research to concentrate heavily on the size of scattering particles, due principally to detector dependence on particle size (Mulholland and Liu, 1980). The tendency of smoke detector work to concentrate on particle size is a consequence of the fundamental sensitivities of the smoke detectors. Ionisation smoke detectors, probably the most common household smoke detector, are sensitive to the product of the number concentration and the particle diameter. This product is also known as the first moment of the size distribution. The response of a photoelectric smoke detector is principally dependent on the aerosol particle volume, which is proportional to the third moment of the size distribution. This leads to ionisation detectors being most sensitive to aerosols with high number concentrations of smaller particles and photoelectric detectors being sensitive to larger particles (Lee and Mulholland, 1977; Mulholland and Liu, 1980). This behaviour is coupled with the generalisation about non-flaming fires producing large particles and those from flaming fires producing small particles. This generalisation appears somewhat anecdotal and has been quoted by Meacham and Motevalli (1992) and referenced to an early edition of Mulholland (1988) although there is no such generalisation made there. The generalisation is common to the smoke detector community. This could result from the size dependent behaviour of ionisation and photoelectric smoke detectors,

observed by many practitioners in the detector community. For example, the findings of Aggarwal and Motevalli (1997) are a result of different size distribution moments of the smoke aerosols; their ionisation instruments were more sensitive to aerosols for which their light scattering apparatus was the least sensitive. Similarly, the Rayleigh-like results observed by Loepfe et al. (1997) for soot but not non-flaming smoke and nuisance aerosols tends to reinforce the size generalisation, without appreciating the fractal aspects of light scattering by soot in their results. The size dependent behaviour of detectors (Mulholland and Liu, 1980) has subsequently been applied to incorrectly generalise the size of the soot and non-flaming smoke aerosols. This size generalisation is not correct in that post-flame soot can be quite large (Samson et al., 1987; Sorensen and Feke, 1996).

### *8.3.2.1 Size distribution of smoke and nuisance aerosols*

Light scattering dependence on size and the modern ease of application of Mie theory has also meant that the size of smoke particles has played an important role in light scattering smoke detector research (Meacham and Motevalli, 1992; Aggarwal and Motevalli, 1997; Nagashima et al., 1999). This is not necessarily for the best since this has led to complex structures like post-flame soot agglomerates being considered as spherical particles (Nagashima et al., 1999), as was case with in early soot experiments (Erikson et al., 1964; Dalzell et al., 1970). The size distributions have been measured for the non-flaming smoke and nuisance aerosols to compare and demonstrate consistency with Mie theory. The size distribution of soot generated by flaming fires was not measured due to the difficulties of equating the aerodynamic properties of a sphere to an agglomerate.

**Table 8.1:** The size distribution parameters of both the non-flaming fire generated smoke and nuisance aerosols measured with the MOUDI cascade impactor.

Fuel or Nuisance Source	Mass Median Aerodynamic Diameter ( $\mu\text{m}$ )	Geometric Standard Deviation
Beech Wood	1.5	1.9
Cotton Lamp Wick	0.31	1.7
Polyurethane	2.0	1.6
Toast	0.43	1.6
Cooking Oil	1.6	2.2
Dust	2.2	1.8

Figure 8.2: Log-probability plot of the size distribution of the non-flaming smoke and nuisance aerosols.

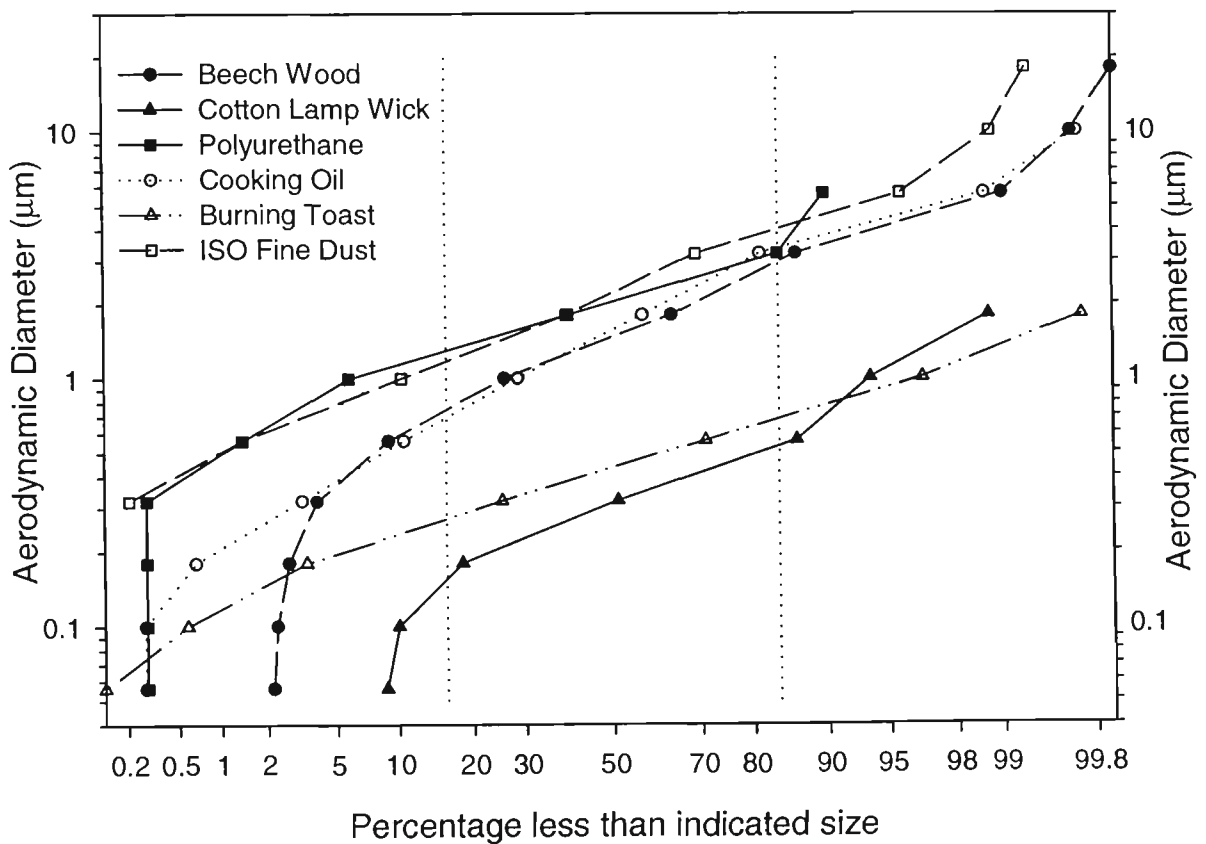


Figure 8.2 presents the size distributions of all the non-flaming smoke and nuisance aerosols as a log-probability plot. In Table 8.1 the results from the MOUDI cascade impactor have been presented for both non-flaming fire generated smoke and nuisance aerosols. Figure 8.2

demonstrates that within the 16<sup>th</sup> and 84<sup>th</sup> percentiles the log-probability plots are well represented by straight lines. This indicates lognormal distributions are a valid approximation for these particles size distributions. At percentiles of 90 % and greater the data deviates from linear behaviour, indicating that there may be a long tail in some of the size distributions, such as polyurethane smoke aerosol.

From **Table 8.1** it can be seen that there is no consistent source based difference in the size of smoke and nuisance aerosols examined. For example, cotton lamp wick and burning toast generate aerosols that have very similar size distributions. Similarly the size distribution parameters of aerosols generated by pyrolysed beech wood and overheating cooking oil are comparable with each other. This result indicates that the size of smoke and nuisance aerosols can be similar size and that any discrimination of smoke from nuisance aerosol based on size is not a robust means of discrimination. It cannot be considered to work in a wide range of possible aerosol exposures. The ISO Fine dust has some uncertainty in the size distribution measurement because of its non-spherical shape and density. The shape and density effects have not been measured in this study. The shape factor is not known and can only be estimated for the dust that is collected in aerosol form (**Sec. 7.4**).

The size distribution parameters measured in this study are complementary to those of past studies (Helsper et al., 1980; Bankston et al., 1981; Mulholland and Ohlemiller, 1982; Cheng et al., 1995; Mulholland, 1995). To summarise these findings smoke aerosols from non-flaming fires ranges from about 0.1  $\mu\text{m}$  to about 5  $\mu\text{m}$  on a volume or mass diameter basis. In the present study it is found that the mass median diameter ranges from 0.3  $\mu\text{m}$  to 2  $\mu\text{m}$  with the majority of the mass distributed in the range from 0.1  $\mu\text{m}$  to 6  $\mu\text{m}$ .

### 8.3.3 FORWARD SCATTERING RATIO

A visual comparison of size affects on scattering can be seen in the small angle scattering of selected aerosol's light scattering data presented in **Figure 8.3**. It is well recognised that the forward scattering is sensitive to the size of particles (Hodkinson, 1962; Kerker, 1969). A complete comparison of the forward scattering ratio for all of the aerosols examined in this study is given in **Table 8.2**. The ratio of forward scattering angles,  $\sigma_{VV}(5^\circ)/\sigma_{VV}(20^\circ)$ , is used to approximate the slope of the angular scattering. From this ratio the strength of the forward scattering can be compared as a measure of relative size for spherical particles and very loosely as the number of primary particles in the agglomerate. With the addition of the impactor data these results are given higher confidence. The results in **Table 8.2** show that many but not all of the soots can be discriminated from the other aerosols. Overlap occurs between the aerosol sets; for example, dust with its large value, 7.1, and ethylene with its smaller ratio, 3.8.

The cotton lamp wick and toast generated aerosols, have slopes typical of particles that are small in size. That is to say small particles cause scattering that approaches Rayleigh scattering at forward angles,  $\sigma_{VV}(5^\circ)/\sigma_{VV}(20^\circ) \sim 1$ , as demonstrated for the cotton lamp wick smoke aerosol in **Figure 8.3**. The large particles have more pronounced forward scattering shown by the high forward angle ratio in **Table 8.2**. It is important to note that smoke aerosol generated by smouldering cotton lamp wick is a clear exception to the generalisation mentioned above about smoke aerosols from non-flaming fires (**Sec. 8.3.2**).

In the case of the post-flame soot agglomerates of this study the forward scattering slope is large, a result of the large number of primary particles making up the agglomerate and thus the large radius of gyration. For an agglomerate made up of a small number of primary

**Figure 8.3:** Differential mass scattering cross section as a function of scattering parameter,  $q$ , for a selection of non-flaming fire generated smoke and nuisance aerosols.

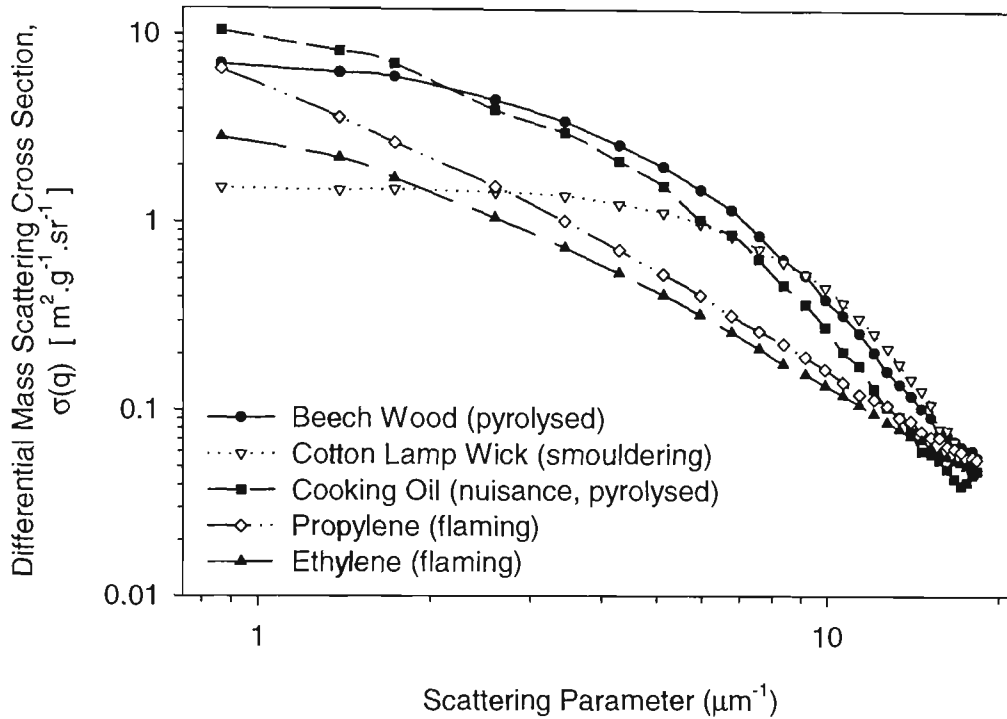


**Table 8.2:** Forward scattering ratio of the aerosol particles examined in this study.

Fuels or Nuisance Aerosols	$\sigma_{VV}(5^\circ) / \sigma_{VV}(20^\circ)$	Flaming Fuels	$\sigma_{VV}(5^\circ) / \sigma_{VV}(20^\circ)$
Beech Wood	2.0	Propylene	6.3
Cotton Lamp Wick	1.1	Heptane	6.4
Polyurethane	3.0	Acetylene	8.7
Toast	1.3	Ethylene	3.8
Cooking Oil	3.4		
ISO Fine Dust	7.1		

spheres, the small angle scattering gives smaller numbers (eg. ethylene in Table 8.2). For very small agglomerates the slope approaches one at small values of  $q$ . This is the so-called Guinear regime of scattering as the radius of gyration or scattering parameter becomes small,  $qR_g < 1$  (Equ. 2.43). The slope of forward scattering does not approach a constant,  $\sigma(q) \propto S(0) \rightarrow 1$ , for the post-flame soot agglomerates because they are so large that the length scale of the scattering is very small in comparison with their radius of gyration. Also the light scattering apparatus does not have the resolution at small values of  $q$ . Thus even at small angles the post-flame soot is in a large  $q$ -regime,  $qR_g \geq 1$ , particularly for acetylene, propylene and heptane (Sec. 2.5.2.3). The ethylene does show some transitional behaviour between different  $q$ -regimes at smaller  $q$ . This strong forward scattering is typical of post flame soot agglomerates (Koylu and Faeth, 1994a), as opposed to inflame soot agglomerates (Gangopadhyay et al., 1991) low in a flame. Shortly after the soot inception zone soot has only a low number of primary particles making up the agglomerate and thus small radius of gyration.

### 8.3.3.1 Soot agglomerate size and post-flame growth

The mean radius of gyration of soot generated at low fuel flow rates for acetylene and ethylene were measured to be about 0.8  $\mu\text{m}$  and 0.6  $\mu\text{m}$ , respectively. These were measured using the Guinier regime approximation. The mean radius of gyration was larger than these results for the soot experiments in Table 8.2 since those were performed at larger fuel flow rates. The LAOF does not have the ability to operate at the small angles required to measure the radius of gyration of these larger soot agglomerates.

The Guinier regime approximation has also been applied to the growth of acetylene and ethylene. This work was essentially a secondary investigation aimed at examining the viability of monitoring post-flame soot agglomerate growth with angular scattering. The ethylene

results in **Sec. 6.4** demonstrate clearly the influence of the agglomerate scattering on the forward scattering results as described by the Guinier regime. The growth results indicate that the acetylene has already grown to a large agglomerate radius of gyration by the time it enters the LAOF.

Quantification of the radius of gyration of the soots was complicated by their large size (ie. the Guinier regime does not apply) and poor statistics associated with scattering by large agglomerates in the ensemble of particles. As time passed during the soot growth experiments the number of these large soot agglomerates increases making the noise level increase over time and dominating the scattering at small angles. This meant that after about 45 minutes the radius of gyration data had large uncertainty.

#### 8.3.4 ASYMMETRY RATIO

The asymmetry ratio,  $\sigma_{VV}(45^\circ)/\sigma_{VV}(135^\circ)$ , is based on the amount of light scattered into forward to backward angles relative to  $90^\circ$ . In **Table 8.3** the asymmetry ratio of the aerosols examined in this study are presented. The difference between values for soot and the other aerosols is most striking. This difference is a direct result of the large soot agglomerates having very different morphologies to the other aerosols. For soot the scattering cross sections at  $45^\circ$  are about 4 to 6 times those of the magnitude at  $135^\circ$ . The differences in magnitude are far greater for spherical particles. Very small particles that scatter light in the Rayleigh regime will give asymmetry ratios of 1 for the VV polarisation. The asymmetry ratio is a method of discriminating soot from the other aerosols.

The asymmetry ratio is a method of discrimination that finds its physical basis most easily described by a scattering parameter representation of scattering results. When the particles scattering light are large soot agglomerates then the structure factor has a power law dependence on the scattering parameter and fractal dimension. Described by a straight line

on a Log-Log plot. As a result of this power law dependence, the asymmetry ratio varies over a small range for different soots fuel sources. This scattering behaviour of large soot agglomerates is universal due to their fractal nature, thus the asymmetry ratio for the soot agglomerates in our study are all very similar. Ideally such agglomerates would have asymmetry ratios ranging from about 4.5 to 4.9 for fractal dimensions of typically 1.7 to 1.8 (Sec. 6.5).

In the case of the polydisperse smoke and nuisance aerosols the ensemble of diameters complicates the light scattering and thus the regime of the scattering parameter the asymmetry ratio corresponds to. This point is dealt with more thoroughly in the section on the scattering parameter and scaling method below. The asymmetry ratios of the smoke aerosols in **Table 8.3** do not show size dependence. The fact that the angle on which the numerator of the asymmetry ratio is dependent,  $\theta = 45^\circ$ , means that forward scattering effects in the asymmetry ratio values are negligible. The slightly lower value of the asymmetry ratio for the ISO Fine Dust nuisance aerosol might be due to irregular (non-spherical) shape but the difference is not substantial enough to be conclusive.

**Table 8.3:** Asymmetry ratio of the aerosol particles examined in this study.

Fuels and Nuisance Aerosols	$\sigma_{VV}(45^\circ) / \sigma_{VV}(135^\circ)$	Flaming Fuels	$\sigma_{VV}(45^\circ) / \sigma_{VV}(135^\circ)$
Beech Wood	15.5	Propylene	4.9
Cotton Lamp Wick	15.7	Heptane	5.6
Polyurethane	13.2	Acetylene	4.0
Toast	17.8	Ethylene	4.5
Cooking Oil	13.6		
ISO Fine Dust	11.3		

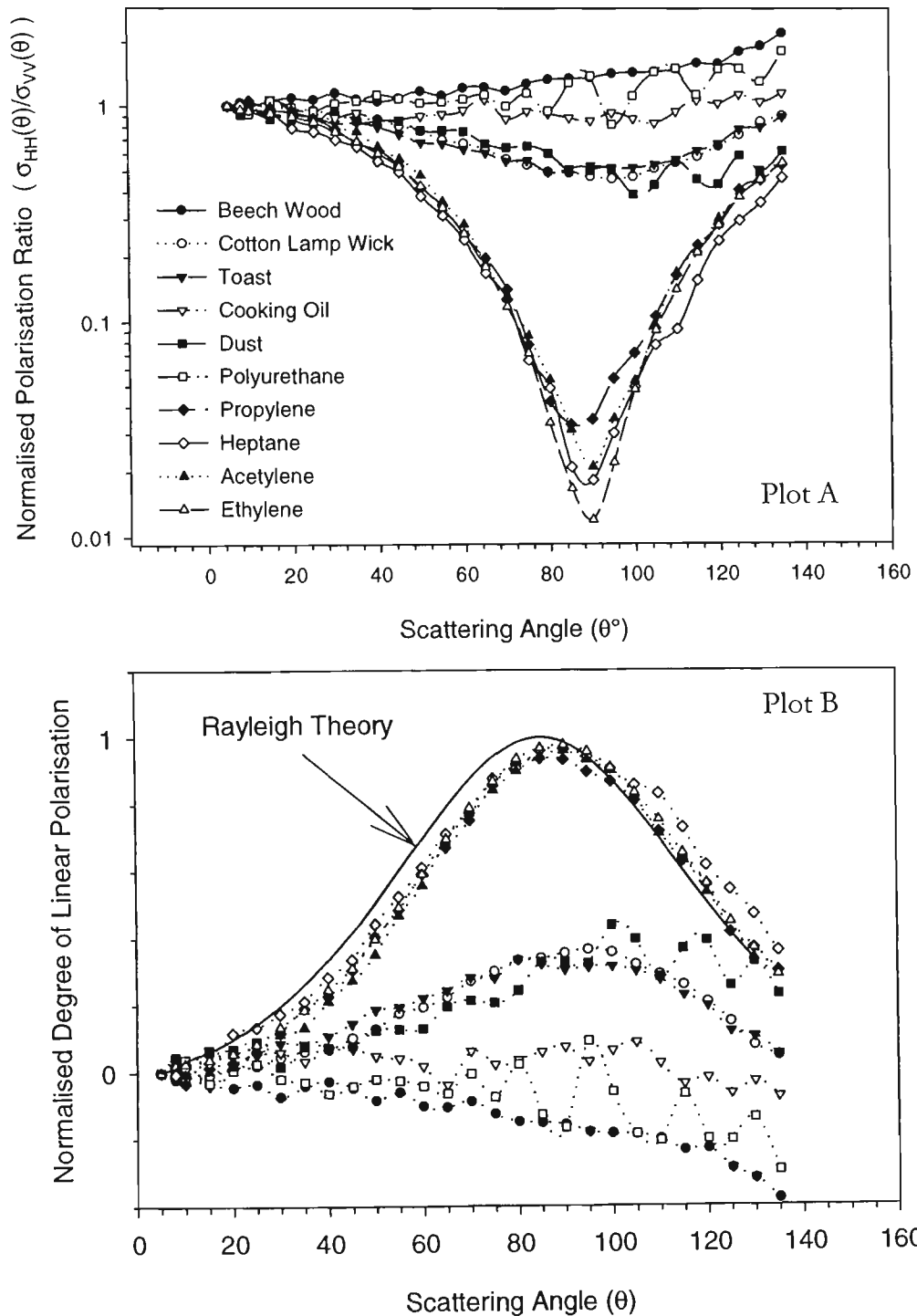
### 8.3.5 POLARISATION RATIO

The polarisation ratio,  $\rho(\theta) = \sigma_{VV}(\theta) / \sigma_{HH}(\theta)$ , is another way of observing differences between soot agglomerates and spherical particles. One approach that has worked well is that detailed in the work by Loepfe et al. (1997) where they measured the degree of linear polarisation (Equ. 2.34), which is related to the polarisation ratio used in this study. Loepfe et al. (1997) found the highest degree of polarisation corresponded to soot particles, a medium value existed for cotton lamp wick smoke, and that the lowest values were found for the pyrolysed wood smoke. In Figure 8.4a the polarisation ratio is plotted and the degree of linear polarisation is also shown in Figure 8.4b along with the theoretical result for Rayleigh scattering. The implication made in the work by Loepfe et al. is that soot is a small Rayleigh scattering particle. The high degree of linear polarisation at  $90^\circ$  indicated to them that the flame generated smoke aerosol size was “small compared to the wavelength of the incident beam”. On the contrary, the post-flame soot agglomerates are far from small in size compared with the wavelength of incident light. The primary particles making up the agglomerates are very small compared with the wavelength, having nearly monodisperse sizes with mean diameters ranging from about 10 nm to 80 nm (Koylu and Faeth, 1994b; Mulholland, 1995). From Sec. 2.5.5 and Equ. 2.41 the light scattering by soot agglomerates can be written in terms of a Rayleigh scattering component from the small primary particles and an agglomerate scattering term due to the interference in the far field. That is (Mountain and Mulholland, 1988),

$$\sigma_{XX} = (S_{ag} \cdot \sigma_r)_{XX} \quad \text{but} \quad (S_{ag})_{VV} \approx (S_{ag})_{HH}$$

where  $\sigma_r$  is the Rayleigh-like scattering component and X denotes a given polarisation. The term  $S_{ag}$  arises from the interference in the far field of the scattering by the individual primary particles making up the agglomerate. The term,  $S_{ag}$ , can vary by a few orders of

**Figure 8.4:** a) The normalised (at 5°) polarisation ratio and b) normalised degree of linear polarisation of the aerosols examined in this study. The result for a Rayleigh scattering has been included in figure (b).



magnitude while for Rayleigh scattering  $(\sigma_r)_{\lambda V}$  is independent of angle. Since  $S_{ag}$  is not strongly dependent on the polarisation direction, the polarisation ratio is primarily caused by the Rayleigh-like scattering by the primary spheres and results in a minimum at  $\theta = 90^\circ$  as seen in Figure 8.4b and similarly the degree of linear polarisation has a maximum near  $\theta = 90^\circ$ . Thus, soot agglomerate scattering appears to be Rayleigh-like in terms of the polarisation ratio and related measures, although the scattering for an agglomerate is not that of a Rayleigh particle.

As can be seen in Figure 8.4a and 8.4b the non-flaming fire and nuisance source aerosols examined are not easily distinguished from each other. The results of this study are comparable to those of Loepfe et al. (1997), not just for the soot but also for the non-flaming fire fuels smouldering cotton lamp wick and pyrolysed beech wood. Loepfe et al. (1997) also noted the dynamic change in their light scattering results for toast aerosol as it burnt.

### 8.3.6 TRUNCATED SCATTERING AND EXTINCTION

The truncated mass scattering cross section,  $\sigma_T$ , has been calculated from the experimental results of the smoke and nuisance aerosols examined. These mass scattering cross section results are presented in Table 8.4. Extinction mass scattering cross section,  $\sigma_E$ , results from experiments in the FE/DE (Sec. 5.3.2) on the non-flaming fire generated smoke aerosols are also presented for comparison in Table 8.4. In the case of the smoke aerosols from non-flaming fires the absorption is expected to be negligible due to a small imaginary component of the refractive index (Mulholland et al., 1985b). For non-absorbing particles the extinction cross section will be equal to the total scattering cross section for these aerosols (Equ. 2.21).

The differences between  $\sigma_T$ , measured in the LAOF, and  $\sigma_E$ , measured in the FE/DE, show the effects of experimental differences and uncertainties. It would be far better in the

future to measure the extinction cross section and total scattering cross section in the LAOF as has been done in the past for soot (Mulholland and Choi, 1998). Seader and Einhorn (1976) found that the mass extinction coefficient for a white light source over a wide selection of smokes generated by non-flaming fires was about  $4.4 \text{ m}^2\cdot\text{g}^{-1}$ . In Table 8.4 the results for beech wood and cotton lamp wick,  $\sigma_T$ , are high compared with the extinction value, a difference that is caused by the experimental uncertainties in both measurements. The values of the extinction,  $\sigma_E$ , are about that of Seader and Einhorn (1976) except for the polyurethane smoke aerosol. The low value of  $\sigma_T$  for the ISO Fine Dust might be a result of some absorption by the iron oxide

**Table 8.4:** The truncated mass scattering cross section (MSCS) of the aerosol particles examined in this study and extinction mass cross sections. The asterix (\*) denotes absorbing particle.

Fuels and Nuisance Aerosols	Truncated MSCS $\sigma_T \text{ (m}^2\cdot\text{g}^{-1}\text{)}$	Extinction MCS $\sigma_E \text{ (m}^2\cdot\text{g}^{-1}\text{)}$	Flaming Fuels	Truncated MSCS $\sigma_T \text{ (m}^2\cdot\text{g}^{-1}\text{)}$
Beech Wood (repeat expmts.)	5.2	4.2	Propylene*	2.3
Cotton Lamp Wick	5.3	4.4	Heptane*	2.2
Polyurethane	4.2	2.8	Acetylene*	1.6
Toast	4.6	3.5	Ethylene*	1.4
Cooking Oil	4.3	4.1		
ISO Fine Dust*	2.4	4.0		

component of the dust, but this is inconclusive given the uncertainties of the measurements. The soot results for  $\sigma_T$  are in fair agreement with Mulholland and Choi (1998) for acetylene and ethylene,  $1.65 \text{ m}^2\cdot\text{g}^{-1}$  and  $1.58 \text{ m}^2\cdot\text{g}^{-1}$  respectively.

### 8.3.7 COMPARISON OF EXPERIMENTAL AND MIE THEORY RESULTS

The qualitative comparison of the experimental and calculated Mie results is excellent. The comparison of experimental with calculated Mie results has been possible due mainly to the size distribution measurements made. As mentioned above the lognormal distribution is apparently a valid approximation but it is not necessarily the actual particle size distribution leading to some uncertainty in the Mie calculations. The experimental uncertainties also contribute to the differences seen between Mie theory and experimental results (Sec. 4.6 and Sec. 5.2.2.3.1). The work of Mulholland et al. (1985b) has been the source of refractive index data for smoke aerosols from non-flaming fires. Inclusion of the complex part of the refractive index determined by Mulholland et al. (1985b) was found to have negligible influence on the computed results. Variation of the mean size used in the computation was far more dominant. This was also the case for the nuisance aerosols.

A factor complicating comparison between experiment and calculated results has been the interference phenomena in theoretical results and the lack of such phenomena in the experimental results. This has strongly influenced the different ratios used for analysis of the calculated angular scattering results. The interference peaks and valleys have also complicated the analysis of the scattering parameter dependence.

The analysis of the light scattering results above indicates that there are some methods better suited to differentiate between soot and other aerosols. The most promising are the polarisation and asymmetry ratios, which have their reasons for working bound up in a structure factor and scattering parameter formalism. This being the case the implication is

that shape is a preferred strategy for discrimination. Traditionally size has been the method of discriminating between particles. The plots of the differential mass scattering cross section as a function of the scattering parameter for the non-flaming smoke and nuisance aerosols, such as those in **Figure 8.3**, show behaviour that is aesthetically pleasing to the eye and positively intriguing. Another approach to discrimination based on the scattering parameter is the subject of the following section. This method also allows the testing of a recent model for scattering by spherical particles that is based on the scattering parameter.

## 8.4 LIGHT SCATTERING AS A FUNCTION OF SCATTERING PARAMETER

### 8.4.1 SCATTERING PARAMETER

Depicting the scattering in terms of scattering angle,  $\theta$ , has been the traditional method of analysing scattering data, which is the approach taken in the last section (**Sec. 8.3**). Similarly the scattering angle has been the simplest parameter for light scattering smoke detector design when considering placement of detectors at particular locations about the scattering volume. The scattering parameter,  $q = 4\pi\lambda^{-1} \sin(\theta/2)$ , on the other hand has remained an instrument of high-energy scattering, crystallographic and dynamic light scattering studies (Sorensen, 2001). The scattering parameter represents the reciprocal length scale of the scattering process and as such has a strong relationship to the geometry of the scattering particle (**Sec. 2.5**). The relationship the scattering parameter has with light scattering by complex structures, in this case soot agglomerates, has brought it into the toolbox of researchers involved with light scattering by small particles. However, it has so far remained in the area of particles with fractal morphologies (soot agglomerates) and is yet to be widely accepted into the domain of light scattering problems associated with spherical particles, that is until recently (Sorensen and Fischbach, 2000).

The striking morphological differences between soot and non-flaming fire generated aerosols were the impetus for this study. As this study has progressed it became clear that the

scattering parameter was the means to understanding the scattering by both the soot agglomerates and the spherical smoke aerosols. The scattering parameter representation is presented here with the purpose of using it as a means of discrimination, as the angular and polarisation analyses have been used in the last section. Another timely benefit of the light scattering survey of smoke and nuisance aerosols has been the opportunity to compare results with and test the model proposed by Sorensen and Fischbach (2000).

#### 8.4.2 SCALING APPROACH

The recent scattering description based on the scaling approach put forward by Sorensen et al. (Oh and Sorensen, 1999; Sorensen and Fischbach, 2000) is a vehicle by which the results of this study are easily understood. The scaling and Fourier methods both describe the behaviour of light scattering by soot agglomerates and are well understood (Sec. 2.5). This is not the case for spherical particles with diameters close to the wavelength of the incident light. Sorensen and Fischbach (2000) demonstrated the  $q$  dependence of the envelope of light scattering using Mie theory for single sized particles. They also tested it against a relatively small set of experimental data from a polydisperse aerosol of water mist. In the case of particles with small phase shift parameter,

$$\gamma_p = kd_p |m - 1|, \quad (8.1)$$

the overall form of scattering is described by (Sorensen and Fischbach, 2000),

$$S(q) \propto \begin{cases} 1 & \text{for } qR < 1 \\ (qR)^{-4} & \text{for } qR > 1 \end{cases} \quad \text{and small } \gamma \quad (8.2)$$

For the case of spheres with large phase shift parameter the scaling method gives the proportional behaviour of the scattering as (Sorensen and Fischbach, 2000),

$$S(q) \propto \begin{cases} 1 & \text{for } q < l^{-1} \\ (qR)^{-2} & \text{for } l^{-1} > q > R^{-1} \text{ and large } \gamma. \\ R^2(qR)^{-4} & \text{for } q > l^{-1} \end{cases} \quad (8.3)$$

Note that the structure factor,  $S(q)$ , is directly proportional to the differential mass scattering cross section,  $\sigma(q)$ . Determining the slope at large values of  $q$  for  $\sigma(q)$  plotted as a log-log graph, yields the indices on which the  $q$  dependence of the scattering relies. The slopes determined in this manner from experimental results can then be compared to what is expected from the scaling method results of Sorensen and Fischbach (2000). In this study the slope of the log-log graph over a fixed range for all the aerosols is being referred to as the  $q$ -slope. The envelope  $q$ -slope is a slope computed over a variable range. The fractal dimension refers to the slope determined for soot agglomerates. The  $q$ -slope of a spherical particle is related to the scaling exponents given in the preceding discussion.

Sorensen and Fischbach (2000) presented results of light scattering by water droplets of about  $0.5 \mu\text{m}$  in diameter. With these results they compared their scaling method, namely **Equ. 8.3**. The number of data points in the different scale regimes (slopes of -2 and -4) were no more than three points. This study presented the results of a direct fit to a larger experimental data set and over a wider range of  $q$  values. In the next section these results are compared between the different aerosols.

#### 8.4.2.1 Comparison of $q$ -slope results

In **Table 8.5** the  $q$ -slope values of the vertical-vertical polarisation for non-flaming fire generated smoke and nuisance aerosols are presented. These  $q$ -slopes were determined by applying a linear regression over the fixed range of  $12 \leq q \leq 18 \mu\text{m}^{-1}$  ( $75^\circ \leq \theta \leq 135^\circ$ ), the linear correlation coefficient,  $r^2$ , and slopes from Mie theory are also given. In **Table 8.6**

**Table 8.5:** Q-slope of aerosols examined in this study for a fixed range, both experimental values and in the case of spherical particles theoretical values from Mie theory. The phase shift parameter is also given for the spherical particles.

Fuel or Nuisance Source	Experimental $12 \leq q \leq 18 \mu\text{m}^{-1}$		Mie Theory $12 \leq q \leq 18 \mu\text{m}^{-1}$	
	q-slope (negative)	Linear correlation coefficient $r^2$	q-slope (negative)	Linear correlation coefficient $r^2$
Beech Wood	3.1	0.98	3.7	0.73
Cotton Lamp Wick	4.2	0.99	3.2	0.99
Polyurethane	3.1	0.91	3.9	0.65
Toast	4.1	0.99	3.3	0.99
Cooking Oil	2.8	0.92	3.6	0.5
Dust	2.9	0.98	3.2	0.48

**Table 8.6:** The fixed range q-slope and fractal dimensions for post-flame soot agglomerates.

Fuel	q-slope (negative)	Fractal Dimension	Fractal Dimension
	$12 \leq q \leq 18 \mu\text{m}^{-1}$	$8 \leq q \leq 18 \mu\text{m}^{-1}$	(Koylu and Faeth, 1994a)
Propylene	1.8	1.8	1.84
Heptane	2.0	1.9	----
Acetylene	1.7	1.6	1.85
Ethylene	1.7	1.7	1.83

**Table 8.7:** The phase shift parameters based on number mean and mass median diameters for the non-flaming smoke aerosols and nuisance aerosols.

Fuel or Nuisance Source	Phase Shift Parameter $\gamma_n$	Phase Shift Parameter $\gamma_m$
Beech Wood	2.2	7.5
Cotton Lamp Wick	0.7	1.5
Polyurethane	5.1	9.9
Toast	1.1	2.1
Cooking Oil	1.2	7.6
ISO Fine Dust	3.6	10.3

the slope for flaming fire generated soot agglomerates is shown along with the fractal dimension determined over the range of  $8 \leq q \leq 18 \mu\text{m}^{-1}$ .

Another parameter necessary for comparison of experimental results with **Equ. 8.2** and **8.3** is the phase shift parameter. In **Table 8.7** the phase parameters of the non-flaming fire and nuisance source aerosols are presented. The number diameter is used for,  $\gamma_n : d_p = d_n$ , determined after applying the Hatch-Cholate equation, **Equ. 2.8**, to the mass median aerodynamic diameter (MMAD),  $d_m$ . Similarly the phase shift parameter related to the mass median diameter is  $\gamma_m : d_p = d_m$ . The number based phase shift parameter,  $\gamma_n$ , results in a close range of values relatively small values when compared to the mass based phase shift parameter,  $\gamma_m$ . The mass based diameter is proportional to the volume diameter and thus more physically relevant to the phase shift parameters role as described by Sorensen and Fischbach (2000).

The results of the slope over the fixed range in **Table 8.5** shows that the aerosols with small phase shift parameters,  $\gamma_m$ , have slopes of about -4 as would be expected from **Equ. 8.2** for  $qR > 1$ . On the other hand, larger values of  $\gamma_m$  lead to slopes closer to -3 while a value of -2 or -4 would be expected from **Equ. 8.3**. The larger aerosols have q-slopes that are influenced by the beginning of backscattering phenomena leading to linear correlation coefficients less than 0.98.

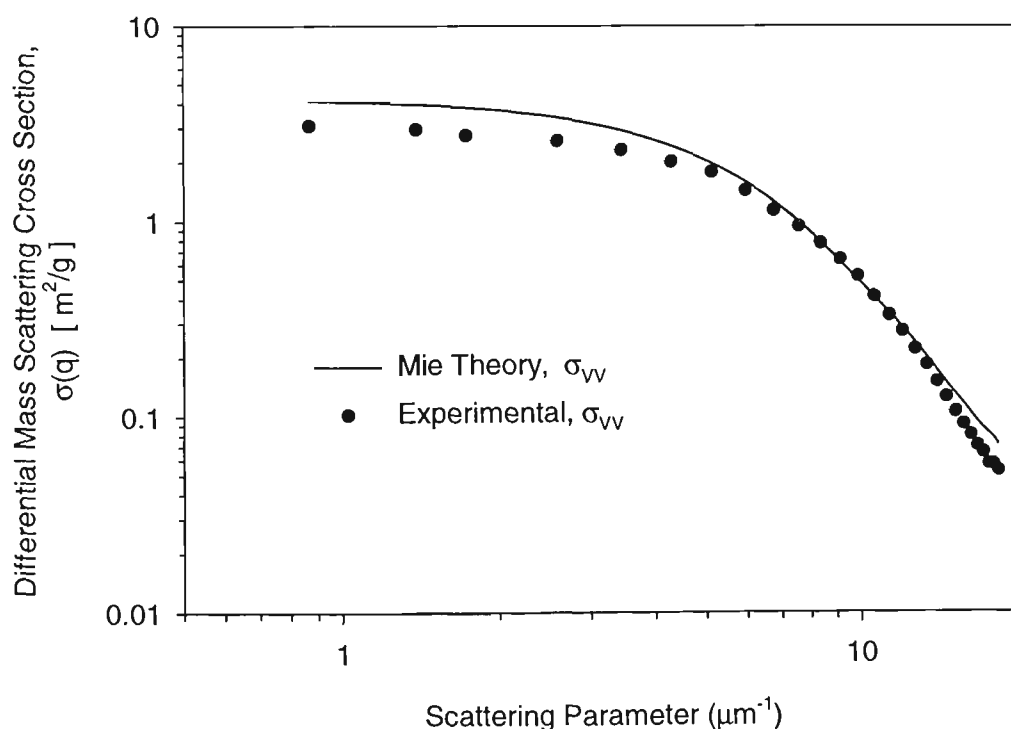
There is a substantial difference between the experimental and calculated Mie theory results of the slope for both small and large phase shift parameter aerosols in **Table 8.5**. For the large  $\gamma_m$  aerosols, interference phenomena in the calculated results makes q-slope calculation difficult, as shown by the small values of the linear correlation coefficient in **Table 8.5**. The linear correlation coefficient is very good for the Mie theory results for small particles (cotton lamp wick and toast sources), but the Mie theory q-slope values are very different from the experimental results and what would be expected from **Equ. 8.2**. **Figure 8.5** shows clearly that experimental results fall faster than that predicted by Mie theory at large q for these small  $\gamma_m$  aerosols. The calculated result for these smaller particles is apparently counter to the findings of Sorensen and Fischbach (2000). Probably a result of the different ranges used in this study and that of Sorensen and Fischbach (2000).

In **Table 8.6**, the agglomerate fixed range slopes do not vary greatly from the fractal dimension figures as would be expected given the large post-flame soot agglomerates. The values determined fall near the range of expected values of around -1.7 to -1.8 (Koylu and Faeth, 1994a; Sorensen and Feke, 1996). The results of fractal dimension measurements on post-flame soots by Koylu and Faeth (1994a) are shown in **Table 8.6** for comparison, they agree well with the values measured in this study. The linear correlation coefficient for

**Table 8.8:** The q-slope envelope of the scattering data, the range used to determine the q-slope is varied, for non-flaming smoke aerosols and nuisance aerosols. The linear correlation coefficient is given in parenthesis.

Fuel or Nuisance Source	Range in q	Experimental Envelope (negative) VV	Theoretical Envelope (negative) VV
Beech Wood	6.79 to 18.3	3.2 (0.99)	3.1 (0.91)
Cotton Lamp Wick	11.4 to 18.3	4.1 (0.99)	3.1 (0.99)
Polyurethane	8.4 to 17.2	3.6 (0.99)	3.5 (0.83)
Toast	10.7 to 18.3	3.9 (0.99)	3.3 (0.99)
Cooking Oil	9.17 to 17.2	3.5 (0.99)	4.0 (0.85)
ISO Fine Dust	9.17 to 18.3	2.9 (0.99)	3.4 (0.77)

**Figure 8.5:** Plot of experimental and Mie theory results of nuisance aerosol generated by burning toast.



all of the experimental results is very good and highlights the first order linearity of the scattering from the large agglomerates at large  $q$  values.

**Table 8.8** presents the results of the envelope slope (the slope computed using a variable range of  $q$ ) determined using different ranges of  $q$  for the polydisperse non-flaming smoke and nuisance aerosols. These range are shown in **Table 8.8** along with the linear correlation coefficient of the regression and Mie theory results of the envelopes' slope. The ranges used to fit a linear regression was chosen to avoid data values that trend upwards at about  $q = 17 \mu\text{m}^{-1}$  (see cooking oil results in **Figure 8.3**), but to also avoid the influence of transitions at  $l^{-1} < q < R^{-1}$ . This is a somewhat subjective process. The results for the two small aerosols are about -4 and their theoretical results are essentially unchanged from those results in **Table 8.5**. The results for aerosols with large phase shift parameters have increased closer to -4. This is a direct result of reducing the variation of data-points about the regression. Interestingly even though the ranges of the large  $\gamma_m$  have moved to smaller  $q$  values no reduction of the slopes has occurred as would be expected for a strong -2 influence on slope. The values for dust in both **Table 8.5** and **Table 8.8** reflect the aerosol has a very linear scattering response on a log-log plot. This is a result of both large mean size and wide distribution, but the effect of irregular shape on this result would require further study. Mie theory results for the larger aerosols in **Table 8.8** are improved in terms of the linear correlation coefficient and closer to the experimental results.

A possible fault with the subjective method of determining the  $q$ -slope of the envelope is that it can extend to smaller values of  $q$  that introduce scattering data from a different length scale regime (e.g.  $l^{-1} < q < R^{-1}$  in **Equ. 8.3**). The large linear correlation coefficient for the results in **Table 8.8** tend to indicate that this is not happening, although it might be having

some effect in the case of the aerosol from burning toast. Extension of that range to smaller  $q$  does lead to smaller  $q$ -slope values.

### 8.4.3 SCALING METHOD AND ENSEMBLE AVERAGING

From the results of Sorrensen and Fischbach (2000), monodisperse particles with large phase shift parameters have a wide range of  $q$  at which the slope of -2 is dominant. The value of -4 applies once the large  $q$  threshold is reached,  $q > l^{-1}$  as described by **Equ. 8.3**. Larger values of the phase shift parameter move the occurrence of the *transition* of slope from -2 to -4, to larger values of  $q$  (Sorensen and Fischbach, 2000). This has the effect of producing  $q$ -slopes of about -3 to -3.6 for the aerosols with large mean phase shift parameters in our study. This is a consequence of averaging over the ensemble of different sized particles with varying slopes between -2 and -4 at large  $q$ . Very large phase shift parameters apparently weight the slope closer to -2 away from -4, as is demonstrated by the dust aerosol.

Empirically then the result for ensembles of particles characterised by a large phase shift parameters is,

$$\sigma_{wv}(q) \propto \begin{cases} 1 & \text{for } q < l^{-1} \\ q^{-2} & \text{for } l^{-1} > q > R^{-1} \\ \langle q^{-3} \rangle_R & \text{for } q > l^{-1} \end{cases} \quad (8.4)$$

In the large  $q$  regime the angled brackets represent an average over the ensemble of the size distribution, thus the subscript R. The intermediate  $q$ -regime,  $l^{-1} > q > R^{-1}$ , is not easily examined with results from aerosols examined in this study since it is harder to define its range. Nevertheless, an examination of a number of  $q$ -slopes in the intermediate range results in  $q$ -slopes of about 1.5 to 2.5 for the aerosols examined in this study.

In the case of the small particles from cotton lamp wick and toast, the phase shift parameters are small enough over the ensemble of particles to have a negligible slope of -2. In this study, the differential mass scattering cross section of polydisperse aerosols with small  $\gamma_m$ , follow Equ. 8.2 with apparently little effect from the larger sizes in the distribution. The subjectiveness of scattering parameter range choice is not such a problem with small particles because it has a very well defined slope at large  $q$ .

The analysis conducted in this section (Sec. 8.4) has demonstrated the discrimination between smokes aerosols from flaming fires from the other aerosols examined in this study. This has been accomplished by using the scattering parameter as opposed to the scattering angle used in Sec. 8.3. The scattering parameter analysis has also allowed comparison with a recent scattering model with a larger data set than originally available to the authors of that model (Sorensen and Fischbach, 2000). In the next section the application of the various methods of analysing the scattering data for discrimination is addressed.

## 8.5 DISCRIMINATION AND APPLICATION TO SMOKE DETECTION

### 8.5.1 LIGHT SCATTERING RATIOS

The forward scattering ratio could not reliably be used for discrimination of soot agglomerates from other aerosols. Large post-flame soot scatters a great deal of light into the near forward angles thus they tend to give forward scattering ratios similar to large aerosols. The measure itself is not simply executed for most smoke detectors, as it requires detectors at very small angles with small fields of view. The forward scattering ratio is not able to differentiate the nuisance aerosols from the non-flaming fire generated smoke aerosols examined in this study. The ratio does separate the aerosols based on their size.

The asymmetry ratio can distinguish soot from the other aerosols due to the fact that the asymmetry ratio reflects fractal scattering by the large post-flame soot. Simply picture the

asymmetry ratio as a function of the scattering parameter,  $\sigma(7.6\mu\text{m}^{-1})/\sigma(18.3\mu\text{m}^{-1})$ , or observe the straight line connecting these points and the fact that its slope is approximately equal to the fractal dimension of the soot. The nature of the universality in light scattering by soot is also reflected by the similar values determined for the soot examined in this study. The asymmetry ratio does not distinguish the nuisance aerosols from the non-flaming smoke aerosol.

The polarisation ratio about  $90^\circ$  is also able to distinguish the soot agglomerates from the other aerosols in this study and has been observed in other studies (Loepfe et al., 1997). The polarisation insensitivity of the agglomerate structure factor due to interference in the far field is the reason for this (Sec. 8.3.5 or Sec. 2.5.2). As with the other ratio approaches the polarisation ratio does not categorically distinguish between the nuisance and smoke aerosols from non-flaming fires. That is not to say that discrimination of particular aerosols is not possible, Loepfe et al. (1997) have shown that the degree of polarisation at  $150^\circ$  might be used to isolate water mist from smoke aerosols.

The inability of the light scattering ratios to discriminate nuisance from non-flaming fire generated aerosols is a result of the morphological similarities between these aerosols. The irregular aerosol examined in this study is the ISO fine dust, but scattering effects due to this irregularity is not conclusively observed.

### 8.5.2 Q-SLOPE

The q-slope results in Table 8.5, 8.6 and 8.8 indicate quite strongly that there is a means of distinguishing soot generated in flaming fires from that of smoke aerosols generated in non-flaming fires. The q-slope for the particles examined here does differentiate between particles with small and large phase shift parameters, and thus mean size differences between particles examined. Unfortunately there is no clear discrimination between the smoke

aerosols from non-flaming fires and nuisance aerosols using the q-slope because of the morphological similarities.

Use of the q-slope for discrimination of flaming fires from other aerosols in smoke detection is a novel approach. A smoke detector's ability to identify a threat as a flaming fire is of most benefit in situations where flaming fires pose a unique and critical risk. A particular risk of this nature might require special preparations or particular actions from respondents. This would most likely occur, but is not restricted to an industrial situation. A discriminating detector based on the q-slope approach would function as normal with the addition that it would have a separate alarm signal for detection of a flaming fire. As demonstrated in this study it would still be susceptible to nuisance alarms from some aerosols.

The practical design of such a detector would be very different from the apparatus used in this study, and in fact might require an array of detectors to determine the slope in the backward angles. This poses many difficulties as the backward angles scatter light weakly and stray light can reduce signal to noise dramatically. It is the aspects associated with the scattering chamber design, detectors and signal handling electronics of a smoke detector that is the crucial factor as to whether it would make it to market. Simply put, the design must be cost effective and that usually means low cost. This would be aided by identifying particular angles for detector positions that could be used to determine the q-slope efficiently, since the fewer the detectors the lower the cost. Similarly, advances in optoelectronic components would be used in developing a practical detector design.

## **8.6 FINAL COMMENTS**

In closing this discussion it must be said that there are still other approaches to discriminating particles based on morphology as opposed to just size. For example, complete polarisation studies of the scattering (Mueller) matrix might be of use for irregular particles, differences of

irregular silica particles were observed by Holland and Grange (1970). Such an approach for industrial installations seems appropriate, however the crux of the problem for light scattering smoke detection is the nuisance aerosols that are very similar to smoke aerosols. The pyrolysis based nuisance aerosol from burning toast are extremely similar to those expected in a non-flaming fire, and to cigarette smoke which is another common nuisance aerosol as well as a fire ignition source. Cooking oil fires themselves are very common causes of fires in homes (Wijayasinghe and Makey, 1997). Given this complicating nature of some nuisance aerosols multi-parameter detection is a serious research and development direction, such as combining gas (CO) and aerosol detection.

Light scattering discrimination is based on differences in morphology and as such will not see the difference between particles with similar optical properties and physical characteristics. On the other hand, *a priori* information on specific particles can be collected to target a particular scattering characteristic of an aerosol. This means characterising a common nuisance aerosol in an environment and building a system to ignore it, given appropriate safety margins. This seems like a lot of effort to go to when other fire safety measures are available, such as human behavioural aspects and environment design. On the other hand critical risk situations do exist.

## CONCLUSIONS

### 9.1 CONCLUSIONS

This study has developed and demonstrated a novel gravimetric calibration method, using polystyrene spheres, for angular light scattering measurement. The calibration development was a necessary step in quantifying the scattering by smoke and nuisance aerosols using a system with low incident beam power compared with gas calibration methods. The calibration method leads directly to an absolute measure of the differential mass scattering cross section [ $\text{m}^2\cdot\text{g}^{-1}\cdot\text{ster}^{-1}$ ] of unknown aerosols. The differential mass scattering cross section has been measured for various non-flaming and flaming fire generated smoke aerosols, as well as nuisance aerosols created in the Fire Emulator/Detector Evaluator at the National Institute of Standards and Technology (USA). These measurements have been determined for two linear polarisation settings (vertical and horizontal to the scattering plane) and a scattering angle range of  $5^\circ$  to  $135^\circ$  at a wavelength of 632.8 nm. The differential scattering cross section measured in terms of aerosol mass facilitates comparison with theory and puts the measure in terms of a unit commonly utilised by fire safety/protection practitioners. The measurement of the differential scattering of various smoke and nuisance aerosols is a valuable database of information for smoke detector designers. Analysis of the differential scattering has led to some astounding findings and verified others.

It has been amply verified in this study that light scattering by smoke aerosols generated in a flaming fire (soot) are distinguishable from those of a non-flaming smoke or nuisance aerosol. A novel method of discrimination based on analysis of scattering results as a function of the scattering parameter,  $q$ , has been demonstrated. This method measures the slope, for large values of  $q$ , of the differential scattering versus the scattering parameter on a

log-log graph. Soots from flaming fires were found to have slopes ranging between -1.6 and -2 while the other aerosols were found to have slopes of between about -2.8 and -4.2. The latter results apply to non-flaming smoke and nuisance aerosols, and are the first time this measure has been reported for natural aerosols. The results for soot are in general agreement with values measured in past studies. Discrimination is then possible based on  $q$ -slopes of about -2 for soot while the spherical aerosols lead to slopes of -2.5 or steeper negative slopes.

The  $q$ -slope analysis of scattering by non-flaming smoke and nuisance aerosols has also allowed testing of the scaling approach of scattering by spheres (Sorensen and Fischbach, 2000). In the case of soot particles the  $q$ -slope corresponds to the fractal dimension of their agglomerate structure, while the other aerosols split into two classes dependent on their phase shift parameters. The phase shift parameter in this study is principally a function of size, in particular the median mass (or volume) diameter of the aerosol distribution. The scattering measurements for aerosols with small phase shift parameter are in agreement with the scaling approach. For aerosols with larger phase shift parameters this study has found  $q$ -slopes of about -3 for large values of  $q$ , while the scaling approach predicts values of about -4 based on the polydisperse aerosol data presented by Sorensen and Fischbach (2000). The scattering is of the form  $\sigma_{VV}(q) \propto \langle q^{-3} \rangle_R$  for  $q > l^{-1}$ , where the angled brackets represent the ensemble average over the size distribution of the particles.

Differential mass scattering cross sections have been measured and compared with theory for the non-flaming smoke and nuisance aerosols. This was made possible by determination of the size distribution measurement of those aerosols. These comparisons have not been made in past studies of light scattering by smoke aerosols. The size measurements have revealed that the non-flaming smoke and nuisance aerosols can have very similar size characteristics.

One example is smoke aerosols generated by smouldering cotton lamp wick and nuisance aerosols from burning toast. The small median mass diameter of the smoke aerosol from smouldering cotton lamp wick is a demonstration of the weakness in the common generalisation that smoke aerosols from flaming fires are much smaller than those from non-flaming fires.

The differential light scattering has been analysed using ratios commonly employed in other studies. The asymmetry ratio and polarisation ratio has been verified as means of discriminating soot from the other aerosols examined. Pleasingly similar values of the asymmetry ratio were measured for all of the large post-flame soot agglomerates. This is a reflection of the fractal universality of those particles morphology. Similarly the polarisation ratio allows discrimination of soot, particularly at scattering angles near  $90^\circ$ . Polarisation discrimination is a result of the polarisation insensitivity of the soot agglomerate structure factor,  $S_{agg}(q)$ , due to interference of light scattering by the primary particles in the far field. In terms of particle size, the forward scattering ratio separates small size particles from large particles; soot agglomerates give similar values to aerosols with large mean sizes. ISO Fine dust can be separated from the other nuisance aerosols and the non-flaming smoke aerosol because of its large forward scattering ratio. The forward scattering ratio in the case of the dust is similar to that of the soot agglomerates, similarly ethylene results in a small value similar to the non-flaming smoke and nuisance aerosols. Discrimination of soot from the other aerosols based on size was not possible.

Discrimination of non-flaming smoke and nuisance aerosols in this study has not been consistently possible. This is a result of the pyrolysis or heat based nuisance aerosols having physically similar morphology to the smoke aerosols generated in non-flaming fires. Light scattering approaches rely on the differences between the scattering signals caused by particle

morphology or refractive index differences. It does not appear that light scattering results presented in this study are adequate by themselves to make definitive separation of all of the non-flaming smoke and nuisance aerosols examined. Light scattering results do distinguish soot aerosols from the other aerosols.

## **9.2 FUTURE WORK**

The q-slope approach would benefit from more work with different nuisance aerosols. Also higher scattering angles and other wavelengths to determine the generality of the present results should be pursued. The use of other wavelengths in particular has application since near infrared is the wavelength utilised by most detector manufacturers.

The scaling approach to light scattering would benefit from an experimental light scattering study using known oils in an aerosol form with well characterised size distributions. The phase shift parameter dependence could be effectively examined with this wider range of known aerosols.

9.1	Conclusions.....	9.1:259
9.2	Future Work.....	9.2:262

Reference List

Sorensen, C.M. and Fischbach, D.J. (2000) Patterns in Mie scattering. *Optics Communications* 173, 145-153.

## APPENDIX I

### **I. INTRODUCTION**

This appendix acts as a summary and guide to the experimental procedure sections in the body of this dissertation and presents details on the experimental procedure not covered in the text. The majority of this information is concerned with the light scattering measurements made with the Large Agglomerate Optical Facility (LAOF).

### **II. CALIBRATION**

#### **POLYSTYRENE SPHERE PREPERATION**

The creation of a suspension of polystyrene spheres for calibration experiments was detailed in **Sec. 4.3.1.1**. This section presents essentially the same information for the polystyrene spheres used in the calibration verification experiments that is 802 nm diameter polystyrene spheres.

The calibration verification working suspension is produced by mixing between 30 and 35 drops, about 1 ml, of the polystyrene sphere base suspension and diluting it with 50 ml of filtered and de-ionised water (filtered with 0.22  $\mu\text{m}$  pore size filter). The working suspension was then briefly agitated in an ultrasonic bath for about 1 minute to mix the polystyrene spheres into the water, before being poured into a larger container (250 ml). This larger storage container was used to store the working polystyrene suspension so that a large quantity was at hand for multiple experiments. An amount of about 35 ml of the working suspension was poured into the clean reservoir of the nebuliser on the calibration aerosol generator.

## CALIBRATION LIGHT SCATTERING MEASUREMENTS

A total of two calibration experiments were conducted in an experiment with an unknown aerosol, one before and one after the unknown aerosol. A single calibration constant was determined and then applied to the volume corrected detector signal of the unknown smoke aerosol. The calibration constant applied was usually the result of the first calibration measurements, the second calibration measurements was a check of the first. If there was a difference greater than a standard deviation between the two calibration constants then the whole set of experiments were discarded, this never occurred except where background artefacts appeared in the measured signal, because of reflections or miss-alignments of the optics.

### III. MASS MEASUREMENT

#### MASS FLOWRATE

The mass flow rate through the LAOF is controlled by a mass flow controller system that is checked using a bubble flow meter (Gilibrator-2 Primary Flow Calibrator, Gilian Instruments Inc.) before and after each filter measurement. The flow rate used in this study was about  $1.66 \times 10^{-4} \text{ m}^3 \cdot \text{s}$  (10 L.min). This flow is usually checked at the by-pass valve below the filter holder as the flow through the LAOF is assumed to be unaffected by leakage. The flow is only checked periodically at the LAOF inlet to check for leaks; usually after some part of the apparatus has been disturbed say by cleaning. A difference of less than 4 % of the flow rate at the by-pass valve is normally measured at the LAOF inlet, a higher difference is indicative a leak out of the LAOF.

#### WEIGHING FILTERS

Some details on the filters are given in **Sec. 4.3.1.2**. After collection of an aerosol sample each filter was weighed on the micro-balance (Sartorius MC5, max 5.1g) before and after collection of the smoke particles of interest:

1. Remove the filter from its petri dish and wave gently between two parallel electrostatic neutralizers (Polonium (Po) 210 isotope). This minimized charge effects, which can cause instabilities and uncertainties in the weighing process.
2. Place the sample on the micro-balance and close the balances door
3. Wait about 30 seconds for the balance to stabilize then record the filter weight. If the balance reading was still fluctuating after 30 seconds, then there were probably charging or external vibrations affecting the reading. More time would be needed to allow the balance to settle.
4. Replace the filter in the petri dish.

#### IV. LIGHT SCATTERING MEASUREMENTS

The experimental procedure for setting-up many of the elements of the Large Agglomerate Optical Facility (LAOF) are detailed in the Apparatus chapter. The experimental steps for making differential (angular) light scattering measurements are described here and are the same for any aerosol flowing in the LAOF. The only aspect that varies significantly in procedure is the aerosol transport to the LAOF. These transport factors have been discussed in the chapters of the dissertation dealing with each type of aerosol examined.

##### DIFFERENTIAL SCATTERING MEASUREMENTS

Prior to an experiment it is best to allow both the laser and mass-flow controller to warm up about 30 minutes prior to beginning an experiment. The first step is to determine the detectors angular zero position before the aerosol is introduced into the LAOF. The zeroing procedure is described in Sec 3.3.1 and is achieved by using the controlling computer program DAMP16. This computer program stays in control of the detector position and records the detector signal,  $U(\theta)$ , throughout measurement of the differential scattering. At

this stage the background signal,  $U'_{I'}(\theta)$  and  $U'_{III}(\theta)$ , with no aerosol present is measured. The main influence of this background signal is measured at the forward angles. This stray light has a small amount of polarisation dependence particularly at the small angles, thus both polarisation background signals are measured. The main laboratory lights are turned off at during the angular scans.

Once this is accomplished a new pre-weighed filter is placed in the filter holder and then the flow rate through the LAOF measured. At this point the apparatus is ready for an aerosol to be introduced in to the LAOF. The visible cue of the laser scattering by the aerosol is used as a gauge that the aerosol is flowing in a well-mixed manner through the LAOF. When the concentration was stable in the LAOF the by-pass valve was closed and the mass filter valve opened (see **Figure 3.2**). At the same time that the mass filter valve was opened a stopwatch was started to record the collection time of the mass sample of smoke aerosol. The signal from the detector positioned at its resting position of  $5^\circ$  is used at this stage to ensure that the signal amplification is at a reasonable level. If it is not the voltage pre-amplifier circuit is used to adjust it, the lock-in amplifier being at its lowest sensitivity because of the strong scattering signal at the small angle. Any changes to the pre-amplifier voltage at this stage means that the background will have to be measured again. The polariser positions are set, based on the results of the test settings using the polarising beam splitter discussed in **Sec. 3.3.1**. The apparatus is now ready for the measurement of the differential scattering by the aerosol.

The computer program, DAMP16, has its instructions entered into two configuration files. One file controls the angles at which to stop and the number of measurements to make at those angles. The other configuration file controls operating parameters of the analogue-to-digital converter installed in the computer. As the detector scans across the angular span,  $5^\circ$  to  $135^\circ$  in nominally  $5^\circ$  steps with the exception of a measurement at  $8^\circ$  as

well, the sensitivity of the amplifier is changed and the output is recorded on the controlling computer. A measurement is also typically made at  $8^\circ$  to increase forward angle data. Ten measurements are made at each angle in quick succession, taking about 7 seconds to move between angles and make the measurements. The measurements at each angle are initiated by pressing a key on the controlling computers keyboard. This manual initiation is necessary so that the sensitivity of the lock-in amplifier can be adjusted to allow measurement of the scattering signal while it falls some two to three orders of magnitude as the detector moves from small to large angles. This raw data (\*.RAW) is saved to the controlling computer along with a working data file (\*.DAT) that contains the average of the ten measurements and their standard deviation. It is this working data file (\*.DAT) that is used in data reduction (volume correction) and analysis.

When the first angular scan at one polarisation is complete, a second scan is conducted at the other polarisation by setting the retarder and analyser to the appropriate settings. Apart from the retarder and analyser, all the other optical components are not changed for this second scan. The filter is kept in place to continue to collect aerosol particles to make sure there is a measurable mass on the filter. The aerosol flow is not disturbed in any way. The controlling computer needs to have new output filenames entered, when this is done the same process as that described for the first scan is repeated.

When the second scan is complete the aerosol is allowed to flow through the system for a short period before the filter is isolated and the mass collection timer stopped. At this point a measurement of the aerosol sampling rate (equal to the flow rate across the filter) through the LAOF is made with a bubble flow meter and recorded.

## APPENDIX II

The following pages contain the reviewed papers generated by this study. The papers are:

Weinert, D. W., Cleary, T. C., and Mulholland, G. W. (2002). Light Scattering Characteristics and Size Distribution of Smoke and Nuisance aerosols. *Fire Safety Science - Proceedings of the Seventh International Symposium* , **To be published**.

Cleary, T.G., Weinert, D.W. and Mulholland, G.W. (2002) Moment method for obtaining particle size measures of test smokes. *NIST Technical Report* , National Institute of Standards and Technology (NIST), Gaithersburg, MD, USA.. **To be published**

The first paper has been fully reviewed and will be published in the Fire Safety Science – Proceedings of the Seventh International Symposium by the International Association of Fire Safety Science. The second paper has undergone an internal NIST review and will initially be published as a NIST Technical Report. Two other papers have been presented (abstract review) to the international smoke detector community.

Those papers are:

Weinert, D. W., Cleary, T. C., and Mulholland, G. W.(2001). Size distribution and light scattering properties of test smokes. *AUBE '01: 12th International Conference on Automatic Fire Detection* , 58-70. National Institute of Standards and Technology, Gaithersburg, MD, USA.

Weinert, D. W., and Mulholland, G. W.(2001). An apparatus for light scattering studies of smoke particles. *AUBE '01: 12th International Conference on Automatic Fire Detection* , 31-42. National Institute of Standards and Technology, Gaithersburg, MD, USA.

# Light Scattering Characteristics and Size Distribution of Smoke and Nuisance Aerosols

DARRYL W. WEINERT<sup>†</sup>, THOMAS G. CLEARY, GEORGE W. MULHOLLAND  
AND PAULA F. BEEVER<sup>‡</sup>

Building and Fire Research Laboratory, National Institute of Standards and  
Technology (NIST), Gaithersburg, 20899, MD, U.S.A.

<sup>†</sup> Center for Environmental Safety and Risk Engineering (CESARE), Victoria  
University, PO Box 14428, Melbourne City MC, Victoria, 8001, Australia

<sup>‡</sup> Principal Fire Engineer, New Zealand Fire Service, PO Box 2133, Wellington,  
New Zealand

## ABSTRACT

This paper presents the differential mass scattering cross section [ $\text{m}^2 \cdot \text{g}^{-1} \cdot \text{sr}^{-1}$ ] of various non-flaming and flaming fire generated smoke aerosols as well as nuisance aerosols created in the Fire Emulator/Detector Evaluator. These measurements have been determined for two linear polarizations and the scattering angle range of  $5^\circ$  to  $135^\circ$  at a wavelength of 632.8 nm. Small diameter particles have been separated from large particles using the forward scattering information. Discrimination of soot generated by flaming fuels from both smoke aerosols generated by non-flaming fires and nuisance aerosols is demonstrated by the ratio of forward ( $45^\circ$ ) to backward scattering ( $135^\circ$ ), the polarization ratio, and dependence on scattering parameter,  $q = 4\pi\lambda^{-1} \sin(\theta/2)$ .

**KEY WORDS:** detection, smoke, nuisance, light scattering, size distribution

## INTRODUCTION

Much of the potential benefit of automatic smoke detection systems is offset by the problem of repeated unwanted alarms. The ability of a system to discriminate the types of airborne particles arising from different fire types, from potential fires and from nuisance aerosols would be of great practical benefit. This study examines light scattering characteristics of smoke and nuisance aerosols for two main goals: (i) to characterize the particles generated and (ii) to investigate the similarities or differences between particles generated. The first point is of benefit to detector response modeling and testing. The latter goal is aimed at examining different discrimination approaches for fire and non-fire generated aerosols using light scattering. Discrimination of light scattering signals generated by the smoke and nuisance aerosols is important information to consider when reducing the incidence of alarms caused by nuisance aerosols.

To obtain detailed information on the light scattering characteristics of smoke aerosols this study has used an approach that measures the angular distribution of scattered light. This measure is expressed as the differential (angular distribution) scattering cross section per mass,  $\sigma(\theta)$ , which has the units of area per unit mass of scattering aerosol per solid angle of detector view [ $\text{m}^2 \cdot \text{g}^{-1} \cdot \text{sr}^{-1}$ ] and will be referred to as the differential mass

scattering cross section. The mass specific scattering measurement is a novel aspect of this work, it enables one to estimate the light scattering of smoke based on a measurement of mass concentration. Previous studies have been conducted with smoke aerosols using normalized scattering data [1] or single angle response [2,3]. In this study soot generated by flaming fires is distinguished from both smoke generated by non-flaming fires and nuisance aerosols using various means. In particular we apply two methods, polarization ratio and  $q$  dependent scattering ( $q = 4\pi\lambda^{-1} \sin(\theta/2)$ ), that are inspired by fundamental differences between light scattering from soot agglomerates and other non-agglomerate aerosols.

The general form of agglomerate light scattering [4] can be expressed in terms of a power law relation that reduces to,

$$\sigma_{VV}(\theta) \propto q^{-D} \text{ for } q > R^{-1}, \quad (1)$$

where  $R$  is the agglomerate characteristic radius (e.g. radius of gyration), and  $D$  is the fractal dimension characterizing the spatial mass distribution of the agglomerate. Various studies for in-flame and post-flame soot have reported fractal dimensions to be about 1.7 to 1.85 using laser scattering techniques [5,6]. Universality in morphology and subsequent scattering is related to the fact that all soot shares the same fundamental mechanisms of agglomerate growth [7].

There has been relatively little study regarding the  $q$ -dependence of scattering by spheres until recent work by Sorensen and Fischbach [8]. This is surprising given the extensive application of Mie theory to the study of light scattering by spheres.

Size distribution measurements were also conducted, as size is an important quantity on which the light scattering depends. Size information is also of benefit for assessing response of detectors based on other principles such as ionization detectors, or examining smoke aerosol kinetics. The size information presented here in terms of aerodynamic diameter is complementary to that published previously [9-11].

## **SMOKE AND NUISANCE AEROSOL GENERATION AND SAMPLING**

The majority of smoke and nuisance aerosols examined in this study were generated in the Fire Emulator/Detector Evaluator (FE/DE), a facility designed to emulate the smoke of a fire for fire detector assessment [12,13]. The operating principle of the FE/DE is that of a single pass wind tunnel, into which a smoke or nuisance aerosol is released. A test sensor section contains smoke detectors and instruments to measure various parameters including the light transmission through the generated aerosol, the air velocity (typically 0.2 m/s), temperature, and response of a measuring ionization chamber (MIC). A sampling line was inserted into this section to sample smoke and nuisance aerosol for size distribution measurement and transport to the light scattering apparatus. The sampling was done at a flow rate of about 8.7 m/s (light scattering) and 13 m/s (size distribution) from 50 mm below the top of the sensor section's duct, which had a height of 304 mm.

The non-flaming fuels examined in the FE/DE for this study were beech wood blocks, cotton lamp wick, and polyurethane foam. The wood blocks are those specified in EN54 (part 9, test fire 2) [14], similarly the cotton lamp wick is the same fuel as specified in EN54 (part 9, test fire 3) and is also used in UL217 [15]. These fuels were stored in a

temperature and humidity controlled conditioning room. The polyurethane was cut from a seat cushion of an armchair. Wood pyrolysis smoke was generated by eight beech wood blocks each 35 mm x 20 mm x 10 mm, arranged on a 250 cm<sup>2</sup>, 750 kW hot plate set on full power. The cotton lamp wicks smoke was generated by a staged-wick-ignition device [13] that was loaded with 32 wicks all about 210 mm long. Polyurethane foam was ignited to smolder by a heating wire inserted into the foam; it was turned off once the foam reached a self-sustained smoldering state. This was not always successful. If the smolder did not self sustain the test was stopped.

Two flaming fuels with different states, propylene gas and liquid heptane, were used in the FE/DE to generate “black” smoke or soot. The propylene gives a high soot yield from a diffusion flame and is ideal for use with the gas burner attached to the FE/DE, which can then output a large amount of soot at moderate fuel flow rate. Soot concentration is controlled by varying the burner fuel flow rate and by venting excess soot. Heptane soot was generated by a small pool fire located in the same section of the FE/DE where non-flaming fuels were placed. A 25 cm<sup>3</sup> pool of heptane is poured on top of 100 cm<sup>3</sup> of water contained in a Pyrex petri dish surrounded by a metal overflow dish. The water helps reduce the effects of the heptane boiling and splashing out of the dish. It also raises the heptane to the lip of the dish reducing lip effect on this small pool fire. Two other types of soot were generated by burning acetylene and ethylene in a separate co-flow diffusion burner used in earlier soot studies [16,17]. This burner was connected directly to the light scattering apparatus providing a repeatable alternative source of soot; it was not a part of the FE/DE.

Some common nuisance aerosols were also generated in the FE/DE and characterized. These aerosols were generated by burning (pyrolyzed) toast, over-heating (pyrolyzed) cooking oil and from a fine grain dust (ISO Fine Dust 121031;A2). The toast and cooking oil aerosols represent both a common nuisance and a hazard, as both have the potential to become fire events. Nuisance toast smoke was generated by placing two slices of white bread in a standard two-slice popup toaster, the lever of which was fixed to the power on position. The smoke concentration produced in this case had a very rapid rate of rise. The toaster was only powered for a short period compared to the sampling time, to avoid a transition to flaming. For the cooking oil, a 5 cm<sup>3</sup> sample of corn-based cooking oil was placed in a petri dish and pyrolyzed on the hotplate, which was set at full power. The dust was introduced to the FE/DE by a screw feeder typical of dry-powder delivery systems. Loss of dust particles larger than about 10 μm was caused by a honeycomb flow stabilizer before the sensor section. Gravity fractionation of the dust was also observed by differences in the transmitted light beams at the top and middle heights of the sensor section. Thus, the final sampled dust aerosol had a different size distribution compared to the original ISO fine dust.

The smoke aerosol was collected and transported into another laboratory where the light scattering apparatus was situated. The transportation method used was a 0.2 m<sup>3</sup> drum into which about 0.12 m<sup>3</sup> of smoke was drawn at a rate of 333 cm<sup>3</sup>/s (20 L/min). The drum collection method results in some settling of larger particles and wall losses in the drum. Some coagulation growth (aging) of the particles in the drum will also occur. The settling of particles mainly affect particles bigger than about 3 μm and the aging of the smoke particle mainly influences the number of particles. Affects on the volume or mass of the

smoke particles, to which light scattering is sensitive, is small in comparison to the aging affect on number concentration [11]. The size distributions of the smoke and nuisance aerosols were determined with a cascade impactor sampling directly from the FE/DE. The parameters of the distributions, the mass median aerodynamic diameter (MMAD) and geometric standard deviation (GSD), are given in Table 1.

**Table 1:** Table of smoke and nuisance aerosol particles characteristics: mass median aerodynamic diameter (MMAD) and geometric standard deviation (GSD); the forward angle scattering ratio and asymmetry ratio for each source is shown as well as the  $q$ -slope.

Aerosols Source or Fuel	Mass Median Aerodynamic Diameter ( $\mu\text{m}$ )	Geometric Standard Deviation	$\sigma_{VV}(5^\circ)/\sigma_{VV}(20^\circ)$	$\sigma_{VV}(45^\circ)/\sigma_{VV}(135^\circ)$	Slope (negative) for $q \geq 12 \mu\text{m}^{-1}$
Beech Wood	1.5	1.9	2.0	15.5	2.7
Cotton Lamp Wick	0.31	1.7	1.1	15.7	4.2
Polyurethane	2.0	1.6	3.0	13.2	3.1
Toast	0.43	1.6	1.3	17.8	4.1
Cooking Oil	1.6	2.2	3.4	13.6	2.8
Dust	2.2	1.8	7.1	11.3	2.9
Propylene	--	--	6.3	4.9	1.8
Heptane	--	--	6.4	5.6	2.0
Acetylene	--	--	8.7	4.0	1.7
Ethylene	--	--	3.8	4.5	1.7

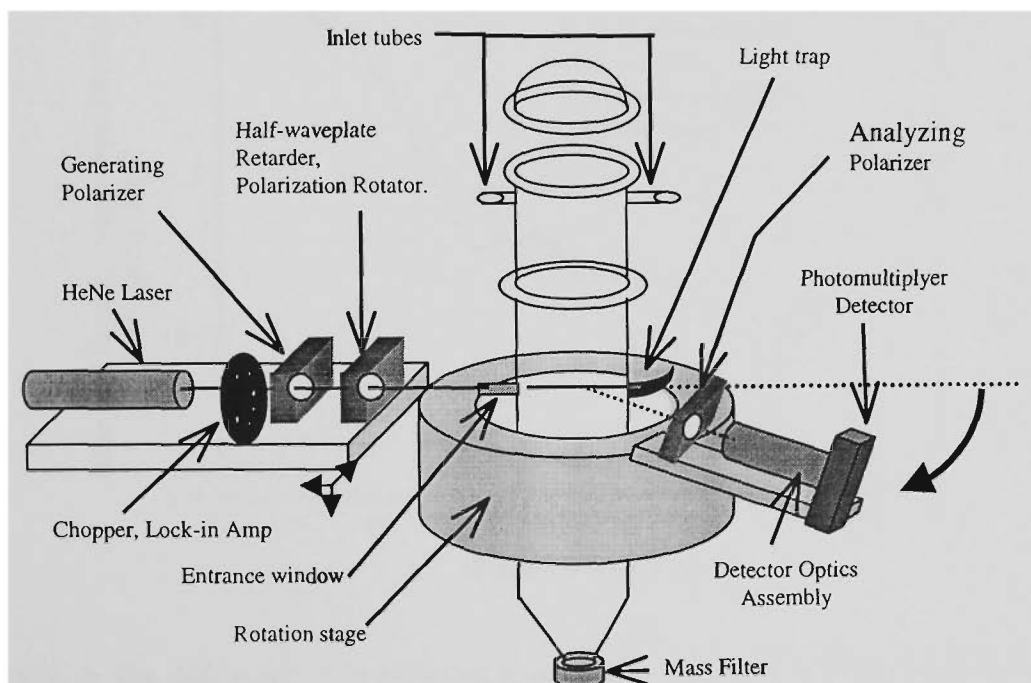


**Fig. 1:** The LAOF light scattering apparatus used to measure the differential mass scattering cross section.

## LIGHT SCATTERING CHARACTERISTICS

The light scattering measurements have been made with the Large Agglomerate Optical Facility (LAOF) [17] shown in Fig. 1. The LAOF determines the smoke particle's differential mass scattering cross sections for different polarizations,  $\sigma_{VV}(\theta)$  and  $\sigma_{HH}(\theta)$ , at the He-Ne wavelength of 632.8 nm for scattering angles between  $5^\circ$  to  $135^\circ$ . The first subscript denotes the incident polarization and the second denotes scattered polarization measured; V for vertical and H for horizontal to the scattering plane. The differential mass scattering cross sections measured by the LAOF have been calibrated using polystyrene (PS) spheres of nominally 500 nm diameter. The detector signal has been calibrated by normalizing to the absolute mass scattering cross section determined using Mie theory [18] for nominally 500 nm diameter monodisperse polystyrene spheres. The spheres have a density of  $1050 \text{ kg/m}^3$  and a refractive index of 1.59 [19]. To determine the calibration constant, a logarithm weighted least square method is used, such that:

$$\ln K = \frac{1}{N} \sum_j \ln \left( \frac{E_j}{T_j} \right), \quad (2)$$

where  $K$  is the calibration constant,  $E_j$  is the experimental result and  $T_j$  is the theoretical result at the  $j$ th scattering angle  $\theta_j$ . Mie theory gives the differential mass scattering cross section of spherical particles as the series expansion [18],

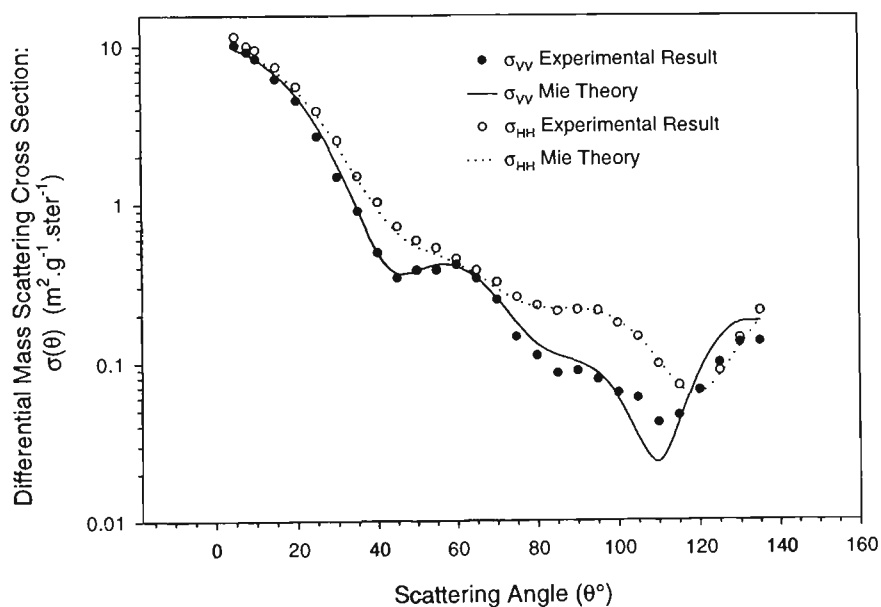


**Fig. 2:** The differential mass scattering cross section of nominally 800 nm polystyrene spheres compared to the theoretical result from Mie Theory.

$$\sigma_{VV}(\theta) = \frac{1}{\rho_p V_p k^2} \left| \sum_n \frac{2n+1}{n(n+1)} (a_n \pi_n + b_n \tau_n) \right|^2 \quad (3a)$$

$$\sigma_{HH}(\theta) = \frac{1}{\rho_p V_p k^2} \left| \sum_n \frac{2n+1}{n(n+1)} (a_n \tau_n + b_n \pi_n) \right|^2 \quad (3b)$$

here  $a_n$  and  $b_n$  are the Mie scattering coefficients that are dependent on the particle size, wavelength and refractive index of scattering particle. The angular functions are  $\pi_n$  and  $\tau_n$ ;  $k = 2\pi/\lambda$  is the wave number and  $\lambda$  the wavelength;  $\rho_p$  is the particle bulk density and  $V_p$  the particles volume. The measured differential mass scattering cross section of an aerosol is determined from the volume corrected detector signal,  $u(\theta)$ , and aerosol mass concentration,  $M$ , using (polarization notation suppressed),

$$\sigma(\theta) = \frac{u(\theta)}{MK}. \quad (4)$$

The calibration was verified by generating a different size of polystyrene sphere and comparing this result to Mie theory. Nominally 800 nm diameter spheres were chosen for their similarity to smoke aerosol sizes. The results of one such calibration verification is shown in Fig. 2. The agreement between experiment and theory in Fig. 2 is good, while the logarithmic scale hides some variation. An uncertainty analysis (Type A, with 95 % confidence level) gives a relative uncertainty of about 40 % and 26 %, measured about the theoretical result for  $\sigma_{VV}(\theta)$  and  $\sigma_{HH}(\theta)$  respectively. There are two main sources of this uncertainty, the manual adjustment of polarization direction and variation in mass concentration of polystyrene particles during the 20 minute collection period.

In Fig. 3 the differential mass scattering cross sections are shown for a selection of smoke and nuisance aerosols generated in the FE/DE. The peaks and valleys obtained from monodisperse particles are “averaged out” by the relatively broad size distributions (geometric standard deviation of about 2) for the polydisperse smokes shown in Fig.3. In Table 1 the effects of size can be seen in a forward scattering ratio  $\sigma_{VV}(5^\circ)/\sigma_{VV}(20^\circ)$ . Small particles have weaker forward scattering than larger particles and as particle size decreases the forward scattering will become less dependent on angle.

A widely used parameter for characterizing aerosol polarization is the polarization ratio, defined as

$$\rho(\theta) = \frac{\sigma_{HH}(\theta)}{\sigma_{VV}(\theta)}. \quad (5)$$

In Fig. 4 the polarization ratio, normalized to 1 at a scattering angle of  $5^\circ$ , has been plotted for all of the aerosol sources examined. The normalization removes a spread of values that occurred at  $5^\circ$  due to the manual setting of the polarization, which mainly affected the VV uncertainty. The results for soot from flaming fuels are very different from the non-flaming and nuisance aerosols near  $\theta = 90^\circ$ . The reason for this minimum

is related to the agglomerate morphology of the soot as discussed below. Another ratio approach which shows discrimination between soot and the other aerosols is the asymmetry ratio defined by the ratio of forward (45°) to backward angles (135°). The results for this ratio are also given in Table 1. While flaming and non-flaming smoke can be distinguished by these methods, it can be seen from Fig. 4 and Table 1 that these methods do not allow complete discrimination between non-flaming smokes and nuisance aerosols.

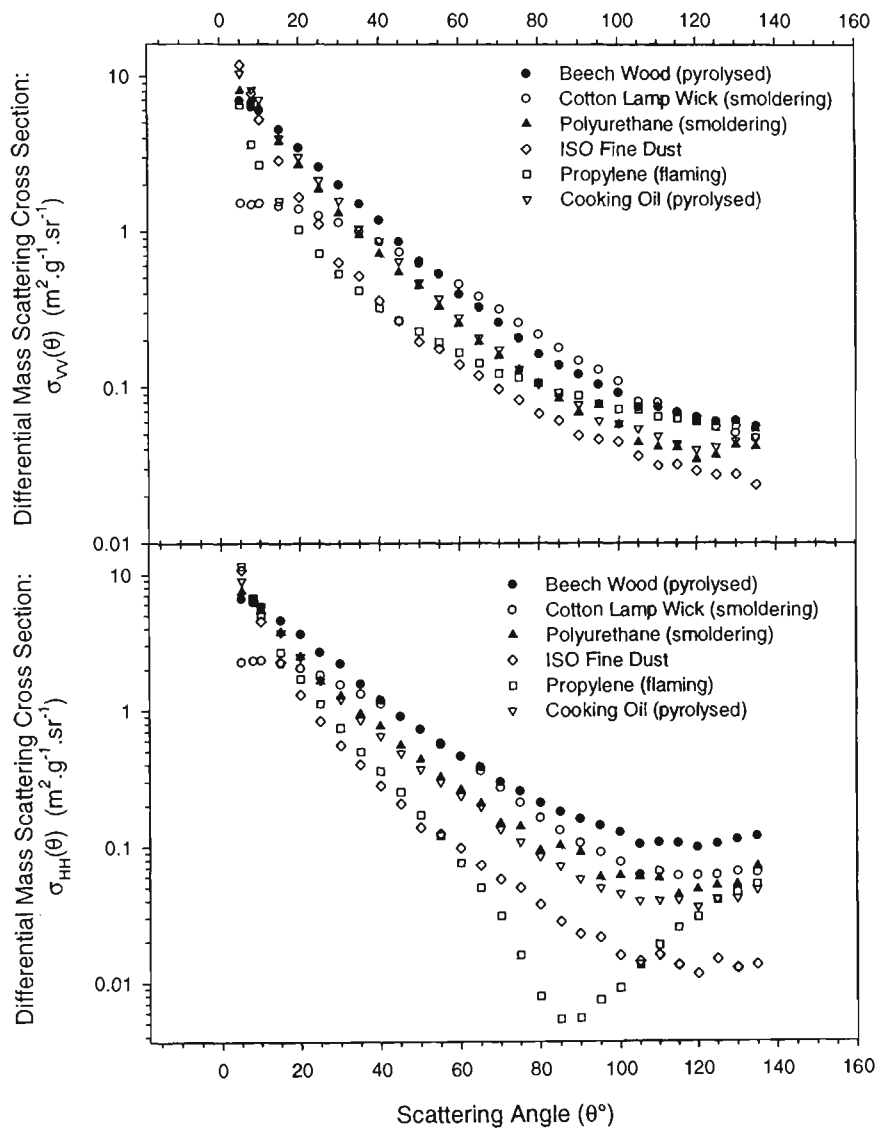


**Fig. 3:** Differential mass scattering cross sections of selected smoke and nuisance aerosols generated in the FE/DE.

Another representation of scattering data is in terms of the elastic scattering wave vector magnitude or scattering parameter,  $q$ . Although this is a common parameter in scattering studies for soot it appears to only recently be considered with more traditional Mie scattering studies for spherical particles [8]. In Fig. 5,  $\sigma_{VV}(\theta)$  is plotted as a function of  $\log q$ , and the slopes of all of the smoke and nuisance aerosols for  $12 \mu\text{m}^{-1} \leq q \leq 18.3 \mu\text{m}^{-1}$  ( $75^\circ \leq \theta \leq 135^\circ$ ) are shown in Table 1. The slopes range from about  $-2$  for soot to between  $-3$  to  $-4$  for the other aerosols. The fractal dimension of the soot agglomerates is equal to negative this slope (see Eq. 1) [16]. Differentiation between soot agglomerates and the other generated aerosols seen in Table 1 is due to the fractal nature of these agglomerates, as will be discussed below.

## DISCUSSION

The differential mass scattering cross sections presented in Fig. 2 and 3 is calculated from gravimetric and angular scattering measurements. This mass based measure has an advantage in that the results can be used for assessing the response of a light scattering smoke detector, given the aerosol mass concentration (Eq. 4).

The light scattering data presented in Table 1 and Fig. 3 shows that aerosols with small particle size, such as the smoke aerosol from cotton lamp wick and burning toast, can be distinguished from larger aerosol particles examined. Discriminating smoke from

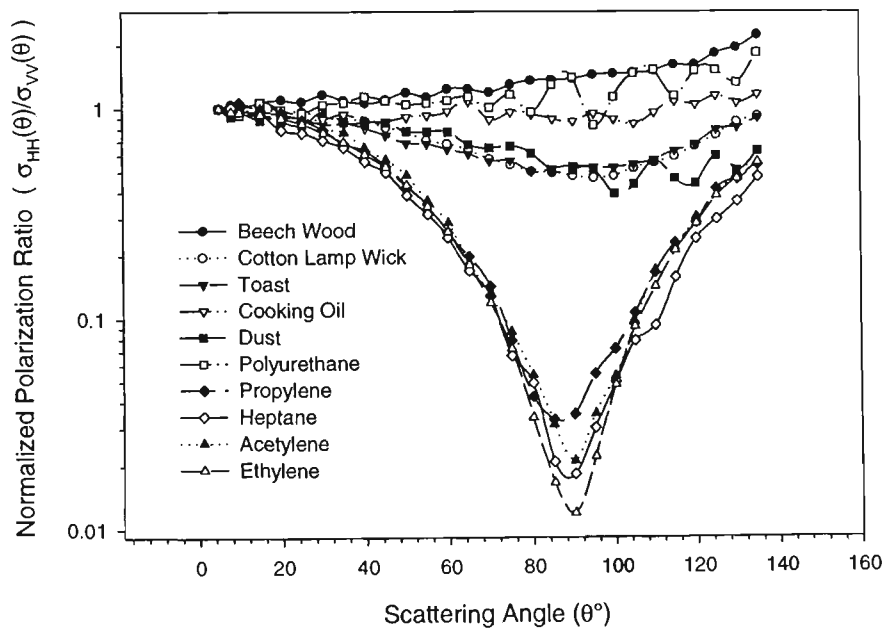


**Fig. 4:** The polarization ratio,  $\rho(\theta)$ , normalized to 1 at  $\theta = 5^\circ$  for all of the aerosol sources examined in this study.

nuisance aerosols would be difficult using the data in Table 1 and the polarization ratio shown in Fig. 4. For example, the difficulty separating cotton lamp wick from toast smoke or cooking oil from polyurethane. The possibility exists that more data closer to scattering angles of  $180^\circ$  would improve the ability to differentiate. However, it does not seem likely based on our data, that light scattering by itself will allow distinction between all nuisance and non-flaming fire generated aerosols.

Discrimination of soot from the other aerosols presented here is possible by various means because of the great differences in morphology. Light interacts with the electrons in matter, thus how mass is distributed in a particle affects the scattering of light. The spatial distribution of mass in a soot agglomerate is very different to that of condensed hydrocarbon droplets (spheres) generated by non-flaming fires and pyrolysis generated nuisance aerosols examined in this work. Droplet particles scatter light as described by Mie scattering theory. In the case of irregular dust particles, the scattering has similarities with Mie scattering although at backward angles Mie theory is not necessarily an acceptable approximation [20]. Soot scatters light in a fundamentally different manner to the other particles (see Eq. 1).

This leads to a novel means of discriminating between the soot agglomerates and the solid structures of other smoke and nuisance aerosols. The  $q$ -slopes results given in Table 1 indicate that the smoke and nuisance aerosols examined have  $q$ -slopes of about -3 to -4, while slopes of about -2 to -1.7 characterize soot. More backward scattering

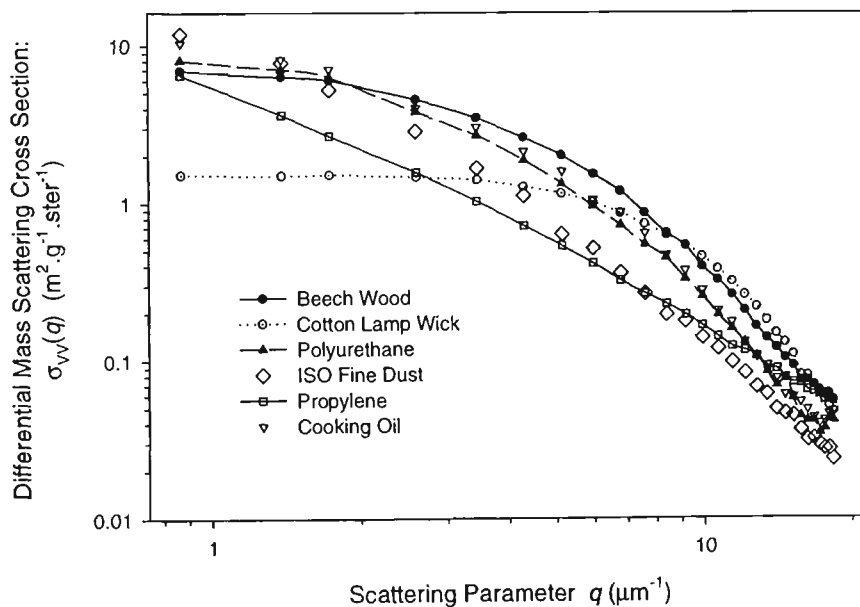


**Fig. 5:** Differential mass scattering cross section  $\sigma_{VV}(\theta)$  as a function of the scattering wave vector,  $q$ .

data,  $\theta \geq 135^\circ$ , would be of benefit in this type of discrimination. Transitions in the scattering of spherical particles occur in the range of  $q$ -slopes of between -2 to -4 [8]. In this study, there is an increase in the  $q$ -slope uncertainty at high values of  $q$ , due to mass loss from the drum.

The scattering mechanism of agglomerate particles can also be represented as (angular notation suppressed) [7],

$$\sigma_{XX} = (S_{ag} \cdot S_r)_{XX} \quad \text{but} \quad (S_{ag})_{VV} \approx (S_{ag})_{HH} \quad (6)$$

where  $S_r$  is the Rayleigh-like scattering component and X denotes a given polarization. The term  $S_{ag}$  arises from the interference in the far field of the scattering by the individual primary particles making up the agglomerate. The term,  $S_{ag}$ , can vary by a few orders of magnitude (Fig. 3) while for Rayleigh scattering,  $(S_r)_{VV}$ , is independent of angle. Since  $S_{ag}$  is not strongly dependent on the polarization direction, the polarization ratio is primarily determined by the Rayleigh-like scattering from the primary spheres and results in a minimum at  $\theta = 90^\circ$  as seen in Fig. 4. Thus, soot agglomerate scattering appears to be Rayleigh-like in terms of the polarization ratio although the differential scattering for a vertical polarization direction is not at all similar to Rayleigh theory.

This fundamental difference in scattering mechanisms allows the polarization ratio to be used to discriminate between flame generated and other non-agglomerate aerosols. Practical use of soot discrimination would be for identification of a flaming fire (high hazard) vs non-flaming fire (lower hazard), possibly changing response actions. The polarization approach has previously been used to measure the degree of linear polarization for EN54 test smokes over an angular range of  $5^\circ$  to  $165^\circ$  [1]. Loepfe et. al. [1] found the highest degree of polarization corresponded to soot particles, a medium value existed for cotton lamp wick smoke, and that the lowest values were found for the pyrolysed wood smoke. The implication of the work by Loepfe et. al. [1] is that soot is a small Rayleigh scattering particle. The two to three orders of variation in  $\sigma_{VV}(\theta)$  and Eq. 6, demonstrates that this is not the case.

Another well-used measure that differentiates soot from the other aerosols examined is the asymmetry ratio. In Table 1 the ratios of  $45^\circ$  to  $135^\circ$  for  $\sigma(\theta)_{VV}$  are used but others are possible. The discrimination seen in this forward to backward ratio is a subsequence of the power law scattering, Eq. 1, being compared to spherical particle scattering [8].

The effect of size (reported in Table 1) on the light scattering results of Fig. 3 is mainly apparent in the forward scattering, as represented by the small angle ratio data in Table 1. Small particles result in scattering that approaches Rayleigh scattering at forward angles,  $\sigma_{VV}(5^\circ)/\sigma_{VV}(20^\circ) \sim 1$ . The large particles have more pronounced forward scattering represented by the high forward angle ratio in Table 1. The particle size distribution parameters given in Table 1 indicates that smoke and nuisance aerosols in some comparisons are different (e.g. cotton from wood or dust) and in others cases similar (cotton and toast, dust and polyurethane). Discrimination based on size alone is not

sufficient to separate the smoke and nuisance aerosols examined. Combining light scattering methods could be of benefit.

## CONCLUSION

This study has presented quantitative results for the differential mass scattering cross section [ $\text{m}^2 \cdot \text{g}^{-1} \cdot \text{ster}^{-1}$ ] of various non-flaming and flaming fire generated smoke aerosols and nuisance aerosols created in the Fire Emulator/Detector Evaluator. These measurements have been determined for two linear polarizations and a scattering angle range of  $5^\circ$  to  $135^\circ$  at a wavelength of 632.8 nm. The differential scattering cross section was measured in terms of aerosol mass to facilitate comparison with theory.

Analysis of scattering data by various means shows that the smoke aerosol generated by a flaming fire (soot) is distinguishable from that of a non-flaming fire or nuisance aerosol. This discrimination is possible due to the soot agglomerate structure, scattering light in a different manner to that of the other aerosols examined in this study. These discrimination methods involve calculating a ratio of forward ( $45^\circ$ ) to backward scattering ( $135^\circ$ ), determining the polarization ratio  $\rho(\theta)$  near a scattering angle of  $90^\circ$  and the scattering parameter approach using the slope of  $\sigma_{VV}(q)$  vs  $\log q$  for  $12 \mu\text{m}^{-1} \leq q \leq 18.3 \mu\text{m}^{-1}$  ( $75^\circ \leq \theta \leq 135^\circ$ ). The scattering parameter approach would benefit from more work with different nuisance aerosols, higher scattering angles and other wavelengths to determine the generality of the present results.

While forward scattering separates small size particles from large particles, our results indicates that this does not translate to a differentiation between non-flaming and nuisance aerosols. It does not appear that light scattering results presented in this study are adequate by themselves to make definitive separation of the non-flaming and nuisance aerosols examined. Light scattering results do distinguish soot aerosols from the other aerosols.

Acknowledgement: DWW would like to thank BFRL-NIST, for their guest researcher program in supporting this work, and Prof. Ian Thomas at CESARE.

## REFERENCES

- [1] Loeffe, M., Ryser, P., Tomkin, C., and Wieser, D., "Optical properties of fires and non-fire aerosols," *Fire Safety Journal* 29: 185-194 (1997).
- [2] Meacham, B. J. and Motevalli, V., "Characterization of smoke from smoldering combustion for the evaluation of light scattering type smoke detector response," *Journal of Fire Protection Engineering* 4: 17-28 (1992).
- [3] Aggarwal, S. and Motevalli, V., "Investigation of an approach to fuel identification for non-flaming sources using light-scattering and ionization smoke detector response," *Fire Safety Journal* 29: 99-112 (1997).
- [4] Sorensen, C. M., "Scattering and absorption of light by particles and aggregates," *Handbook of Surface and Colloid Chemistry*, Birdi, K. S., CRC Press, 1997, 533-558.
- [5] Sorensen, C. M. and Feke, G. D., "The morphology of macroscopic soot," *Aerosol Science and Technology* 25: 328-337 (1996).
- [6] Koylu, U. O., Faeth, G. M., Farias, T. L., and Carvalho, M. G., "Fractal and  
page number

- projected structure properties of soot agglomerates," *Combustion and Flame* 100: 621-633 (1995).
- [7] Mountain, R. D. and Mulholland, G. W., "Light scattering from simulated smoke agglomerates," *Langmuir* 4: 1321-1326 (1988).
  - [8] Sorensen, C. M. and Fischbach, D. J., "Patterns in Mie scattering," *Optics Communications* 173: 145-153 (2000).
  - [9] Helsper, C., Fissan, H. J., Muggli, J., and Scheidweiler, A., "Particle number distributions of aerosols from test fires," *Journal of Aerosol Science* 11: 439-446 (1980).
  - [10] Bankston, C. P., Zinn, B. T., Browner, R. F., and Powell, E. A., "Aspects of the mechanisms of smoke generation by burning materials," *Combustion and Flame* 41: 273-292 (1981).
  - [11] Lee, T. G. K. and Mulholland, G., "Physical properties of smokes pertinent to smoke detector technology," National Bureau of Standards, NBSIR 77-1312, Washington, D.C., 1977.
  - [12] Grosshandler, W. L., "Towards the development of a universal fire emulator-detector evaluator," *Fire Safety Journal* 29: 113-127 (1997).
  - [13] Cleary, T. C., Donnelly, M., and Grosshandler, W. "The Fire Emulator/Detector Evaluator: Design, Operation and Performance," -- AUBE '01: 12th International Conference on Automatic Fire Detection, NIST, Gaithersburg, 2001, pp. 312-323.
  - [14] "EN54-9: Components of automatic fire detection systems, part 9: Fire sensitivity Test," *Committee for Standardization* (1982).
  - [15] "UL 217: Standard for single and multiple station smoke detectors," *Underwriters Laboratories Inc., Northbrook IL* (1993).
  - [16] Samson, R. J., Mulholland, G. W., and Gentry, J. W., "Structural analysis of soot agglomerates," *Langmuir* 3: 272-281 (1987).
  - [17] Mulholland, G. W. and Choi, M. Y. "Measurement of the mass specific extinction coefficient for acetylene and ethylene smoke using the large agglomerate optics facility," -- Twenty-Seventh Symposium (International) on Combustion, The Combustion Institute, Pittsburgh, 1998, pp. 1515-1522.
  - [18] Bohren, C. F. and Huffman, D. R., *Absorption and scattering of light by small particles*, John Wiley & Sons, New York (1998).
  - [19] Mulholland, G. W., Hartman, A. W., Hembree, G. G., Marx, E., and Lettieri, T. R., "Development of a one-micrometer-diameter particle size standard reference material," *Journal of Research of the National Bureau of Standards* 90: 3-26 (1985).
  - [20] Holland, A. C. and Gagne, G., "The scattering of polarized light by polydisperse systems of irregular particles," *Applied Optics* 9: 1113-1121 (1970).

Thomas G. Cleary, Darryl W. Weinert\*, and George W. Mulholland  
National Institute of Standards and Technology, Gaithersburg, MD 20899 U.S.A.

\* Guest Researcher at NIST on leave from the Center for Environmental Safety and Risk Engineering,  
Victoria University, Melbourne, Victoria 8001 Australia

## Moment Method for Obtaining Particle Size Measures of Test Smokes

### Abstract

The number concentration, ionization chamber output, and mass concentration were recorded continuously for five different test smokes generated in the fire emulator/detector evaluator. The number and the mass concentrations are direct measures of the zeroth and third moments of the aerosol size distribution, while the ionization chamber output is correlated to a measurement of the first moment. The ratio of the first to zeroth moment and the cube root of the ratio of the third to zeroth moment yielded the count mean diameter ( $d_{10}$ ) and the diameter of average mass ( $d_{30}$ ) with peak values ranging from 0.20  $\mu\text{m}$  to 0.75  $\mu\text{m}$  for  $d_{10}$  and 0.25  $\mu\text{m}$  to 1.0  $\mu\text{m}$  for  $d_{30}$  for the smolder/pyrolysis smokes generated. Assuming a log-normal size distribution, estimates of the geometric standard deviation were computed from the two moment average diameter measurements. Additionally, comparisons of the mass median diameter estimated from moment analysis to the mass median aerodynamic diameter obtained from an 11-stage cascade impactor were made.

### 1. Introduction

Prediction of smoke detector response requires an understanding of the aerosol transport to a detector's sensing volume, the sensing principle (including raw sensor output as a function of the environment and detector logic), and the concentration, physical properties and size distribution of the aerosol. The main sensing principles used in current smoke detectors are light scattering by smoke particles in photoelectric detectors and current decrease due to ion scavenging of smoke particles in ionization smoke detectors. These two detector types have much different response characteristics as function of particle size [1]. Real fire smokes and nuisance source aerosols exhibit both fluctuating concentration and changing particle size distribution as the local conditions producing the aerosol change, and/or particle growth through coagulation or agglomeration takes place. A relatively simple method to continuously monitor the particle statistics along with the concentration as a function of time and possibly at multiple locations would facilitate detector response model, and CFD smoke transport and growth model verification. Such a method is described here which relies on standard aerosol and smoke detector test equipment with no complicated data inversion required. The impetus for choosing the moment method based on the zeroth, first, and third moments is two-fold. First, these moments are obtained by standard equipment. Second, they yield a moment averaged diameter (count mean diameter) that is directly related to ionization detector response normalized by the number concentration, while the third moment (mass concentration) is related to the light extinction through the specific extinction coefficient, and remains unchanged by coagulation or agglomeration.

### 2. Moment Analysis

Moment distributions describe the particle size distribution in terms of a specific weighting function (i.e. weighted by number, volume, surface area, etc.) The general form of a moment average of a particular moment distribution is given by [Hinds, 1999]:

$$d_{qp} = \left( \frac{\sum n_i d_i^q d_i^p}{\sum n_i d_i^q} \right)^{1/p}$$

Where  $p$  and  $q$  are integers defining the  $p$ th moment average of the  $q$ th moment distribution. When  $p = 1$  and  $q = 0$  the count mean diameter is obtained, and when  $p = 3$  and  $q = 0$  the diameter of average mass is obtained. A third diameter of interest is the mass median aerodynamic diameter which is directly obtained from gravimetric analysis of inertially-separated particles in a cascade impactor. The aerodynamic diameter is defined as a unit density sphere with the same inertial characteristics of the real particle.

Defining the functional form of the aerosol size distribution allows for a more complete and compact description of the size distribution. Frequently aerosols are described by the log-normal size distribution because it tends to fit a wide range of skewed aerosol size distributions found in nature, and its form is convenient for analysis. It is functionally similar to the normal distribution in that it is a two-parameter distribution with the logarithm of the diameter being normally distributed. The frequency function is

$$df = \frac{1}{\sqrt{2\pi}d_p \ln \sigma_g} \exp\left(-\frac{(\ln d_p - \ln d_g)^2}{2(\ln \sigma_g)^2}\right) dd_p$$

Where  $d_g$ , the geometric mean diameter, and  $\sigma_g$ , the geometric standard deviation, are given by

$$\ln d_g = \frac{\sum n_i \ln d_i}{\sum n_i}$$

$$\ln \sigma_g = \left( \frac{\sum n_i (\ln d_i - \ln d_g)^2}{N-1} \right)^{1/2}$$

The benefit of fitting the distribution to the log-normal form is that any moment average can be computed quite simply with the use of a conversion equation first derived by Hatch and Choate [1929]. That conversion equation is

$$d_{qp} = d_g \exp\left[\left(q + \frac{p}{2}\right) \ln^2 \sigma_g\right]$$

The mass median diameter is obtained by setting  $p = 0$  and  $q = 3$  in the above equation. For a log-normal distribution it is possible to obtain the geometric mean diameter and the geometric standard deviation by measuring 3 moments of the distribution. For the case of the diameter of average mass and the count mean diameter, the geometric standard deviation is given by

$$\sigma_g = \exp(\ln d_{30} - \ln d_{10})^{1/2}$$

Real aerosol distributions will only approximate the log-normal distribution and significant errors can arise when predicting higher order moment averages of distributions that are not well characterized by the log-normal distribution.

### 3. Experimental Method

The test smokes were sampled in the NIST fire emulator/detector evaluator, a single-pass flow tunnel in which smokes are generated or introduced [Cleary *et al.* 1999, 2001]. A horizontal-flow test section approximately 4 m downstream from the point where the aerosols are generated or introduced is the location where detectors are placed for evaluation and where the aerosols were sampled in this study. The tunnel cross-section is 0.30 m high by 0.60 m wide. The aerosols are well mixed in the cross-section by the time they reach the test section. Mean flow velocity in the tunnel was fixed at approximately 20 cm/s for these tests. Five test smokes were generated and sampled; smoldering cotton wicks from a staged wick ignition device, smoldering polyurethane foam from an upholstered chair seat cushion, beech wood blocks heated on an electrical hot plate, corn oil placed in a glass dish and heated on an electrical hot plate, and bread toasted in a two-slice toaster.

The smoldering cotton wicks are the same fuel specified in EN 54 part 9 test fire 3 [1982]. The staged wick ignition device allows for computer controlled ignition of 8 sets of up to 4 individual wicks 20 cm long in a predetermined sequence [Cleary *et al.*, 2001]. Here, after an initial 60 second delay, four sets of 2 wicks were ignited at 200 s intervals, followed 200 s later by two sets of 4 wicks at a 200 s interval. The long time between subsequent ignitions allows for the ignited wicks to approach a steady burning rate.

A slab of flexible polyurethane foam approximately 15 cm by 10 cm by 7 cm was removed from a chair seat cushion. The chair was a duplicate of the smoldering chair specified for the Home Smoke Alarm Tests being performed by NIST for several sponsors [Peacock *et al.*, 2001]. A nichrome wire loop was inserted in a slit in the foam and after a 60 second delay from the start of data recording 10 volts of alternating current was applied to the loop. The wire heating was sufficient to cause self-sustaining smolder of the foam slab. The smoke production from repeats of this test varies significantly over the test time.

Eight beech wood blocks nominally 3.5 cm by 2.0 cm by 1.0 cm were placed on a square (15.8 cm by 15.8 cm) 750 watt hot plate. The wood blocks are the same fuel source used in EN 54 part 9 test fire 2 [1982], while the number of blocks, hot plate size and power output are differ. After an initial 60 seconds from the start of data collection, the hot plate was turned on to full power causing the wood blocks to pyrolyze. The hot plate was turned off at 1200 s.

Approximately 5.0 cm<sup>3</sup> of corn oil was placed in a 10 cm diameter glass petri dish and heated by the same hot plate used to heat the wood blocks above. Sixty seconds after the data collection started, the oil was continuously heated until it was transformed into a highly-viscous, blackened residue. The power to the hotplate was turned off at 1610 s.

A single slice of white sandwich bread was placed in a two-slice toaster, which had been modified by disabling the pop-up power cutoff switch. After 120 of background data collection, power was applied to the toaster continuously until the bread was charred black. Power was turned off at 390 s.

The zeroth moment is just the number concentration of smoke particles. It was measured by a continuous flow condensation particle counter (CPC - TSI model 3022a<sup>1</sup>). This device counts all particles greater than 10 nm over a concentration range of less than 1 particle/cm<sup>3</sup> to 5 x 10<sup>5</sup> particles/cm<sup>3</sup> With an uncertainty of 3 %. The ambient particle concentration was diluted with particle-free air by a factor of approximately 100:1 so that the upper limit of the instrument was not surpassed. The recorded number concentration was multiplied by the dilution factor for each test to recover the actual number concentration. The flow was sampled from a 7 mm ID copper tube with the opening midway across the tunnel at the upper laser height, pointing in the direction of the oncoming flow.

The first moment was obtained by applying the simple ionization chamber theory of Hosemann [1970] to the current output from a measuring ionization chamber (MIC) placed on the tunnel ceiling at the test section. The opening to the flow starts 2 cm below the ceiling and extends down to 6 cm below the ceiling. The voltage potential and flow through the MIC were typical values of 17 volts and 30 l/min. The first moment ( $M_1$ ) is approximated by

$$M_1 = \frac{1}{K} \frac{\Delta I}{I_0} \frac{2^{-\Delta I/I_0}}{1 - \Delta I/I_0}$$

Where  $\Delta I$  is the current reduction from the initial current  $I_0$ , and  $K$  is a chamber constant. Helsper *et al.*[1983] report a MIC chamber constant of 0.033 cm<sup>2</sup> for smolder smokes whose size distributions were independently measured. The MIC in this study was operated at nominally the same conditions and their chamber constant was used in the analysis.

<sup>1</sup> Certain commercial equipment, instruments, or materials are identified to specify adequately the experimental procedure. Such identification does not imply recommendation or endorsement by the National Institute of Standards and Technology.

Alternatively, a device was built consisting of a residential smoke detector with the outer housing removed and placed inside a 15 cm diameter plenum 20 cm long. Two openings at each end of the plenum allow for smoke to be sucked through it and conversely through the ionization chamber. At a flow of 15 l/min, the ion chamber current monitored from the voltage follower of the smoke detector IC chip.

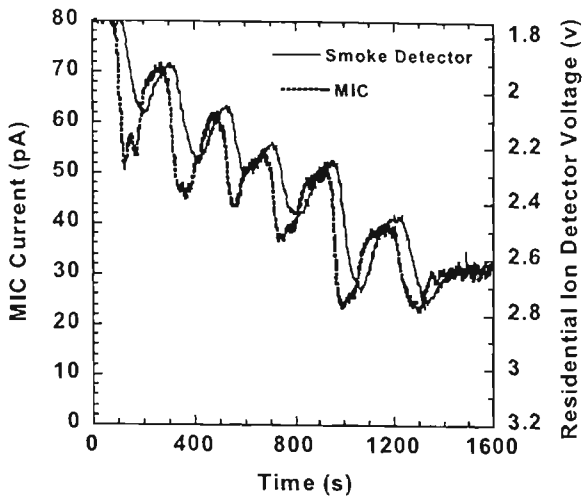


Figure 1. Comparison of MIC current to residential ion chamber voltage during cotton smoke exposure.

Figure 1 shows the response of the MIC and the ionization chamber in the plenum when exposed to the staged wick ignition source described above. The residential ion chamber responds almost identically compared to the MIC with the properly scaled magnitude change identical, but with a slight lag in response. This device would be suitable for, and has been used in field experiments. In the analysis following, the MIC output is used since it responds faster.

The third moment was obtained from direct measurement of the mass concentration from a tapered element oscillating microbalance (TEOM), a device that continuously monitors the aerosol mass concentration. The instrument resolution is  $0.2 \text{ mg/m}^3$  with a range up to several  $\text{g/m}^3$ , which

is well within the smoke concentration ranges being investigated. In the analysis particle density was assumed to be equal to  $1 \text{ g/cm}^3$  since direct measurement of the particle density was not made. Therefore, the diameter of average mass is an apparent diameter that under-predicts the true diameter if the bulk density is less than  $1 \text{ g/cm}^3$  or over-predicts the true diameter if the bulk density is greater than  $1 \text{ g/cm}^3$ . The smoke was sampled at the same location as the CPC. The velocity in the sampling tube was higher than the tunnel flow velocity which will tend to bias the measurement toward a smaller than true mass concentration, however, given the small particle sizes for these aerosols, this sampling bias should be negligible.

An 11 stage cascade impactor [micro-orifice uniform deposit impactor, [Marple *et al.*, 1991]] was used to obtain time averaged mass median aerodynamic diameter of repeated runs of the five sources tested. The aerodynamic diameter cutoff values range from  $18 \text{ }\mu\text{m}$  to  $0.056 \text{ }\mu\text{m}$ , while a zeffluor filter collects all particle mass with diameters less than  $0.056 \text{ }\mu\text{m}$ .

#### 4. Results and Analysis

Figure 2 is a graph of the cotton smolder smoke measurements made inside the test section and through extraction of smoke from the tunnel. All measurements follow the dynamic change of the smoke concentration in time. Figure 3 shows the computed count mean diameter ( $d_{10}$ ), diameter of average mass ( $d_{30}$ ) and the geometric standard deviation ( $\sigma_g$ ) assuming an log-normal distribution. Even though the wick ignition process produces the cyclic concentration change, the computed  $d_{30}$  is relatively steady, and rises from about  $0.20 \text{ }\mu\text{m}$  to  $0.24 \text{ }\mu\text{m}$  during the test. The count mean diameter,  $d_{10}$ , fluctuates more pronounced which appears to be due in part to instrument response differences. The time-smoothed value rises from about  $0.19 \text{ }\mu\text{m}$  to  $0.21 \text{ }\mu\text{m}$  during the test. The computed geometric standard deviation also fluctuates, however, the time-smoothed value of 1.4 was relatively stable throughout the test.

Figure 4 is a graph of the polyurethane smolder smoke measurements made inside the test section and through extraction of smoke from the tunnel. The number concentration shows an early peak at 240 s before any mass concentration was recorded. The MIC also shows an early peak at 230 s which suggests a large quantity of relatively small particles were generated early during foam heating. At 660 s the power to the igniter coil was turned off and smoke production ceased by 800 s. This particular slab of foam did not

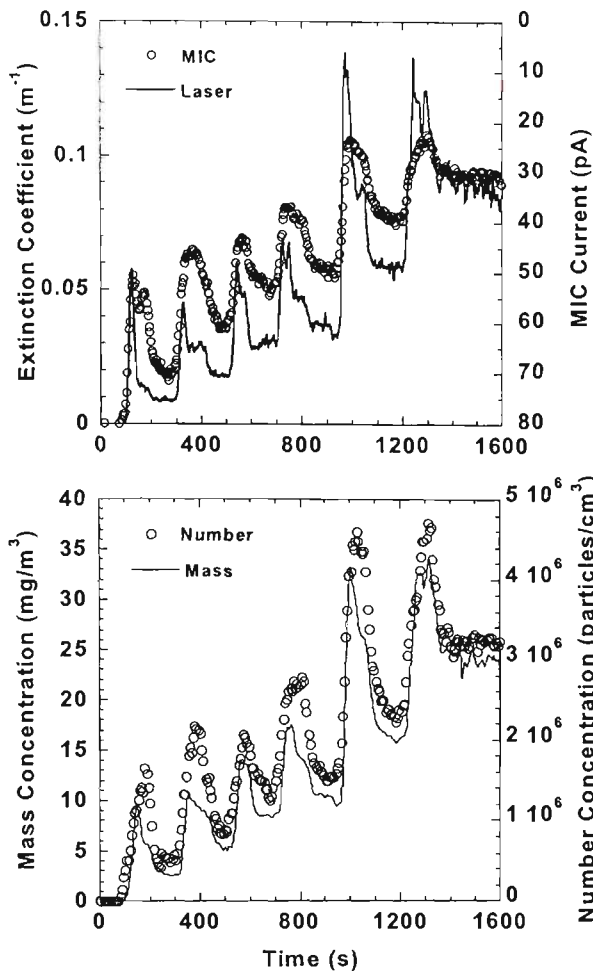


Figure 2. Cotton smolder smoke from staged wick ignition device.

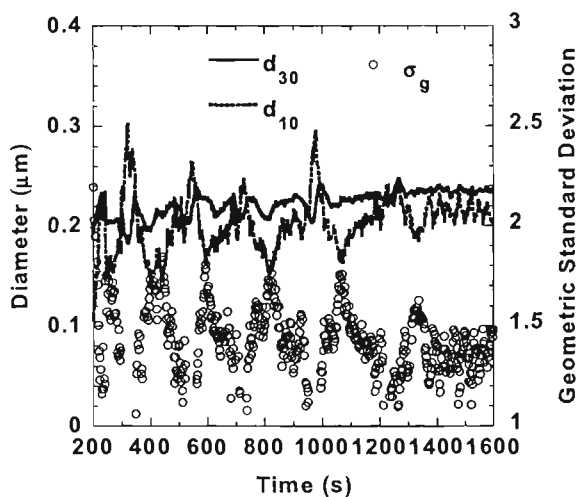


Figure 3. Diameter of average mass ( $d_{30}$ ) and count mean diameter ( $d_{10}$ ) for cotton smolder smoke.

continue to smolder as other nearly identical slabs did. Figure 5 shows the computed moment-averaged diameters. There was a steady rise in  $d_{30}$  from  $0.10 \mu\text{m}$  at 250 s to  $0.75 \mu\text{m}$  at 450 s where it leveled out until rising again at 600 s with a rapid increase occurring at 700 s. After an initial jump to  $0.25 \mu\text{m}$  at 300 s  $d_{10}$  rose steadily until 700 s where it began to rapidly increase. Beginning at 300 s the computed geometric standard deviation rose from about 1.5 to 2.2 at 400 s then fell to a steady value of about 1.5.

Figure 6 is a graph of the smoldering wood block measurements made inside the test section and through extraction of the smoke from the tunnel. The striking observation in the number count is the strong peak at 600 s which is also seen in an early peak in the MIC output. This early peak is associated with residue on the hot plate from previous tests. By about 800 s the smoke contribution is from the smoldering wood blocks alone. The sharp decrease in mass concentration by 1500 s was due to filter clogging in the TEOM rendering the data beyond 1400 s invalid. Figure 7 shows the computed moment-averaged diameters. Both  $d_{10}$  and  $d_{30}$  rise from 600 s to 1000 s where they remain constant until beginning to fall at 1300 s. The computed geometric standard deviation is relatively steady value of about 2.2 during the test.

Figure 8 is a graph of the heated corn oil smoke measurements made inside the test section and through extraction of the smoke from the tunnel. Again, an early peak in number concentration was observed similar to the wood blocks test. Notice that by the time the hot plate is turned off (1610 s) most of the smoke production had ceased. Figure 9 shows the computed moment-averaged diameters. The early oscillation in  $d_{10}$  from 400 to 500 s show is due to randomly fluctuating MIC and CPC values before any real smoke production. The resolution of instruments used here is not sufficient to resolve the particle size statistics of ambient air. Both  $d_{30}$  and  $d_{10}$  begin to rise at 700 s and peak at 1400 s before falling to a steady value at 1500 s. The computed geometric standard deviation show the widest range (1.5 to 3) of any source examined for valid moment data.

Figure 10 is a graph of the toasting bread smoke measurements made inside the test section and through extraction of the smoke from the tunnel. Both number concentration and the MIC output rise prior to any measurable smoke mass and

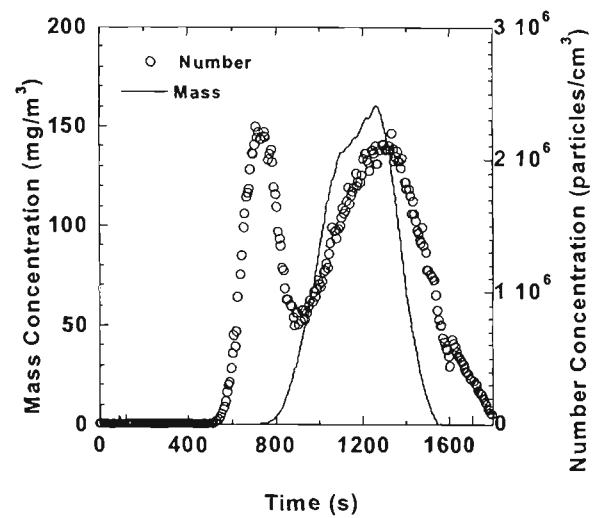
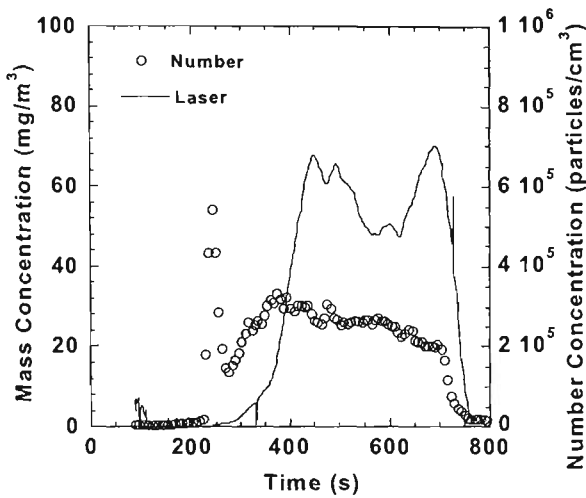
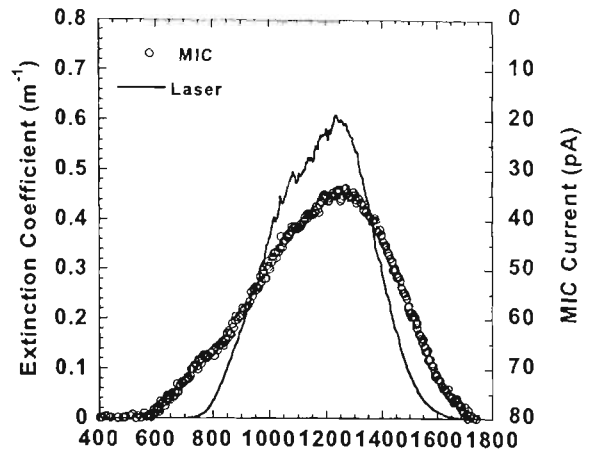
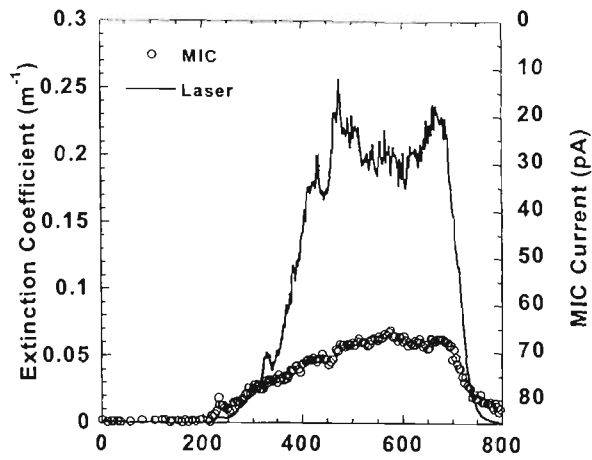


Figure 4. PU foam smolder smoke.

Figure 6. Wood smolder smoke.

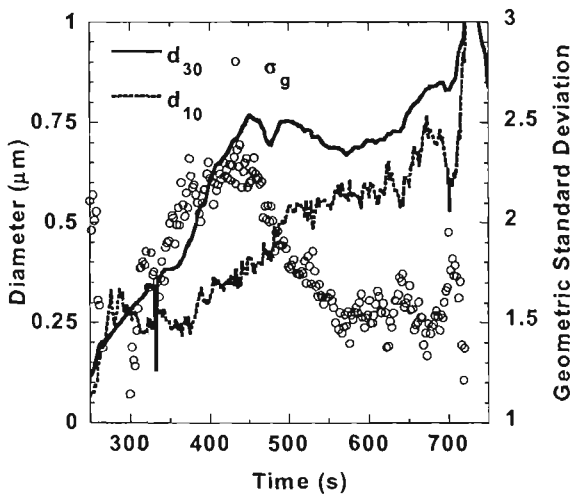


Figure 5. Diameter of average mass ( $d_{30}$ ) and count mean diameter ( $d_{10}$ ) for PU foam smolder smoke.

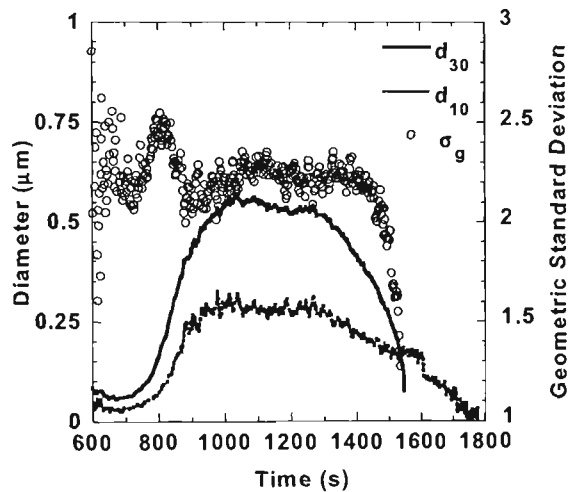


Figure 7. Diameter of average mass ( $d_{30}$ ) and count mean diameter ( $d_{10}$ ) for wood smolder smoke.

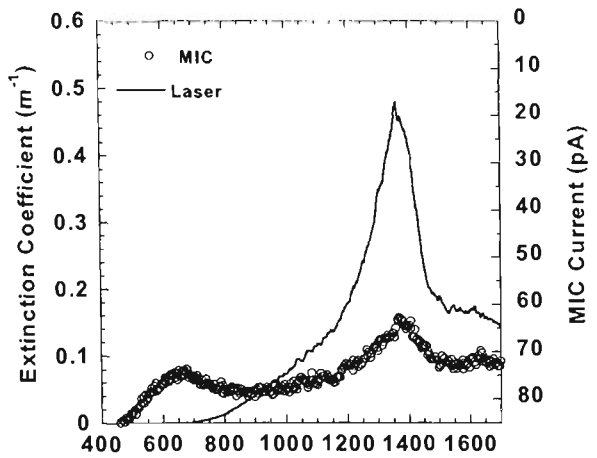


Figure 8. Cooking oil smoke.

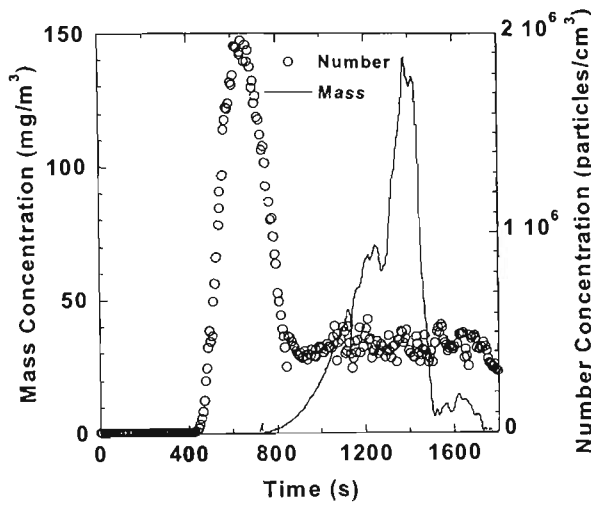


Figure 9. Diameter of average mass ( $d_{30}$ ) and count mean diameter ( $d_{10}$ ) for cooking oil smoke.

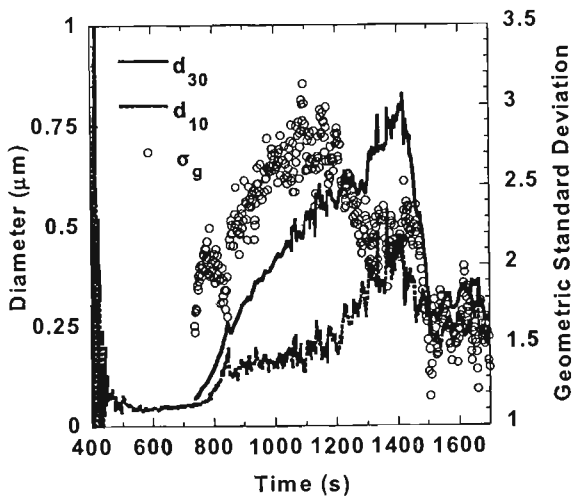


Figure 10. Toasting bread smoke.

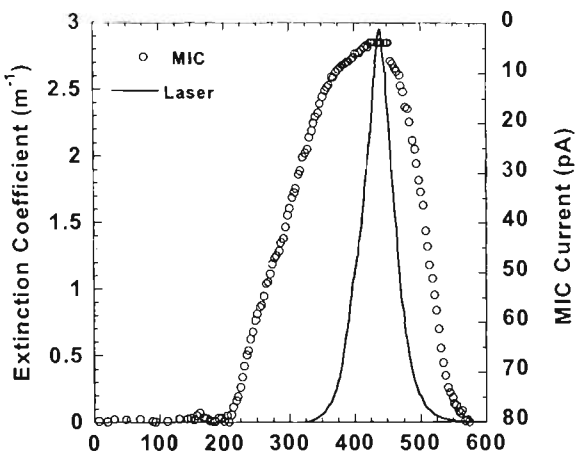


Figure 11. Diameter of average mass ( $d_{30}$ ) and count mean diameter ( $d_{10}$ ) for toast smoke.

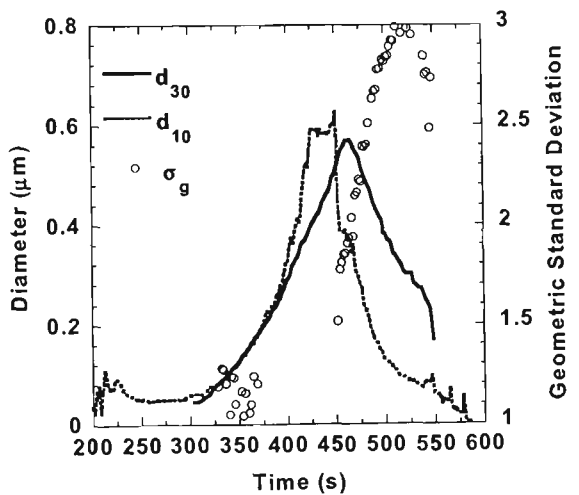


Figure 12. Diameter of average mass ( $d_{30}$ ) and count mean diameter ( $d_{10}$ ) for toasting bread smoke.

appears to be particles shed from the toaster heating elements. As the bread darkens then chars, the mass concentration and extinction coefficient rise rapidly. The source produced both the highest number count and mass concentration of all sources examined. Figure 11 show the computed moment-averaged diameters. The count mean diameter starts at about 0.05  $\mu\text{m}$  then steadily rises to 0.6  $\mu\text{m}$  at 450 s then drops back down to 0.10  $\mu\text{m}$  at 550 s before measurement resolution is lost. The diameter of average mass starts at 0.05  $\mu\text{m}$  at 300 s then steadily rises to a peak of 0.55  $\mu\text{m}$  at 465 s before dropping off. The computation of valid geometric standard deviations was prevented for most of the test when  $d_{10}$  was greater than  $d_{30}$ . It appears that the rapid mass concentration change causes a pronounced shift in the  $d_{30}$  curve allowing  $d_{10}$  to surpass it.

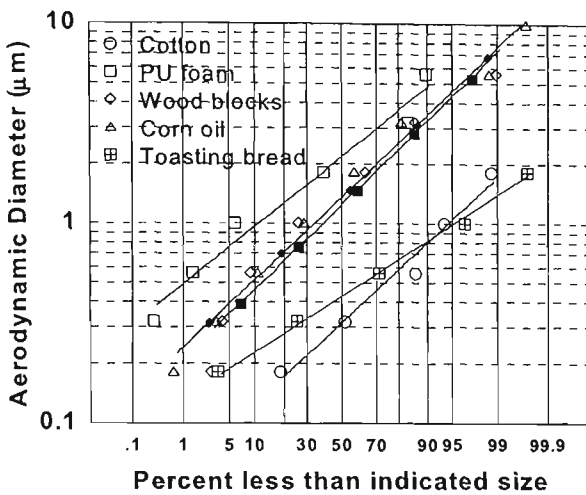


Figure 12. Cascade Impactor results for test smokes.

The impactor data is presented in Figure 12 in a standard analysis form. The percent mass that passes a particular stage is plotted against the stage cutoff aerodynamic diameter. The 50 % less than indicated size value interpolated from a straight line passing through the data is the mass median aerodynamic diameter (MMAD). If a straight line fits the data accurately, it is an indication that a size distribution is uni-modal and would fit a log-normal distribution. The geometric standard deviation is estimated by the ratio of the diameter at 84.1 less than indicated size to the mass median aerodynamic diameter. The mass median diameter and geometric standard deviation for each smoke sample are tabulated in Table 1.

From a time-averaged computed diameter of average mass and geometric standard deviation, a prediction of the mass median diameter was made using the Hatch-Choate equations. The averaging time period was equal to the cascade impactor collection time of a repeated run to facilitate comparison. This prediction is tabulated in Table 1 along with  $d_{30}$  and  $\sigma_g$ . The predicted mass median diameter is nearly equivalent to a mass median aerodynamic diameter since the particles are most likely spherical and  $1 \text{ g/cm}^3$  was the assumed density for the  $d_{30}$  computation. The predictions compare favorably with the impactor MMAD. The biggest deviation is in the polyurethane foam prediction, which is understandable since this test is highly variable and  $d_{30}$  was changing dramatically over the impactor sampling time. The computed and impactor geometric standard deviations compare favorably.

Table 1.

Smoke	Mean $D_{30}$ ( $\mu\text{m}$ )	Mean $\sigma_g$	Predicted MMAD ( $\mu\text{m}$ )	Impactor MMAD ( $\mu\text{m}$ )	$\sigma_g$
Cotton Wick	0.24	1.4	0.28	0.31	1.7
PU foam	1.0	1.6	1.4	2.0	1.6
Wood	0.53	2.25	1.4	1.5	1.9
Corn Oil	0.50	2.5	1.8	1.6	2.2
Toast	0.32	1.6*	0.45	0.43	1.6

\*the geometric standard deviation estimated from the impactor data was used.

## 4. Conclusions

From the results of this study, it is concluded that the moment method described here is robust and produces two continuous size estimates that are consistent and compare favorably with independent measurements of the test smoke size distributions. The early aerosol production from the cooking oil, toasting bread, and wood blocks sources was characterized by large number of small particles, most-likely associated with residual material burning off heated surfaces. All test smokes fit a log-normal size distribution in the latter stages of test runs after the initial aerosol generation (the size distribution of the initial smoke was not characterized.)

The test smokes examined represent a range sources that can cause typical smoke detectors to alarm. It is not surprising that the smoke size distribution evolves in time since source material changes as it heated and degrades or burns. The exception is the stable particle size distribution from the smoldering cotton smoke when all wicks are burning in a self-sustained smolder. Analyzing the size distribution of soot from flaming fuels by the method described here is not as straight forward since soot has a fractal agglomerate structure. More work is planned for soot.

While this method was validated in a laboratory setting, it is easily to implement in a field-test setting. In fact, measurement of the number concentration, mass concentration, and ion chamber output have been made in several field tests as part of an ongoing test program on residential smoke detection.

## 5. References

- Cleary, T., Chernovsky, A., Grosshandler, W., and Anderson, M., "Particulate Entry Lag in Spot-Type Smoke Detectors," Proceedings of the Sixth International Symposium on Fire Safety Science, University of Poitiers, France, pp. 779-790, 1999.
- Cleary, T., Donnelly, M., and Grosshandler, W., "The Fire Emulator/Detector Evaluator: Design, Operation, and Performance," Proceedings of the 12th International Conference on Automatic Fire Detection - AUBE '01, Gaithersburg, MD, pp. 312-323, 2001.
- EN54-9:Components of Automatic Fire Detection Systems, Part 9: Fire Sensitivity Test. *European Committee for Standardization*, 1982.
- Hatch T., and Choate, S., "Statistical Description of the Size Properties of Non-Uniform Particulate Substances," *J. Franklin Inst.*, **207**, 369, 1929.
- Helsper, C., Fissan, H., Muggli, J., and Scheidweiler, A., "Verification of Ionization Chamber Theory," *Fire Technology*, Vol. 19, No. 1, pp. 14-21, 1983.
- Hinds, W.C., "Aerosol Technology: Properties, Behavior, and Measurement of Airborne Particles;" Wiley-Interscience, New York, 1999.
- Hosemann, J., P., "Uber Verfahren zur bestimmung der Korngrossenverteilung hockkonzentrierter Polydispersionen von dielektrischen Miepartileln," Ph.D. thesis, Aachen, 1970.
- Marple, V.A., Rubow, K.L., and Behm, S.M., "A Microorifice Uniform Deposit Impactor (MOUDI): Description, Calibration, and Use," *Aerosol Science and Technology* Vol. 14, pp. 434-446, 1991.
- Peacock, R.D., Averill, J.D., Bukowski, R.W., and Reneke, P.A., "Home Smoke Alarm Tests, Test Series 1," NIST Report of Test FR 4016. National Institute of Standards and Technology, Gaithersburg MD, October, 2001.

REFERENCES

- Abramowitz, M. and Stegun, I.A. (1968) *Handbook of Mathematical Functions*, Dover, New York.
- Aggarwal, S. and Motevalli, V. (1997) Investigation of an approach to fuel identification for non-flaming sources using light-scattering and ionization smoke detector response. *Fire Safety Journal* **29**, 99-112.
- Aherns, M. (1998) Batteries not included. *NFPA Journal* **92**, 98-109.
- Bankston, C.P., Zinn, B.T., Browner, R.F. and Powell, E.A. (1981) Aspects of the mechanisms for smoke generation by burning materials. *Combustion and Flame* **41**, 273-292.
- Beall, K., Grosshandler, W., Luck, H. (Eds.) (2001). Session: Fire Detection in Aircraft, Transport Systems and Special Hazards . In: *AUBE '01: 12th International Conference on Automatic Fire Detection*, pp. 615-700. National Institute of Standards and Technology (NIST), Gaithersburg, MD, USA.
- Berry, M.V. and Percival, I.C. (1986) Optics of fractal clusters such as smoke. *Optica Acta* **33**, 577-591.
- Bohren, C.F. and Huffman, D.R. (1998) *Absorption and scattering of light by small particles*, John Wiley & Sons, New York.
- Born, M. and Wolf, E. (1999) *Principles of Optics: Electromagnetic theory of Propagation, Interference and Diffraction of light*, 7th edn. Cambridge University Press, Cambridge.
- Bottiger, J.R., Edward, S.F. and Thompson, R.C. (1980) Phase matrix measurements for electromagnetic scattering by sphere aggregates. In: Shuerman, D.W., (Ed.) *Light Scattering by Irregularly Shaped Particles*, pp. 283-290. Plenum Press, New York.
- Bryner, N.P. and Mulholland, G.W. (1991) Smoke emission and burning rates for urban structures. *Atmospheric Environment* **25A**, 2553-2562.
- Calcraft, A. M., Green, R. J. S., and McRoberts, T. S. (1975). Burning plastics: smoke formation. *International Symposium on the Fire Safety of Combustible Materials* , 253-257. University of Edinburgh Press, Edinburgh.
- Charalampopoulos, T.T. (1992) Morphology and dynamics of agglomerated particulates in combustion systems using light scattering techniques. *Progress in Energy and Combustion Science* **18**, 13-45.
- Charlson, R.J., Horvath, H. and Pueschel, R.F. (1967) The direct measurement of atmospheric light scattering coefficient for studies of visibility and pollution. *Atmospheric Environment* **1**, 469-478.

- Cheng, Y.S., Bechtold, W.E., Yu, C.C. and Hung, I.F. (1995) Incense smoke: Characterisation and dynamics in indoor environments. *Aerosol Science and Technology* **23**, 271-281.
- Cleary, T., Samson, R. and Gentry, J.W. (1990) Methodology for fractal analysis of combustion aerosols and particle clusters. *Aerosol Science and Technology* **12**, 518-525.
- Cleary, T. C., Donnelly, M., and Grosshandler, W.(2001). The Fire Emulator/Detector Evaluator: Design, Operation and Performance. *AUBE '01: 12th International Conference on Automatic Fire Detection* , pp. 312-323. National Institute of Standards and Technology (NIST), Gaithersburg, MD, USA..
- Cleary, T.G. (1989) *Measurements of the size distribution and aerodynamic properties of soot*, M.Sc. Thesis, The University of Maryland, Maryland, USA.
- Cleary, T.G., Weinert, D.W. and Mulholland, G.W. (To be published) Moment method for obtaining particle size measures of test smokes. *NIST Technical Report* , National Institute of Standards and Technology (NIST), Gaithersburg, MD, USA..
- Colbeck, I., Atkinson , B. and Johar, Y. (1997) The morphology and optical properties of soot produced by different fuels. *Journal of Aerosol Science* **28**, 715-723.
- Crosby, P. and Koerber, B.W. (1963) Scattering of light in the atmosphere. *Journal of the optical society of America* **53**, 358-361.
- Dalzell, W.H., Williams, G.C. and Hottel, H.C. (1970) A light scattering method for soot concentration measurements. *Combustion and Flame* **14**, 161-170.
- Dobbins, R.A., Fletcher, R.A. and Chang, H.C. (1998) The evolution of soot precursor particles in a diffusion flame. *Combustion and flame* **115**, 285-298.
- Dobbins, R.A. and Megaridis, C.M. (1991) Absorption and scattering of light by polydisperse aggregates. *Applied Optics* **30**, 4747-4754.
- Dobbins, R.A., Santoro, R.J. and Semerjian, H.G. (1984) Interpretation of optical measurements of soot in flames. *Progress in Astronautics and Aeronautics: Combustion Diagnostics by Nonintrusive Methods* **92**, 208-237.
- Drysdale, D. (1990) *An introduction to Fire Dynamics*, Wiley-Interscience, Chichester.
- Eccleston, A.J., King, N.K. and Packham, D.R. (1974) The scattering coefficient and mass concentration of smoke from some Australian forest fires. *APCA Journal* **24**, 1049.
- EN54, p.9. (1982) EN54-9: Components of automatic fire detection systems, part 9: Fire sensitivity Test. *Committee for Standardisation*, European Union.
- Erikson, W.D., Williams, G.C. and Hottel, H.C. (1964) Light scattering measurements on soot in a Benzene-Air flame. *Combustion and Flame* **8**, 127-132.
- Forest, S.R. and Witten, T.A. (1979) Long-range correlations in smoke-particle aggregates. *Journal of Physics A.* **12**, L109-L117

- Foster, W.W. (1959) Attenuation of light by wood smoke. *British Journal of Applied Science* **10**, 416-420.
- Gangopadhyay, S., Elminyawi, I. and Sorensen, C.M. (1991) Optical structure factor measurements of soot particles in a premixed flame. *Applied Optics* **30**, 4859-4864.
- Gerber, H.E. and Hindman, E.E. (1982) *Light absorption by aerosol particles*, Spectrum Press, Hampton.
- Germer, T. A.. (2001) SCATMECH: Polarized light scattering C++ class library, Version 3.0, available at <http://physics.nist.gov/Divisions/Div844/facilities/scatmech/html/>
- Glassman, I.(1988). Soot formation in combustion processes. *Twenty-Second Symposium (International) on Combustion*, pp. 295-311. The Combustion Institute, Pittsburgh.
- Grosshandler, W.L. (1997) Towards the development of a universal fire emulator-detector evaluator. *Fire Safety Journal* **29**, 113-127.
- Gucker, F.T. and Egan, J.J. (1961) Measurement of the angular variation of light scattered from single aerosol droplets. *Journal of Colloid Science* **16** , 68-84.
- Guinier, A., Fournet, G., transltn. Walker, C.B. and biblio. Yudowitch, K.L. (1955) *Small-angle scattering of X-rays*, Wiley, New York.
- Haynes, B.S. and Wagner, H.GG. (1981) Soot Formation. *Progress in Energy and Combustion* **7**, 229-273.
- Helsper, C., Fissan, H.J., Muggli, J. and Scheidweiler, A. (1980) Particle number distributions of aerosols from test fires. *Journal of Aerosol Science* **11**, 439-446.
- Hinds, W.C. (1982) *Aerosol Technology: properties, behaviour, and measurement of airborne particles.*, John Wiley & Sons, New York.
- Hobbie, E.K. and Sung, L. (1996) Rayleigh-Gans scattering from polydisperse colloidal suspensions. *American Journal of Physics* **64**, 1298-1303.
- Hodkinson, J. R.(1962). Light scattering and extinction by irregular particles larger than the wavelength. *Proceedings of the Interdisciplinary Conference on Electromagnetic Scattering* , pp. 87-100. Pergamon Press, London.
- Holland, A. (1980) Problems in calibrating a polar nephelometer. In: Schuerman, D., (Ed.) *Light Scattering by irregularly shaped particles*, pp. 247-254. Plenum, New York.
- Holland, A.C. and Draper, J.S. (1967) Analytical and experimental investigation of light scattering from polydispersions of Mie Particles. *Applied Optics* **6**, 511-518.
- Holland, A.C. and Gagne, G. (1970) The scattering of polarized light by polydisperse systems of irregular particles. *Applied Optics* **9**, 1113-1121.
- Hotta, H. and Horiuchi, S.(1985). Detection of smouldering fire in electrical equipment with high internal air flow. *Fire Safety Science - Proceedings of the Second International Symposium*, pp. 699-708. Inter. Assoc. for Fire Safety Science, London.

- Hsu, J.C.L., Presser, C. and Clay, D.T. (1991) In-situ fume particle size and number density measurements from a synthetic smelt. *Chemical Engineering Communication* **102**, 189-209.
- Hunt, A.J. and Huffman, D.R. (1973) A new polarization-modulated light scattering instrument. *Review of Scientific Instruments* **44**, 1753-1762.
- Jin, T. (1978) Visibility through fire smoke. *Journal of Fire and Flammability* **9**, 135-157.
- Johnson D. W., Kilsby, C.G., McKenna, D.S., Saunders, R.W., Jenkins, G.J., Smith, F.B. and Foot, J.S. (1991) Airborne observations of the physical and chemical characteristics of the Kuwait oil smoke plume. *Nature* **353**, 617-621.
- Jones, D.S. (1955) On the scattering cross section of an obstacle. *Philosophical Magazine* **7**, 957-962.
- Jullien, R. and Botet, R. (1987) *Aggregation and Fractal Aggregates*, World Scientific, Singapore.
- Kemp, J.C. (1969) Piezo-Optical Birefringence Modulators: New use for a long-known effect. *Journal of the Optical Society of America* **59**, 950-954.
- Kerker, M. (1969) *The scattering of light and other electromagnetic radiation*, Academic Press, New York.
- Kerker, M. (1991) Founding fathers of light scattering and surface-enhanced Raman scattering. *Applied Optics* **30**, 4699-4705.
- Kolb, M., Botet, R. and Jullien, R. (1983) Scaling of kinetically growing clusters. *Physical Review Letters* **51**, 1123-1126.
- Koylu, U.O. and Faeth, G.M. (1994a) Optical properties of over fire soot in buoyant turbulent diffusion flames at long residence times. *Journal of Heat Transfer* **116**, 152-159.
- Koylu, U.O. and Faeth, G.M. (1994b) Optical properties of soot in buoyant laminar diffusion flames. *Journal of Heat Transfer* **116**, 971-979.
- Koylu, U.O., Faeth, G.M., Farias, T.L. and Carvalho, M.G. (1995) Fractal and projected structure properties of soot agglomerates. *Combustion and Flame* **100**, 621-633.
- Lee, T.G.K. and Mulholland, G. (1977) Physical properties of smoke pertinent to smoke detector technology, NBSIR 77-1312, Washington, D.C.: National Bureau of Standards.
- Leonard, S., Mulholland, G.W., Puri, R. and Santoro, R.J. (1994) Generation of CO and smoke during underventilated combustion. *Combustion and Flame* **98**, 20-34.
- Lilionfeld, P. (1991) Gustav Mie: the person. *Applied Optics* **30**, 4696-4698.
- Loepfe, M., Ryser, P., Tomkin, C. and Wieser, D. (1997) Optical properties of fires and non-fire aerosols. *Fire Safety Journal* **29**, 185-194.

- Lu, N. and Sorensen, C.M. (1994) Depolarized light scattering from soot agglomerates. *Physical Review E* **50**, 3109-3115.
- Mandelbrot, B.M. (1983) *The Fractal Geometry of Nature*, W. H. Freeman, San Francisco.
- Marple, V.A., Rubow, K.L. and Behm, S.M. (1991) A micro-orifice uniform deposit impactor (MOUDI): Description, calibration and use. *Aerosol Science and Technology* **14**, 434-446.
- Martin, J.E. and Hurd, A.J. (1987) Scattering from fractals. *Journal of Applied Crystallography* **20**, 61-78.
- Marx, E. and Mulholland, G.W. (1983) Size and refractive index determination of single polystyrene spheres. *Journal of Research of the National Bureau of Standards* **88**, 321-338.
- Meacham, B.J. and Motevalli, V. (1992) Characterisation of smoke from smouldering combustion for the evaluation of light scattering type smoke detector response. *Journal of Fire Protection Engineering* **4**, 17-28.
- Meakin, P. (1984) Effects of cluster trajectories on cluster-cluster aggregation: A comparison of linear and Brownian trajectories in two- and three-dimensional simulations. *Physical Review A* **29**, 997-999.
- Meakin, P. (1998) *Fractals, scaling, and growth far from equilibrium*, Cambridge University Press, New York.
- Mie, G. (1908) Beitrage zur optik truber medion speziell kolloidaler metallosungen. *Annalen der Physik* **25**, 377-445.
- Mountain, R.D. and Mulholland, G.W. (1988) Light scattering from simulated smoke agglomerated. *Langmuir* **4**, 1321-1326.
- Moussa, N. A., Toong, T. Y, and Garris, C. A(1979). Mechanisms of smouldering of cellulosic materials. *Sixteenth Symposium (International) on Combustion* , 1447-1457. The Combustion Institute, Pittsburgh.
- Mulholland, G.W. (1982) How are we measuring smoke? *Fire and Materials* **6**, 65-67.
- Mulholland, G.W. (1995) Smoke production and properties. In: DiNenno, P.J., Beyler, C.L., Custer, R.L.P., Walton, W.D., Watts, J.M., Drysdale, D. and Hall, J.R., (Eds.) 2nd edn. *SFPE Handbook of Fire Protection Engineering*, pp. 2-217-227. National Fire Protection Association and the Society of Fire Protection Engineers, Massachusettes.
- Mulholland, G.W. and Bryner, N.P. (1994) Radiometric model of the transmission cell-reciprocal nephelometer. *Atmospheric Environment* **28**, 873-887.
- Mulholland, G.W., Bryner, N.P. and Croarkin, C. (1999) Measurement of the 100 nm NIST SRM 1963 by Differential Mobility Analysis. *Aerosol Science and Technology* **31**, 39-55.
- Mulholland, G. W. and Choi, M. Y.(1998). Measurement of the mass specific extinction coefficient for acetylene and ethylene smoke using the large agglomerate optics facility. *Twenty-Seventh Symposium (International) on Combustion*, pp. 1515-1522. The Combustion Institute, Pittsburgh.

- Mulholland, G.W. and Croarkin, C. (2000) Specific extinction coefficient of flame generated smoke. *Fire and Materials* **24**, 227-230.
- Mulholland, G.W., Hartman, A.W., Hembree, G.G., Marx, E. and Lettieri, T.R. (1985a) Development of a one-micrometer-diameter particle size standard reference material. *Journal of Research of the National Bureau of Standards* **90**, 3-26.
- Mulholland, G. W, Henzel, V., and Babrauskas, V.(1989). The effect of scale on smoke emission. *Fire Safety Science - Proceedings of the Second International Symposium*, pp. 347-357. Inter. Assoc. for Fire Safety Science, London.
- Mulholland, G.W. and Liu, B.Y.H. (1980) Response of smoke detectors to monodisperse aerosols. *Journal of research of the National Bureau of Standards* **85**, 223-238.
- Mulholland, G.W., McKenzie, R.L., Marx, E. and Fletcher, R.A. (1985b) Refractive index and evaporation rate of individual smoke droplets. *Langmuir* **1**, 367-372.
- Mulholland, G.W. and Ohlemiller, T.J. (1982) Aerosol characterisation of a smouldering source. *Aerosol Science and Technology* **1**, 59-71.
- Nagashima, T., Mammoto, A., Yamauchi, Y., Watanabe, K., and Mizobuchi, M.(1999). Optimization of sensitivity characteristics of photoelectric smoke detector to various smokes. *AUBE '01: Proceedings 12th International Conference on Automatic Fire Detection*, pp. 319-331. Gaithersburg, MD, USA .
- National Fire Protection Association (1993) *NFPA 92B Guide of Smoke Management Systems in Malls, Atria and Large Areas*. NFPA, Quincy, MA.
- Napper, D.H. and Ottewill, R.H. (1964) Multiple scattering effects in polystyrene latex dispersions. *Journal of Colloid Science* **19**, 72-80.
- National Toxicology Program (2002) NTP Chemical Repository: Corn Oil. Access available at <http://ntp-server.niehs.nih.gov/>
- Odian, G. (1991) *Principles of Polymerization*, John Wiley and Sons, New York.
- Oh, C. and Sorensen, C.M. (1999) Scaling approach for the structure factor of a generalized system of scatterers. *Journal of Nanoparticle Research* **1**, 369-377.
- Ohlemiller, T.J. (1995) Smouldering Combustion. In: DiNunno, P.J., Beyler, C.L., Custer, R.L.P., Walton, W.D., Watts, J.M., Drysdale, D. and Hall, J.R., (Eds.) 2 edn. *SFPE Handbook of Fire Protection Engineering*, pp. 2-171-179. National Fire Protection Association and the Society of Fire Protection Engineers, Massachusetts.
- Packham, D.R., Gibson, L. and Linton, M. (1975) The detection of smoke in air-conditioned and ventilated buildings. *Telecommunications Journal of Australia* **25**, 261
- Palmer, H.B. and Seery, D.J. (1973) Chemistry of pollutant formation in flames. *Annual Review of Physical Chemistry* **24**, 235-262.
- Paul, M., Issacci, F., Catton, I. and Apostolakis, G.E. (1997) Characterisation of smoke particles generated in terrestrial and microgravity environments. *Fire Safety Journal* **28**, 233-252.

- Perry, R.J., Hunt, A.J. and Huffman, D.R. (1978) Experimental determinations of Muller scattering matrices for nonspherical particles. *Applied Optics* **17**, 2700-2710.
- Phalen, R.F., Cannon, W.C. and Esparza, D. (1976) Comparison of impaction, centrifugal separation and electron microscopy for sizing cigarette smoke. In: Liu, B.Y.H., (Ed.) *Fine Particles*, pp. 732-735. Academic Press, New York.
- Pinnick, R.G., Carroll, D.E. and Hofmann, D.J. (1976) Polarised light scattered from monodisperse randomly orientated nonspherical aerosol particles: measurements. *Applied Optics* **15**, 384-393.
- Pluchino, A.B., Goldberg, S.S., Dowling, J.M. and Randall, C.M. (1980) Refractive-index measurements of single micron sized carbon particles. *Applied Optics* **19**, 3370-3372.
- Press, W.H., Teukolsky, S.A., Vetterling, W.T. and Flannery, B.P. (1995) *Numerical Recipes in C: The art of scientific computing*, 2nd edn. Cambridge University Press, New York.
- Prichard, B.S. and Elliot, W.G. (1960) Two instruments for atmospheric optics measurements. *Journal of the Optical Society of America* **50**, 191-202.
- Quirantes, A., Arroyo, F. and Quirantes-Ros, J. (2001) Multiple light scattering by spherical particle systems and its dependence on concentration: A T-Matrix study. *Journal of Colloid and Interface Science* **240**, 78-82.
- Rasbash, D.J. and Phillips, R.P. (1978) Quantification of smoke produced at fires: Test methods for smoke and methods of expressing smoke evolution. *Fire and Material* **2**, 102-109.
- Rau, J.A. (1989) Composition and size distribution of residential wood smoke particles. *Aerosol Science and Technology* **10**, 181-198.
- Sachweh, B.A., Dick, W.D. and McMurry, P.H. (1995) Distinguishing between spherical and nonspherical particles by measuring the variability in azimuthal light scattering. *Aerosol Science and Technology* **23**, 373-391.
- Samson, R.J., Mulholland, G.W. and Gentry, J.W. (1987) Structural analysis of soot agglomerates. *Langmuir* **3**, 272-281.
- Schaefer, D.W., Martin, J.E., Wiltzius, P. and Cannell, D.S. (1984) Fractal Geometry of colloidal aggregates. *Physical Review Letters* **52**, 2371-2374.
- Seader, J. D. and Einhorn, I. N. (1976). Some physical, chemical, toxicological and physiological aspects of fire smoke. *Sixteenth Symposium (International) on Combustion*, 1423-1445. The Combustion Institute, Pittsburgh.
- Simmons, R.F. (1995) Fire Chemistry. In: Cox, G., (Ed.) pp. 405-473. Academic Press, London.
- Sivathanu, Y.R. and Faeth, G.M. (1990) Soot volume fractions in overfire region of turbulent diffusion flames. *Combustion and Flame* **81**, 133-149.
- Smith, L.E., Smith, C.L. and Ayres, J.L. (1997) When detectors don't work. *National Fire Protection Association Journal* **91**, 41-45.

- Sorensen, C.M. (1997) Scattering and absorption of light by particles and aggregates. In: Birdi, K.S., (Ed.) *Handbook of Surface and Colloid Chemistry*, pp. 533-558. CRC Press.
- Sorensen, C.M. (2001) Light scattering from fractal aggregates. *Aerosol Science and Technology* **35**, 648-687.
- Sorensen, C.M., Cai, J. and Lu, M. (1992) Light-Scattering measurements of monomer size, monomers per aggregate, and fractal dimension for soot aggregates in flames. *Applied Optics* **31**, 6547-6557.
- Sorensen, C.M. and Feke, G.D. (1996) The morphology of macroscopic soot. *Aerosol Science and Technology* **25**, 328-337.
- Sorensen, C.M. and Fischbach, D.J. (2000) Patterns in Mie scattering. *Optics Communications* **173**, 145-153.
- Sorensen, C.M. and Wang, G.M. (1999) Size distribution effect on the power law regime of the structure factor of fractal aggregates. *Physical Review E* **60**, 7143-7148.
- Taylor, B.N. and Kuyatt, C.E. (1993) Guidelines for evaluating and expressing the uncertainty of NIST measurement results. *NIST Technical Note, 1297*
- Thompson, R.C., Bottiger, J.R. and Fry, E.S. (1980) Measurement of polarised light interactions via the Muller matrix. *Applied Optics* **19**, 1323-1332.
- UL 217 (1993) Standard for single and multiple station smoke detectors. Underwriters Laboratories Inc., Northbrook, IL, USA.
- van de Hulst, H.C. (1981) *Light Scattering by small particles*, reprint of 1957 edition edn. Dover Publications, New York.
- Waggoner, A.P., Weiss, R.E., Ahlquist, N.C., Covert, D.S., Will, S. and Charlson, R.J. (1981) Optical characteristics of atmospheric aerosols. *Atmospheric Environment* **15**, 1891-1909.
- Wagner, H. G.(1979). Soot formation in combustion. *Seventeenth Symposium (International) on Combustion* , 3-19. The Combustion Institute, Pittsburgh.
- Watanabe, A., Sasaki, H., and Unoki, J. (1985). Overview on Fire Detection in Japan. *Fire Safety Science – Proceedings of the First International Symposium*, 679-687. Inter. Assoc. for Fire Safety Science, London.
- Weinert, D. W., Cleary, T. C., and Mulholland, G. W.(2001). Size distribution and light scattering properties of test smokes. *AUBE '01: 12th International Conference on Automatic Fire Detection*, pp. 58-70. National Institute of Standards and Technology, Gaithersburg.
- Weinert, D. W., Cleary, T. C., and Mulholland, G. W. (2002). Light Scattering Characteristics and Size Distribution of Smoke and Nuisance aerosols. *Fire Safety Science - Proceedings of the Seventh International Symposium* , **To be published**.
- Wijayasinghe, M. S. and Makey, T. B. (1997) Cooking Oil: A home fire hazard in Alberta, Canada. *Fire Technology* **33**, 140-166.

- Wiscombe, W.J. (1980) Improved Mie scattering algorithms. *Applied Optics* **19**, 1505-1509.
- Witten, T.A. and Sander, L.M. (1981) Diffusion-limited aggregation, a kinetic critical phenomenon. *Physical Review Letters* **47**, 1400-1403.
- Wu, M.K. and Friedlander, S.K. (1993) Note on the power law equation for fractal-like aerosol agglomerates. *Journal of Colloid and Interface Science* **159**, 246-248.
- Wyatt, P.J. (1980) Some chemical, physical and optical properties of fly ash particles. *Applied Optics* **19**, 975-983.
- Wyatt, P.J. and Phillips, D.T. (1972) Structure of single bacteria from light scattering. *Journal of Theoretical Biology* **37**, 493-501.
- Yoshiyuki, E., Da-Ren, C. and Pui, D.Y.H. (1998) Effects of particle polydispersity and shape factor during dust cake loading. *Powder Technology* **98**, 241-249.
- Zhang, H.X., Sorensen, C.M., Ramer, E.R., Oliver, B.J. and Merklin, J.F. (1988) In situ optical structure factor measurements of an aggregating soot aerosol. *Langmuir* **4**, 867-871.